

Air Force Institute of Technology

AFIT Scholar

Theses and Dissertations

Student Graduate Works

6-1996

Direct Measurement of Skin Friction in High Temperature and Impulsively Started Supersonic Flowfields

David M. Hazelton

Follow this and additional works at: <https://scholar.afit.edu/etd>



Part of the [Aerodynamics and Fluid Mechanics Commons](#)

Recommended Citation

Hazelton, David M., "Direct Measurement of Skin Friction in High Temperature and Impulsively Started Supersonic Flowfields" (1996). *Theses and Dissertations*. 6079.

<https://scholar.afit.edu/etd/6079>

This Dissertation is brought to you for free and open access by the Student Graduate Works at AFIT Scholar. It has been accepted for inclusion in Theses and Dissertations by an authorized administrator of AFIT Scholar. For more information, please contact AFIT.ENWL.Repository@us.af.mil.



DISTRIBUTION STATEMENT A

Approved for public release;
Distribution Unlimited

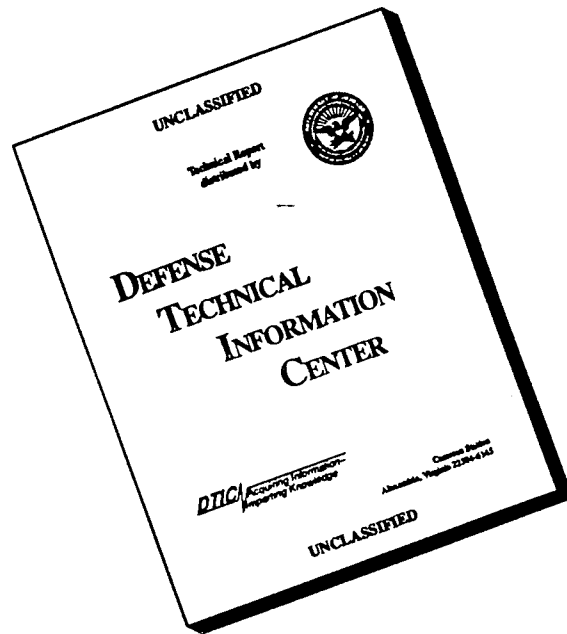
19960719 092

DEPARTMENT OF THE AIR FORCE
AIR UNIVERSITY
AIR FORCE INSTITUTE OF TECHNOLOGY

Wright-Patterson Air Force Base, Ohio

DTIC QUALITY INSPECTED 4

DISCLAIMER NOTICE



THIS DOCUMENT IS BEST QUALITY AVAILABLE. THE COPY FURNISHED TO DTIC CONTAINED A SIGNIFICANT NUMBER OF PAGES WHICH DO NOT REPRODUCE LEGIBLY.

AFIT/DS/ENY/96-9

**DIRECT MEASUREMENT OF SKIN FRICTION
IN HIGH TEMPERATURE AND IMPULSIVELY
STARTED SUPERSONIC FLOWFIELDS**

DISSERTATION

David M. Hazelton, Major, USAF

AFIT/DS/ENY/96-9

Approved for public release; distribution unlimited

DTIC QUALITY INSPECTED 4

AFIT/DS/ENY/96-9

**DIRECT MEASUREMENT OF SKIN FRICTION
IN HIGH TEMPERATURE AND IMPULSIVELY STARTED
SUPERSONIC FLOWFIELDS**

DISSERTATION

Presented to the Faculty of the Graduate School of Engineering

of the Air Force Institute of Technology

Air University

in Partial Fulfillment of the

Requirements for the degree of

Doctor of Philosophy

David M. Hazelton, B.S., M.E.

Major, USAF

June 1996

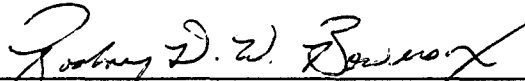
Approved for public release; distribution unlimited

**DIRECT MEASUREMENT OF SKIN FRICTION IN HIGH TEMPERATURE
AND IMPULSIVELY STARTED SUPERSONIC FLOWFIELDS**

David M. Hazelton, B.S., M.E.

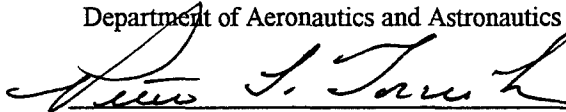
Major, USAF

Approved:



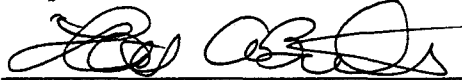
27 June 1996

RODNEY D. W. BOWERSOX, Research Advisor
Assistant Professor of Aerospace Engineering
Department of Aeronautics and Astronautics



4 June 1996

PETER J. TORVIK, Committee Member
Professor Emeritus of Aerospace Engineering and Engineering Mechanics
Department of Aeronautics and Astronautics



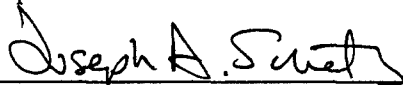
4 June '96

THOMAS A. BUTER, Committee Member
Major, USAF
Assistant Professor of Aerospace Engineering
Department of Aeronautics and Astronautics



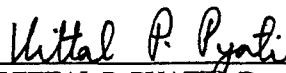
4 Jun 96

MICHAEL G. STOECKER, Committee Member
Captain, USAF
Assistant Professor of Mathematics
Department of Mathematics and Statistics



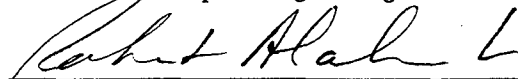
4 June 1996

JOSEPH A. SCHETZ, Committee Member
J. Byron Maupin Professor
Department of Aerospace and Ocean Engineering
Virginia Polytechnic Institute and State University



4 June 1996

VITTAL P. PYATI, Dean's Representative
Associate Professor of Electrical Engineering
Department of Electrical and Computer Engineering



ROBERT A. CALICO, JR.
Dean, Graduate School of Engineering

Preface

The purpose of this research was to develop and use a method to accurately measure skin friction in high enthalpy shock tunnel tests. This research continues an effort begun by Drs. Bowersox and Schetz, who first developed the miniature plastic cantilever floating element skin friction gauge upon which the present research is based.

The impetus for the proposed research came from the need to assess the skin friction in scramjet development efforts undertaken by the Air Force and NASA. However, the research was aimed more toward investigation of the physics of high temperature flows and the mechanics of the skin friction gauge than at specific scramjet applications. The skin friction gauges developed in this research can be used for any short duration, high temperature testing, and the directional gauge technology can be adapted for lower speed and long duration flows.

Many people have contributed to the success of this research. First, I want to thank my advisor, Dr. Rodney Bowersox, for all of the guidance and assistance that he provided, as well his ideas, enthusiasm, and patience. I also want to thank the other members of my research committee, Dr. Peter Torvik, Dr. Joseph Schetz, Major Tom Buter, and Captain Mike Stoecker, and the Dean's representative, Dr. Vittal Pyatti, for their assistance in improving this document. I would also like to thank Lt Col Jerry Bowman, who gave me some timely advice on both thermocouples and shock tunnels. In the laboratory, I want to thank Charlie McNeely, who helped me with the shock tunnel, Andy Pitts, who calibrated the pressure transducers and helped assemble several of the skin friction gauges, and Jay Anderson, who helped with the amplifiers and computers. In the AFIT model fabrication shop, I need to thank John Brohas, who made the gauges, and Dave Driscoll and Jack Tiffany, who made the shock tunnel models. I also need to thank Chris O'Brien in the cooperative electronics laboratory for sputtering the gauges..

At NASA Ames, I need to thank John Cavolowsky, Mark Loomis, and Jamie Dunn for their assistance and interest in the research. At the General Applied Science

Laboratories (GASL), I would like to thank John Calleja and Renaldo Perez, who were very helpful. In the Wright Laboratory, I need to thank Dick Neumann and Jim Hayes for their assistance in the Mach 6 tests. I also want to thank Michael Novean, who as a fellow Ph.D. student pursued research along related lines at Virginia Tech and whose advice in the NASA Ames and GASL tests was very useful.

I want to thank the most important people in my life, my wife, Linda, and my children, Lisa and David, for their support and understanding during the long hours that I spent doing this research. I also want to thank Linda for her help with organizing the research, editing the paper, and making copies.

Finally, and most importantly, I want to thank God, my Eternal Father, and Jesus my Lord and Savior, for giving me the strength and wisdom to complete this research, the Holy Spirit for guiding me, and the angels for watching over me. I owe all of the success that I have had, both in my professional and personal life, to the grace that God has shown me because of my faith in Jesus. I have completed this research with the strength that God provides, so that in all things God may be praised through Jesus Christ. To Him be the glory and the power for ever and ever.

David M. Hazelton

Table of Contents

	Page
Preface	iii
List of Figures.....	xiii
List of Tables	xx
List of Symbols	xxii
Abstract	xxvi
I. Introduction.....	1
1.1 Overview	2
1.2 Statement of the Problem and Synopsis of Work	5
1.3 Significance of the Contribution	6
1.4 Overview of the Dissertation	8
II. Background	10
2.1 Hypersonic Flight and Hypersonic Testing	10
2.2 Skin Friction	13
2.2.1 Significance of Skin Friction	13
2.2.2 Prediction of Skin Friction	15
2.2.3 Measurement of Skin Friction	16
2.2.3.1 Direct Measurement Techniques.....	17
2.2.3.2 Indirect Measurement Techniques	18
2.2.4 Literature Review of Skin Friction Measurement Techniques	20
2.3 The Cantilever Floating Element Skin Friction Gauge.....	21
2.3.1 Gauge Operation	24
2.3.2 Calibration.....	25
III. Skin Friction Gauge Mechanics.....	28
3.1 Static Response.....	28

3.1.1	Gauge Sensitivity	29
3.1.2	Tip Deflection.....	32
3.1.3	Protrusion of the Sensor Head into the Flow due to Deflection	34
3.1.4	Effect of Canting the Gauge.....	38
3.2	Dynamic Response	39
3.2.1	Natural Frequency	39
3.2.2	Critical Damping.....	44
3.2.3	Effect of Vibrating Base.....	52
3.3	Material Mechanics	56
3.3.1	Failure Limits.....	56
3.3.2	Viscoelasticity	57
3.3.2.1	Mechanical Model	58
3.3.2.2	Experimental Measurements.....	60
3.3.2.3	Potential Error in Calibration and Use	62
3.4	Pressure Sensitivity	63
3.4.1	Normal Pressure Sensitivity	64
3.4.1.1	Experimental Evidence	65
3.4.1.2	Analysis.....	67
3.4.2	Pressure Gradient Sensitivity.....	68
3.4.2.1	Analysis.....	69
3.4.2.2	Experimental Results	72
3.5	Gauge Performance Optimization and Alternative Geometries	75
3.5.1	Gauge Performance Optimization	76
3.5.2	The I-Beam Cantilever Gauge.....	79
3.5.3	Hollow Beam Sensor	82
3.6	Directional Gauge	83
3.6.1	Theory.....	84
3.6.1.1	Ideal Relations.....	84
3.6.1.2	Misalignment of Strain Gauges and Apparent Axis Effect	86
3.6.1.3	Non-Orthogonal Axes	89
3.6.2	Calibration.....	90
3.6.3	Gauge Evaluation	93
3.6.3.1	Static Calibration Test.....	94
3.6.3.2	Wind Tunnel Gauge Evaluation Tests.....	97
IV.	Skin Friction Gauge Application Issues	100

4.1	Thermal Effects	100
4.1.1	Heat Transfer Analysis.....	100
4.1.2	Surface Thermal Characteristics	104
4.1.2.1	Effect on Flowfield of Variation in Wall Temperature ..	104
4.1.2.2	Analytical Quantification of Gauge/Wall Thermal Mismatch Effect	105
4.1.2.3	Experimental Analysis of Effect of Gauge/Wall Thermal Mismatch.....	106
4.1.3	Strain Gauge Thermal Effects	108
4.1.4	Thermal Effects on Material Properties	111
4.2	Surface Durability	112
4.3	Gauge Servicing	114
4.3.1	Oil Insertion.....	115
4.3.1.1	Pressure and Surface Tension Effects	115
4.3.1.2	Oil Insertion Process	118
4.3.1.3	Time Requirements for Oiling the Gauge	123
4.3.2	Wind Tunnel Response	124
4.3.2.1	Pressure Difference Between Top and Bottom of Gauge.....	124
4.3.2.2	Pressure Gradient.....	125
4.3.2.3	Oil Loss Due to Evaporation and Heating Effects	126
4.3.2.4	Shock Test.....	127
4.3.2.5	Operating the Gauge in an Inverted Position.....	128
4.3.3	Replenishment Device.....	129
4.4	Electrical Response and Calibration	129
4.4.1	Electrical Analysis.....	131
4.4.2	Calibration.....	133
V.	Skin Friction Gauge Application in Scramjet Tests.....	136
5.1	NASA Ames Scramjet Shock Tunnel Tests	136
5.1.1	Application of measurements	138
5.1.2	Gauge Analysis.....	139
5.1.3	Reported Data and Discussion of Traces	142
5.2	Wright Laboratory Mach 6 Inlet Tests.....	146

5.2.1	Skin Friction Correlations and Data Analysis.....	148
5.2.2	Discussion of Results	149
5.2.3	Re-Calibration and Pressure Test	154
5.3	Hypulse Scramjet Combustor Test.....	154
5.3.1	Overview of the Tests.....	155
5.3.2	Oil Problem	156
5.3.3	Results.....	157
VI.	Shock Tunnel Characterization.....	160
6.1	Theoretical Characterization.....	160
6.1.1	Shock Tunnel Description.....	160
6.1.2	Shock Tube Calculations	162
6.1.2.1	Incident Shock	163
6.1.2.2	Reflected shock and Nozzle.....	165
6.1.2.3	Diverging Nozzle	166
6.1.2.4	Test Section Stagnation Conditions	167
6.1.3	Steady Flow Time.....	167
6.1.3.1	Time for Reflected Shock to Reach the Contact Surface.....	167
6.1.3.2	Tailored Condition and Type and Speed of Second Reflection.....	169
6.1.3.3	Test Section Starting Dynamics.....	171
6.1.3.4	Test Section Evacuation	173
6.1.4	Helium.....	174
6.1.5	Expansion at Nozzle Exit.....	175
6.1.6	Results of Shock Tunnel Characterization Studies.....	176
6.1.7	Data Reduction.....	178
6.2	The AFIT Shock Tunnel Facility	179
6.2.1	Description of Facility.....	180
6.2.2	Instrumentation.....	182
6.2.2.1	Data Acquisition System	182
6.2.2.2	Pressure Transducers.....	183
6.2.2.3	Thermocouple	184
6.2.2.4	Skin Friction Gauges	185
6.2.3	Shock Tunnel Operation	185
6.3	Experimental Characterization of the Shock Tunnel.....	186
6.3.1	Pressure and Temperature Traces	186
6.3.2	Shock Attenuation	188

6.3.3	Pressure Variation	190
6.3.4	Helium Temperature	191
6.4	Analysis of Representative Flight Conditions	192
6.4.1	Equivalent Mach Number	193
6.4.2	Equivalent Altitude	194
VII.	Application of Directional Skin Friction Gauge in a Flow About a Sharp Fin Mounted on a Flat Plate.....	197
7.1	Nature of the Flowfield	198
7.2	Overview of the Experiment	202
7.3	Analysis of Flowfield.....	204
7.3.1	Inviscid analysis	204
7.3.1.1	Shock Waves	205
7.3.1.2	Expansion Fans	205
7.3.1.3	Wake Region.....	207
7.3.2	Swept Shock/Boundary Layer Interaction.....	208
7.3.3	Design Factors.....	209
7.3.4	Results of Flowfield Analysis	210
7.4	Experimental Setup	211
7.4.1	Starting Dynamics.....	212
7.4.2	Instrumentation.....	212
7.4.3	Data Reduction and Analysis	215
7.5	Experimental Results.....	216
7.5.1	Shock (Stations 1, 1a, 2, and 2a).....	216
7.5.2	Flow between shock and expansion (Station 3)	220
7.5.3	Expansion (Station 4)	220
7.5.4	Wake (Stations 5 and 6).....	221
7.5.5	Flat Plate	221
VIII.	Conclusions and Recommendations.....	223
8.1	Conclusions.....	223
8.1.1	Pressure Gradient Sensitivity.....	224
8.1.2	Gauge Performance	225
8.1.3	Error Analysis.....	226
8.1.4	AFIT Shock Tunnel	226

8.2	Recommended Further Research	226
8.2.1	Aluminum Skin Friction Gauge	227
8.2.2	Rubber-Filled Gauge	227
8.3	Lessons Learned.....	229
8.3.1	Sensor Base Diameter.....	229
8.3.2	Metal Versus Plastic Housing	229
8.3.3	Wires.....	229
8.3.4	Gluing the Strain Gauges	230
8.3.5	Soldering.....	231
8.3.6	Assembly of the Gauge	231
8.3.7	Balancing Resistor	232
8.3.8	Oiling	232
8.3.9	Inserting into Model	233
8.4	Summary.....	233
Appendix A - Dimensions and Calibrations.....		234
A.1	Skin Friction Gauges	234
A.1.1	Gauge Dimensions.....	234
A.1.2	Oil Cavity Dimensions and Volume.....	236
A.1.3	Skin Friction Gauge Calibration Constants.....	238
A.2	Instrument Calibration Values	239
A.3	Material Properties.....	
A.3.1	Silicone Oil.....	241
A.3.2	Plastic.....	242
A.3.3	Strain Gauges	243
A.4	Model and Nozzle	243
Appendix B - Mathematical Derivations.....		247
B.1.	Viscoelastic Cantilever Beam	247
B.2	Unsteady One Dimensional Heat Conduction with Constant Surface	
	Heat Flux.....	250

B.3. Application of Common Skin Friction Correlations to High Temperature	258
B.3.1 Van Driest II	258
B.3.2 Spalding and Chi.....	264
B.3.2.1 Skin Friction Correlation	265
B.3.2.2 Calculation of Thermal Effect by Holding Momentum Thickness Constant.....	266
B.3.3 White and Christoph	267
B.3.4 Sommer and Short.....	268
B.4. Effective Strain Point for Strain Gauge at Base of Cantilever.....	268
B.5. Moment of Inertia and Effect of Strain Gauge and Glue.....	270
B.6. Trigonometric Identities	272
B.7. Solution to Equation of Motion for Vibrating Base.....	272
B.8. Electrical Response	276
B.9. Helium/Air Mixture	280
Appendix C - Numerical Procedures.....	283
C.1. Unsteady One Dimensional Heat Conduction with Convective Surface Heating	283
C.1.1 Heat Flux from Measured Wall Temperature	283
C.1.2 Wall Temperatures from Predicted Heat Flux.....	287
C.2. Unsteady Laminar Flow Through Concentric Annulus with Decreasing Pressure Gradient.....	295
C.2.1 Analytical Computation	295
C.2.2 Numerical Solution.....	298
C.2.2.1 Entrance Region.....	298
C.2.2.2 Equations for Numerical Solution.....	299
C.2.2.3 Numerical Implementation.....	303
C.2.2.4 Convergence	307
C.3. Thomas Algorithm	307
C.4. Unsteady Reflected Expansion Wave.....	309
C.4.1 Method of Characteristics	310
C.4.2 Numerical Procedure	312
C.4.3 Calculation of Contact Surface Intercept Point.....	314
C.4.4 Convergence.....	314
Appendix D - High Temperature Gas Dynamics Iterative Procedures.....	316
D.1. Shock Tunnel Analysis	316

D.1.1	Initial Shock	316
D.1.2	Reflected Shock and Converging Nozzle.....	317
D.1.3	Diverging Nozzle.....	318
D.1.4	Test Section Stagnation Conditions.....	319
D.1.5	Tailored Condition.....	319
D.1.6	Speed of Second Shock Reflection.....	320
D.1.7	Starting Dynamics.....	321
D.2.	Shock Tunnel Data Reduction Program.....	322
D.2.1	Incident Shock, Reflected Shock, and Converging Nozzle.....	323
D.2.2	Diverging Nozzle.....	325
D.3.	Oblique Shock.....	325
D.4.	Centered Expansion Fan.....	326
Appendix E - Summary of Runs.....		329
Appendix F - Predicted Performance of AFIT Shock Tunnel		332
Appendix G - Uncertainty Analysis.....		333
Bibliography		333
Vita		245

List of Figures

Figure	Page
1-1 Airframe-Integrated Supersonic Combustion Ramjet	3
1-2 Specific Impulse for Various Propulsion Devices.....	3
1-3 Cantilever Skin Friction Gauge.....	6
1-4 Test Model--Sharp Fin Mounted on a Flat Plate	7
2-1 Velocity and Temperature Distribution for Hypersonic Boundary Layer	11
2-2 Ranges of Vibrational Excitation, Dissociation, and Ionization for Air at 1 Atmosphere.....	11
2-3 Typical Shock Tunnel	12
2-4 Comparison of Flat Plate Skin Friction Correlations for High Temperature Flow.....	16
2-5 Typical Floating Element Skin Friction Gauges	17
2-6 Skin Friction Sensor Made Up of a Floating Element Supported by a Cantilever Beam.....	21
2-7 Deflected Cantilever Skin Friction Gauge	22
2-8 Skin Friction Gauge with Oil-Filled Cavity	23
2-9 Sensor Dimension Nomenclature.....	24
2-10 Wheatstone Bridge Circuit Diagram	25
2-11 Calibration Method for Skin Friction Gauge	26
2-12 Typical Calibration Data for Skin Friction Gauges used at NASA Ames	26
3-1 Cantilever Beam.....	29
3-2 Beam Dimension Notation	30
3-3 Protrusion of Deflected Sensor Lip	34
3-4 Deflection Angle	35
3-5 Distortion Caused by Shear Strain.....	35
3-6 Ratio of Sensor Lip Protrusion to Momentum Thickness for Different Wall Shear Stresses	37

3-7	Time Response of 2 kHz Directional Gauge	43
3-8	Frequency Spectrum for 2 kHz Directional Gauge.....	43
3-9	Effect of Overdamping.....	44
3-10	Critical Damping Viscosities	52
3-11	Magnification Factor.....	54
3-12	Relative Sensor Displacement	55
3-13	Skin Friction Traces Showing Effects of Base Vibration, AFIT Run 16	56
3-14	Burgers Model Curve Fit for Average Creep Response of Sensors Made of Ultem Plastic.....	61
3-15	Spike Followed by Steady Load	62
3-16	Calibration Error Due to Viscoelastic Response	63
3-17	Load Response from Data Acquisition System for a Typical Calibration.....	64
3-18	Pressure Sensitivity for 2 kHz Directional Gauge (Longitudinal Axis)	66
3-19	Bending Forces Caused by Pressure Gradient.....	69
3-20	Pressures Inside and Outside the Gauge	70
3-21	Sensor Head Geometry	71
3-22	Corrected and Uncorrected Wall Shear Stress Measurements for 2 kHz Directional Gauge, AFIT Run 16.....	73
3-23	GASL Run 37 Showing Effect of Transient Pressure Gradient (I-beam gauge)..	74
3-24	Transient Shock Effect.....	75
3-25	I-Beam Geometry	78
3-26	I-Beam Gauge.....	79
3-27	I-Beam Gauge Trace--NASA Ames Run 2086, Combustor Port #1.....	80
3-28	I-Beam Gauge Comparison in the AFIT Shock Tunnel, Run 32.....	81
3-29	Response of Hollow-Beam Sensor with Stainless Steel Head Compared to Plastic Solid Beam Gauge	83
3-30	Angle of flow deflection.....	84
3-31	Rotated Directional Gauge.....	86
3-32	Apparent Axis Effect.....	88
3-33	Directional Gauge Axes	89

3-34	Misalignment of Axes	91
3-35	Measurement of Alignment Angle	93
3-36	10 kHz Direction Gauge #2 with 4 Pairs of Strain Gauges.....	94
3-37	Calibration Data for 10 kHz Directional Gauge #1	95
3-38	Nozzle Floor Extension.....	97
3-39	Duct Test Section (Top View)	98
3-40	Wall Shear Stress Direction and Magnitude Traces, 10 kHz Gauge #1, AFIT Run 21.....	99
4-1	Calculated Surface Temperatures for NASA Ames Run 2066 Inlet Conditions.....	103
4-2	Calculated Surface Temperature for Wright Laboratory	103
4-3	Measured Wall Shear Stress by Plastic and Stainless Steel Gauges, AFIT Shock Tunnel Run 9	107
4-4	Calculated Wall Temperatures for AFIT Shock Tunnel Run 9	108
4-5	Measured Wall Shear Stress by Plastic and Stainless Steel Gauges, AFIT Run 33.....	109
4-6	Oil Depletion and Resulting Strain Gauge Thermal Effect (Wright Laboratory's Mach 6 Run 19)	110
4-7	Calculated Temperature Distribution in Metal, Plastic, and Oil after 6 msec for NASA Ames Run 2066.....	111
4-8	Gauge Surface Erosion	113
4-9	Dimensions and Pressures for Gauge in Oil Beaker.....	117
4-10	Oil Insertion Process	118
4-11	Oil Bubble Location (Upright Gauge)	121
4-12	Oil Bubble Location (Prone Gauge)	122
4-13	Oil Insertion Time for 10,000 cSt Oil	125
4-14	Oil Loss Induced by Pressure Gradient.....	126
4-15	Air Circulating through Oil Cavity.....	127
4-16	Skin Friction Gauge Re-Oiling Device.....	130
5-1	NASA Ames 16 Inch Shock Tunnel	136
5-2	NASA Ames Scramjet Model.....	137

5-3	Scramjet model in NASA Ames Shock Tunnel	138
5-4	NASA Ames Run 2089 Combustor Wall Shear Stress.....	138
5-5	CFD Data Analysis of NASA Ames Run 2089	139
5-6	NASA Ames Run 2066 Inlet Wall Shear Stress	140
5-7	Comparison of Skin Friction Theories with Average Measured Wall Shear Stress for NASA Ames Run 2066	141
5-8	Spectrum Analysis for Run 2066	142
5-9	NASA Ames Run 2060 Combustor Wall Shear Stress.....	143
5-10	NASA Ames Run 2060 Inlet Wall Shear Stress	144
5-11	NASA Ames Run 2061 Combustor Wall Shear Stress.....	144
5-12	NASA Ames Run 2062 Combustor Wall Shear Stress.....	145
5-13	NASA Ames Run 2082 Combustor Wall Shear Stress.....	145
5-14	NASA Ames Run 2088 Combustor Wall Shear Stress.....	146
5-15	Mach 6 Wind Tunnel Model Injection	147
5-16	Wright Laboratory Mach 6 Inlet Model.....	147
5-17	Wright Laboratory Run 57 Wall Shear Stress (Flat Plate, Sharp Nose, $p_t=11$ MPa).....	150
5-18	Wright Laboratory Run 55 Wall Shear Stress (Flat Plate, Sharp Nose, $p_t=5.5$ MPa).....	151
5-19	Wright Laboratory Run 56 Wall Shear Stress (Flat Plate, Sharp Nose, $p_t=8.3$ MPa).....	152
5-20	Wright Laboratory Run 2 Wall Shear Stress (Flat Plate, Blunt Nose, $p_t=5.5$ MPa).....	152
5-21	Wright Laboratory Run 19 Wall Shear Stress (Flat Plate, Blunt Nose, $p_t=13.8$ MPa).....	153
5-22	Hypulse Test Facility.....	154
5-23	Hypulse Scramjet Combustor Model.....	155
5-24	Expansion Tube	155
5-25	Hypulse Skin Friction Gauge Locations.....	156
5-26	GASL Run A37 Skin Friction and Pressure Traces, Port #4 (AFIT Baseline Gauge).....	157

5-27	GASL Run A37 Skin Friction and Pressure Traces, Port #5 (AFIT I-Beam Gauge).....	158
5-28	GASL Run A38 Skin Friction and Pressure Traces, Port #5 (AFIT I-Beam Gauge).....	159
6-1	AFIT High-Pressure Shock Tunnel	160
6-2	Shock Tube Before Diaphragm Rupture.....	161
6-3	Shock Tube After Diaphragm Rupture	161
6-4	Shock Tube with Reflected Shock.....	162
6-5	Moving Shock and Equivalent Stationary Shock	163
6-6	Duration of Steady Flow in Shock Tube.....	168
6-7	Tailored Interface.....	169
6-8	Second Reflected Shock.....	170
6-9	Shock Tunnel Nozzle with Low Back Pressure	171
6-10	Shock Tunnel Underexpanded Nozzle with Moderately High Backpressure.....	172
6-11	Figure 6-11 Test Section Length	173
6-12	Nozzle Exit Jet.....	176
6-13	Shock Tube Double Diaphragm	178
6-14	AFIT High Pressure Shock Tunnel.....	180
6-15	Breech Section for Diaphragm Access.....	180
6-16	Helium Bottle Farm	181
6-17	Shock Tunnel Control Panel.....	181
6-18	Duct Test Section with Fin.....	181
6-19	Dump Tank.....	181
6-20	Gas Temperature Thermocouple	184
6-21	Shock Tube Pressure Traces	187
6-22	Reflection of Shock from Contact Surface.....	187
6-23	Pressure and Thermocouple Traces	188
6-24	Predicted vs. Actual Performance of AFIT Shock Tunnel.....	190
6-25	Scramjet Compression System with Four Oblique Shocks	193
6-26	Oblique shock geometry.....	195

7-1	Test Model (Wedge-Shaped Fin on Flat Plate)	197
7-2	Reflected Shock/Boundary Layer Interaction	198
7-3	Side View of Swept Shock/Boundary Layer Interaction	199
7-4	Top View of Shock/Boundary Layer Interaction Showing Conical Similarity...	200
7-5	Computed Surface Skin Friction Lines	201
7-6	Test Section with Fin	202
7-7	Top View of Test Section	203
7-8	Expansion Fan	205
7-9	Wake Region	208
7-10	Test Section Pressures with Fin, Run 24.....	212
7-11	Nozzle Entrance Pressure vs. Thermocouple Temperature, Run 24	213
7-12	Measurement Stations.....	214
7-13	Yaw Angle vs. Mach Number, Run 24	218
7-14	Flowfield Map (Mach 2.9, $\alpha=10$ deg)	219
8-1	Skin Friction Gauge with Rubber-Encased Strain Gauges.....	228
A-1	Sensor Dimension Nomenclature.....	235
A-2	I-Beam Nomenclature	235
A-3	Oil Cavity Dimensions.....	237
A-4	AFIT Shock Tunnel Test Section Floor.....	244
A-5	AFIT Shock Tunnel Test Section Fin	244
A-6	Instrument Wheel.....	245
A-7	Instrument Strip.....	245
B-1	Geometry for 1-D Heat Transfer	251
B-2	Modeling of Strain Gauge Stiffness	271
B-3	Effect of Glue	271
C-1	Geometry for Numerical Solution to 1-D Heat Conduction	284
C-2	Numerical vs. Exact solution, Heat Flux from Wall Temperature, with Temporal Clustering.....	286
C-3	Numerical vs. Exact Solution, Heat Flux from Wall Temperature, without Temporal Clustering.....	287

C-4	Run 57 Heat Flux Calculation	288
C-5	Calculated Wall Temperature for Constant Heat Flux of $4,000,000 \text{ W/m}^2$ (Numerical vs. Exact).....	294
C-6	Calculated Temperature Distribution for Constant Heat Flux of $4,000,000 \text{ W/m}^2$ after 6 msec (Numerical vs. Exact).....	294
C-7	Final Velocity Profiles for Different Spatial Increments	308
C-8	Time to Fill for Different Temporal Increments	308
C-9	Characteristics for Reflected Expansion Wave.....	310

List of Tables

Table	Page
2-1 Dimensions of Skin Friction Gauge Sensors	23
3-1 Predicted vs. Actual Calibration Constants for Various Skin Friction Gauges	31
3-2 Approximate vs. Exact Eigenvalues for Vibration of Uniform Beam with End Mass.....	42
3-3 Predicted vs. Actual Natural Frequency for Various Skin Friction Gauges	44
3-4 Reynolds Numbers for Sensor Beam Vibrating in Oil	48
3-5 Damping Constants.....	51
3-6 Viscoelastic Constants for Different Sensor Materials.....	61
3-7 Pressure Gradient Sensitivity Factor for Different Gauges	72
3-8 Calibration Constants for Directional Gauges	94
3-9 Angle and Magnitude Accuracy of 10 kHz Directional Gauge in Static Calibration	96
3-10 Wind Tunnel Directional Tests	99
4-1 Unfilled Portion of Oil Cavity.....	121
5-1 Summary of NASA Ames Wall Shear Stress Measurements	143
7-1 Calculated Flow Conditions	211
7-2 Peak heat flux and pressure for the swept-shock/boundary layer interaction.....	211
7-3 Station Positions	214
7-4 Measured Skin Friction and Pressure.....	217
A-1 Dimensions of Skin Friction Gauge Sensors	234
A-2 Skin Friction Gauge Housing Dimensions.....	236
A-3 Oil Cavity Volumes.....	238
A-4 Skin Friction Gauge Calibration Values.....	239
A-5 Directional Gauge Calibration Values.....	239
A-6 Amplifier Gain and Excitation Voltage	240
A-7 DL1200 Waveform Recorder Correction Factors	241

A-8	Oil Properties and Typical Dimensions for Oil Filling.....	242
A-9	Plastic Material Properties.....	242
A-10	Strain Gauge Properties	243
A-11	Mach 3 Nozzle Contour.....	246
E-1	NASA Ames Run Summary	330
E-2	Summary of AFIT High Pressure Shock Tunnel Runs	331
F-1	Predicted Performance of AFIT Shock Tunnel	332
G-1	Wall Shear Stress Error.....	333

List of Symbols

A (without subscript).....	Calibration constant
A (with subscript).....	Area
a.....	Speed of sound
b.....	Calibration voltage slope (=V/m)
C_f	Skin friction coefficient (= τ_w/q)
c_p	Specific heat at constant pressure
c_v	Specific heat at constant volume
D (without subscript).....	Voltage factor
D (with subscript).....	Diameter
E.....	Modulus of elasticity.
F_G	Gain factor
G.....	Shear modulus
G_p	Total pressure gradient sensitivity factor
g.....	Acceleration of gravity; gap width
g_p	Pressure gradient sensitivity factor
Ha.....	Dimensionless damping factor
h.....	Specific enthalpy, height
I.....	Moment of inertia
I_{sp}	Specific impulse
K.....	Bulk modulus
k.....	Thermal conductivity, generalized stiffness coefficient
L.....	Length
L_{sgt}	Total strain gauge length
L_s	Distance from sensor top to midpoint of strain gauge
M.....	Mach number
M_{13}	Bending moment

m.....	Mass
P.....	Loading force
p.....	Pressure
p(t).....	Generalized loading
Pr.....	Prandtl number ($=\mu c_p/k$)
R.....	Radius; distance from neutral axis
R _o	Outer radius
R _i	Inner radius
q.....	Dynamic pressure $\left(=\frac{1}{2}\rho u^2 \right)$
\dot{q}	Heat flux
St.....	Stanton number
T.....	Temperature
T _H	Sensor head thickness
T _R	Sensor head root thickness
t.....	Time
t _f	Thickness of I-beam flange
t _w	Thickness of I-beam web
U.....	Velocity (freestream or boundary layer edge)
u.....	Velocity
v.....	Displacement
V(x,t).....	Displacement
V.....	Voltage, volume
V _e	Excitation voltage
W.....	Gap width
w.....	Displacement relative to base
Y.....	Yield strength
Z.....	Displacement of base
Z.....	Magnitude of base displacement

Greek

α	Thermal diffusivity (=); misalignment angle
γ	Ratio of specific heats ($=c_p/c_v$)
δ	Boundary layer thickness; small disturbance
ε	Strain
κ	Von Karman constant (≈ 0.41)
μ	Dynamic viscosity
ν	Kinematic viscosity ($=\mu/\rho$); Poisson's ratio
ρ	Density
σ (without subscript).....	Surface tension coefficient
σ (with subscript).....	Stress
τ	Dummy variable for time
τ_w	Wall shear stress
ψ	Assumed mode
ω_d	Damped circular frequency
ω_n	Circular natural frequency
ω_{Hz}	Natural frequency in Hz ($=\omega_n/2\pi$)

Subscripts

aw.....	Adiabatic wall
b.....	Beam
c.....	Compression
cal.....	Calibration
e.....	Boundary layer edge
f.....	Final
H,h.....	Head
SG.....	Strain gauge

s.....Shock
sr.....Reflected shock
t.....Stagnation (total) property, tension
th.....Throat
w.....Wall
0.....Initial
 ∞Infinity, free stream

Abstract

This study investigated a method for direct measurement of skin friction in high-enthalpy shock tunnel tests. Shock tunnels use a shock wave to generate a high temperature supersonic flow in order to test hypersonic vehicles and components at realistic enthalpies. Such tests place extreme demands on the instruments, both because of the high temperatures and the short duration of the flow (from 0.3 to 2 msec).

To measure the skin friction, a miniature plastic cantilever floating element skin friction gauge with a natural frequency of 10 kHz was further developed and improved. The cantilever beam is mounted so that the tip of the beam is flush with the wall. The wall shear stress imposed by the fluid results in a lateral force on the beam tip that causes the beam to deflect. Semiconductor strain gauges are mounted at the base of the cantilever to measure the deflection. The beam's small size (6.4 mm long) combined with the light weight of the plastic results in the high frequency response necessary for short duration flows. The cavity surrounding the beam is filled with silicone oil in order to thermally isolate the strain gauges, provide vibration damping, and provide a smooth aerodynamic surface.

The miniature plastic cantilever gauge had previously been developed by other researchers but improvements were made to the gauge design, construction, and operation during the course of this research. The goals of the research were to improve the usability and durability of the existing 10 kHz gauge, rigorously assess the accuracy of the gauge, develop a new gauge with higher frequency response, develop and demonstrate a directional sensing capability, and measure skin friction in supersonic combustion ramjet (scramjet) tests undertaken by NASA and the Air Force. Gauge durability was improved by using electronically deposited metallic and ceramic coatings. Methods of preventing oil loss were investigated and improved, and a re-oiling device was designed to improve the usability of the gauge. Potential sources of error were investigated and quantified both analytically and experimentally. A high frequency 30 kHz gauge was constructed by using

a miniature I-beam cantilever rather than a round cantilever beam. A directional gauge, capable of measuring, not only the magnitude, but also the direction of the wall shear stress was developed by adding a second set of strain gauges. The directional gauge was demonstrated by measuring the flowfield about a sharp fin in the AFIT high pressure shock tunnel. The baseline 10 kHz gauge and the I-beam gauge were used to measure combustor and inlet wall shear stresses in two sequences of scramjet tests. The first test sequence was conducted at Mach 14 enthalpies at the NASA Ames 16 inch shock tunnel with stagnation temperature of 6,000K and steady run time of 2 msec. The second test sequence was conducted at the General Applied Science Laboratories' Hypulse facility, also at Mach 14 enthalpy and 6,000K stagnation temperature but run time of only 0.4 msec. In addition, a lower frequency gauge was used to measure skin friction in a series of scramjet inlet tests conducted by the Wright Laboratory in the Mach 6 wind tunnel.

The cantilever floating element gauge proved to be a rugged and accurate method of measuring skin friction. The I-beam gauge has provided high frequency capability for facilities with very short run times, and the directional gauge has facilitated the measurement of skin friction in flow situations where a significant crossflow component exists. Finally, the measurements undertaken in support of scramjet tests have provided the engine developers with valuable data on the efficiency of their designs.

DIRECT MEASUREMENT OF SKIN FRICTION IN HIGH TEMPERATURE AND IMPULSIVELY STARTED SUPERSONIC FLOWFIELDS

I. Introduction

One of the major problems encountered today in hypersonic research is the determination of skin friction. Skin friction can be a substantial part of the total drag force for a hypersonic vehicle and plays a significant role in the efficiency of airbreathing hypersonic propulsion systems. However, hypersonic ground test facilities such as shock tunnels present unique challenges in the measurement of skin friction. This dissertation presents a research effort to develop and improve skin friction measurement techniques for use in high enthalpy shock tunnels. The research consisted of developing new types of skin friction gauges, analyzing and improving the operation of existing gauges, measuring skin friction in shock tunnel hypersonic propulsion tests conducted by NASA and the Air Force, and demonstrating a new directional gauge by characterizing the flowfield about a sharp fin.

The original contribution of this multidisciplinary research is three-fold. First, the various skin friction gauges developed during this research are a major advancement to hypersonic research. This technology can be used by other researchers to characterize viscous effects in flow regimes in which skin friction measurements could not be undertaken with instruments previously available. Second, the skin friction measurements that were undertaken in the shock tunnel tests have contributed to the understanding of the efficiency and feasibility of various engine designs. Third, the measurements in the AFIT

shock tunnel are a significant contribution to the body of knowledge of shock/boundary layer interactions and wake/boundary layer interactions.

1.1. Overview

Skin friction is the frictional force resulting from the relative motion between a body surface and a fluid. For most applications, skin friction has proven to be difficult to predict analytically, so researchers have relied on experimental measurements. Skin friction measurement techniques can generally be classified as direct or indirect. Direct measurement uses an element in the wall which either moves in response to the frictional force or to which a force must be applied to prevent movement. Indirect techniques measure a quantity such as temperature, pressure, or velocity which is then correlated to skin friction.

Direct measurement of skin friction is a fairly old experimental technique, being first undertaken in water in 1872 and in air in 1940 (Winter, 1977). However, interest in direct measurement techniques languished during much of the early development of aeronautical theory. Due to the relatively small magnitude of the skin friction in subsonic applications, as well as the primitive instrumentation then available, indirect techniques proved more robust and reliable. When research into supersonic and hypersonic flight moved to the forefront in the 1950s, the indirect techniques proved uncertain and difficult to apply in an environment of shock waves and high heating. This, combined with the increased magnitude of the frictional force in supersonic flow, resulted in a resurgence of interest in the development of direct measurement techniques.

The present investigation was generated by research into the supersonic combustion ramjet, commonly called a scramjet (Figure 1-1). The scramjet is an effort to apply the efficiency of airbreathing propulsion to the hypersonic flight regime. All hypersonic flights to date, including space launch vehicles and the X-15, have been powered by rocket engines, which require the vehicle to carry both oxidant and fuel. An air-breathing propulsion system would be more efficient (Figure 1-2), but current engines, the turbojet and

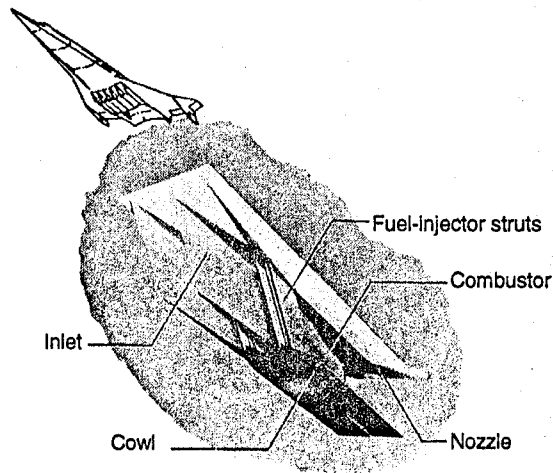


Figure 1-1 Airframe-Integrated Supersonic Combustion Ramjet (Baals and Corliss, 1981:130)

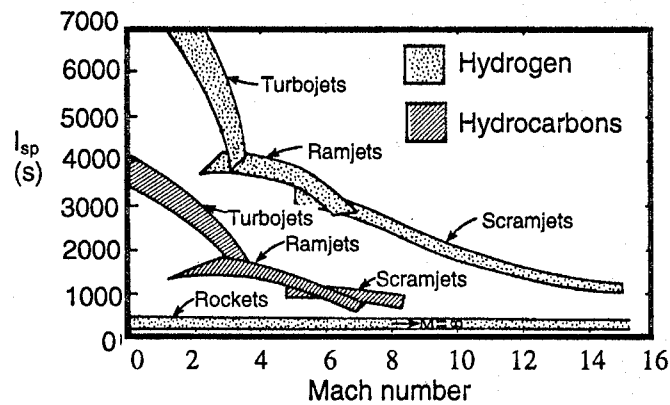


Figure 1-2 Specific Impulse for Various Propulsion Devices (Bertin, 1994:592)

ramjet, decelerate the air to subsonic speeds prior to combustion. This would be inefficient at hypersonic speeds for two reasons. First, when air is decelerated from supersonic to subsonic speeds, the resulting shock waves cause pressure losses which decrease the thrust. The amount of pressure loss increases with Mach number, and, for hypersonic speeds, these losses become extreme. Second, the slowing of the air causes an increase in the static air temperature as kinetic energy is converted to thermal energy. For very high static temperatures, much of the energy gained by combustion would be lost to dissocia-

tion of the reaction products. The net result of using a subsonic combustion airbreathing engine at hypersonic speeds would be that drag would exceed thrust.

In the current alternative, the scramjet, the combustion would take place at supersonic speeds. The benefits of this are twofold. First, the pressure losses associated with decelerating the airflow to subsonic velocities are removed. Second, the air static temperature in the combustion chamber remains low, increasing the efficiency of the combustion process. Supersonic combustion has not yet been used to power a flight vehicle, although researchers have reported success in attaining supersonic combustion in wind tunnel tests and in flight tests conducted with a scramjet model attached to a rocket.

For scramjets, skin friction is a more critical factor than for other airbreathing engines or for rockets. The difference in propulsion skin friction between rockets and the scramjet is obvious; in the scramjet, the air must flow through an inlet/compression system before reaching the combustor, while in a rocket engine, the flow originates in the combustor. For the scramjet, therefore, a larger surface area is exposed to the flow. Even if the wall shear stress (frictional force divided by surface area) were the same for both systems, the larger wetted surface area of the scramjet would make skin friction more critical. When comparing the scramjet to other airbreathing engines, the importance of skin friction is more subtle. The air moves through the scramjet at supersonic speeds, and, as discussed in Chapter 2, the magnitude of the wall shear stress increases greatly at supersonic speeds. Since in other airbreathing engines, as well as in rockets, the combustion takes place at subsonic speeds, skin friction is a less critical factor.

The increased magnitude of the wall shear stress, combined with the fact that scramjets currently in research are designed close to the margin of producing negative thrust (which would occur if the drag from the engine exceeds the thrust produced), means that accurate knowledge of the skin friction is essential in order to determine whether a hypersonic vehicle will fly.

1.2. Statement of the Problem and Synopsis of Work

An accurate determination of the skin friction in a hypersonic application is a difficult problem. Most analytical relationships are valid only for simple geometries. Numerical results rely on turbulence models that may not be valid for high speed, high temperature, three-dimensional, combusting flow. Thus, for complex geometries, it is necessary to experimentally measure the skin friction.

For lower speeds, several techniques have been developed to measure skin friction. These techniques have been used successfully up into the supersonic and even low hypersonic regimes. However, hypersonic flight, particularly at higher Mach numbers, involves high skin temperatures in the thousands of degrees. Shock tunnels, which provide the most realistic temperatures, have short run-times on the order of several milliseconds. These conditions pose problems in designing wind tunnel instrumentation, due to both the rapid response required, in order to obtain the measurement before the test is over, and the necessary ability to withstand high temperatures. Most common skin friction measurement techniques either will not work in shock tunnels or have questionable validity (see Chapter 2).

The problem of measuring directly the skin friction in shock tunnels was solved by Dr. Bowersox at AFIT and Dr. Schetz at Virginia Polytechnic Institute (Virginia Tech), who developed a floating element skin friction gauge that uses a miniature, plastic, cantilever beam instrumented with semiconductor strain gauges (Figure 1-3). This "baseline" gauge has been used successfully to measure skin friction in several shock tunnel tests (Bowersox, et al., 1993). Two advances have made such a gauge possible: the development of lightweight machinable plastics able to withstand high temperatures, and the semiconductor strain gauge, which is about 70 times more sensitive than normal metal strain gauges. The cantilever skin friction gauge concept was used as the basis of the current research.

The research consisted of several phases. The first phase of the research concentrated on improving the skin friction gauge and verifying its accuracy. Improvements included higher frequency response, better durability and usability, and directional sensing of

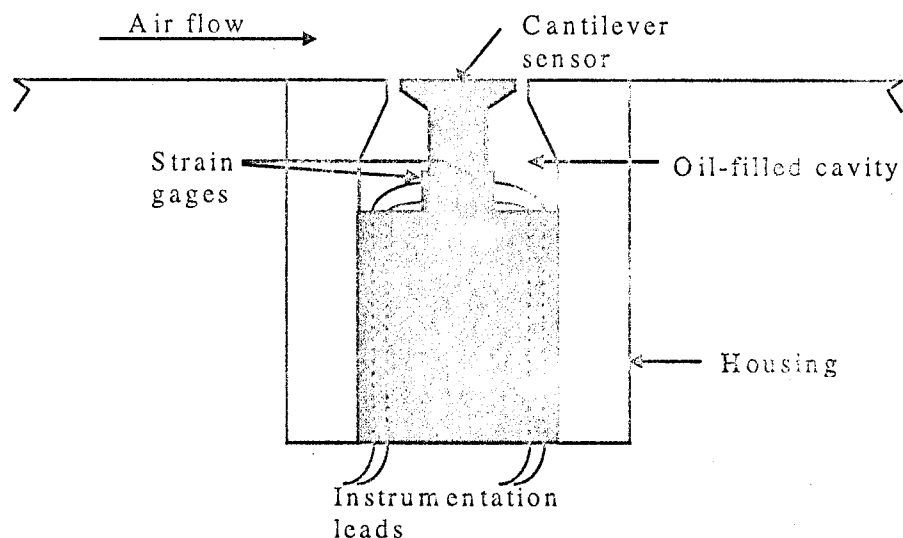


Figure 1-3 Cantilever Skin Friction Gauge

skin friction. Two new skin friction gauges were developed as part of this research: the I-beam gauge, which has sensitivity comparable to the baseline gauge but three times the natural frequency; and the directional sensor, which measures both magnitude and direction of skin friction. Accuracy verification included investigation of thermal, vibrational, electrical, and viscoelastic effects. The next phase consisted of using the gauge to measure skin friction in three series of scramjet tests. These tests were conducted by the NASA Ames Research Center in Sunnyvale, California, in the 16 inch shock tunnel, by the Air Force Wright Laboratory at Wright-Patterson AFB in the Mach 6 wind tunnel, and at the Hypulse facility operated by General Applied Science Laboratories (GASL) on Long Island, New York. The last part of the research consisted of demonstrating the improved directional skin friction gauge by measuring wall shear stress in a previously uncharacterized flowfield, specifically a sharp fin mounted on a flat plate (Figure 1-4) similar to a strut that might be found in a hypersonic scramjet propulsion system as shown in Figure 1-1.

1.3. Significance of the Contribution

The research is significant for three reasons. First, the improved skin friction gauge will be a valuable tool for measuring the flow conditions in shock tunnels and other

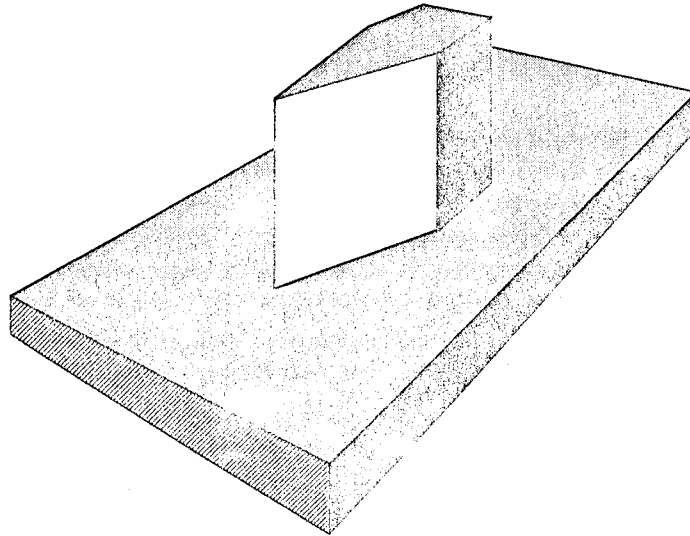


Figure 1-4 Test Model--Sharp Fin Mounted on a Flat Plate

short duration test facilities. Skin friction is a key factor in the efficiency of a hypersonic propulsion system, and the prediction of skin friction, particularly under high heat loads, involves a high degree of uncertainty. Even for the simplest geometries, the most commonly used skin friction correlations exhibit a great deal of scatter when high temperatures are involved (see Chapter 2). Turbulence models used in computational fluid dynamics (CFD) have also shown high degrees of inaccuracy for high temperature flows with high heating rates. Experimental measurements are required to resolve the uncertainty, but until the present skin friction gauge technique was developed, no reported method existed to measure skin friction under realistic conditions. In particular, the high frequency I-beam gauge has been valuable in measuring skin friction in very short duration facilities, and the directional gauge will be useful in measuring complex flowfields where a cross flow component exists in the flow.

A second reason the research is significant is because of the accurate scramjet skin friction measurements obtained at NASA Ames, GASL, and the Wright Laboratory. These measurements, previously unobtainable, were used by the engine designers to determine the combustor and inlet efficiency.

A third significant feature of this research is that the problem of the fin on the flat plate has been studied extensively, but directional measurements of the skin friction are

extremely scarce. The sharp leading edge of the fin creates a swept shock that disrupts the established boundary layer on the flat plate in a three-dimensional interaction, but the few experimental skin friction measurements that have been reported for the interaction involved wall shear magnitude only, not direction. The present research effort filled this gap by providing the measurements that until now have been lacking. In addition, the research effort characterized the problem under a flow regime in which experimental measurements have rarely been taken, specifically a high temperature, chemically reacting flow. These measurements will add to the data base that researchers use to verify the accuracy of CFD codes and turbulence models. The wake region is of particular interest here, as the wake from the fin interacts with the boundary layer on the flat plate. CFD turbulence models generally treat wakes differently than boundary layers; wakes belong to a class of flows termed free shear layers (Schetz, 1993:359), while the boundary layer on the flat plate is classified as a wall-bounded flow (Schetz, 1993:202). However, the measurements were in a flow regime that consisted of a wake/boundary layer combination, which provided new information for development and verification of turbulence models.

1.4. Overview of the Dissertation

The dissertation is organized into eight chapters. Chapters 1 and 2 together provide an overview of the research topic. Chapter 1 has provided an introduction to the proposed research. Chapter 2 provides general background on hypersonic testing and skin friction measurement techniques, an introduction to the operation and calibration of the miniature cantilever floating element skin friction, and a review of the literature on skin friction measurement.

The further development, validation, and analysis of the cantilever skin friction gauge are described in Chapters 3 and 4. Chapter 3 analyzes the gauge mechanics and alternative gauge geometries. Chapter 4 looks at several issues of skin friction gauge application, such as thermal effects, durability, oil retention and servicing, and electrical response and calibration.

The application of the skin friction gauge in the three sequences of scramjet tests is described and analyzed in Chapter 5. Analysis and experimental characterization of the AFIT high pressure shock tunnel is presented in Chapter 6. In addition, the shock tunnel data reduction program, which computes stagnation and freestream conditions based on pressure measurements, is discussed.

Chapter 7 describes the use of the directional gauge to characterize a high temperature supersonic flowfield about a sharp fin mounted on a flat plate. Chapter 8 presents conclusions and recommendations for future research.

II. Background

Hypersonic flight involves high temperatures which result in so-called "real-gas effects:" molecular vibration, dissociation, and ionization. These high temperatures must be duplicated in ground test facilities in order to test scramjet combustion. This has been done primarily through use of the shock tunnel. Because of the shock tunnel's high temperatures and short run times, conventional skin friction measurement techniques could not be applied. However, skin friction measurement is important in scramjet testing because of its effect on efficiency. Thus, the miniature plastic cantilever floating element skin friction gauge was developed to obtain the required measurements. These aspects of the skin friction gauge application will be discussed in this chapter to provide general background for the dissertation research topic.

2.1. Hypersonic Flight and Hypersonic Testing

Hypersonic flight is often defined as flight with speeds in excess of Mach 5, but there are several distinguishing physical and mathematical characteristics of hypersonic flight. These include high temperatures, thin shock layers, viscous interactions, a pressure gradient across the boundary layer, a large entropy layer, and non-linear small disturbance equations (Anderson, 1989:14-21,83-89). Because of these factors, many of the analytical and numerical techniques which have been applied to solve problems at lower speeds are not valid for hypersonic flow. However, of the above distinguishing characteristics of hypersonic flows, the one which requires the use of the shock tunnel, and thus plays a major part in this dissertation research, is the high temperature aspect.

Although the upper atmosphere is colder than at sea level, high speed flight inevitably involves high temperatures. The reason for this is that the slowing of the air near the vehicle by pressure effects and viscosity causes an increase in temperature as kinetic energy is converted into thermal energy. Figure 2-1 shows an example of this temperature rise in the boundary layer.

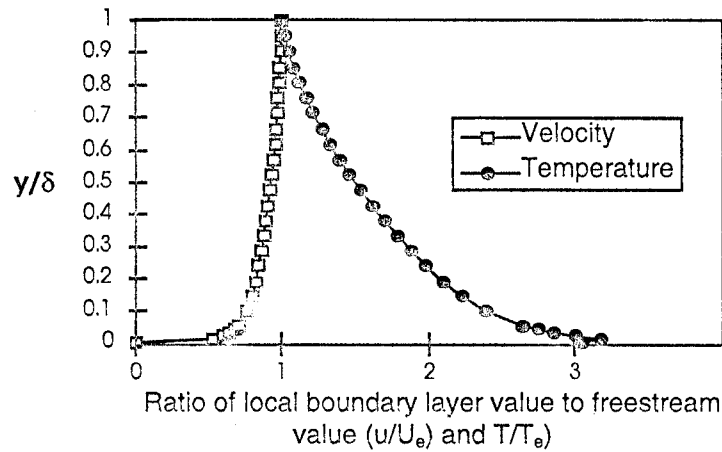


Figure 2-1 Velocity and Temperature Distribution for Hypersonic Boundary Layer

For an ideal gas, a change in thermal energy changes only the translational and rotational energy of the molecules, which is reflected as a change in temperature. At lower temperatures, air behaves as an ideal gas. However, as illustrated in Figure 2-2, at higher temperatures, the molecules begin to vibrate (the two atoms which make up the diatomic molecule vibrate relative to each other), dissociate, and then ionize (Anderson, 1989:374); as a result, some of the thermal energy that would have otherwise gone into raising the gas temperature goes instead into these chemical reactions.

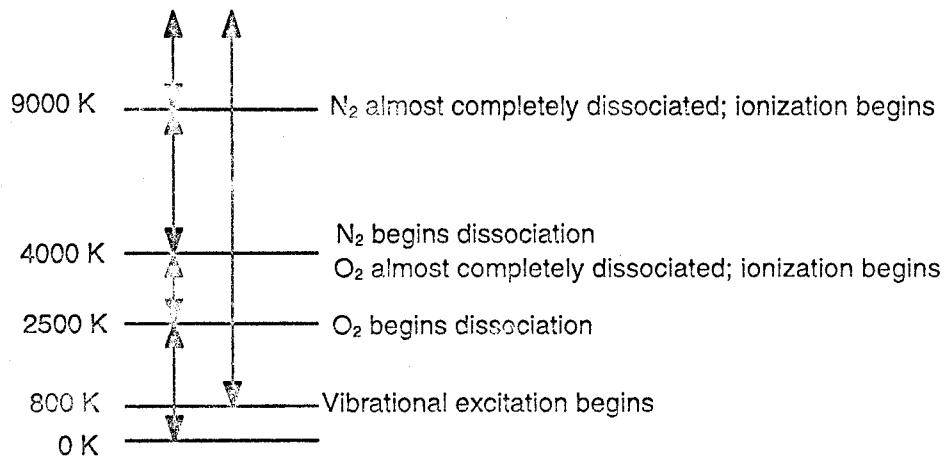


Figure 2-2 Ranges of Vibrational Excitation, Dissociation, and Ionization for Air at 1 Atmosphere

Both the NASA Ames tests and the GASL tests were conducted at stagnation temperatures of 6000K (Mach 14 enthalpy). As can be seen from Figure 2-2, at this temperature, much of the nitrogen is dissociated, while the oxygen is completely dissociated and partially ionized. For a scramjet combustor test, a realistic stagnation temperature is important because combustion in the presence of ionization and dissociation is considerably different than combustion with molecular oxygen.

To provide these realistic stagnation temperatures, shock tunnels are used. A shock tunnel is a shock tube connected to a wind tunnel (Figure 2-3). The shock tube consists of a driver section, with high pressure gas, and a driven section, with low pressure air. Some shock tubes use compressed gas in the driver section, while in others, the high pressure is created by combustion or a moving piston. The driver and driven sections are initially separated by a diaphragm, which is caused to rupture to begin the test. The high pressure gas then begins to expand into the driven section, causing a shock wave to travel into the low pressure gas. The effect of the shock is to equalize the pressure between the driver gas and the driven gas through which the shock has passed. This sudden increase in pressure causes the temperature of the gas to rise. When the shock reaches the end of the tube, it reflects, causing further increase in pressure and temperature. This high temperature gas is then exhausted through a converging-diverging nozzle to achieve the desired Mach number in the test section of the tunnel. The length of the test is very short, 0.4-10 milliseconds, because once the driver gas has expanded to the end of the shock tube, the high temperature test run is over (Nagamatsu, 1961:566-573).

The high temperatures, impulsive start, and short run times of the shock tunnel present difficulties in instrumentation. Shock tunnel instruments must have very fast response times as well as ability to withstand very high acceleration loads and temperatures

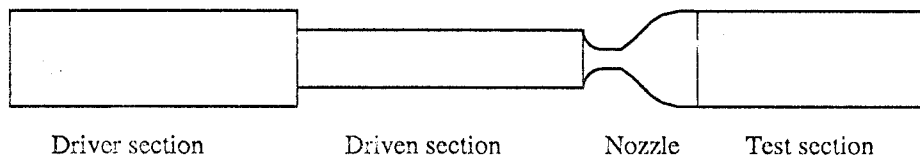


Figure 2-3 Typical Shock Tunnel

while still providing accurate data.

2.2. Skin friction

The drag force acting on a vehicle moving through a fluid can be separated into two components. The first, pressure drag, is caused by higher pressure on the front of the vehicle than on the back. In supersonic flow, the pressure drag is increased by a phenomenon known as wave drag. The shock waves which exist at the bow of the vehicle cause an increase in pressure on the front of the vehicle which is only partially recovered by the subsequent expansion at the rear. In supersonic flow, pressure drag has been fairly well characterized, and can be predicted by applying analytical or numerical methods to the inviscid flow field.

The second component of drag, skin friction, is not easily determined through analytical or numerical means. For incompressible laminar flow over a flat plate, the Blasius solution provides an exact solution for skin friction, but for flows with pressure gradients, turbulent flows, and compressible flows, the only solutions are semi-empirical.

Skin friction is usually characterized by normalizing the wall shear stress by the free stream dynamic pressure to form the skin friction coefficient C_f :

$$C_f \equiv \frac{\tau_w}{q} \quad (2-1)$$

where the freestream dynamic pressure is defined as

$$q \equiv \frac{1}{2} \rho_e U_e^2 \quad (2-2)$$

2.2.1. Significance of Skin Friction

For liquids, skin friction is an important component of the drag, but for air flow at lower speeds, most of the drag consists of pressure drag. At higher speeds, however, particularly hypersonic speeds, the skin friction becomes a large component of the total drag. For a slender vehicle designed to avoid a large bow shock, the magnitude of the pressure drag and the skin friction drag can be approximately the same (Anderson, 1989:214).

There are two reasons for this increase in skin friction at high speeds. First, the magnitude of the wall shear stress depends in large part on the dynamic pressure. As velocity increases, the dynamic pressure, which varies with the square of velocity, increases much faster. Although C_f generally decreases gradually with Mach number, this does not represent a decrease in τ_w . This can be seen by rearranging Equation (2-2) using perfect gas relations to obtain the following:

$$\tau_w = \frac{1}{2} M_e^2 \gamma p_e C_f \quad (2-3)$$

Because τ_w increases by a factor of M_e^2 as M_e increases, the increase in τ_w is much faster than the gradual decrease in C_f .

The skin friction also increases because of the heating of the boundary layer. Unlike liquids, the viscosities of gases increase with temperature, and hence the high temperatures near the wall serve to increase viscosity, which increases the wall shear stress (Anderson, 1990:15).

Skin friction is important not only because of its increased magnitude at high speeds but also because it is used as a scaling parameter in turbulent flow calculations (Schetz, 1993:420). Since the boundary layers on an aircraft surface are usually turbulent, an understanding of the turbulent flow is important in order to predict, not only drag, but also flow separation and convection heating effects.

Skin friction is used as a scaling parameter in a turbulent boundary layer through the friction velocity, which is defined as

$$u^* \equiv \sqrt{\frac{\tau_w}{\rho_w}} \quad (2-4)$$

The friction velocity is used to scale the velocity in the turbulent boundary layer. The scaled, non-dimensionalized velocity is

$$u^+ \equiv \frac{\bar{u}}{u^*} \quad (2-5)$$

where \bar{u} is the time-averaged mean velocity. The non-dimensional distance from the wall is also defined in terms of the friction velocity:

$$y^+ \equiv \frac{\rho y u^*}{\mu_w} \quad (2-6)$$

When expressed in terms of the correct u^+ and y^+ , the velocity profile in the inner region ($y^+ < 300$) of the incompressible turbulent boundary layer collapses to a universal curve called the law of the wall (Schetz, 1993:208-212). For the outer region, the defect law holds. For compressible flow, the Van Driest transformation (Van Driest, 1951) is used in conjunction with u^+ and y^+ to obtain the “compressible” law of the wall and “compressible” defect law (Bradshaw, 1977). However, for both the incompressible and compressible cases, the friction velocity must be known (or assumed) *a priori* in order to properly scale the velocity profile.

In order to implement CFD simulations of turbulent flow, a turbulence model must be used. The turbulence model, together with the equations of motion, can predict the skin friction, but turbulence models invariably include constants that are empirically derived and must be adjusted for each new flow situation, such as pressure gradient, mixing layer, etc. Thus, in a situation where the skin friction has not been experimentally determined, the turbulence model may produce a result that appears reasonable but is not accurate. This is a particular problem in a complex flow situation such as a scramjet combustor. Such flows are not easily analyzed through numerical methods, and the numerical results need to be validated through experimental measurements.

2.2.2. Prediction of Skin Friction

Many theories and correlations have been developed for predicting skin friction in compressible turbulent flow, but these have been developed only for simple geometries, primarily flow over a flat plate (White, 1991:549). The skin friction values predicted by these theories vary widely, particularly when applied to high temperature flows. The theories generally considered the most accurate are the Van Driest II theory (Van Driest, 1951, 1956) and the Spalding and Chi theory (Spalding and Chi, 1964). While these and other theories are useful, they have limited application, because many flow situations involve complicated geometries and chemical reactions, to which empirical and analytical

correlations do not apply. In addition, most of these theories are based on perfect gas assumptions and must be modified in order to be applicable to high temperature flows.

Figure 2-4 illustrates the varying values that several flat plate skin friction theories predict for a specific high temperature flow. This figure was developed from skin friction correlations that have been adapted for high temperature flows as discussed in Appendix B. The horizontal axis of the chart in Figure 2-4 reflects the ratio of wall temperature to adiabatic wall temperature (T_w/T_{aw}), which is a measure of the coldness of the wall. A cold wall, or cooled wall, would have a low value for T_w/T_{aw} , with resulting high rate of heat transfer from the air to the wall. It can be seen from Figure 2-4 that the scatter of predicted skin friction values increases considerably as the wall becomes colder.

2.2.3. Measurement of Skin Friction

Several methods exist for measurement of skin friction. As described in Chapter 1, these methods can be divided into two categories, direct and indirect.

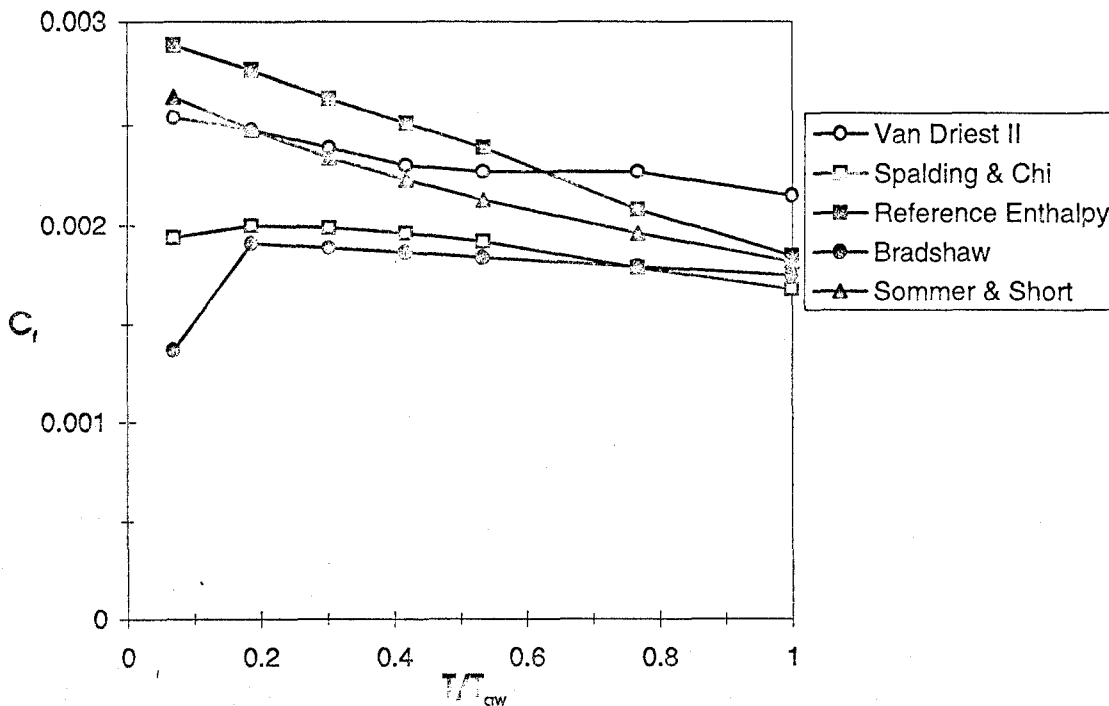


Figure 2-4 Comparison of Flat Plate Skin Friction Correlations for High Temperature Flow

2.2.3.1. Direct Measurement Techniques

The first recorded direct measurement of skin friction was by Froude in 1870, who used planks towed through water to obtain an integrated value of skin friction. More recent applications of direct measurement have used a floating element. A floating element is a movable surface mounted in the wall tangent to the flowfield (Figure 2-5). The shear force, or skin friction, of the flow moves the floating element against a resistant force. The amount of displacement of the floating element then provides the shear force experienced by the floating element.

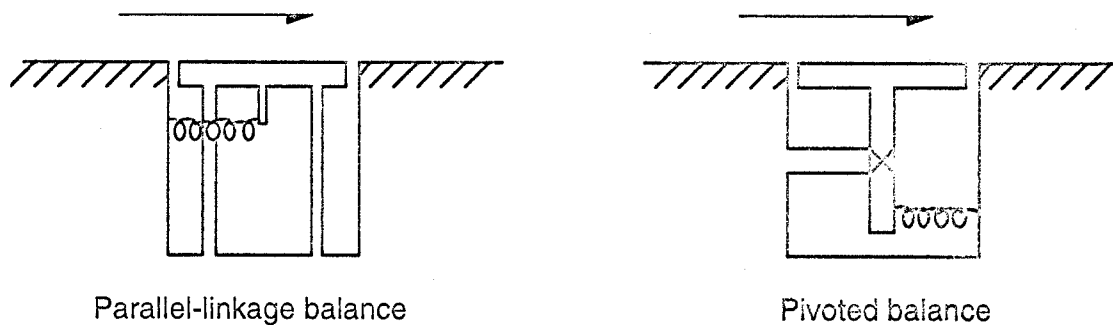


Figure 2-6 Typical Floating Element Skin Friction Gauges

A floating element device was first used to measure skin friction in water in 1929 (Winter, 1977). The first use of the floating element to measure skin friction in an air flow was by Schultz-Grunow in 1940, who used a rather large floating element (0.3m x 0.5m) to measure friction in a low-speed (20 m/s) air flow. The first use of a floating element gauge to measure skin friction in high-speed (compressible) air-flow was by Dhawan (1953). Dhawan's floating element was smaller than Schultz-Grunow's (2 mm x 20 mm), but compared to the skin friction gauge developed in the present research effort, all of these early devices had rather large floating elements. This was necessary due to the comparatively small skin friction force and the relatively insensitive force/displacement measurement devices then in use. The primary drawbacks of the direct measurement methods as applied to shock tunnels are the relatively slow response (since a mass is being physically displaced), acceleration effects, and sensitivity to high temperature of the electronic instrumentation used to measure the displacement.

2.2.3.2. Indirect Measurement Techniques

Several indirect techniques have been used to measure skin friction. The temperature or heat flux indirect measurement technique is based on the Reynolds analogy between heat transfer and skin friction, which for turbulent flow can be stated in its simplest form as (Van Driest, 1951)

$$St = \frac{C_f}{2} \quad (2-7)$$

where the Stanton number defined as follows:

$$St \equiv \frac{\dot{q}_w}{\rho_e U_e c_p (T_{aw} - T_w)} \quad (2-8)$$

The Reynolds analogy for compressible turbulent flow is based on assumptions of constant c_p , zero pressure gradient, and $Pr = 1$. More accurate versions of the Reynolds analogy have been expressed by using a Reynolds analogy factor (Cebeci and Bradshaw, 1984:349):

$$St = 1.16 \frac{C_f}{2} \quad (2-7a)$$

The first skin friction measurements using the Reynolds analogy were by Ludwig in 1949, who used a surface hot film. The surface hot film, which is still widely used, is a heated element embedded in the wall. In the airflow, heat is transferred from the hot film to the air in the boundary layer. The film is maintained at constant temperature by an electrical current. The amount of current required to heat the film can then be correlated to the convective heat loss, which then provides the skin friction from Eqs (2-7) and (2-8). This method has the advantage of a fast low response time and has been used to measure the fluctuating component of skin friction in turbulent flow (Cook, 1994). The skin friction can also be inferred from direct heat flux measurements by either heat flux gauges or thermocouples; however, this method can only be used in situations in which a sufficiently high heat flux is present to be measured; for example, a hypersonic flow with a cold wall.

Experimentally, the Reynolds analogy has been shown to be valid for conditions other than a flat plate, but in a hypersonic, high temperature environment with varying

pressure gradients and specific heat, the Reynolds analogy becomes questionable. Even with a flat plate, the Reynolds analogy is not well defined when cold walls are involved (as is the case for a shock tunnel), or for Mach numbers in excess of 5 (Cebeci and Bradshaw, 1988:349). The Reynolds analogy method also fails for a separated boundary layer; for this case, the wall shear stress goes to zero, but the heat flux can remain non-zero.

Indirect skin friction measurement methods involving pressure measurements use an obstruction in the boundary layer to measure the stagnation pressure of the oncoming flow. This stagnation pressure is then correlated to velocity, which in turn, through the law of the wall, provides the skin friction. Examples of this method are the sublayer fence and the Preston tube. However, these methods require calibration to known flow conditions and are therefore unsuitable to situations that involve considerable flow uncertainties such as pressure gradient and heat flux. In addition, these methods are somewhat intrusive to the flow and are best suited to subsonic flow where they will not create a shock wave.

In the velocity measurement technique, hot wires are used to measure the velocity in the boundary layer, which is then correlated to the skin friction using the law of the wall and a calibration to known flow conditions as for the pressure techniques. This method is subject to some of the same draw-backs as the pressure method, primarily sensitivity to pressure gradient and heat flux.

Two methods of measuring skin friction that appear to cross the line between the classification of direct and indirect methods are the use of surface oil coating and surface coating with liquid crystals. The liquid crystals work by reflecting different wavelengths of light under different shearing stresses (Klein and Margozzi, 1969). This method is sensitive to heat transfer effects. The oil coating method, also called laser interferometry, uses laser methods to track the thinning of an oil surface, which is then correlated to a skin friction. Originally developed for low speed flow, this technique has been applied successfully to complex supersonic flows up to a wall shear stress of 700 Pa. Beyond this point, however, the oil begins to form surface waves, and the calibration is no longer valid (Garrison, et al., 1994). Both the liquid crystals and the oil coating techniques would be

difficult to employ in a high temperature environment (the coating would be melted or boiled or entrained by the flow); in addition, the supporting instrumentation required (light and camera for the liquid crystals; laser for the oil coating) would be intrusive and difficult to use in a situation such as the scramjet tests conducted by NASA Ames.

2.2.4. Literature Review of Skin Friction Measurement Techniques

A comprehensive review of skin friction measurement techniques was undertaken by Winter in 1977. Winter's paper covers both direct and indirect techniques. Results of 153 published papers on skin friction measurement from 1872 through 1977 are presented, including 25 papers on direct measurement of skin friction. Nitsche, Haberland, and Thunker reviewed indirect skin friction measurement techniques in 1984. Results of 17 papers from 1954 through 1984 are presented.

Allen (1976) investigated pressure-induced errors associated with floating element skin friction gauges. Westkaemper (1963), O'Donnell and Westkaemper (1965), and Paik (1993) investigated temperature mismatch errors in floating element gauges.

Research on floating element skin friction measurement that has occurred since Winter's review paper include papers by Schetz and Nerny (1977), Voisenet (1978), Allen (1980), DeTurris, Schetz, and Hellbaum (1990), Chadwick (1992), Bowersox and Schetz (1993), Bowersox, Schetz, Chadwick, and Deiwert (1995), Novean, Schetz, Hazelton, and Bowersox (1995), and Hazelton, Bowersox, and Schetz (1996). The Novean et al. paper summarizes the skin friction measurements at NASA Ames, as well as initial thermal and pressure sensitivity analyses, that were undertaken as part of the present dissertation research, while the Hazelton et al. paper discusses the directional skin friction gauge that was developed as part of this research.

Of all of the other literature, the only reported effort that has been directed at shock tunnels was that of MacArthur (1963), who used parallel linkage with piezoelectric beams; and the Bowersox and Schetz paper (1993) and Bowersox et al. paper (1995) upon which the current research effort is based.

2.3. The Cantilever Floating Element Skin Friction Gauge

The present research effort is based on work begun by Drs. Bowersox and Schetz at AFIT and Virginia Tech to adapt the floating element gauge to shock tunnel use (Bowersox, Schetz, Chadwick, and Deiwert, 1995). The primary difficulties in adapting the floating element gauge to shock tunnel use were the slow response time and acceleration effects, due to the mass of the floating element, as well as inability to withstand high temperatures. These difficulties were overcome by designing a sensor in which the floating element is supported by a cantilever made of lightweight plastic (Figure 2-6). The shear force of the fluid flow causes the cantilever to bend slightly (Figure 2-7). The amount of bending is measured by semiconductor strain gauges mounted vertically at the bottom of the cantilever.

The strain gauge, which is used to measure the deflection, is a resistor through which an electrical current flows. When the strain gauge is stretched or compressed (i.e., undergoes strain), the resistance changes. The amount of change of the resistance is then compared against previously calibrated values to determine the skin friction force. The semiconductor strain gauges are much more sensitive than ordinary metal strain gauges,

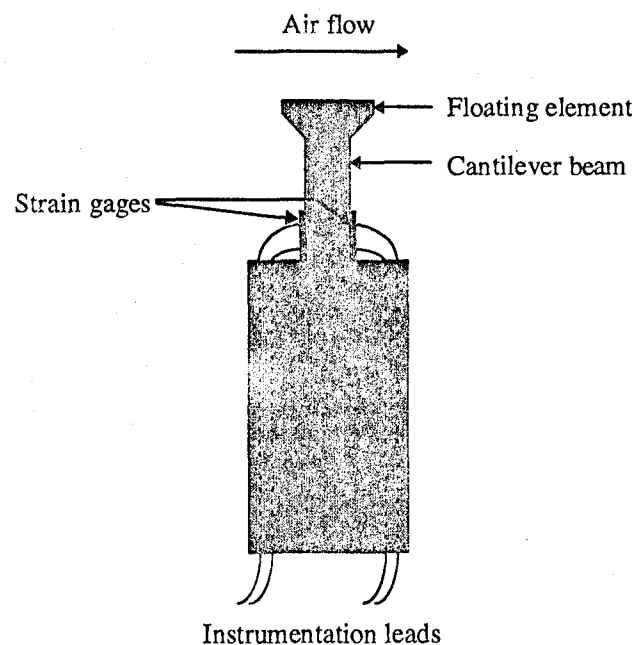
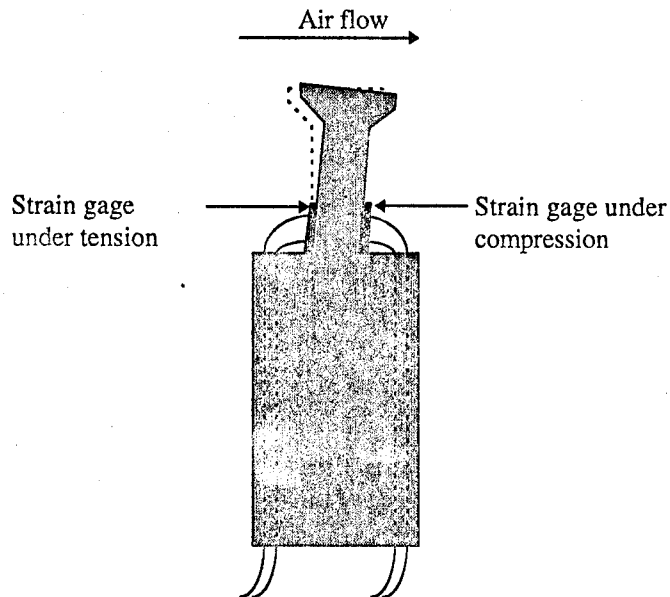


Figure 2-6 Skin Friction Sensor Made Up of a Floating Element Supported by a Cantilever Beam



**Figure 2-7 Deflected Cantilever Skin Friction Gauge
(amount of deflection is exaggerated for illustrative purposes)**

meaning that a very small displacement can be measured with high accuracy. This allows the size of the floating element (the sensor head) to be reduced. The small size of the sensor head, combined with the light weight of the plastic, results in a natural frequency of 10 kHz for the "baseline" gauge.

Besides light weight, there are two other reasons for making the cantilever of plastic. First, the strain gauges are very sensitive to temperature variation, and making the cantilever of plastic slows the heat conduction through the beam. Second, the plastic is more flexible than metals and most composite materials, so the cantilever does not have to be very long in order to provide the required sensitivity. This improves the frequency response.

The sensor is encased in a housing that is filled with silicon oil (Figure 2-8). The oil serves four purposes: first, to provide an aerodynamically smooth surface (by filling in the gap between the sensor head and the surrounding surface); second, to minimize pressure gradient effects; third, to thermally isolate the strain gauges from the high temperature flow, and fourth, to dampen vibrations of the cantilever .

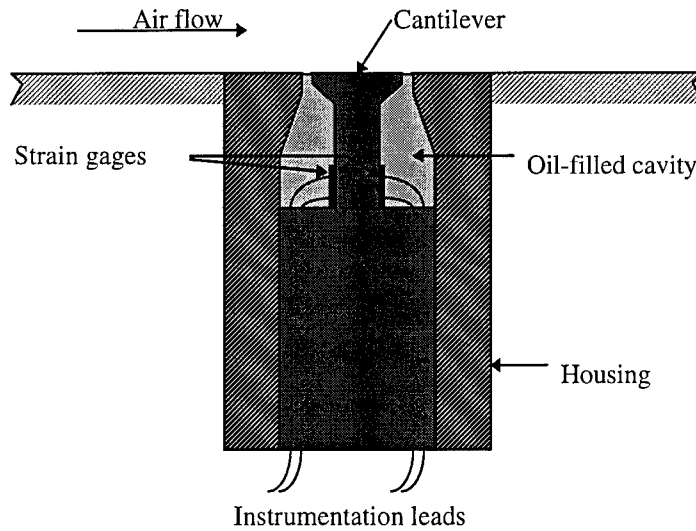


Figure 2-8 Skin Friction Gauge with Oil-Filled Cavity

In order to increase the sensitivity of the gauge, the sensor head is larger than the cantilever beam. The strain felt by the beam is proportional to the end loading given by

$$P = \tau_w A_H \quad (2-9)$$

Thus, increasing the head size increases P , which in turn increases the gauge response (although, as previously discussed, increasing the mass of the head would decrease the frequency response).

The size of the skin friction gauge varies depending on the size of the model being tested, the required frequency response, and the expected magnitude of the skin friction. The sensor sizes are shown in Table 2-1. Dimension notation is shown in Figure 2-9.

Table 2-1 Dimensions of Skin Friction Gauge Sensors

	Baseline	I-beam	Mach 6	Directional
Beam length (mm)	6.400	5.000	13.335	13.500
Beam diameter (mm)	2.540	2.000	3.175	2.500
Head diameter (mm)	4.600	3.476	6.350	6.350
Head tip thickness (mm)	.254	0.100	1.270	.500
Head root thickness (mm)	.762	0.200	1.270	1.000
Natural frequency (kHz)	10.09	32.14	2.43	1.63

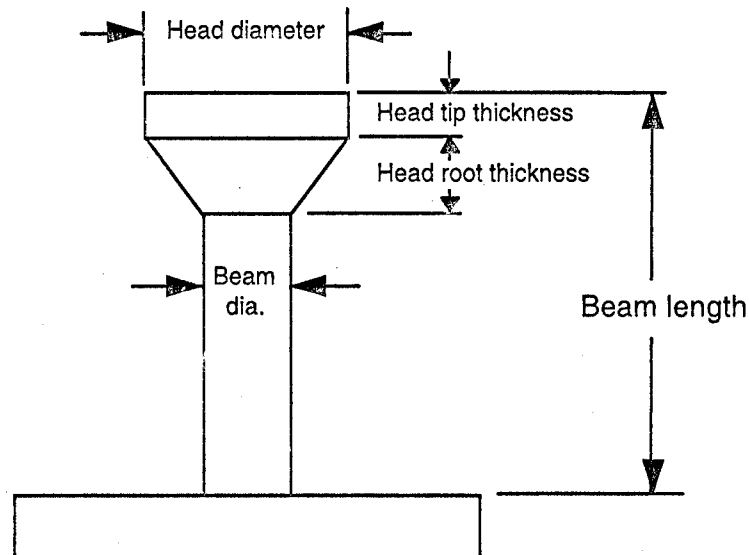


Figure 2-9 Sensor Dimension Nomenclature

2.3.1. Gauge Operation

The response of the gauge is measured through use of a Wheatstone bridge (Figure 2-10). A Wheatstone bridge allows instantaneous measurement of changes of resistances, which makes this arrangement suitable for dynamic measurements (Dally and Riley, 1978:229-231). The two strain gauges in the skin friction gauge provide two of the resistors in the Wheatstone bridge and the other two resistors are provided by an amplifier which also filters and amplifies the signal.

The Wheatstone bridge is balanced before the gauge is used in order to provide a zero voltage output. When the sensor is deflected, the resistances of the strain gauges change, which unbalances the bridge. This causes a voltage output. The gauge is calibrated prior to use so that the voltage reading corresponds to a known force. Slight variations in the positioning of the strain gauges during construction of the skin friction gauge can vary the calibration factor, so each skin friction gauge must be individually calibrated (detailed analysis of the electrical response and calibration is presented in Chapter 3).

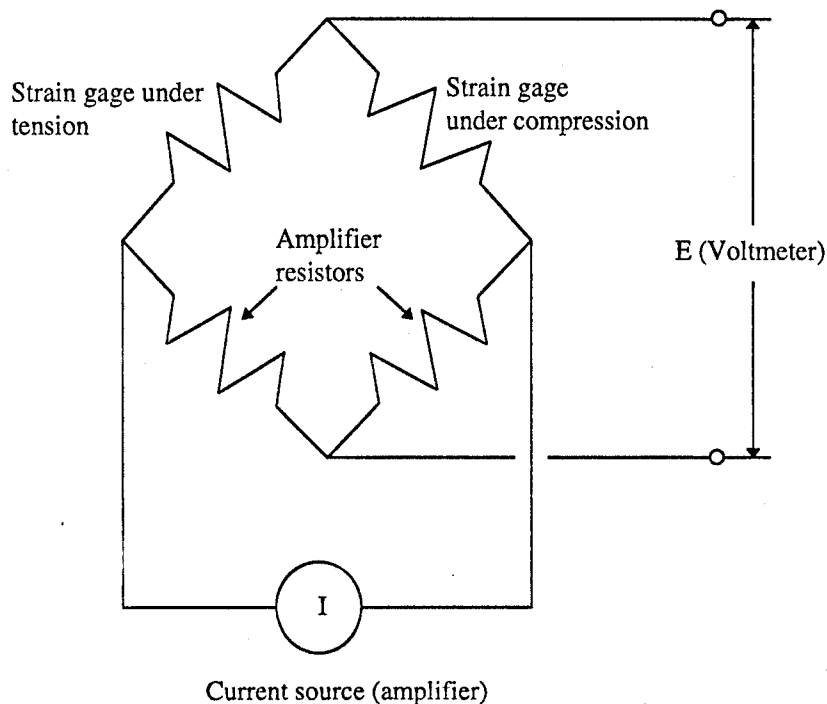


Figure 2-10 Wheatstone Bridge Circuit Diagram

During wind tunnel use, the voltage output of the gauge is read and stored by a data acquisition system. The sampling rate of the gauge output has ranged from 100 Hz for tests in the Wright Laboratory's Mach 6 blow-down tunnel (where the run lasts for 3 seconds) to 100 kHz for the NASA Ames shock tunnel (where the steady flow part of the run lasts for 2 milliseconds).

2.3.2. Calibration

The skin friction gauge is calibrated by putting the gauge in a horizontal position and hanging small weights of known mass from the end of the sensor (Figure 2-11). The gauge is connected in a Wheatstone bridge with an amplifier as described above. The voltage response for each weight is measured with a voltmeter or data acquisition system. In both theory and practice, the result is linear. Once a sufficient number of weights have been used to cover the entire expected range of skin friction values, the calibration value b is computed, where

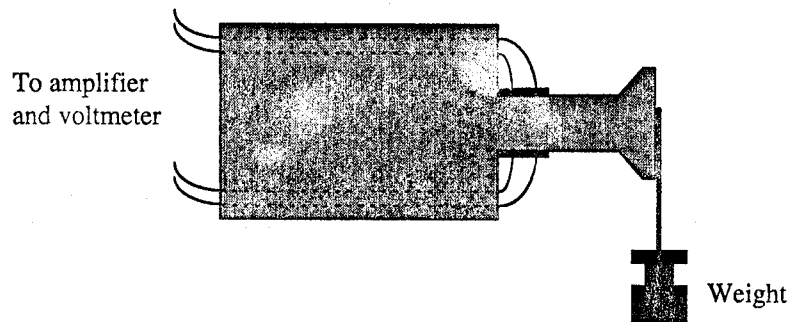


Figure 2-11 Calibration Method for Skin Friction Gauge

$$b \equiv \frac{V}{m} \quad (2-10)$$

Since the response is linear, the b value is approximately the same for every weight; the calibration curve is a straight line with slope b (Figure 2-12).

The calibration value A of the skin friction gauge is defined so that

$$\tau_w = AV \quad (2-11)$$

where the units of A are in Pa/V. Using Newton's second law in the form $P=mg$ along with Eq (2-9), the calibration constant is related to the voltage slope b through

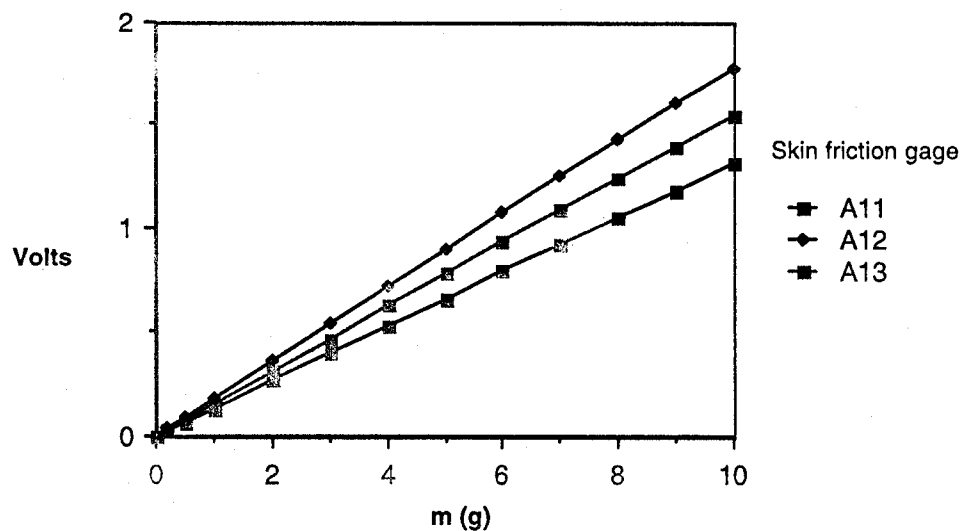


Figure 2-12 Typical Calibration Data for Skin Friction Gauges used at NASA Ames

$$A = \frac{g}{bA_H} \quad (2-12)$$

The calibration value A is valid only if used at the same gain (factor by which the voltage response is amplified by the amplifier) and excitation voltage (voltage provided by the amplifier through the Wheatstone bridge). If either of these are changed, the new calibration factor becomes.

$$A_{\text{new}} = A_{\text{cal}} \frac{F_{G(\text{cal})}}{F_{G(\text{new})}} \frac{V_{e(\text{cal})}}{V_{e(\text{new})}} \quad (2-13)$$

This relation is derived in Chapter 4.

III. Skin Friction Gauge Mechanics

The mechanical response of the gauge is a key factor that governs both performance and accuracy. The objective of this part of the research was to determine ways to increase the frequency response and sensitivity of the gauge, develop directional sensing capability, identify any limiting factors in the gauge design, and identify and quantify potential sources of error.

The optimum gauge design for a particular flow situation must consider both the sensitivity and the response time required. To determine the sensitivity, the static response was analyzed, while the dynamic response was analyzed to determine the response time. In addition, both the static and dynamic responses were examined as potential sources of error. The failure process was analyzed in order to determine the limits that must be placed on the design. Viscoelastic effects and pressure sensitivities were investigated in order to identify possible causes of error.

Several alternative skin friction gauge geometries were evaluated in the course of this research. First, a sensor beam with an I-shaped cross-section, rather than a round cross-section, was introduced to increase the frequency response. Second, a hollow beam gauge with stainless steel head was constructed for thermal comparison purposes. Third, a directional gauge was developed to measure, not only wall shear stress magnitude, but also direction.

3.1. Static Response

The static response reflects the amount of deflection that will occur under a given loading if the loading is maintained for a sufficient length of time to allow the response to stabilize. Thus, the static response determines the gauge sensitivity and the calibration constant.

Elasticity theory was used to evaluate the state of strain in the cantilever in order to determine the sensitivity of the gauge. In addition, displacement during maximum

loading was determined in order to ensure a large enough gap for sensor motion. Also, the amount and effect of the protrusion of the sensor head into the flow due to deflection were calculated. Finally, the effect of canting the gauge was examined.

3.1.1. Gauge Sensitivity

In beam theory, a cantilever beam is defined as a beam with a loading force applied to one end and with the other end fixed (Beer and Johnston, 1981:398). Since the fluid wall shear stress results in an end-loading force on the skin friction gauge sensor beam, the sensor beam is considered to be a cantilever. For a linearly elastic, isotropic material, the normal stresses for a cantilever beam (Figure 3-1) are given by (Saada, 1974:370)

$$\sigma_{11} = -\frac{P(L - x_1)x_2}{I} \quad \sigma_{22} = \sigma_{33} = 0 \quad (3-1)$$

The stress-strain relation can be stated (Saada, 1974:203):

$$\epsilon_{11} = \frac{1}{E}(\sigma_{11} - \nu\sigma_{22} - \nu\sigma_{33}) \quad (3-2)$$

Combining Eqs (3-1) and (3-2) results in the following relation:

$$\epsilon_{11} = -\frac{P(L - x_1)x_2}{EI} \quad (3-3)$$

It can be seen from Eqs (3-4) that the strain increases with distance away from the end-loading. The strain is greatest at the base of the cantilever, where $x_1 = 0$. However, the effective strain measured by the strain gauge is at the midpoint of the strain gauge

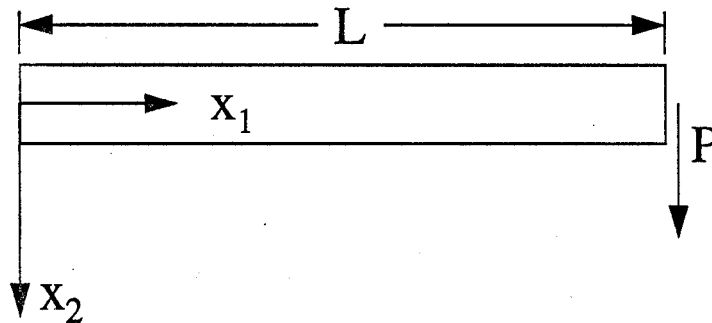


Figure 3-1 Cantilever Beam

(Appendix B). Thus, the tension strain measured by a strain gauge mounted at the base of the cantilever at $x_2 = -R$ is (Figure 3-2)

$$\epsilon_{11t} = \frac{P(L - L_{sgt})R}{EI} \quad (3-4)$$

while the measured strain on the compression side is equal in sign and opposite in magnitude. Substituting Eq (2-9) into Eq (3-4) and rearranging then gives the final relation for the skin friction gauge sensitivity.

$$\frac{\epsilon_{SG(t)}}{\tau_w} = \frac{A_H \left(L - \frac{1}{2} L_{sgt} \right) R}{EI} \quad (3-5)$$

If the actual distance to the midpoint of the strain gauge is used, then Eq (3-5) becomes

$$\frac{\epsilon_{SG(t)}}{\tau_w} = \frac{A_H L_s R}{EI} \quad (3-5a)$$

where $L_s = L - x_1$ when x_1 is taken as the centerpoint of the strain gauge.

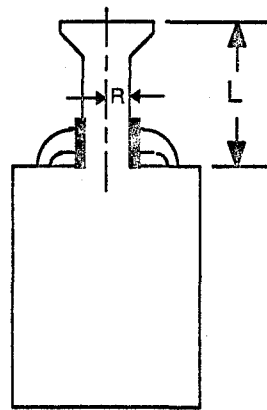


Figure 3-2 Beam Dimension Notation

In practice, the sensitivity of the skin friction gauges has been somewhat less than predicted. In Chapter 4, it will be shown that the gauge calibration factor is related to the sensor sensitivity by

$$A = \frac{2EI}{F_G V_e k} \left(\frac{\tau_w}{\epsilon_{SG(t)}} \right) = \frac{2EI}{F_G V_e k A_H \left(L - \frac{1}{2} L_{sgt} \right) R} \quad (3-6)$$

However, the actual calibration factors have always been higher than predicted, as well as showing a great deal of variation between gauges of the same type. (A higher calibration value indicates a less sensitive gauge.) Table 3-1 shows the predicted versus actual calibration factors for the gauges used in the NASA Ames, Hypulse, and Wright Laboratory's Mach 6 tests. The actual calibration factor for these gauges is 1.51 to 3.24 times the predicted value.

Table 3-1 Predicted vs. Actual Calibration Constants for Various Skin Friction Gauges

Gauge	Type	A _{predicted} (Pa/V)	A _{actual} (Pa/V)	Gauge	Type	A _{predicted} (Pa/V)	A _{actual} (Pa/V)
A1	Baseline	1758	3964	A10	Baseline	1758	5701
A2	Baseline	1758	4266	A11	Baseline	1758	4531
A3	Baseline	1758	4273	A12	Baseline	1758	3323
A4	Baseline	1758	3362	A13	Baseline	1758	3818
A5	Baseline	1758	2654	CFU4	Baseline	1758	4759
A6	Baseline	1758	2708	A14	I-beam	1859	3069
A7	Baseline	1758	2950	A15	I-beam	1859	4168
A8	Baseline	1758	3072	CFU5	I-beam	1859	4930
A9	Baseline	1758	2921	G4	Mach 6	1084	2248

There are several reasons for this variation. First, the strain gauge increases the stiffness of the beam and the glue increases the R-dimension of the beam. In Appendix B, it is shown that the combined effect of the strain gauge and the glue increases the moment of inertia for the baseline gauge by 45-107 percent ($R_{actual}/R_{beam}=1.1-1.25$). This accounts for most of the variation between predicted and actual calibration factor for the gauges with the lower calibration factors. Second, while the objective is to mount the strain gauges at the base of the beam for maximum sensitivity, some clearance exists between the strain gauge and the sensor beam base. A millimeter of clearance would increase the calibration factor by 23 percent for the baseline gauge. Third, the strain gauges may not be completely straight on the beam, causing further loss of sensitivity. A 20 degree mis-

alignment would result in the effective gauge factor being 94 percent ($=\cos 20^\circ$) of the actual gauge factor; this would result in a 6.4 percent increase in the calibration factor. These three factors alone could increase the calibration factor by 45-171 percent, since from Eq (3-6) these factors must be multiplied to calculate the total effect on the calibration factor. Another possible cause is incomplete bonding of the strain gauge to the plastic, reducing the effective gauge factor. Also, the gauge factor for the strain gauges may not be as high as the manufacturer reports. Finally, simple beam theory assumes that the beam length is much greater than the diameter. For the baseline gauge, the beam length is 2.52 times the diameter, so it is possible that the simple beam assumptions are not completely valid, particularly when the strain gauges are placed closer to the sensor head.

There are several factors that can probably be ruled out as a cause of the variation between predicted and actual sensitivity. First, electronic variations (gain and voltage) could just as easily increase the sensitivity as decrease it, but the observation is that the sensitivity is always lower. If the dimension of the sensor were somewhat different from the design or if the manufacturer's value for the Young's modulus was incorrect, then the sensitivity could also be affected. However, both of these would also affect the frequency response. It will be shown in Section 3.2 that the frequency response is very close to the predicted value. The reason that the increase in the moment of inertia due to glue and strain gauge does not significantly affect the natural frequency response is that the natural frequency depends on the square root of I . Thus a 45 percent increase in I would increase natural frequency by only 20 percent. Second, the 45 percent increase in I applies only to the base of the beam where the strain gauges are located; the upper part of the beam is unaffected. Third, the increase in natural frequency due to the increase in I would be partially offset by the increase in beam mass due to the mass of the glue and strain gauges.

3.1.2. Tip Deflection

The deflection of the sensor tip is calculated using the deflection curve of the neutral axis, which is referred to as the elastic curve. The elastic curve can be derived from

the following relation from the elementary theory of beams, which relates curvature to bending moment (Saada, 1974:355):

$$\frac{d^2 v_2}{dx_1^2} = -\frac{M_{13}}{EI} \quad (3-7)$$

For the cantilever beam, the moment is given by (Saada, 1974:370):

$$M_{13} = -P(L - x_1) \quad (3-8)$$

The following boundary conditions can be applied to the fixed end of the beam (Saada, 1974:363):

$$v_2(0) = 0 \quad \left. \frac{dv_2}{dx_1} \right|_{x_1=0} = 0 \quad (3-9)$$

Substituting Eq (3-8) into Eq (3-7), integrating once and applying the second boundary condition results in the slope of the elastic curve, which is used in determining the protrusion:

$$\frac{dv_2}{dx_1} = \frac{P \left(Lx_1 - \frac{1}{2} x_1^2 \right)}{EI} \quad (3-10)$$

Integrating again and applying the first boundary condition results in the elastic curve:

$$v_2 = \frac{P}{6EI} (3Lx_1^2 - x_1^3) \quad (3-11)$$

The tip deflection at $x_1=L$ is then given by

$$v_2(L) = \frac{PL^3}{3EI} = \frac{\tau_w A_H L^3}{3EI} \quad (3-12)$$

The minimum size for the gap between the sensor head and the housing can be calculated using the maximum expected value for the wall shear stress. However, when initially loaded, the sensor vibrates. For an undamped step loading, the initial deflection is twice that predicted by static theory (Craig, 1981, 112). Therefore the minimum gap size should be twice what would be predicted from Eq (3-26), that is

$$W_{\min} = \frac{2\tau_{w(\max)} A_H L^3}{3EI} \quad (3-13)$$

In practice, the deflection is very small; so minimum gap size is very small. For the baseline sensor at a maximum loading of 10,000 Pa, the predicted deflection is only 4.3 μm . However, machining tolerances require the gap size to be somewhat larger than the minimum size of Eq (3-13); the smallest gap size used in any of the AFIT gauges was 63.5 μm . In addition, Allen (1976), in a study of potential errors associated with floating element skin friction gauges, has shown that increasing the gap size can help to compensate for measurement errors introduced due to a protruding sensor head.

3.1.3. Protrusion of the Sensor Head into the Flow due to Deflection

When the sensor is deflected, the sensor head is tilted, so the edge of the sensor head may protrude into the flow (Figure 3-3). Because the deflection is small, the protrusion is small. However, the degree to which the sensor head protrudes into the flow when deflected is important because this protrusion can disrupt the flow.

The size of the protrusion will be estimated using the elastic curve calculated in the previous section in Eq (3-10):

$$\left. \frac{du_2}{dx_1} \right|_{x_1=L} = \frac{PL^2}{2EI} = \frac{\tau_w A_H L^2}{2EI} \quad (3-14)$$

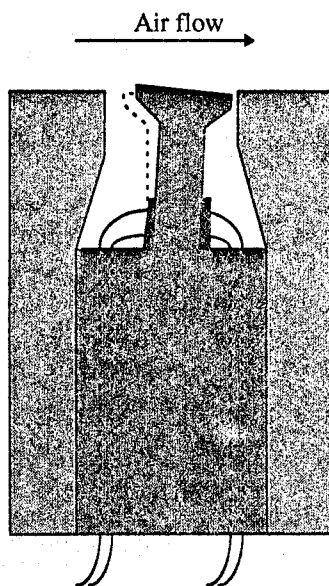


Figure 3-3 Protrusion of Deflected Sensor Lip

Since the slope of the undeflected beam is zero, the angle of the deflection is given by (Figure 3-4)

$$\tan \theta = \frac{PL^2}{2EI} \approx \theta \quad (3-15)$$

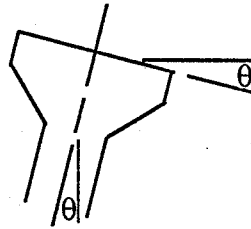


Figure 3-4 Deflection Angle

where the small angle approximation $\tan \theta \approx \theta$ was used. The surface of the sensor is deflected at a different angle than the beam neutral axis because the presence of shear stress causes a shear strain that distorts the angles (Figure 3-5). The shear strain at the sensor surface can be calculated is given by (Saada, 1974:203)

$$\epsilon_{12} = \frac{1 + \nu}{E} \sigma_{12} = \frac{1}{2} \frac{\sigma_{12}}{G} \quad (3-16)$$

Since $\gamma \approx 2\epsilon_{12}$ (Eringen, 1980:35) and $\sigma_{12} = \tau_w$, the angle of deflection β of the sensor surface is given by

$$\beta = \theta - \gamma_{12} = \frac{\tau_w A_H L^2}{2EI} - \frac{\tau_w}{G} \quad (3-17)$$

Using the relation $G = E/2(1+\nu)$ along with $A_H = \pi R_H^2$, Eq (3-17) can be written

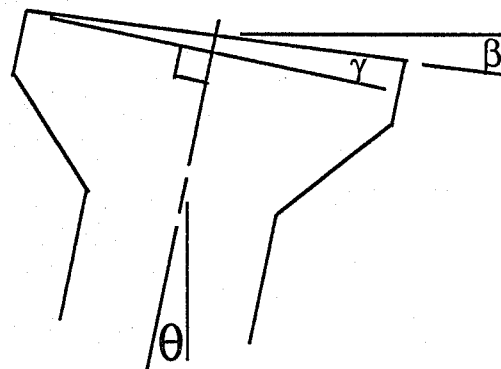


Figure 3-5 Distortion Caused by Shear Strain

$$\beta = \frac{\tau_w \pi R_H^2 L^2}{2EI} \left(1 - \frac{4I(1+\nu)}{\pi R_H^2 L^2} \right) \quad (3-18)$$

Order of magnitude analysis then indicates that the shear stress distortion term $4I(1+\nu)/\pi R_H^2 L^2$ is on the order of 10^{-2} and to first order can be neglected so

$$\beta \approx \frac{\tau_w \pi R_H^2 L^2}{2EI} \quad (3-19)$$

The protrusion is then given by $L_p = R_H \sin \beta \approx R_H$, or, using the result from Eq (3-19),

$$L_p \approx \frac{\pi \tau_w R_H^3 L^2}{2EI} \quad (3-20)$$

For the baseline sensor, Eq (3-20) predicts a rise of 1.2 μm under loading of 10,000 Pa. This appears to be insignificant; however, at high wall shear stresses, the boundary layer thickness is very small, so the protrusion can be of the same order of magnitude as the boundary layer thickness. At lower wall shear stresses, such as that encountered in the NASA Ames run 2066 in the inlet ($\tau_w = 1200$ Pa), the rise of the sensor lip is less (0.17 μm), and the boundary layer is thicker, so the rise of the sensor lip is less than 0.04 percent of the boundary layer momentum thickness, with the momentum thickness calculated as described in Section 4.1.2.3.

The effects of sensor lip protrusion in a supersonic flow were investigated in experiments conducted by Allen (1976:41). Based on Allen's data, for the ratio of sensor head diameter to gap width used in the present research effort, the effect of sensor head protrusion is insignificant if the protrusion is less than 3 percent of the momentum thickness. The error remains less than 10 percent if the protrusion is less than about 7 percent of the momentum thickness. It should be noted that Allen reported his data based on boundary layer thickness rather than momentum thickness. The preceding figures made use of Allen's reported boundary layer and momentum thickness to normalize his data by momentum thickness.

Using the momentum thickness formulation of the Spalding and Chi skin friction correlation as described in Appendix B-4, an analysis was performed for two separate run conditions to determine the effect of sensor lip protrusion. The run conditions were the

NASA Ames Run 2066 inlet and the AFIT shock tube Run 24. Both analyses used the baseline sensor. In this analysis, a momentum thickness was chosen, the wall shear stress computed using the Spalding and Chi correlation, and the sensor lip protrusion calculated using Eq (3-20). Results are shown in Figure 3-6.

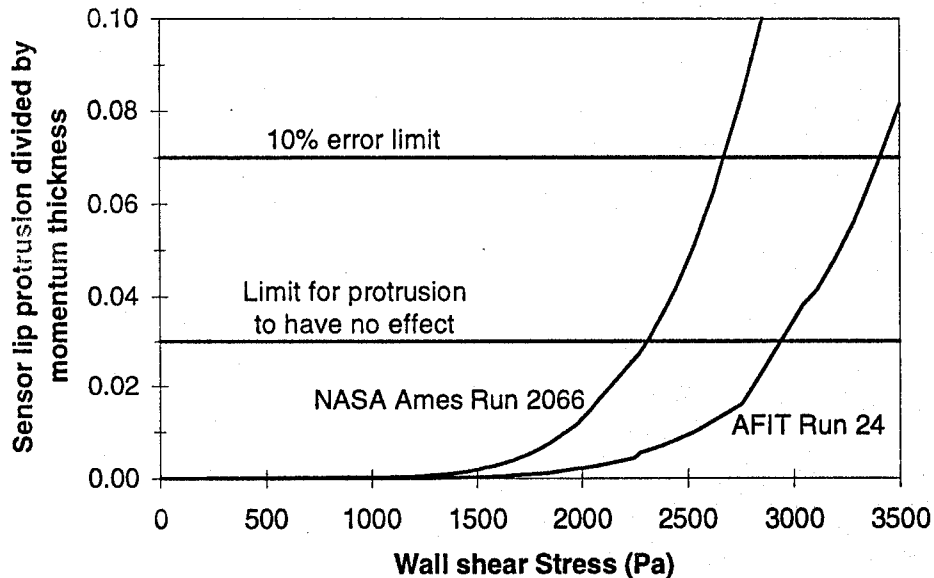


Figure 3-6 Ratio of Sensor Lip Protrusion to Momentum Thickness for Different Wall Shear Stresses

It can be seen from this analysis that, using Allen's findings, the accuracy would be affected above wall shear stresses of about 2300 Pa for the NASA Ames run and 3900 Pa for the AFIT run (in both runs, the measured wall shear stress at the location of the skin friction gauge did not approach these values). However, several factors need to be considered in evaluating this information. First, Allen's tests had the entire sensor head protruding and not just the leading edge as would be the case for the sensor deflection. Second, Allen found that an increased gap width resulted in less degradation of accuracy due to protrusion. Allen used a large sensor with a small gap, so the largest gap width to sensor head ratio that he used was 0.01. With the sensors used in the present research, the gap to head ratio is considerably greater (the gap is small but so is the sensor), ranging from 0.018 for the I-beam gauge to 0.028 for the baseline gauge, so the accuracy degradation may be less. Third, Allen used a larger sensor and thicker boundary layer, so ex-

trapolation to a thin boundary layer may not be valid. Fourth, given that the sensor head protrusion due to deflection is very small, other factors such as machining tolerances may play a greater role than the deflection protrusion. Finally, the boundary layer thickness is a function of the distance from the leading edge; so long as the gauge is not placed in the immediate proximity of the leading edge, a thin boundary layer would not usually be a concern.

3.1.4. Effect of Canting the Gauge

During calibration, the gauge is placed in a horizontal position. This places additional stress on the sensor beam, because both the weight of the sensor head and the weight of the beam itself tend to bend the beam. Bending due to the weight of the beam also occurs when the gauge is used in a slanted position, for example, on a flat plate at angle of attack (both the NASA Ames and Wright Laboratory tests used the gauge in a slanted position).

The principle of superposition was used to evaluate this interaction. The principle of superposition applies to linear elasticity and states that the stress resulting from a combination of several loadings is equivalent to the sum of the stresses that would occur if each load were applied separately (Saada, 1974:215):

$$\sigma_{ij} = \sigma_{ij(P)} + \sigma_{ij(0)} \quad (3-21)$$

Using Eq (3-2), the strain is

$$\epsilon_{11} = \frac{1}{E} (\sigma_{11(P)} + \sigma_{11(0)} + \nu\sigma_{22(0)} + \nu\sigma_{33(0)}) = \epsilon_{11(P)} + \epsilon_{11(0)} \quad (3-22)$$

The change in strain is then

$$\Delta\epsilon_{11} = \epsilon_{11} - \epsilon_{11(0)} = \epsilon_{11(P)} \quad (3-23)$$

Thus, the change in strain due to the loading is the same as the strain if there were no pre-existing strain. In Chapter 4, it will be shown that $\tau_w = A\Delta V$ where ΔV is the difference in voltage resulting from $\Delta\epsilon$. So long as the bridge is balanced prior to applying the load or if the difference in voltage is measured, then any pre-existing strain does not affect the result.

3.2. Dynamic Response

The dynamic response determines how quickly the deflection reaches and stabilizes about the static point and the amount of oscillation. For an accurate measurement of the skin friction, the dynamic behavior of the gauge must approach the statically calculated calibration point within the steady run time. The dynamic response is therefore the key factor in determining the suitability of a particular design for shock tunnel applications. In addition, the dynamic behavior can be a significant factor in introducing error into the response.

The dynamic response of the gauge was evaluated first of all for the purpose of optimizing the gauge design. This required calculation and measurement of the natural frequency. In addition, two vibrational effects were analyzed in the context of error analysis, specifically, the possibility of overdamping, caused by high viscosity oil, and the effect of vibrations being present in the model in which the gauge is mounted.

3.2.1. Natural Frequency

Vibration theory was used to determine the natural frequency of the sensor. The natural frequency is proportional to the inverse of the response time, so a high natural frequency is desired in order to have minimum response time. Three methods were applied. First, an exact solution was developed. Since this solution is a transcendental equation which requires an iterative solution, an approximate solution was also developed to allow direct calculation. Third, the natural frequency was measured experimentally.

The equation of motion for a linearly elastic prismatic beam with constant material properties undergoing transverse vibration is

$$EI \frac{\partial^4 v}{\partial x^4} + \rho A \frac{\partial^2 v}{\partial t^2} = 0 \quad (3-24)$$

Four spatial boundary conditions are required. For the fixed end, Craig (1981:195) gives the boundary conditions as

$$v(0, t) = 0 \quad (3-25)$$

$$\left. \frac{\partial v}{\partial x} \right|_{x=0} = 0 \quad (3-26)$$

For the free end, with a point mass m_h attached, the boundary conditions are

$$EI \left. \frac{\partial^3 v}{\partial x^3} \right|_{x=L} = m_h \left. \frac{\partial^2 v}{\partial t^2} \right|_{x=L} \quad (3-27)$$

$$\left. \frac{\partial^2 v}{\partial x^2} \right|_{x=L} = 0 \quad (3-28)$$

Equation (3-24) is solved by assuming a solution of the form (Craig, 1981:211)

$$v(x, t) = V(x) \cos(\omega_n t - \alpha) \quad (3-29)$$

Equation (3-24) then becomes

$$\frac{d^4 V}{dx^4} - \lambda^4 V = 0 \quad (3-30)$$

where

$$\lambda^4 \equiv \frac{\rho A \omega_n^2}{EI} \quad (3-31)$$

The solution to Eq (3-99) is obtained by assuming a solution of the form (Kreyszig, 1979:104)

$$V = e^{\beta_n x} \quad (3-32)$$

Substituting into Eq (3-30), and applying boundary conditions, the following characteristic equation is obtained:

$$1 + \cosh(\lambda L) \cos(\lambda L) + \frac{m_h}{m_b} \lambda L [\sinh(\lambda L) \cos(\lambda L) - \cosh(\lambda L) \sin(\lambda L)] = 0 \quad (3-33)$$

The quantity λL represents the eigenvalues of the equation of motion. Equation (3-33) is a transcendental equation, so the eigenvalues must be determined using an iterative process. The circular natural frequency is related to the eigenvalues through Eq (3-31). The natural frequency measured in Hz is calculated by dividing the circular natural frequency by 2π :

$$\omega_{Hz} = \frac{(\lambda L)^2}{2\pi L^2} \sqrt{\frac{EI}{\rho A}} \quad (3-34)$$

For specific values of m_h/m_b , Eq (3-118) can be solved using an iterative process. The lowest positive value of λL is used to calculate the natural frequency. Higher values of λL can also be calculated which represent secondary vibration frequencies. For the special case when $m_b=0$, Eq (3-118) collapses to the characteristic equation for a uniform beam (Craig, 1981:215):

$$1 + \cosh(\lambda L)\cos(\lambda L) = 0 \quad (3-35)$$

While Eq (3-33) provides the exact solution for the natural frequency of the sensor, the usefulness of this equation for gauge optimization purposes is limited due to the requirement for an iterative solution. An approximate solution was therefore developed using Rayleigh's method as described by Craig (1981:218).

In Rayleigh's method, the natural frequency is approximated by

$$\omega_n^2 \approx \frac{k}{m} \quad (3-36)$$

where k is a generalized stiffness coefficient defined by

$$k = \int_0^L EI(\psi'')^2 dx + k_i [\psi(x_i)]^2 \quad (3-37)$$

and m is a generalized mass defined by

$$m = \int_0^L \rho A \psi^2 dx + m_s [\psi(x_s)]^2 \quad (3-38)$$

The parameter ψ is an assumed mode for the deflection curve; for this reason, the Rayleigh method is sometimes called the method of assumed modes.

For the problem at hand, the assumed mode will be taken from the deflection curve. Using the elastic curve as given by Eq (3-11), the non-dimensionalized assumed mode is

$$\psi = \frac{3Lx^2 - x^3}{L^3} \quad (3-39)$$

For the case of a beam with a lumped end mass, Eq (3-37) reduces to

$$k = EI \int_0^L (\psi'')^2 dx = \frac{12EI}{L^3} \quad (3-40)$$

the generalized mass expression, (3-38) reduces to

$$m = \rho A \int_0^L \psi^2 dx + m_h [\psi(L)]^2 = \frac{33}{35} m_b + 4m_h \quad (3-41)$$

Substituting Eqs (3-40) and (3-41) into Eq (3-36) and dividing through by 2π to convert the circular natural frequency to Hz results in the following:

$$\omega_{Hz} = \frac{1}{\pi L^{3/2}} \sqrt{\frac{3EI}{\frac{33}{35} m_b + 4m_h}} = \frac{1}{2\pi L^2} \sqrt{\frac{12}{\left[\frac{33}{35} + 4\left(\frac{m_h}{m_b}\right)\right]}} \sqrt{\frac{EI}{\rho A}} \quad (3-42)$$

When Eq (3-42) is compared to the exact solution given by Eq (3-34), it is apparent that the eigenvalue λL is approximated as follows:

$$\lambda L \approx \sqrt[4]{\frac{12}{\left[\frac{33}{35} + 4\left(\frac{m_h}{m_b}\right)\right]}} \quad (3-43)$$

The accuracy of this approximation is shown in Table 3-2, where the approximate value of the eigenvalue calculated from Eq (3-43) is compared to the exact value of the eigenvalue calculated iteratively from Eq (3-34). For design purposes, the difference is negligible.

Table 3-2 Approximate vs. Exact Eigenvalues for Vibration of Uniform Beam with End Mass

$\frac{m_h}{m_b}$	Approximate value of λL from Rayleigh method	Exact value of λL
0.0	1.88879	1.87510
0.1	1.72897	1.72274
0.2	1.61987	1.61640
0.3	1.53832	1.53614

Frequency analysis was conducted by mounting the gauge in a vise or in the shock tunnel mount and initiating vibration by either striking the vise with a mallet or by manually deflecting the sensor head and releasing (both procedures were used). The voltage response was captured using the Datalab DL1200 waveform recorder set at a sampling

rate of 100 kHz. The frequency response was analyzed by using the Fast Fourier Transform along with Hamming window contained in the Data Analysis and Display (DADiSP) software (DSP Development Corp., 1992:7-9). The frequency analysis could also be performed using the wind tunnel trace.

An example of the actual response for the 2 kHz directional gauge is shown in Figure 3-7 along with the frequency spectrum in Figure 3-8. The spike in the trace in

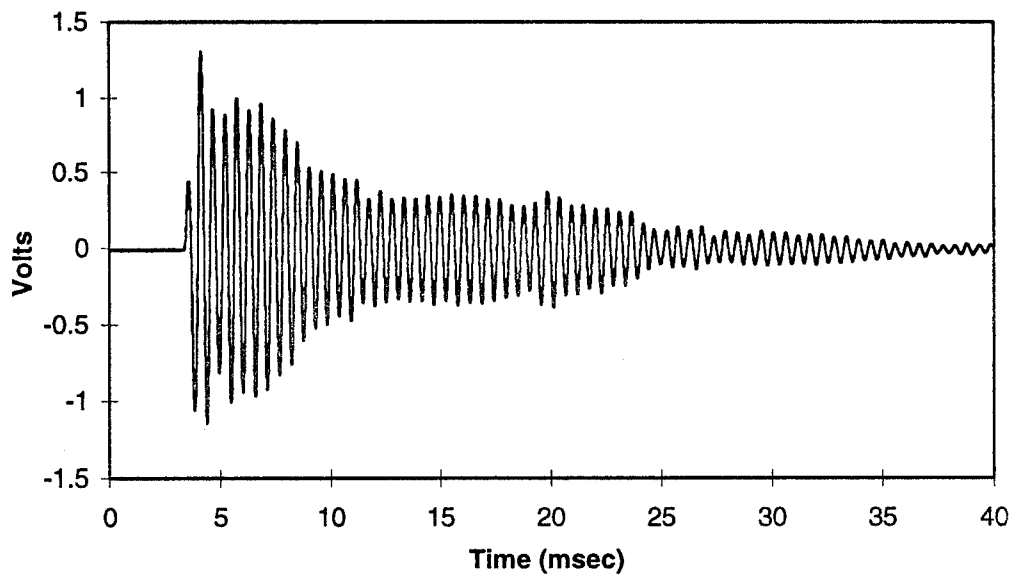


Figure 3-7 Time Response of 2 kHz Directional Gauge

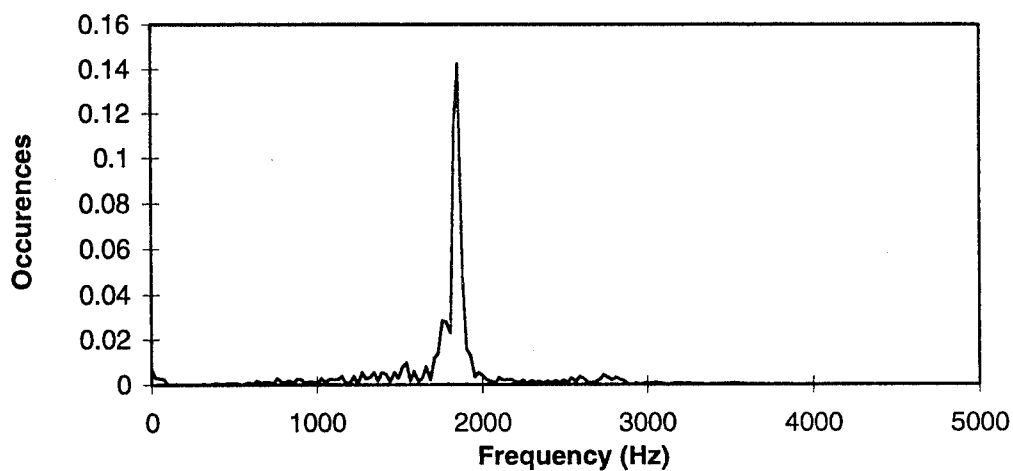


Figure 3-8 Frequency Spectrum for 2 kHz Directional Gauge

Figure 3-8 represents the natural frequency of the gauge, in this case 1.856 kHz. In general, the measured natural frequency compared well with the calculated natural frequency from Eq (3-42) as shown in Table 3-3.

Table 3-3 Predicted vs. Actual Natural Frequency for Various Skin Friction Gauges

Gauge	Type	ω_h (predicted) (kHz)	ω_h (actual) (kHz)
A5	Baseline	10.09	12.62
A7	Baseline	10.09	10.87
10 kHz Directional	Baseline	10.09	9.08
2 kHz Directional	2 kHz	1.63	1.86

3.2.2. Critical Damping

Damping is provided by both the oil and the internal material friction of the beam itself. While damping is desired in order to quickly eliminate the vibration due to the initial deflection of the sensor, if the damping exceeds the critical damping level (i.e., is overdamped), then, as shown in Figure 3-9, the beam slowly and asymptotically approaches

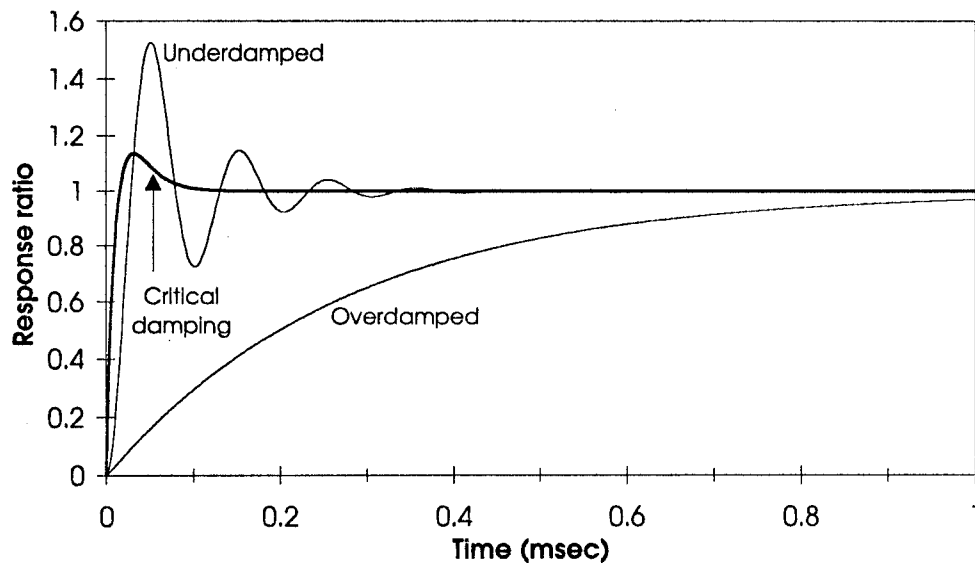


Figure 3-9 Effect of Overdamping

full deflection and may not reach full deflection prior to the end of the run. Thus, overdamping is undesirable.

To determine the critical damping, a single degree of freedom lumped-parameter model will be used. This model, also known as the method of assumed modes, is similar to Rayleigh's method of the previous section. The following equation of motion will be used (Craig, 1981:49):

$$m\ddot{v} + c\dot{v} + kv = p(t) \quad (3-44)$$

where v is a generalized displacement defined by (Craig, 1981:34):

$$V(x, t) = \psi(x)v(t) \quad (3-45)$$

The coefficients m and k are the generalized mass and stiffness defined in the previous section, while c is the generalized viscous damping defined by (Craig, 1981:41)

$$c = \int_0^L c(x)\psi^2 dx + \sum_r c_r \psi_r^2 \quad (3-46)$$

The generalized loading $p(t)$ is given by

$$p(t) = \int_0^L P(x, t)\psi dx + \sum_j P_j \psi_j \quad (3-47)$$

The assumed mode was given in Eq (3-39) in the previous section.

Equation (3-139) will first be solved for a step function with $p(t)=p_0$:

$$m\ddot{v} + c\dot{v} + kv = p_0 \quad (3-48)$$

subject to the following initial conditions:

$$v(0) = 0 \quad (3-49)$$

$$\dot{v}(0) = 0 \quad (3-50)$$

The general solution consists of the sum of the homogenous solution and the particular solution. By inspection, the particular solution is

$$v_p = \frac{p_0}{k} \quad (3-51)$$

For the homogenous equation, a solution of the form $v = e^{st}$ will be used. For critical damping (Craig, 1981:49)

$$c_{cr} = 4mk = \frac{2k}{\omega_n} \quad (3-52)$$

and the homogeneous solution is

$$v_h = (C_1 + C_2 t)e^{-\omega_n t} \quad (3-53)$$

The general solution, formed by combining the homogenous and particular solutions and applying boundary conditions, is

$$v = \frac{P_0}{k} [1 - (\omega_n t + 1)e^{-\omega_n t}] \quad (3-54)$$

The actual displacement as a function of time is obtained by substituting Eq (3-53) into Eq (3-45). The velocity is then found by differentiating with respect to time:

$$U(x, t) = \dot{V}(x, t) = \psi(x) \frac{P_0}{k} \omega_n^2 t e^{-\omega_n t} \quad (3-55)$$

For ideal linear viscous damping, the damping is proportional to velocity. For the case of the sensor beam moving in the oil, however, the drag is not proportional to velocity. Therefore, the concept of equivalent viscous damping will be employed. Following the procedure outlined by Craig (1982:98), the work done by linear damping is given by

$$W_{D(L)} = \int_{t_1}^{t_2} f_D U dt \quad (3-56)$$

where f_D is the drag force per unit length which is first calculated using the linear relation $f_D = cU$. Equation (3-56) then becomes

$$W_{D(L)} = \int_{t_1}^{t_2} cU^2 dt \quad (3-57)$$

The equivalent viscous damping is usually calculated over 1 cycle, but for the critically damped case, a cycle is meaningless. Therefore, this calculation integrates over the time period required for the displacement to achieve 99 percent of its final value, which from Eq (3-53) can be calculated as $3\pi/\omega_n$. Substituting Eq (3-55) into Eq (3-57) and integrating by parts results in the following:

$$W_{D(L)} = \frac{c\psi^2 P_0^2 \omega_n}{4k^2} [1 - (18\pi^2 + 6\pi + 1)e^{-6\pi}] \quad (3-58)$$

In the next part of this derivation, the dimensionless parameter Ha will be used, which was defined here as

$$Ha \equiv \frac{p_0 \omega_n D}{k\nu} \quad (3-59)$$

where ν is the fluid kinematic viscosity and D is the diameter of the sensor beam. Since $1 - (18\pi^2 + 6\pi + 1)e^{-6\pi} = 1.000000007 \approx 1$, Eq (3-58) can be rearranged and written in terms of Ha as

$$c_{eq} = \frac{4\omega_n D^2 W_D}{\psi^2 Ha^2 \nu^2} \quad (3-60)$$

The motion of the beam through the oil will be modeled as a two-dimensional problem, with the velocity of the beam varying according to the position. By differentiating the velocity equation, Eq (3-55), with respect to time and setting equal to zero, the maximum velocity can be found as occurring at time $t=1/\omega_n$.

The quantity p_0 is a generalized loading that can be related to the wall shear stress through Eq (3-142). Since the loading is concentrated at the tip, where $\psi=2$, the generalized loading is given by

$$p_0 = 2P = 2\tau_w A_H \quad (3-61)$$

Substituting this result along with Eq (3-40), $t=1/\omega_n$, and $\psi=2$, into Eq (3-178) gives the maximum velocity as $U_{max} = \tau_w A_H \omega_n L^3 / 6EIe$. The maximum Reynolds number, $Re_D = UD/\nu$, encountered with critical damping is then

$$Re_{D(max)} = \frac{\tau_w A_H \omega_n L^3 D}{6EI\nu e} \quad (3-62)$$

The results of this calculation for the different sensors used in this research are summarized in Table 3-4.

As can be seen from Table 3-4, the Reynolds numbers are very low, so the motion can be characterized as creeping flow. For these flows, the drag coefficient,

$$C_D = \frac{f_d}{\frac{1}{2}\rho U^2 D} \quad (3-63)$$

Table 3-4 Reynolds Numbers for Sensor Beam Vibrating in Oil

	Baseline	I-beam	Mach 6	Directional
Maximum wall shear (τ_w)	5000	5000	500	3000
Natural frequency ($\omega_n/2\pi$)(kHz)	10.09	30.00	2.43	1.63
Maximum velocity (U_{max})(m/sec)	0.0019	0.0048	0.0003	0.0023
Re_D for $v=200$ cSt	0.0441	0.0830	0.0085	0.0724
Re_D for $v=10,000$ cSt	0.0009	0.0017	0.0002	0.0014

can be represented by the Lamb's solution (White, 1991:183):

$$C_D \approx \frac{8\pi}{Re_D \left[.5 - \Gamma + \ln \left(\frac{8}{Re_D} \right) \right]} \quad (3-64)$$

where Euler's constant $\Gamma \approx 0.577216$. Lamb's solution is valid up to a Reynolds number of 1. At the very low Reynolds numbers shown in Table 3-4, Equation (3-64) can be represented by the logarithmic curve fit

$$C_D \approx b Re_D^\Phi \quad (3-65)$$

where b and Φ are constants with values of $b=2.5581$ and $\Phi=-.96553$. This curve fit is valid for Reynolds numbers below 1×10^{-2} .

Rearranging Eq (3-63), substituting the results of Eq (3-65), and writing in terms of the Reynolds number,

$$f_d = \frac{1}{2} b Re_D^{1+\Phi} \mu U \quad (3-66)$$

The work due to viscous drag is given by substituting this result into Eq (3-164) with the upper limit of integration $3\pi/\omega_n$. The result is then written in terms of the non-dimensional time $\hat{t} \equiv t\omega_n$:

$$W_D = \frac{1}{2\omega_n} \int_0^{3\pi} b Re_D^{1+\Phi} \mu U^2 d\hat{t} \quad (3-67)$$

Writing U and Re_D in terms of \hat{t} and Ha , and substituting into Eq (3-67),

$$W_D = \frac{\rho v^3}{2D^2 \omega_n} (Ha \psi)^2 Y \quad (3-68)$$

where

$$Y \equiv bHa^{1+\Phi} \psi^{1+\Phi} \int_0^{3\pi} \hat{t}^{3+\Phi} e^{-(3+\Phi)\hat{t}} d\hat{t} \quad (3-69)$$

Substituting Eqs (3-68) into Eq (3-60), the equivalent viscous damping is given by

$$c_{eq} = 2\mu Y \quad (3-70)$$

Because of the fractional exponents in Eq (3-69), the integral in Y will be evaluated numerically using Simpson's 1/3 rule, which, for an even number of intervals of equal width, is (Gerald, 1978:214):

$$\int_{x_1}^{x_2} f(x) dx = \frac{\Delta x}{3} (f_0 + 4f_1 + 2f_2 + 4f_3 + \dots + 4f_{n-3} + 2f_{n-2} + 4f_{n-1} + f_n) \quad (3-71)$$

Using 1000 increments and double precision, the value of the integral in Y was found to be

$$\int_0^{3\pi} \hat{t}^{2.03447} e^{-2.03447\hat{t}} d\hat{t} = 0.239309 \equiv \Lambda \quad (3-72)$$

The value of Λ is dependent only on the values chosen for b and m and is not geometry-dependent. The value of Y is then $Y = b\Lambda Ha^{1+\Phi} \psi^{1+\Phi}$ and Eq (3-70) becomes

$$c_{eq} = 2\mu b \Lambda Ha^{1+\Phi} \psi^{1+\Phi} \quad (3-73)$$

The generalized damping coefficient can now be calculated from Eq (3-46) which for this problem can be written

$$c = \int_0^L c_{eq}(x) \psi^2 dx \quad (3-46a)$$

The value of Ha depends on the diameter, which is not constant in the head region of the sensor. If Ha is defined in terms of the head diameter

$$Ha_H \equiv \frac{\rho_0 \omega_n D_H}{k v} \quad (3-59a)$$

then the variable Ha quantity can be expressed as

$$\text{Ha}(x) = \frac{P_0 \omega_n D_H}{k\nu} \hat{D} = \text{Ha}_H \hat{D} \quad (3-74)$$

where the nondimensional diameter \hat{D} is given in terms of $\hat{x} = x/L$:

$$\begin{aligned} \hat{D}(x) &= \frac{D_B}{D_H} \equiv \hat{D}_B & \hat{x} \leq \hat{x}_1 \\ \hat{D}(x) &= n(\hat{x} - \hat{x}_1) + \hat{D}_B & \hat{x}_1 < \hat{x} < \hat{x}_2 \\ \hat{D}(x) &= 1 & \hat{x}_2 \leq \hat{x} \leq L \end{aligned} \quad (3-75)$$

and

$$\begin{aligned} \hat{x}_1 &= \frac{L - T_R - T_H}{L} \\ \hat{x}_2 &= \frac{L - T_H}{L} \\ n &= \frac{1 - \hat{D}_B}{(T_R/L)} \end{aligned} \quad (3-76)$$

The equivalent viscosity as a function of x can then be expressed

$$c_{\text{eq}}(x) = \begin{cases} 2\mu b \Lambda \text{Ha}_H^{1+\Phi} D_B^{1+\Phi} \psi^{1+\Phi} & \hat{x} \leq \hat{x}_1 \\ 2\mu b \Lambda \text{Ha}_H^{1+\Phi} [n(\hat{x} - \hat{x}_1) + D_B]^{1+m} \psi^{1+m} & \hat{x}_1 < \hat{x} < \hat{x}_2 \\ 2\mu b \Lambda \text{Ha}_H^{1+\Phi} \psi^{1+\Phi} & \hat{x}_2 \leq \hat{x} \leq L \end{cases} \quad (3-77)$$

The assumed mode will also be written in terms of the non-dimensional \hat{x} is $\psi = 3\hat{x}^2 - \hat{x}^3$.

Substituting this and Eq (3-77) into Eq (3-46a),

$$c = \int_0^L c_{\text{eq}}(x) \psi^2 L d\hat{x} = 2b\Lambda L \mu \text{Ha}_H^{1+\Phi} A_D \quad (3-78)$$

where the damping constant A_D is defined by

$$\begin{aligned} A_D &\equiv D_B^{1+\Phi} \int_0^{\hat{x}_1} (3\hat{x}^2 - \hat{x}^3)^{3+\Phi} d\hat{x} + \int_{\hat{x}_1}^{\hat{x}_2} [n(\hat{x} - \hat{x}_1) + \hat{D}_B]^{1+\Phi} (3\hat{x}^2 - \hat{x}^3)^{3+\Phi} d\hat{x} \\ &\quad + \int_{\hat{x}_2}^L (3\hat{x}^2 - \hat{x}^3)^{3+\Phi} d\hat{x} \end{aligned} \quad (3-79)$$

The dimensionless constant A_D is geometry dependent and must be evaluated for each sensor design. The integrals were evaluated numerically using Simpson's 1/3 rule as described in Eq (3-71), again using 1000 increments. The numerically calculated constants are shown in Table 3-5.

Table 3-5 Damping Constants

Gauge	Damping Constant A_D
Baseline	0.941542
I-beam	0.938615
Mach 6	0.942346
Directional	0.932473

Rearranging Eq (3-79) and substituting the results from Eq (3-52), (3-40), and the definition $\nu = \mu/\rho$, the critical viscosity is then

$$\nu_{cr} = \frac{3EI}{b\Lambda L^4 \rho_{oil} \omega_n Ha_H^{1+\Phi} A} \quad (3-80)$$

Now, using the value of p_0 as given by Eq (3-61), and k as given by Eq (3-40), Ha_H can be written:

$$Ha_H = \frac{2\tau_w A_H \omega_n D_H}{(12EI/L^3)\nu} = \frac{\tau_w A_H \omega_n D_H L^3}{6EI\nu} \quad (3-81)$$

Substituting into Eq (3-80)

$$\nu_{cr} = \frac{EI}{L^4 \rho_{oil} \omega_n} \left(\frac{3}{b\Lambda A_D} \right)^{-1/\Phi} \left(\frac{6E^2 I^2}{L^7 \rho_{oil} \omega_n^2 \tau_w A_H D_H} \right)^{-(1+\Phi)/\Phi} \quad (3-82)$$

Using Eq (3-82), the critical damping viscosities were calculated for each sensor geometry for various τ_w values. The results are plotted in Figure 3-10.

As can be seen from Figure 3-10, the oil viscosities required for critical damping levels are very high. This finding allowed the use of high viscosity oils in the latter part of this research effort, which provided improved oil retention. The oil viscosities used in

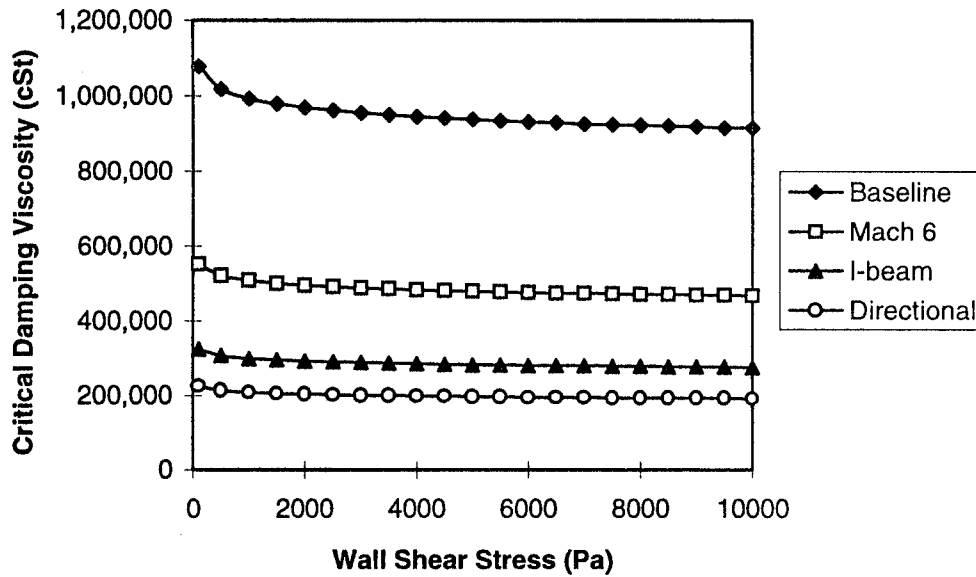


Figure 3-10 Critical Damping Viscosities

these later tests were 10,000 cSt for the GASL tests and 1,000 cSt for the AFIT tests. Previously, the primary viscosities used in the research were 200 cSt and 350 cSt.

3.2.3. Effect of Vibrating Base

Vibrations of the wind tunnel and model can result in vibration of the sensor, and hence affect the measured wall shear stress. The effect of the vibrating base will be analyzed using a single degree of freedom model. The single degree of freedom model for the base in motion is (Craig, 1981:21)

$$m\ddot{w} + c\dot{w} + kw = p(t) - m\ddot{z} \quad (3-83)$$

The base motion is given by

$$z = Z \cos \Omega t \quad (3-84)$$

Solving for the situation where the system is initially at rest, the initial conditions are

$$w(0) = 0 \quad \dot{w}(0) = 0 \quad (3-85)$$

If underdamping is assumed and the loading is taken as a step function such that $p(t)=p$, then, as derived in Appendix B, the solution to the differential equation is

$$\begin{aligned}
w(t) = & \frac{p}{k} \left[1 - e^{-\zeta\omega_n t} \left(\cos \omega_d t + \frac{\zeta\omega_n}{\omega_d} \sin \omega_d t \right) \right] \\
& + r^2 D_s Z \left\{ \cos \Omega t \cos \alpha + \sin \Omega t \sin \alpha \right. \\
& \left. - e^{-\zeta\omega_n t} \left[\cos \alpha \left(\cos \omega_d t + \frac{\zeta\omega_n}{\omega_d} \sin \omega_d t \right) + \frac{\Omega \sin \alpha}{\omega_d} \sin \omega_d t \right] \right\} \quad (3-86)
\end{aligned}$$

where

$$r \equiv \frac{\Omega}{\omega_n} \quad (3-87)$$

$$\zeta \equiv \frac{c}{c_{cr}} = \frac{c}{2k/\omega_n} = \frac{c\omega_n}{2k} \quad (3-88)$$

$$D_s = \frac{1}{\sqrt{(1-r^2)^2 + (2\zeta r)^2}} \quad (3-89)$$

If W is defined as the magnitude of the induced sensor vibration relative to the base, then, as shown in Appendix B,

$$\frac{W}{Z} = 2 \left(\frac{1}{\omega_n^2} \right) \left(\frac{\omega_n}{2\zeta} \right) \Omega \zeta r D_s = r^2 D_s \quad (3-90)$$

Since the skin friction measurement is inferred from the sensor displacement relative to the base, W is an error term. Z is the magnitude of the base vibration. If Z is considered fixed, then minimizing the error is dependent upon minimizing the $r^2 D_s$ term. D_s is a function of only r and ζ , so the error factor $r^2 D_s$ is dependent only on r and ζ .

A plot of $r^2 D_s$ for various values of ζ is shown in Figure 3-11. In this figure, it can be seen that $r^2 D_s$ decreases as r decreases for r less than 1. The spike for values of r near to 1 is the resonance condition where the frequency of the base vibration is the same as the natural frequency of the sensor. For values of r above 1 (base frequency greater than the sensor natural frequency), the sensor head tends to remain stationary as the base vibrates, causing a relative vibration near equal in magnitude to the base motion. For skin friction

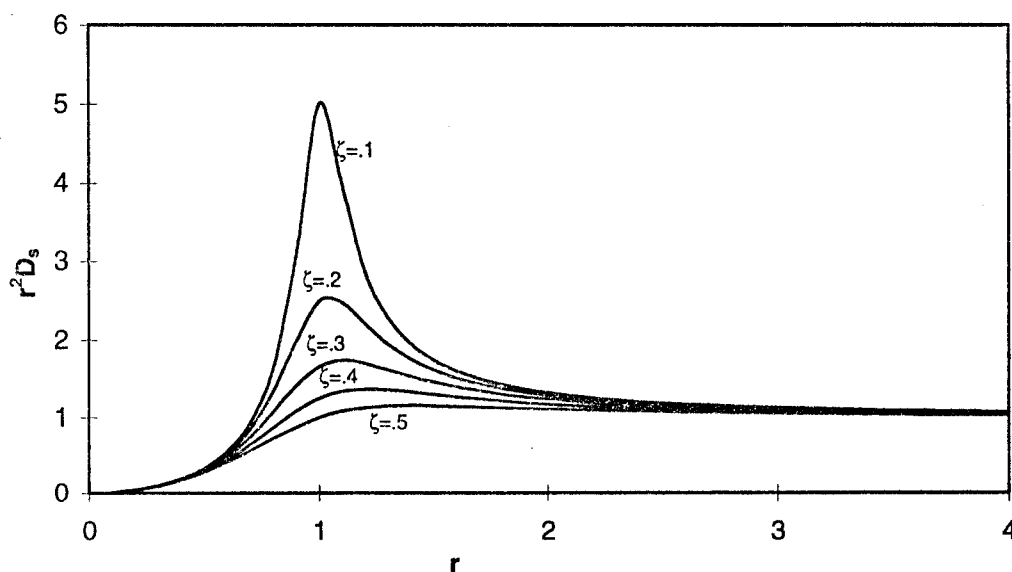


Figure 3-11 Magnification Factor

gauges, this would occur rarely, since the sensor is designed for high frequency, and the base (the wind tunnel model) is more massive and tends to vibrate at lower frequencies.

The r factor can be decreased by increasing the natural frequency. In addition, as can be seen in Figure 3-11, increasing the damping also decreases the magnitude of the relative vibration as r approaches 1 (the resonance condition).

The r factor is governed only by natural frequency. However, the damping level is affected by both the natural frequency and mass. From Eq (3-36), $k = m\omega_n^2$. Substituting this result into Eq (3-88),

$$\zeta = \frac{c}{2m\omega_n} \quad (3-91)$$

The implication is that for two sensors of the same natural frequency, the same viscosity of oil would give a lower damping level for the sensor with higher mass. Thus the more massive sensor would have a more pronounced sensitivity to base vibration as the resonance condition is approached.

Figure 3-12 shows a plot of the motion given by Eq (3-86) for several cases with a 900 Hz base vibration with displacement half that of the deflected sensor displacement.

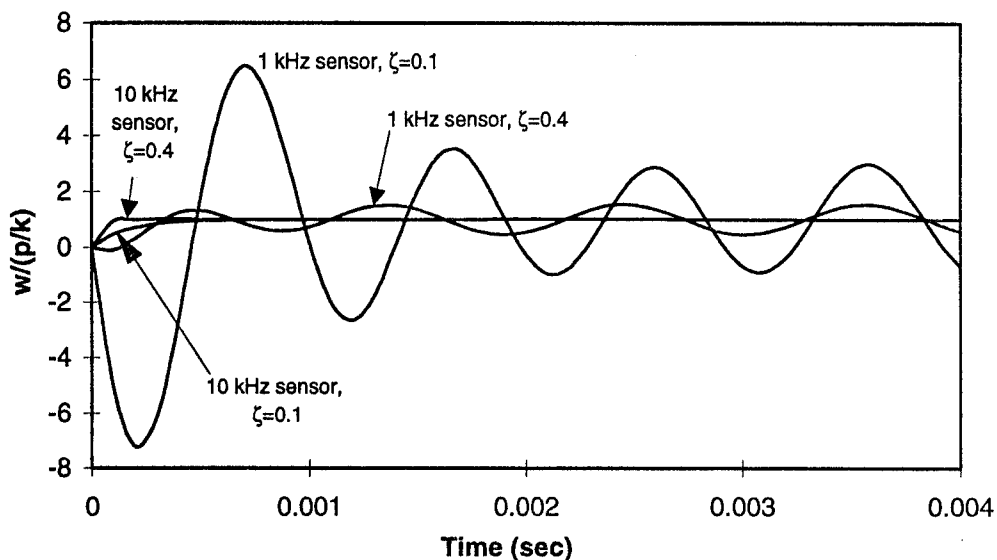


Figure 3-12 Relative Sensor Displacement

The abscissa of the plot is the deflection of the sensor (w) normalized by what the deflected position would be without base vibration (p/k). Thus, a y -reading of 1 represents means that the sensor position corresponds to the correct static calibration position, while a reading of other than 1 represents error. The low frequency sensor (1 kHz, near resonance) continues to oscillate broadly about the deflected position, although this oscillation is decreased by increased damping. The high frequency sensor (10 kHz) exhibits little sensitivity to the base vibration.

Figure 3-13 shows the skin friction traces for Run 16 conducted in the AFIT shock tunnel. In this run, the 10 kHz and 2 kHz directional gauges were both aligned under the shock coming off a sharp fin with 10 degree half-angle. A base vibration is evident in both traces. An FFT analysis showed that the base vibration was at a frequency of 1.43 kHz. Thus, the base vibration is close to the natural frequency of the 2 kHz gauge. However, it is the 10 kHz gauge that shows the greatest sensitivity to the base vibration. This is due primarily to the damping. Both gauges were oiled with 1,000 cSt oil. It was shown in the previous section that the viscosity required for critical damping of the baseline gauge is 5

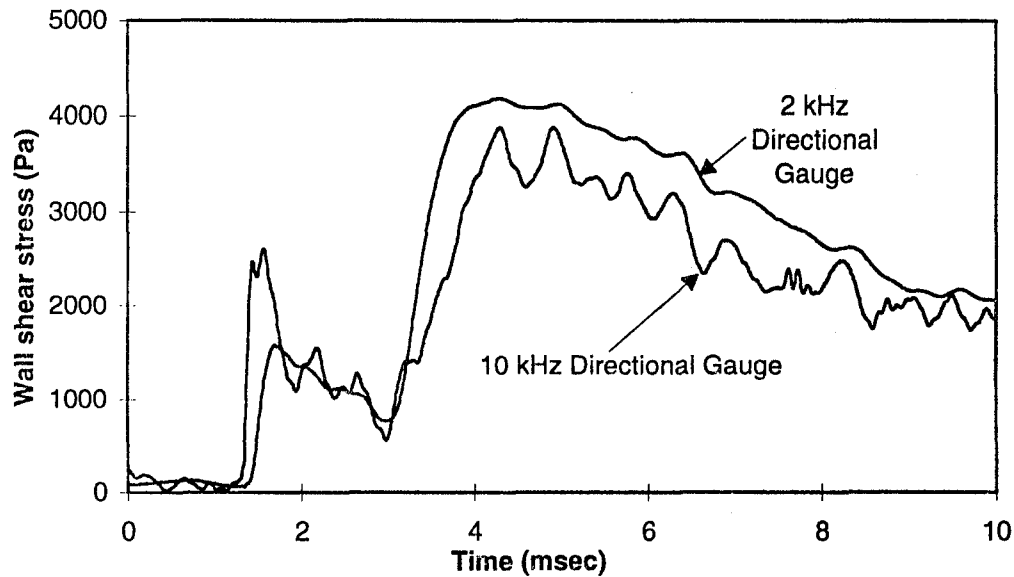


Figure 3-13 Skin Friction Traces Showing Effects of Base Vibration, AFIT Run 16

times higher than that required for the 2 kHz directional gauge. Thus, the same viscosity oil provides a higher level of damping for the 2 kHz gauge.

3.3. Material Mechanics

Material mechanical effects are important both for gauge design purposes and because of potential error effects. Failure limits were investigated to ensure that the loading did not exceed the material yield limit. Viscoelasticity was evaluated because of its potential effect on gauge accuracy.

3.3.1. Failure Limits

Two of the more common theories for predicting the onset of yield are those of von Mises and Tresca (Hosford and Caddell, 1983:31-33). Both of these theories reflect the experimentally observed fact that hydrostatic stress does not affect the onset of yield.

The von Mises criterion, which is based on distortion energy reaching a critical level, predicts the onset of yield when (Hosford and Caddell, 1983:33)

$$(\sigma_1 - \sigma_2)^2 + (\sigma_2 - \sigma_3)^2 + (\sigma_3 - \sigma_1)^2 = 2Y^2 = 6k^2 \quad (3-92)$$

On the outer edge at the base of the beam, with $x_1=0$, $x_2=R$, and $x_3=0$, the principal stresses are given from Eq (3-1) by

$$\sigma_1 = \sigma_{11} = -\frac{PLR}{I} \quad \sigma_2 = \sigma_3 = 0 \quad (3-93)$$

For this location, the von Mises criteria becomes $|\sigma_1| = Y$, so, from Eq (3-93), yielding occurs when

$$P = \frac{YI}{LR} \quad (3-94)$$

For a circular beam, Eq (3-94) becomes $P = \pi Y R^3 / 4L$. For the baseline sensor, with $R = .00254$ m, $L = .0064$ m, and $Y = 105 \times 10^6$ Pa, the yield load was calculated from Eq (3-94) as 211 N, equivalent to a loading mass of 21.5 kg or a wall shear stress of 5,151 kPa.

The Tresca criterion states that yielding occurs when the largest shear stress reaches a critical value. In terms of principal stresses, with $\sigma_1 > \sigma_2 > \sigma_3$, the Tresca criteria can be stated as (Hosford and Caddell, 1983:31)

$$\sigma_1 - \sigma_3 = Y \quad (3-95)$$

At the point of maximum stress, the Tresca criterion yields the same result as the von Mises.

The failure limit for the beam is high due to the shortness of the beam as well as the high yield strength of the plastic (approximately half the yield strength of steel). Considering this analysis, it appears that yield should not be an area of concern.

3.3.2. Viscoelasticity

Viscoelastic behavior is a combination of elastic behavior for which the material stress is independent of the rate of strain, and viscous behavior, for which the stress is dependent on the rate of strain. While all materials exhibit some degree of viscoelasticity, plastics typically exhibit a greater amount of viscoelastic behavior than do metals. Examples of viscoelastic behavior include creep, where under a constant load, the resulting strain continues to increase, and stress relaxation, where a stress that initially produces a given strain can be relaxed while the strain is maintained at a constant level. This could be

a source of inaccuracy for the skin friction gauge, since the calibration factor is considered to be constant, not time-dependent.

Linear viscoelastic theory was applied to determine the effect of viscoelasticity on the gauge performance. Experimental measurements were also undertaken to determine the viscoelastic behavior of the material. The goal of this part of the research was to determine the error introduced by viscoelastic response.

3.3.2.1. Mechanical Model

A common technique in the study of viscoelasticity is to convert the problem to an equivalent elastic problem by using the Laplace transform. Using this technique as described in Appendix B, the strain for a viscoelastic cantilever beam for the time dependent loading

$$P(t) = P_0 [H(t) - H(t - t_1)] \quad (3-96)$$

is given by

$$\epsilon(t) = \left[\frac{P_0(L - x_1)R}{I} \right] [J(t) - H(t - t_1)J(t - t_1)] \quad (3-97)$$

where $J(t)$ is the creep compliance, which is a function that depends on the viscoelastic model.

The above solution represents the strain that would be encountered during calibration of the skin friction gauge, when a weight is abruptly applied and then removed. This solution can be extended to a load function consisting of several incremental step loadings such as could be encountered in a shock tunnel run or in a calibration series in which weights are added incrementally. This type of load function could be represented by

$$P(t) = H(t)P_1 + H(t - t_1)P_2 + H(t - t_2)P_3 - H(t - t_3)(P_1 + P_2 + P_3) \quad (3-98)$$

For this loading, the strain solution is

$$\begin{aligned} \epsilon(t) = \left[\frac{(L - x_1)R}{I} \right] & \left[J(t)P_1 + H(t - t_1)J(t - t_1)P_2 \right. \\ & \left. + H(t - t_2)J(t - t_2)P_3 - H(t - t_3)J(t - t_3)(P_1 + P_2 + P_3) \right] \end{aligned} \quad (3-99)$$

The Burgers model was selected to model the viscoelastic response. The creep compliance for this model is (Findley, Lai, and Onaran, 1989:73-75)

$$J(t) = \frac{1}{R_1} + \frac{1}{R_2} \left(1 - e^{-R_2 t / \eta_2}\right) + \frac{t}{\eta_1} \quad (3-100)$$

It can be seen through an examination of Eq (3-100) that the constant R_1 represents an instantaneous response and is analogous to the elastic modulus E . The second term in J represents a curve which over time approaches a constant $1/R_2$. The third term represents a time dependent term with constant slope $1/\eta_1$.

Rather than attempt to determine the material constants, the effect of the viscoelasticity on the voltage response of the sensor will be evaluated. In Appendix B, it is shown that the voltage response when the strain gauges are in a Wheatstone bridge is given by

$$V = \frac{V_e k \epsilon D}{2} \quad (3-101)$$

The elastic response can be written from Eq (3-4) as

$$\epsilon = \frac{P L_s R}{EI} \quad (3-4a)$$

where L_s , the actual distance from the sensor top to the midpoint of the strain gauge has replaced $L - L_{sgt}/2$, the design distance. The voltage slope $b_i = V/m = Vg/P$ for the elastic response can be written by substituting Eq (3-4a) into Eq (3-101) and multiplying by g/P :

$$b_i = \frac{V_e k D L_s R g}{2EI} \quad (3-102)$$

The viscoelastic strain for the calibration case where a weight is abruptly applied and then abruptly removed is provided by Eq (3-97). Substituting into Eq (3-101), letting $L - x_1 = L_s$, and multiplying through by g/P , the viscoelastic voltage slope b_t is obtained

$$b_t = \frac{V_e k D}{2E} \left(\frac{L_s R g}{I} \right) E [J(t) - H(t - t_1) J(t - t_1)] \quad (3-103)$$

which by comparison with Eq (3-102) can be written

$$b_t = b_i E [J(t) - H(t - t_1) J(t - t_1)] \quad (3-104)$$

3.3.2.2. Experimental Measurements

The viscoelastic measurements were conducted in the same manner as the calibration described in Chapter 2. The gauge was placed in a prone position in a vise, with a weight suspended from the sensor head. In this case, however, the weight was left suspended for approximately 80 seconds. The voltage response was recorded using the Datablab DL1200 waveform recorder that was also used for the AFIT shock tunnel tests. The sampling interval was set at 20 msec to provide an 80 second record. One of each sensor type used in this research was tested.

The viscoelastic constants were then calculated by normalizing the data by the instantaneous (initial) response. From Eqs (3-104), voltage response to a step function can be represented by

$$\frac{b_t}{b_i} = EJ(t) \quad (3-105)$$

If E is considered to be equal to $1/R_1$, then J(t) can be written

$$J(t) = \frac{1}{E} [1 + B_1(1 - e^{-\beta t}) + B_2 t] \quad (3-106)$$

where

$$B_1 = \frac{1}{ER_2} \quad B_2 = \frac{1}{E\eta_1} \quad \beta = \frac{R_2}{\eta_2} \quad (3-107)$$

Substituting Eq (3-106) into Eq (3-105) and using the definition $b=V/m$,

$$\frac{V_t}{V_i} = 1 + B_1(1 - e^{-\beta t}) + B_2 t \quad (3-108)$$

The constants are then fit to the normalized V curve as follows: The constant B_2 is the slope to which the curve asymptotes with units sec^{-1} . The constant B_1 is a dimensionless value that represents the offset between the final response and a line with slope B_2 drawn from the instantaneous response. The constant β is calculated by rearranging Eq (3-108) into the form

$$\beta = -\frac{1}{t} \ln \left(\frac{B_1 + 1 + B_2 t - \frac{V_t}{V_i}}{B_1} \right) \quad (3-109)$$

The units of β are sec^{-1} .

The constants thus calculated are shown in Table 3-6. An example of the measured voltage response and the curve fit are shown in Figure 3-14.

Table 3-6 Viscoelastic Constants for Different Sensor Materials

	Ultem	Victrex
B_2 (sec^{-1})	0.000135	0.000123
B_1	0.042122	0.035985
β (sec^{-1})	0.081190	0.075832

In theory, the viscoelastic constants should be the same for each gauge because the calibration constant takes into account variations in dimensions and strain gauge placement. In practice, however, some variation is seen due to the effect of the interaction of

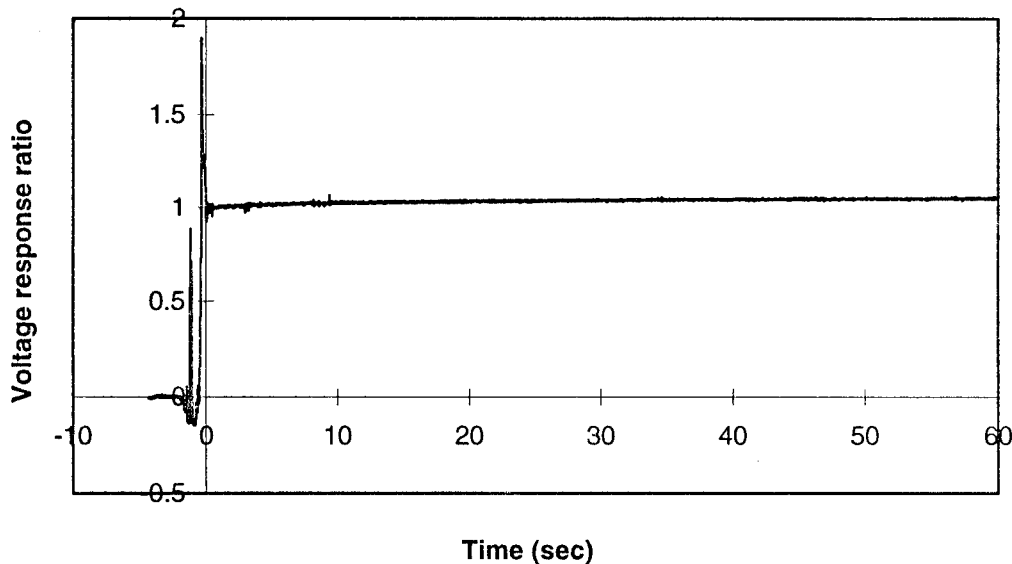


Figure 3-14 Burgers Model Curve Fit for Average Creep Response of Sensors Made of Ultem Plastic

the strain gauge and glue with the plastic material. Hence, the calculated viscoelastic constants are not truly material constants but are somewhat dependent on the particular gauge. However, the goal of this part of the research is not to accurately determine the material constants but to quantify the potential error, and the constants shown in Table 3-6 are adequate for this purpose.

3.3.2.4. *Potential Error in Calibration and Use*

If the instantaneous voltage response is used for the calibration value, then the potential error can be estimated from Eq (3-108). For a simple step change in loading, the error at the end of a 5 msec run is 0.0018 percent. If a spike occurs at the beginning of the run, similar to the model shown in Figure 3-15, then the error at the end of a 5 msec run is 0.0032 percent. (This value is for the particular spike shown. Increasing the magnitude or duration of the spike increases the error.) For a blowdown tunnel, the error at the end of a 5 sec run is 1.5 percent. The error here is greater because the time scales are seconds rather than milliseconds. Since the voltage increases for a set loading, the error is an overestimate of the wall shear stress.

In calibration, the potential error is more serious because again the time scales are seconds rather than milliseconds. Figure 3-16 shows an idealized calibration loading. The

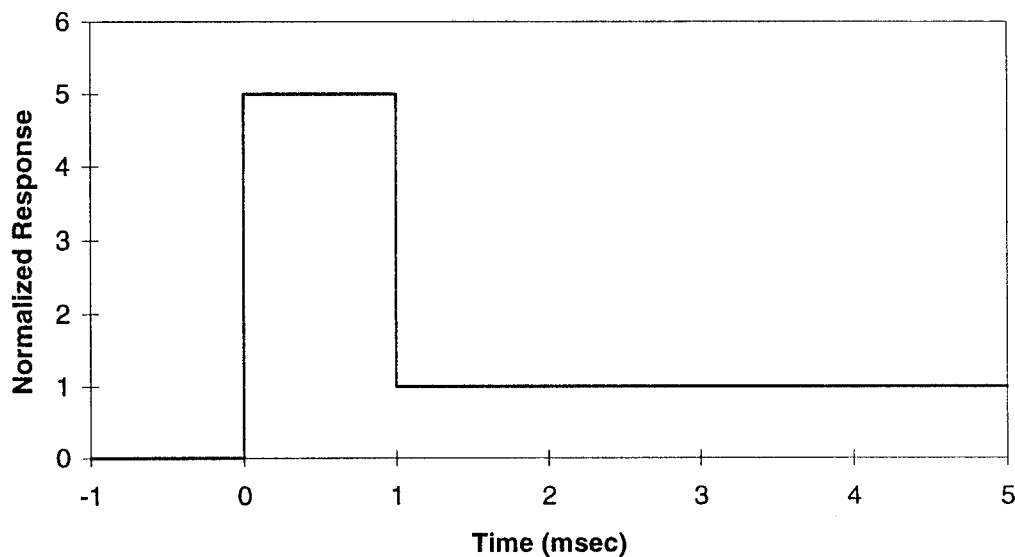


Figure 3-15 Spike Followed by Steady Load

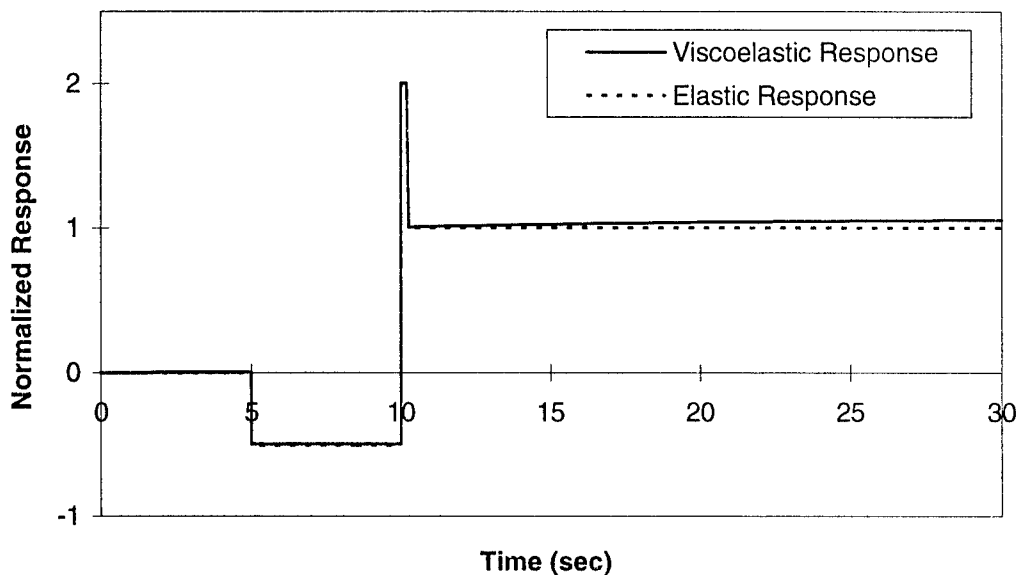


Figure 3-16 Calibration Error Due to Viscoelastic Response

dip is caused by the lifting of the weight holder, followed by a spike upon load application, and then the steady response to the weight. If the response were read at the end of the time period on the chart, the error would be 5.6 percent for this particular case. However, if the response were taken immediately after the spike, and the difference between this point and the point immediately prior to the lifting of the weight holder is used, then the error is reduced to 0.09 percent.

The instantaneous response can best be determined by calibration with a data acquisition system and then taking the initial voltage jump as the instantaneous response (Figure 3-17). The response on unloading can also be used, but it was more difficult to precisely determine the unloading instantaneous response. For the gauges used in this research, the Datalab DL1200 data acquisition system was used along with Data Analysis and Display (DADiSP) software. The DADiSP software has a cursor system that allows the voltage difference between two points to be easily determined.

3.4. Pressure Sensitivity

Pressure changes could affect the accuracy of the wall shear stress if the skin friction gauge is sensitive to pressure effects. Two types of pressure sensitivity were investi-

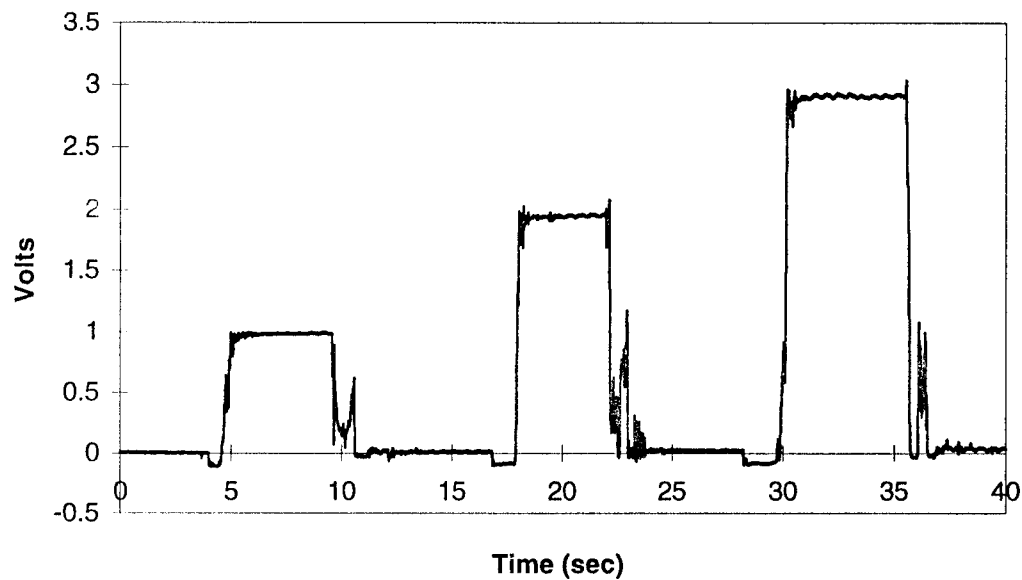


Figure 3-17 Load Response from Data Acquisition System for a Typical Calibration

gated. First, sensitivity to changes in normal pressure was evaluated, with the normal pressure assumed to be constant everywhere on the sensor head. Second, the effect of a pressure gradient across the sensor head was considered.

3.4.1. Normal Pressure Sensitivity

The cantilever skin friction gauge is designed to be insensitive to changes in normal pressure. However, normal pressure on the sensor head causes strain in the cantilever which changes the resistance of the strain gauges, and variations in normal pressure are significant compared to the magnitude of the wall shear.

The normal pressure is hydrostatic in nature and is approximately the same all around the cantilever (the weight of the oil surrounding the sensor causes the pressure to be slightly greater at the base of the cantilever). The strain imparted by this pressure is given by (Saada, 1974:201)

$$\epsilon_{11} = \epsilon_{22} = \epsilon_{33} = -\frac{p}{3K} \quad (3-110)$$

The shear strains are zero. Thus, in theory, for a cantilever with a solid core, the strain is the same at all points on the cantilever, and whatever strain is imparted to one strain gauge should also be imparted to the other, resulting in cancellation of any voltage changes due to changes in the normal pressure. This would be true even if the strain gauges are misaligned. The strain gauges themselves are also sensitive to hydrostatic pressure apart from the strain caused by the dilatation of the cantilever (Neubert, 1967:11). However, in theory, cancellation should also be obtained for this effect. For a hollow sensor, where the core is maintained at a fixed pressure, cancellation may not be obtained if the strain gauges are misaligned, because stresses other than hydrostatic are involved, and Eq (3-110) no longer holds.

3.4.1.1. Experimental Evidence

Two sets of experiments were conducted in which the output of the skin friction gauge was monitored while the pressure was varied. These experiments were carried out with a vacuum pump since the static pressures of most of the wind tunnels used in this research are less than atmospheric pressure.

The first experiment used the re-oiling device described in Section 4.3.3 to test the pressure sensitivity of the 2 kHz gauge. This re-oiling device is primarily a vacuum mechanism that fits over the top of the gauge and uses suction to obtain a seal. The air is then evacuated, oil is poured over the gauge, and then a partial pressure of approximately 1/2 atmosphere is restored to force the oil in while maintaining enough vacuum to retain a good seal.

In using this device for the pressure sensitivity test, the skin friction gauge was operated in a Wheatstone bridge arrangement with signal conditioner/amplifier and the voltage output was monitored. The suction device was placed over the top of the skin friction gauge. The pressure was reduced to near-vacuum. A valve was then opened to rapidly change the pressure to partial vacuum. The pressure was then returned to atmospheric. The voltage output was initially set to zero. While air was flowing into the suction device, the voltage spiked, probably from vibrations, but immediately returned to zero

at both 1/2 atmosphere and 1 atmosphere. Thus, this gauge had no detectable normal pressure sensitivity.

The second pressure test was conducted on the baseline, 2 kHz directional gauge, and the hollow beam gauge. This test was conducted by mounting the skin friction gauges along with a pressure transducer in a vacuum chamber. The voltage response of the gauges, along with the pressure, was recorded with the Datalab DL1200 data acquisition system as the pressure was reduced and then increased. At minimum pressure, the change in voltage for all three gauges was slight, but definite, amounting to 5-10 percent of the expected reading due to wall shear in the shock tunnel runs (Figure 3-18). However, the voltage response lagged the pressure change by approximately 2 msec. While a pressure correction could be developed, the test section pressure in the present shock tunnel runs is close to atmospheric, and the steady portion of the run is only 2 msec. In addition, the pressure variation during this test was much larger than would be experienced in the wind tunnel. For these reasons, it was concluded that pressure induced error would be negligi-

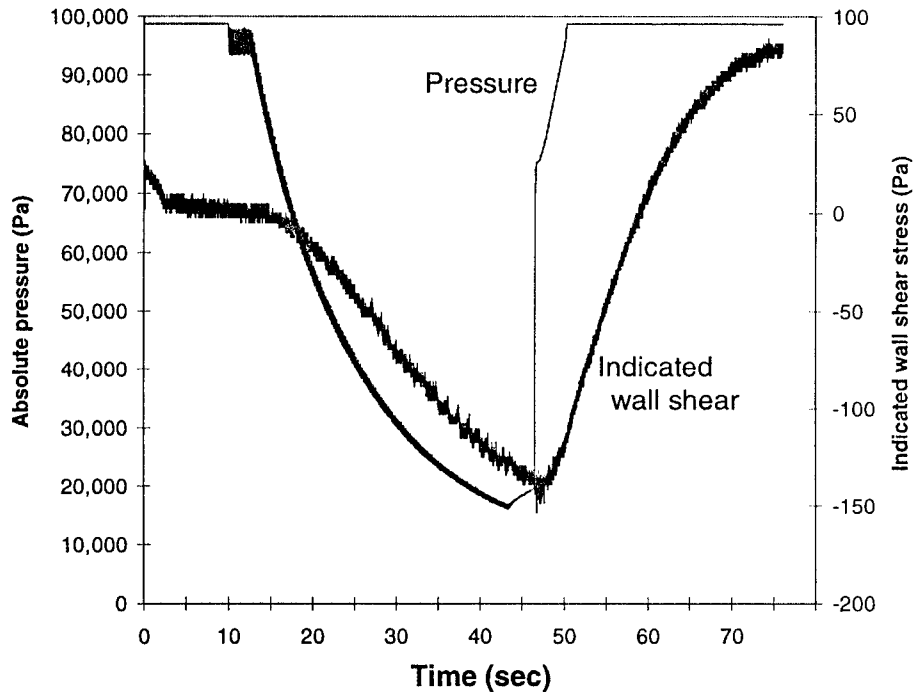


Figure 3-18 Pressure Sensitivity for 2 kHz Directional Gauge (Longitudinal Axis)

ble, and the skin friction readings were not corrected for pressure.

3.4.1.2. Analysis

The probable cause for the pressure sensitivity is that the gauge factor is not the same for the different strain gauges. The strain gauges are manufactured with a 5 percent tolerance in gauge factor. With different gauge factors, the change in strain would be the same, but the change in resistance would differ, thereby causing a change in voltage.

The pressure sensitivity due to a difference in gauge factors is calculated in Appendix B as

$$V = \frac{V_e k \epsilon \delta_k}{4} \quad (3-111)$$

where

$$k_c = (1 + \delta_k) k_t = (1 + \delta_k) k \quad (3-112)$$

Since $\epsilon = -p/3K$, and the bulk modulus can be written in terms of the elastic modulus as $K = E/3(1-2\nu)$ (Saada, 1974:203), the hydrostatic strain can be written $\epsilon = -p(1-2\nu)/E$.

The hydrostatic voltage response is then

$$V_p = \frac{V_e k \delta_k p (1-2\nu)}{4E} \quad (3-113)$$

Also from Appendix B, the voltage response for a strain caused by deflection is $V = V_e k \epsilon / 2$. The strain response under endloading is given by Eq (3-5a), so the endloading voltage response is then

$$V_\tau = \frac{V_e k \tau_w A_H L_s R}{2EI} \quad (3-114)$$

For a circular beam, $I = \pi R^4 / 4$, so if Poisson's ratio is taken as 1/3, then the ratio of the pressure response to the wall shear response is

$$\frac{V_p}{V_\tau} = \frac{p}{\tau_w} \left(\frac{\delta_k \pi R^2}{24 A_H L_s} \right) \quad (3-115)$$

The ratio of the pressure variation to the wall shear can typically be 50 - 100, but even for the maximum value of $\delta_k = 0.1$, for the gauge designs used for this research, the calculated

ble, and the skin friction readings were not corrected for pressure.

3.4.1.2. Analysis

The probable cause for the pressure sensitivity is that the gauge factor is not the same for the different strain gauges. The strain gauges are manufactured with a 5 percent tolerance in gauge factor. With different gauge factors, the change in strain would be the same, but the change in resistance would differ, thereby causing a change in voltage.

The pressure sensitivity due to a difference in gauge factors is calculated in Appendix B as

$$V = V_e k \epsilon \delta_k \quad (3-111)$$

where

$$k_c = (1 + \delta_k) k_t = (1 + \delta_k) k \quad (3-112)$$

Since $\epsilon = -p/3K$, and the bulk modulus can be written in terms of the elastic modulus as $K = E/3(1-2\nu)$ (Saada, 1974:203), the hydrostatic strain can be written $\epsilon = -p(1-2\nu)/E$.

The hydrostatic voltage response is then

$$V_p = \frac{V_e k \delta_k p (1-2\nu)}{4E} \quad (3-113)$$

Also from Appendix B, the voltage response for a strain caused by deflection is $V = V_e k \epsilon / 2$.

The strain response under endloading is given by Eq (3-5a), so the endloading voltage response is then

$$V_\tau = \frac{V_e k \tau_w A_H L_s R}{2EI} \quad (3-114)$$

For a circular beam, $I = \pi R^4 / 4$, so if Poisson's ratio is taken as 1/3, then the ratio of the pressure response to the wall shear response is

$$\frac{V_p}{V_\tau} = \frac{p}{\tau_w} \left(\frac{\delta_k \pi R^2}{24 A_H L_s} \right) \quad (3-115)$$

The ratio of the pressure variation to the wall shear can typically be 50 - 100, but even for the maximum value of $\delta_k = 0.1$, for the gauge designs used for this research, the calculated

ratio of the pressure induced voltage to the wall shear induced voltage is less than 2 percent.

From Eq (3-115), it can be seen that to reduce pressure sensitivity, the beam radius should be decreased, while the sensor head area and L_s , the distance from the top of the sensor to the strain gauge midpoint, should be increased. All of these are things that would be done to increase the wall shear sensitivity of the gauge. Essentially, as can be seen from Eq (3-113), the normal pressure sensitivity is fixed except for δ_k which cannot be determined beforehand. To increase the ratio of wall shear sensitivity to pressure sensitivity, then, the wall shear sensitivity must be increased.

3.4.2. Pressure Gradient Sensitivity

If the pressure varies across the head of the sensor, then this pressure gradient can impart both a bending moment and a lateral force to the cantilever. The strain due to these forces is indistinguishable from that resulting from wall shear stress, so the pressure gradient could introduce error into the measurement. However, since the head is small, and since the boundary layer attenuates the pressure gradient, a large pressure difference should not exist across the sensor head except in the presence of a shock or rapid expansion.

The effect of a pressure-gradient bending moment is illustrated in Figure 3-19. The effect of this bending moment is to bend the sensor toward the high pressure side. The pressure gradient is also imparted to the oil. Larger pressure gradients will cause the oil to begin to flow out of the gauge, but in a shock tunnel run, the brevity of the test will result in little oil loss even for a standing shock across the gauge. Because the narrow annulus between the sensor head and the housing is the most constricted part of the flow passage, it is expected that the pressure gradient within the oil will occur primarily in the gap. Within the oil cavity, the flow is very slow, and viscous effects would be confined to a boundary layer, so the pressure within the cavity can be considered to be fairly constant. The lateral force imparted by the pressure gradient is hence concentrated primarily in the

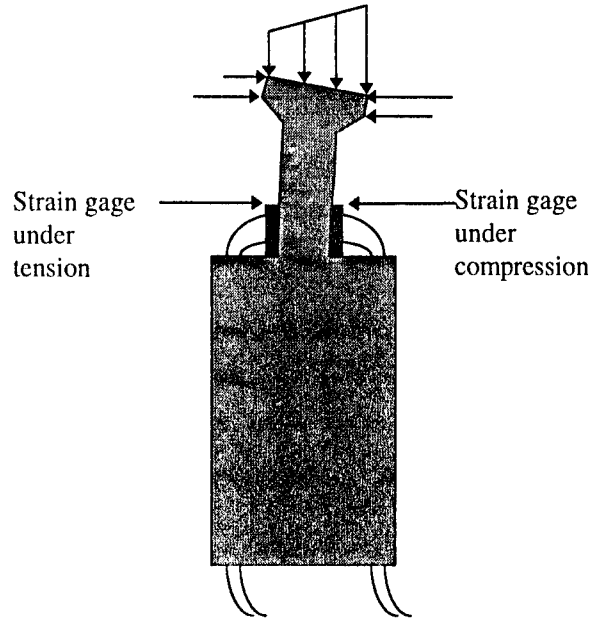


Figure 3-19 Bending Forces Caused by Pressure Gradient

head region of the sensor. This lateral force is toward the low pressure side and hence causes bending in the direction opposite to that caused by the bending moment.

3.4.2.1. Analysis

The bending moment imparted by a pressure gradient will first be calculated. The pressure gradient will be considered to be constant across the gauge. Because of the small size of the sensor head, a constant pressure gradient is representative of a shock-boundary layer interaction, which results in dispersion of the pressure gradient, as well as any other flow-induced pressure gradient.

The width of the head at any longitudinal position is given by $W = \sqrt{R_H^2 - x^2}$.

The differential force is then given by

$$dF = pWdx = p\sqrt{R_H^2 - x^2} dx \quad (3-116)$$

The bending moment is then calculated by integrating the pressure over the sensor head:

$$M = \int_{-R_H}^{R_H} x dF = \int_{-R_H}^{R_H} xp\sqrt{R_H^2 - x^2} dx \quad (3-117)$$

The pressure can be represented by

$$p = p_c + \left(\frac{dp}{dx}\right)x \quad (3-118)$$

where P_c is the pressure at the centerpoint of the sensor head. The moment integral becomes

$$M = p_c \int_{-R_H}^{R_H} x \sqrt{R_H^2 - x^2} dx + \frac{dp}{dx} \int_{-R_H}^{R_H} x^2 \sqrt{R_H^2 - x^2} dx \quad (3-119)$$

The first integral is zero, so evaluation of the second integral (Weast, 1973:A-128) provides the moment expression

$$M = \frac{\pi R_H^4}{8} \frac{dp}{dx} \quad (3-120)$$

The average lateral pressure gradient within the gap is used to calculate the lateral force. The oil pressure gradient is calculated as follows (Figure 3-20):

$$\left.\frac{dp}{dx}\right|_{oil} = \frac{\frac{1}{2}(p_2 + p_1) - \frac{1}{2}(p_2 + p_1)}{R_H} = \frac{\frac{1}{2}(p_2 - p_1)}{R_H} = \left.\frac{1}{2} \frac{dp}{dx}\right|_{air} \quad (3-121)$$

The lateral force created by the pressure gradient in the oil can be calculated from the differential force (Figure 3-21)

$$dF_x = -T_h p R_H \cos \theta d\theta \quad (3-122)$$

The pressure can be represented $p = p_i + \frac{1}{2} \left(\frac{dp}{dx}\right)x$. Letting $x = R_H \cos \theta$, the net lateral force is given by

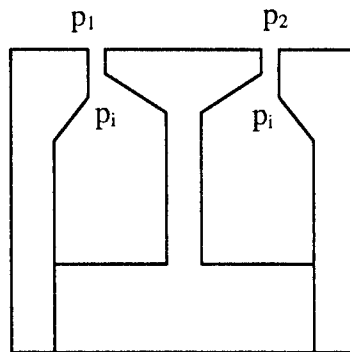


Figure 3-20 Pressures Inside and Outside the Gauge

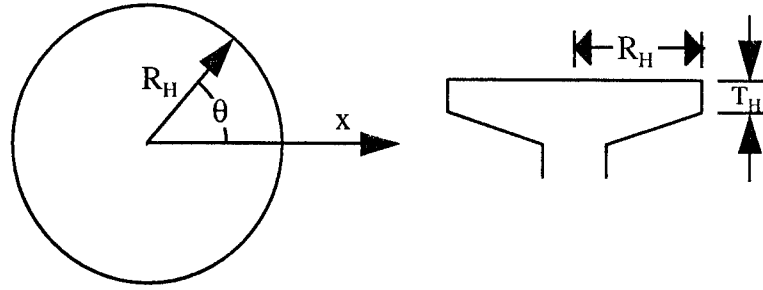


Figure 3-21 Sensor Head Geometry

$$F_x = \int_0^{2\pi} -T_H \left[p_i + \frac{1}{2} \left(\frac{dp}{dx} \right) R_H \cos \theta \right] R_H \cos \theta d\theta = -\frac{1}{2} \frac{dp}{dx} \pi R_H^2 T_H \quad (3-123)$$

Using the distance from the strain gauge mid-point to the sensor head midpoint, the moment is

$$M_x = -\frac{1}{2} \frac{dp}{dx} \pi R_H^2 T_H \left(L_s - \frac{1}{2} T_H \right) \quad (3-124)$$

and the total moment resulting from the pressure gradient is then given by the sum of the bending moment from Eq (3-120) and the lateral force moment from Eq (3-124):

$$M_{dp/dx} = \frac{1}{8} \pi R_H^4 \frac{dp}{dx} - \frac{1}{2} \frac{dp}{dx} \pi R_H^2 T_H \left(L_s - \frac{1}{2} T_H \right) = \frac{1}{8} g_p A_H R_H^4 \frac{dp}{dx} \quad (3-125)$$

where the pressure gradient sensitivity factor g_p is given by

$$g_p = 1 - 4 \frac{T_H}{R_H} \left(\frac{L_s - \frac{1}{2} T_H}{R_H} \right) \quad (3-126)$$

The value of g_p depends only on the gauge geometry. As g_p goes to zero, the pressure gradient sensitivity also goes to zero. Equation (3-126) can be used to design a gauge to be insensitive to pressure gradient. For $g_p=0$,

$$R_H = 2 \sqrt{T_H \left(L_s - \frac{1}{2} T_H \right)} \quad (3-126a)$$

The resulting strain from the bending moment from Eq (3-125) is given by (Saada, 1974:355)

$$\epsilon_{dp/dx} = \frac{M_{dp/dx} x_2}{EI} \quad (3-127)$$

In a wind tunnel measurement, this strain would appear to be a response to the wall shear stress. Substituting Eq (3-127) into Eq (3-5a) to eliminate ϵ and rearranging results in

$$\tau_{w(\text{false})} = \frac{2M_{dp/dx}}{A_H L_s} = \frac{g_p R_h^2}{4L_s} \frac{dp}{dx} = G_p \frac{dp}{dx} \quad (3-128)$$

where the total pressure gradient sensitivity factor G_p is given by

$$G_p = \frac{g_p R_h^2}{4L_s} \quad (3-129)$$

The units for G_p are Pa/(Pa/m), equivalent to m. Values of G_p for different skin friction gauges are shown in Table 3-7. As can be seen, the baseline gauge is very close to having zero pressure gradient sensitivity. For the gauges with a positive value of G_p , the pressure gradient causes deflection toward the high pressure, while a negative value of G_p results in deflection toward the low pressure.

Table 3-7 Pressure Gradient Sensitivity Factor for Different Gauges

Gauge	$G_p \times 10^5$ (m)
Baseline	0.2340
I-beam	9.5666
Mach 6	-93.9323
2 kHz Directional	-7.6652

3.4.2.2. Experimental Results

Experimental data for the effect of severe pressure gradients were obtained in both the GASL Hypulse tests and in the AFIT shock tunnel. In the GASL runs, a transient shock traversed the test section during the steady run time. Pressure measurements at the same location as the skin friction gauges were available, allowing correlation of shock and skin friction gauge response. In the AFIT shock tunnel, data for both transient shocks

(during the tunnel start) and standing shocks (generated by a sharp fin) were obtained. The AFIT measurements were made with directional gauges, allowing analysis of both the magnitude and directional effects of the pressure gradient.

As predicted by Eq (3-126), the baseline directional gauge showed little evidence of sensitivity to a standing shock in the AFIT shock tunnel runs. As discussed in Chapter 7, both the magnitude and direction of the wall shear stress measurements under the shock agreed well with previous measurements, flow visualization, and computational studies. The 2 kHz directional gauge was generally used in regions where the pressure gradient was less severe, but for three runs, the 2 kHz gauge was used under the shock. As described in Chapter 7, these measurements were adjusted for pressure gradient effects using Eq (3-128). As shown in Figure 3-22, the pressure gradient affected the measured flow direction by about 10 degrees, but the wall shear stress magnitude was not affected. This lack of effect on the magnitude is due to the pressure gradient being almost perpendicular to the flow direction. The pressure gradient effect is much smaller than the wall shear stress magnitude, so from vector relations, the effect of the correction is

$$\tau_{w(\text{uncorrected})} = \sqrt{\tau_w^2 + (\delta\tau_w)^2} = \tau_w \sqrt{1 + \delta^2} \approx \tau_w \left(1 + \frac{1}{2}\delta^2\right) \approx \tau_w \quad (3-130)$$

The theory developed for pressure gradient sensitivity does not apply to transient shocks because the boundary layer does not attenuate a transient shock as much as a

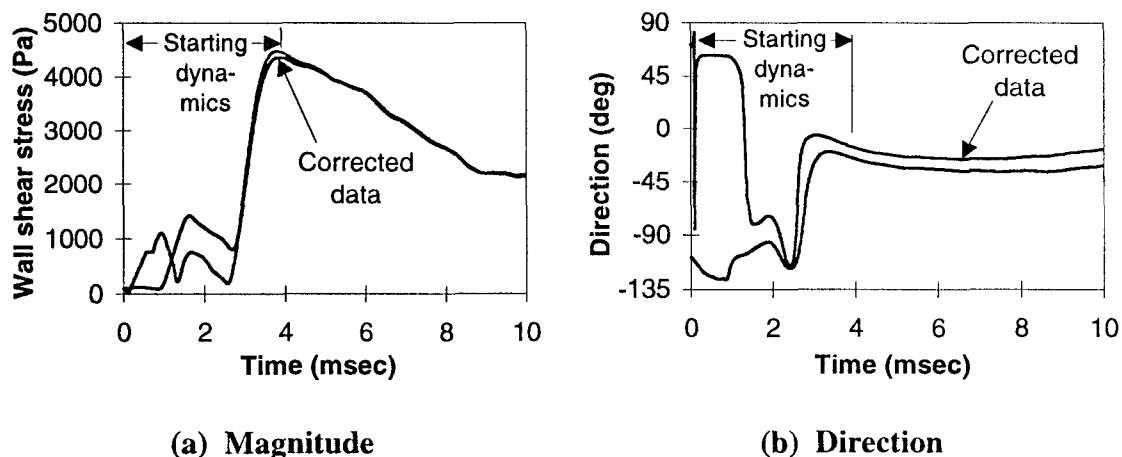


Figure 3-22 Corrected and Uncorrected Wall Shear Stress Measurements for 2 kHz Directional Gauge, AFIT Run 16

standing shock; the assumption of constant pressure gradient is therefore not valid. In addition, the theory reflected in Eq (3-128) is based on a static analysis, while a transient shock is a dynamic situation.

All gauges showed sensitivity to transient shocks. However, this may not be entirely a pressure gradient effect. As shown in Figure 3-23, the spike observed with a transient shock is always positive (away from the high pressure), while for both the baseline and I-beam gauges, a pressure gradient effect should cause bending toward the high pressure. There are several possible causes for effect of the transient shock to be a positive spike, rather than a negative one. First, the wall shear stress magnitude varies with dynamic pressure, which in turn varies with static pressure. Thus, the high pressure region immediately behind the shock would be expected to have a higher skin friction. In addition, the boundary layer behind a shock is caused by the induced velocity behind the shock, so the boundary layer immediately behind the shock is very thin and analogous to the boundary layer on the leading edge of a flat plate where the wall shear stress is maximum. In the AFIT shock tunnel, the starting shock is followed by a second shock, with lower pressure behind the second shock, so the skin friction would be expected to de-

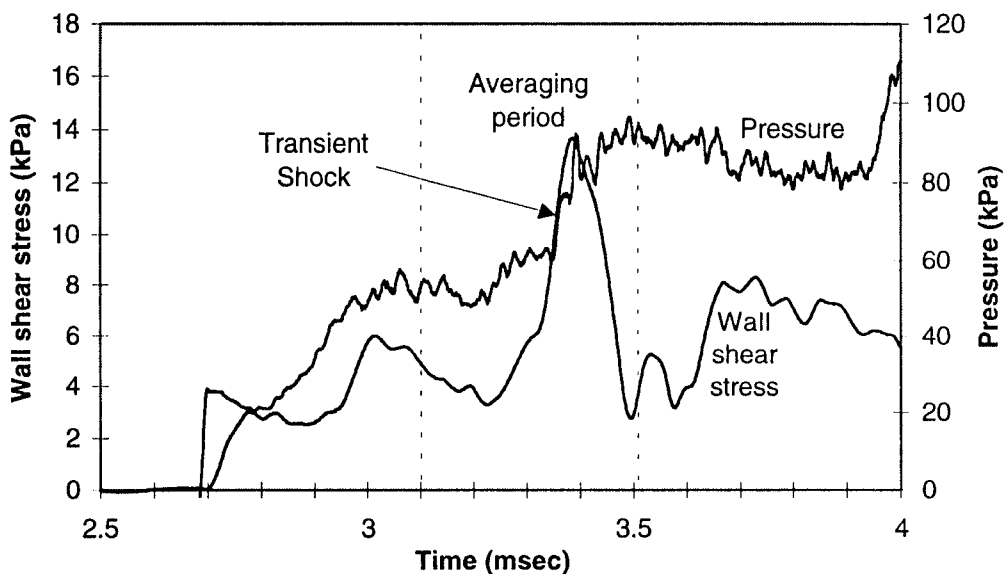


Figure 3-23 GASL Run 37 Showing Effect of Transient Pressure Gradient (I-beam gauge)

crease after the second shock, which in fact it does.

A second possible explanation for the transient shock effect is that the shock strikes the oil first. The high pressure on the leading edge of the oil is transmitted very quickly through the oil, since the oil is virtually incompressible and thus has a very high speed of sound. Thus, the lateral force from the high pressure in the oil would be felt by the sensor prior to the bending moment caused by the transient shock. This would cause a positive deflection (Figure 3-24).

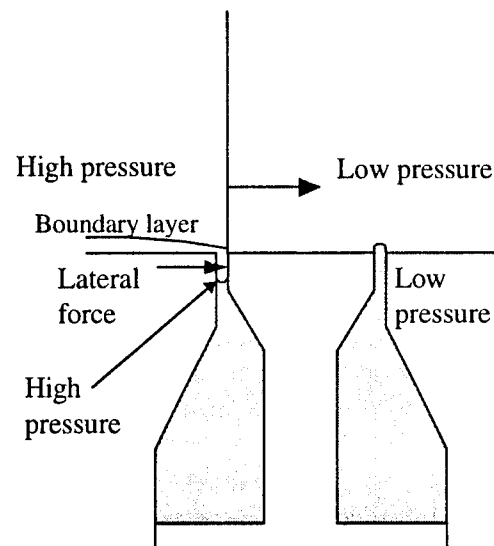


Figure 3-24 Transient Shock Effect

3.5. Gauge Performance Optimization and Alternative Geometries

Optimizing the gauge performance requires balancing the requirements for sensitivity and frequency response. Optimizing performance can also involve using a different beam geometry to improve the frequency response without sacrificing sensitivity. Two alternative geometries were evaluated in the course of this research. First, a sensor beam with an I-shaped cross-section, rather than a round cross-section, was introduced to increase the frequency response. Second, a hollow beam gauge with stainless steel head was constructed for thermal comparison purposes.

3.5.1. Gauge Performance Optimization

Design parameters that increase frequency response tend to decrease sensitivity. The goal of this part of the research was to identify ways to increase frequency response while maintaining satisfactory sensitivity.

To optimize the gauge performance, the ratio of the sensitivity to the inverse of the frequency is used. The inverse of the frequency represents the time response. Since it is desired to increase the sensitivity while decreasing the time response (equivalent to increasing the frequency response), maximizing this ratio provides the optimum gauge performance design. From Eqs (3-5) and (3-42), the ratio can be written

$$\frac{\epsilon_{SG}/\tau_w}{1/\omega_{Hz}} = \frac{1}{\pi} \frac{1}{\sqrt{\rho E}} \frac{A_H R}{L\sqrt{IA_b}} \frac{1 - \frac{1}{2} \frac{L_{sgt}}{L}}{\sqrt{\frac{33}{35} + 4 \frac{m_h}{m_b}}} \quad (3-131)$$

where the relation $m_b = \rho LA_b$ was used in the derivation.

In Equation (3-131) the second term consists of material properties, while the third and fourth terms reflect the design characteristics. In comparing materials, the optimum material for gauge performance will have the minimum value of the product ρE . From the third term, it can be seen that increasing A_H will increase gauge performance, while decreasing L , I , and A_b will increase gauge performance. Likewise, from the fourth term, decreasing the ratio of strain gauge length to beam length, and the ratio of the head mass to the beam mass, will increase gauge performance. It might appear that increasing R would increase the optimization ratio; however, R is also contained in the moment of inertia. It should be noted that m_h denotes the mass in the sensor head that excludes the beam mass; for a fixed head size, as m_b decreases, m_h increases.

For comparing different types of beams, it is useful to write the optimization ratio in terms of the total head mass:

$$\frac{\varepsilon_{SG}/\tau_w}{1/\omega_{Hz}} = \frac{1}{\pi\sqrt{E}} \frac{A_H R}{L\sqrt{I}} \frac{1 - \frac{1}{2} \frac{L_{sgt}}{L}}{\sqrt{m_b \left(\frac{33}{35} - 4 \frac{L_H}{L_b} \right) + 4m_{h(tot)}}} \quad (3-132)$$

From this form of the equation, it can be seen that if A_H , R , L , and I are held constant, then the sensitivity is unchanged. The frequency, however, can be increased by decreasing the head mass $m_{h(tot)}$. A second way to increase the frequency is to decrease the beam mass by using a different shaped cross-section, such as an I-beam or a hollow beam. This allows the moment of inertia, and hence the sensitivity, to be maintained at the same level.

For a round solid beam, the moment of inertia is given by $I=\pi R^4/4$ (Avalone and Baumeister, 1987:5-30), while the cross-sectional area is given by $A_b=\pi R^2$. Substituting into Eq (3-131), the following optimization ratio is obtained:

$$\frac{\varepsilon_{SG}/\tau_w}{1/\omega_{Hz}} = \frac{2}{\pi^2} \frac{1}{\sqrt{\rho E}} \frac{A_H}{LR^2} \frac{1 - \frac{1}{2} \frac{L_{sgt}}{L}}{\sqrt{\frac{33}{35} + 4 \frac{m_h}{m_b}}} \quad (3-133)$$

From this equation, it can be seen that the optimum round beam design minimizes R . Because R is squared, reducing R is more effective than reducing L .

The moment of inertia for a round hollow beam is $I=\pi(R_o^4-R_i^4)/4$ (Avalone and Baumeister, 1987:5-31), while the cross-sectional area is $A_b=\pi(R_o^2-R_i^2)$. The optimization ratio is then

$$\frac{\varepsilon_{SG}/\tau_w}{1/\omega_{Hz}} = \frac{2}{\pi} \frac{1}{\sqrt{\rho E}} \frac{A_H}{LR_o^2} \frac{1 - \frac{1}{2} \frac{L_{sgt}}{L}}{\sqrt{\frac{1}{4} \pi \left(1 - \frac{R_i^4}{R_o^4} \right) \left(1 - \frac{R_i^2}{R_o^2} \right) \sqrt{\frac{33}{35} + 4 \frac{m_h}{m_b}}}} \quad (3-134)$$

The conclusions to be drawn from Eq (3-134) are similar to those for the solid round beam. The optimum design would have the outer diameter minimized, while the inner diameter, relative to the outer diameter, should be maximized (that is, the walls of the hollow beam should be thin).

For an I-beam sensor (Figure 3-25), the moment of inertia is $I=(BH^3-bh^3)/12$ (Avallone and Baumeister, 1987:5-30), while the cross-sectional area is $A_b=BH-bh$. With $R=H/2$, the optimization ratio is then

$$\frac{\varepsilon_{SG}/\tau_w}{1/\omega_{Hz}} = \frac{1}{2\pi} \frac{1}{\sqrt{\rho E}} \frac{A_H}{LBH \sqrt{\left(1 - \frac{b}{B} \frac{h^3}{H^3}\right) \left(1 - \frac{b}{B} \frac{h}{H}\right)}} \frac{1 - \frac{1}{2} \frac{L_{sgt}}{L}}{\sqrt{\frac{33}{35} + 4 \frac{m_h}{m_b}}} \quad (3-135)$$

It can be concluded from Eq (3-135) that decreasing L , B , and H and increasing b and h relative to B and H (i.e., the flange and web should be thin) will increase the optimization ratio.

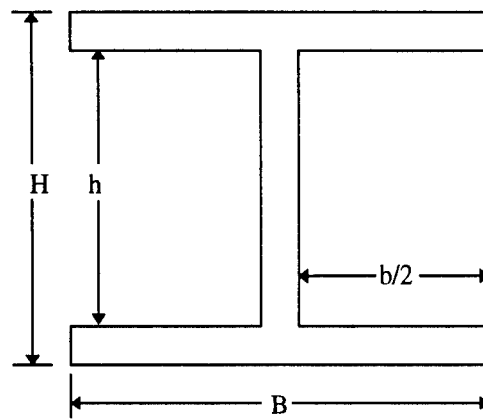


Figure 3-25 I-Beam Geometry

To optimize the gauge performance for a particular geometry, a desired frequency is first selected. A sensor length is then selected. A range of beam widths is evaluated with the head size being varied to provide the desired frequency. This process is then repeated with different beam lengths to provide a range of options of different lengths and widths, all providing the desired frequency. The gauge with the highest sensitivity is the optimum gauge for that frequency. Alternatively, one could start with a desired sensitivity and use the optimization process to determine the optimum frequency response.

This process was used to design both the I-beam gauge and the 2 kHz directional sensor. In both of these cases, the desired sensitivity was fixed and the parameters varied to obtain the highest frequency.

3.5.2. The I-Beam Cantilever Gauge

The I-beam cantilever gauge (Figure 3-26) was designed in an effort to increase gauge frequency response while maintaining sensitivity equivalent to the baseline gauge. Increased frequency response is particularly useful in facilities with very short run times such as the GASL Hypulse facility (test time ≈ 0.4 msec); in addition, the increased frequency response decreases the vibrations due to base motion, allows quicker recovery from passing shocks, and improves the capture of transient flow phenomena. The I-shaped cross-section reduced the beam mass, while a thinner sensor head was used in order to reduce the head mass without decreasing the surface area. These two design changes allowed the frequency response of the gauge to be increased without sacrificing sensitivity.

To optimize the gauge design process, a computer program was developed to allow the effect of different dimensions to be quickly assessed. Then, using the optimization procedure described in Section 3.5.1, a gauge was designed with a natural frequency of 30 kHz, three times that of the baseline gauge.

The I-beam gauge was constructed of Ultem plastic and consists of a 5.0 mm long

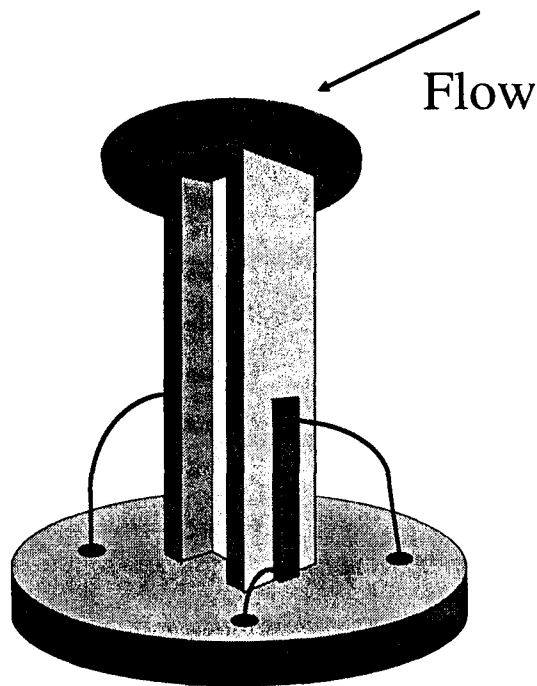


Figure 3-26 I-Beam Gauge

sensor stem with a 3.476 mm diameter head. In addition, the gap width between the sensor head and the housing was decreased to 0.0635 mm to improve oil retention.

Calibration of the I-beam gauge followed the procedure described in Chapter 2. Frequency analysis was conducted by mounting the gauge in a vise and initiating vibration by striking the vise with a mallet. The voltage response was captured using the Datalab DL1200 waveform recorder set at sampling rate of 100 kHz. The frequency response was analyzed by using the Fast Fourier Transform along with Hamming window contained in the Data Analysis and Display (DADiSP) software as described in Section 3.2. Results of the spectrum analysis showed the gauge to have a natural frequency of 32 kHz.

The sensitivity of this I-beam gauge is only slightly less than the baseline gauge: the I-beam gauge used in the GASL Hypulse facility had a calibration factor of 4930 Pa/V (with 0.5 volts excitation and gain of 1000) compared to 4759 Pa/V for the baseline gauge at the same settings.

The I-beam gauges were used in the NASA Ames shock tunnel tests, the GASL Hypulse expansion tube, and the AFIT high pressure shock tunnel. Only two runs were conducted with the I-beam gauge at NASA Ames. On the first run, a data acquisition failure occurred, and on the second run the results were inconclusive (Figure 3-27).

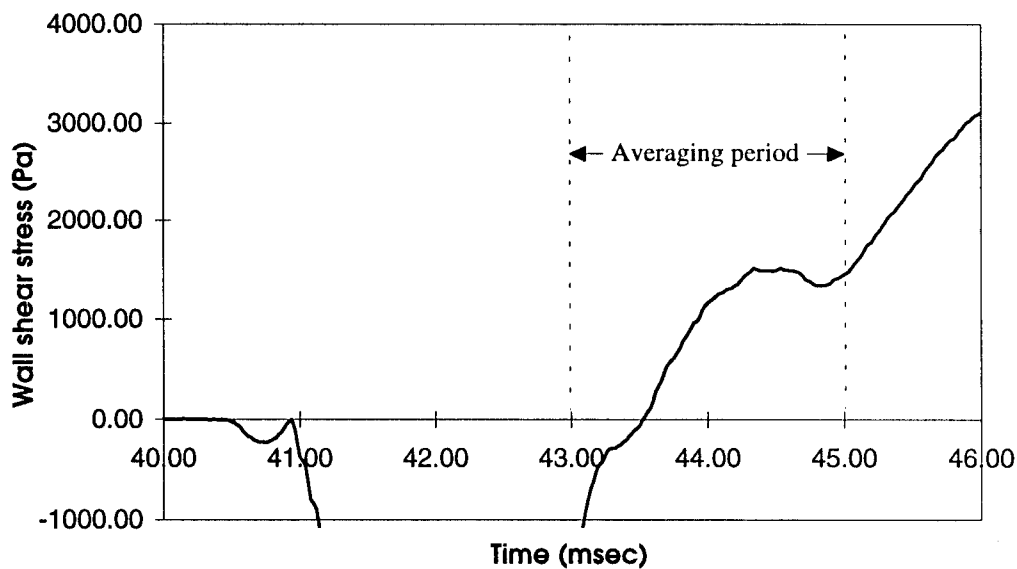


Figure 3-27 I-Beam Gauge Trace--NASA Ames Run 2086, Combustor Port #1

Based on similar occurrences elsewhere, it appears that the large dip in the trace is a result of a passing shock wave.

Better results were obtained from the GASL Hypulse tests. The Hypulse facility has a steady flow time of only 0.4 msec, so the quick response time of the I-beam gauge was ideal. The only drawback was that the gauges were operated in an inverted position, so it was difficult to retain oil in the gauge. However, the I-beam gauge appeared to give satisfactory results as previously shown in Figure 3-23.

An I-beam gauge was also tested in the AFIT shock tunnel with good results. Shown in Figure 3-28 are the traces from a run in which the I-beam gauge and the 2 kHz directional gauge were mounted in line in the duct. Agreement between the gauges was excellent. The spike at the beginning of the run is due to the passing shocks that are part of the starting dynamics of the nozzle. The directional gauge shows a similar but more restrained reaction to these passing shocks.

In many of the I-beam gauge traces, the sensor appears to react severely to transient pressure changes. However, this is simply a function of the high frequency of the gauge and not an indication of any particular sensitivity to pressure gradients. The I-beam gauge reacts more quickly to flow phenomena, such as transient shocks, but also recovers

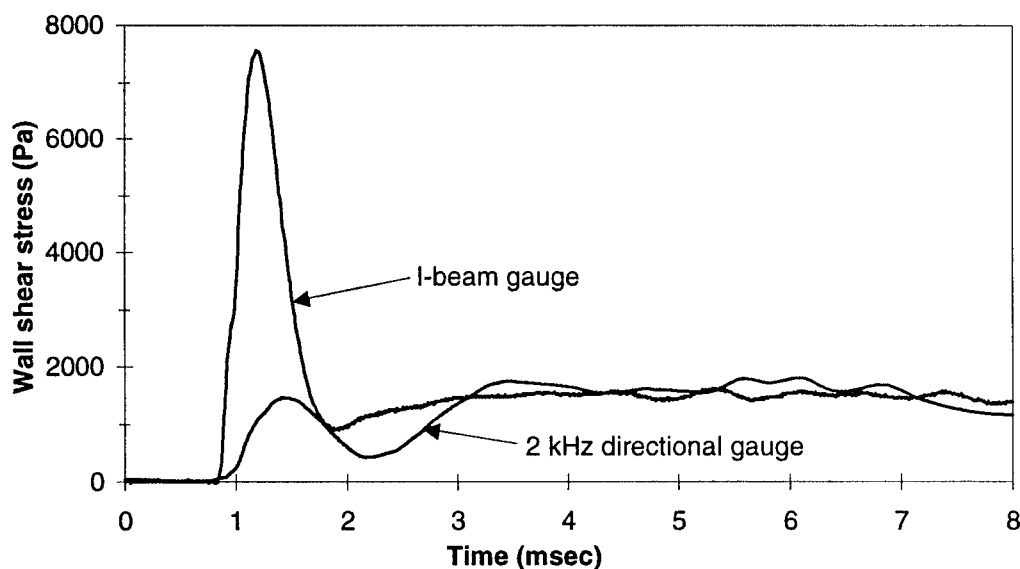


Figure 3-28 I-Beam Gauge Comparison in the AFIT Shock Tunnel, Run 32

more quickly.

3.5.3. Hollow Beam Gauge

A hollow beam provides similar effects to an I-beam in that the mass is reduced without significantly affecting stiffness. A low frequency hollow beam gauge made of Ultem plastic with a stainless steel head was constructed for the Wright Laboratory's Mach 6 test in order to thermally match the stainless steel model wall. The hollow beam was used in order to partially compensate for the additional mass of the head. The purpose of this gauge was to experimentally determine if the thermal mismatch between the plastic sensor and the stainless steel model wall affected the skin friction measurement. Due to time constraints and facility access problems, the hollow beam gauge was not used in the Mach 6 tests (all the measurements were taken by the plastic gauge), but the hollow beam gauge with the stainless steel head was later used for thermal comparison tests in the AFIT shock tunnel.

The added mass of the stainless steel head resulted in a natural frequency of 1 kHz, which was adequate for the test time of the AFIT shock tunnel when operated with pressurized driven section in order to increase test time. However, the vibrations associated with the diaphragm burst causes the skin friction sensors to vibrate, and the lower frequency and increased mass of the hollow beam gauge exacerbated this effect. Figure 3-29 shows the results of a test in which the hollow beam gauge with stainless steel head was mounted beside the 2 kHz directional gauge on an extension of the nozzle floor. Vibrational effects associated with both the diaphragm burst (which are transmitted through the metal of the shock tube and induce vibrations prior to the initiation of flow) and with the recoil of the nozzle start prevented the hollow beam gauge from tracking the flow until close to the end of the steady flow. The results of this test are discussed more fully in Chapter 4. It should be noted, however, that the low frequency hollow beam gauge was not designed for the AFIT shock tunnel, and the difficulties encountered with its use in the shock tunnel do not imply that the gauge is unsuitable for blow down tunnels.

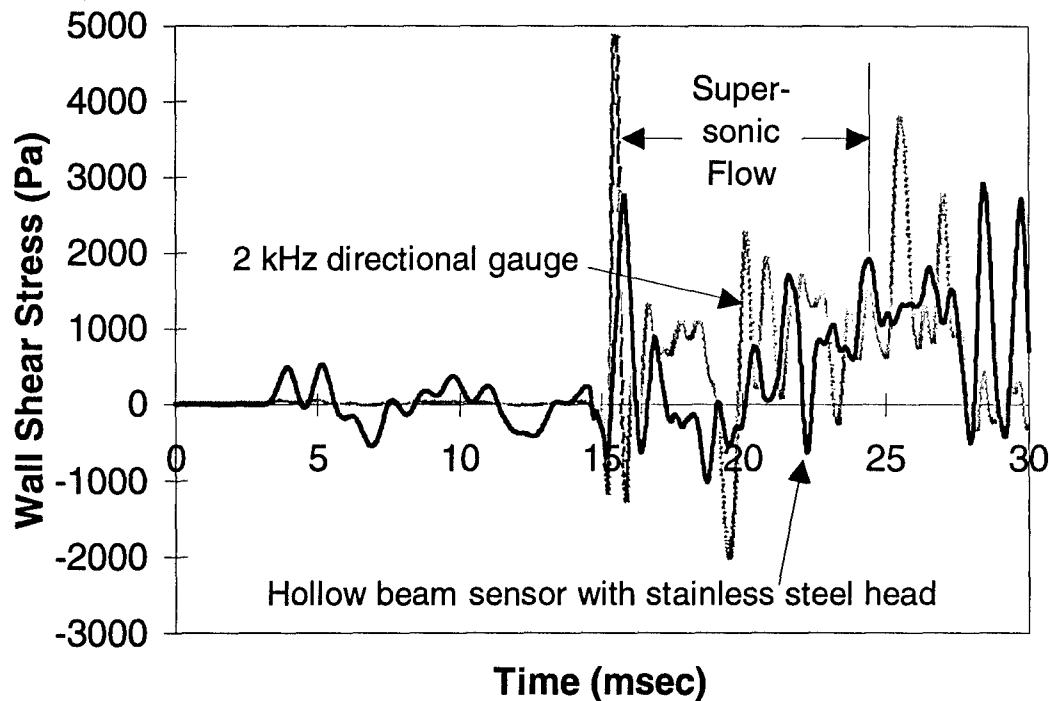


Figure 3-29 Response of Hollow-Beam Sensor with Stainless Steel Head Compared to Plastic Solid Beam Gauge, AFIT Run 9

3.6. Directional Gauge

Previous versions of the plastic cantilever skin friction gauge, both those constructed by Virginia Tech and at AFIT, were instrumented to detect deflection in only one direction. This required the flow direction to be known and the gauge aligned with the flow in order to obtain an accurate response. The directional gauge, developed as part of this research, uses a sensor instrumented with two sets of strain gauges in order to determine, not only wall shear stress magnitude, but also the shear direction. With such a gauge, the flow direction does not have to be known beforehand.

The directional gauge functions by providing two voltage responses, one corresponding to the deflection in the lateral direction and the other corresponding to a cross-flow deflection. Provided that the strain response at the four strain gauge locations at the base of the sensor is a linear function of the vector components of the load, the direction

of the flow can be resolved using vector relations. The magnitude of the skin friction is then given by

$$\tau_w = \sqrt{\tau_L^2 + \tau_c^2} \quad (3-136)$$

where τ_L represents the lateral component of the wall shear force and τ_c the cross flow component. The angle of the flow deflection (see Figure 3-30) is given by

$$\theta = \text{Tan}^{-1}\left(\frac{\tau_c}{\tau_L}\right) \quad (3-137)$$

In practice, however, due to strain gauge misalignment, the axes of the strain gauge are not precisely orthogonal, so the calculation of direction and magnitude is more complicated, as will be discussed in Section 3.6.1.2.

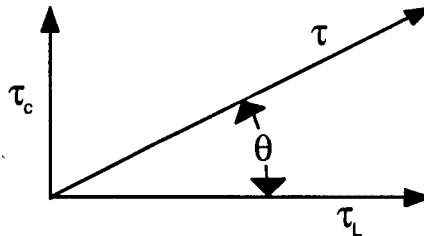


Figure 3-30 Angle of flow deflection

3.6.1. Theory

The wall shear stress is a vector quantity. For an orthogonal coordinate system, the vector can be broken into its components according to the following relations:

$$\tau_{w1} = \tau_w \cos \theta \quad \tau_{w2} = \tau_w \sin \theta \quad (3-138)$$

In this section, it will first be shown that a skin friction gauge instrumented with two pairs of strain gauges aligned along orthogonal axes can measure the components of the wall shear stress vector. Then, the case of misaligned strain gauges will be considered.

3.6.1.1. Ideal relations

The directional skin friction gauge uses two pairs of strain gauges. For the ideal case, the two axes of maximum sensitivity are orthogonal. For sake of convenience, these

axes will be referred to as the longitudinal and transverse axes. Using Eq (3-3), the strain response to endloading can be represented by

$$\epsilon = -\frac{PL_s x_2}{EI} \quad (3-3a)$$

For the loading aligned with the longitudinal axis, the location of the strain gauge in tension is given by $x_2 = -R$ and

$$\epsilon_L = \frac{PL_s R}{EI} \quad (3-4b)$$

The voltage response is given by (Appendix B)

$$V = \frac{F_G V_e k \epsilon D}{2} \quad (3-101a)$$

where the voltage response has been multiplied by a gain factor F_G . Substituting Eq (3-4b) into Eq (3-101a), letting $P = \tau_w A_H$, and rearranging results in

$$\tau_{w(L)} = A_L V_L \quad (2-11a)$$

where

$$A_L = \frac{2EI}{F_G V_e k_T A_H L_{s(T)} R D_L} \quad (3-6a)$$

The calculations above can also be applied to the case where the load is aligned with the transverse axis resulting in $\tau_{w(T)} = A_T V_T$.

Now if the axes are rotated so that the load aligns with neither axis as shown in Figure 3-31, then the x_2 location of the lateral strain gauge in tension is $x_2 = -R \cos \theta$. Substituting this into Eq (3-3a), letting $P = \tau_w A_H$, and substituting the result into Eq (3-101a) yields

$$V_L = \frac{F_G V_e k_L \tau_w A_H L_{s(L)} R D_L \cos \theta}{2EI} \quad (3-139)$$

Using this result in Eq (2-11a), and applying the Eq (3-6a) results in

$$\tau_{w(L)} = \tau_w \cos \theta \quad (3-140)$$

Similarly, the x_2 location of the lateral strain gauge in tension is given by $x_2 = -R \cos \theta$. Car-

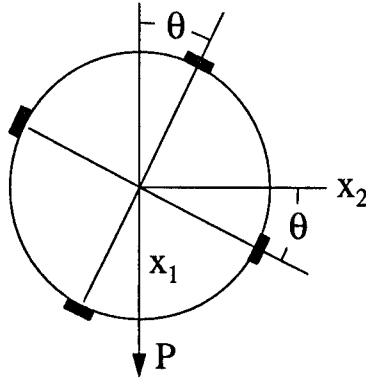


Figure 3-31 Rotated Directional Gauge

rying out the same analysis as for the longitudinal axis, it is found that $\tau_{w(1)} = \tau_w \sin\theta$. Thus, the vector relations described in Eq (3-138) are recovered.

3.6.1.2. Misalignment of Strain Gauges and Apparent Axis Effect

Misalignment of strain gauges can have two effects. First, if the strain gauges are not aligned precisely opposite each other, then an apparent axis is created. Second, if the axes are not precisely aligned, which may be due in part to the apparent axis effect, then the axes will no longer be orthogonal, and calculation of shear stress magnitude and direction must take into account the non-orthogonality of the axes.

If non-linear and second order effects are neglected, then the factor D appearing in Eq (3-101a) has the value (Appendix B)

$$D = \frac{2(2 + 2\delta_R + \delta_e + \delta_k)}{(2 + \delta_R)^2} \quad (3-141)$$

where misalignment of strain gauges causes the measured compression strain to be

$$\epsilon_c = -(1 + \delta_e)\epsilon \quad (3-142)$$

Neglecting higher order terms, Eq (3-378) can be expressed as

$$D = \left(1 + \frac{1}{2}\delta_e\right)D_2 \quad (3-143)$$

where $D_2 = 2(2 + 2\delta_R + \delta_k)/(2 + \delta_R)^2$. Substituting Eq (3-143) into Eq (3-101a),

$$V_L = \frac{1}{2} V_e k_L \epsilon_L \left(1 + \frac{1}{2} \delta_e \right) D_{2L} \quad (3-144)$$

For the case where the two strain gauges are not precisely on the same axis, when the tension strain gauge is rotated at an angle of θ relative to the load, the compression strain gauge will be placed at an angle of $\theta + \xi$ relative to the load. The angle ξ is small, but may be positive or negative. The strain in tension will then be

$$\epsilon = \frac{PL_s R \cos \theta}{EI} \quad (3-145)$$

while the strain in compression will be

$$\epsilon_c = -\frac{PL_s R \cos(\theta + \xi)}{EI} \quad (3-146)$$

Using the identity $\cos(\theta + \xi) = \cos \theta \cos \xi - \sin \theta \sin \xi$, and applying the small angle approximations $\cos \xi \approx 1$ and $\sin \xi \approx \xi$, Eq (3-146) becomes

$$\epsilon_c = -\frac{PL_s R (\cos \theta - \xi \sin \theta)}{EI} \quad (3-147)$$

From Eq (3-142), $\delta_e = -\epsilon_c / \epsilon - 1$. Then using Eqs (3-147) and (3-145), $\delta_e = -\xi \tan \theta$.

Substituting this and Eq (3-145) into Eq (3-144), results in

$$V_L = \frac{V_e k_L PL_{s(L)} R \left(\cos \theta - \frac{1}{2} \xi \sin \theta \right) D_{2L}}{2EI} \quad (3-148)$$

By taking the derivative with respect to θ , the angle at which the voltage is maximum can be obtained. This will allow the determination of the effective axis, which is at the angle of maximum sensitivity for the strain gauge pair. The derivative is given by

$$\frac{dV_L}{d\theta} = \frac{V_e k_L PL_{s(L)} R \left(-\sin \theta - \frac{1}{2} \xi \cos \theta \right) D_{2L}}{2EI} \quad (3-149)$$

The value of V_L will be maximum when the derivative is zero, which occurs when $-\sin \theta - (\xi/2) \cos \theta = 0$ or, $\tan \theta = -\xi/2$. This implies that θ is small when the voltage is maximum, so applying the small angle approximation $\tan \theta \approx \theta$, the following is obtained:

$$\theta = -\frac{1}{2}\xi \quad (3-150)$$

Thus the effective axis is at an angle which is half the misalignment angle (Figure 3-32).

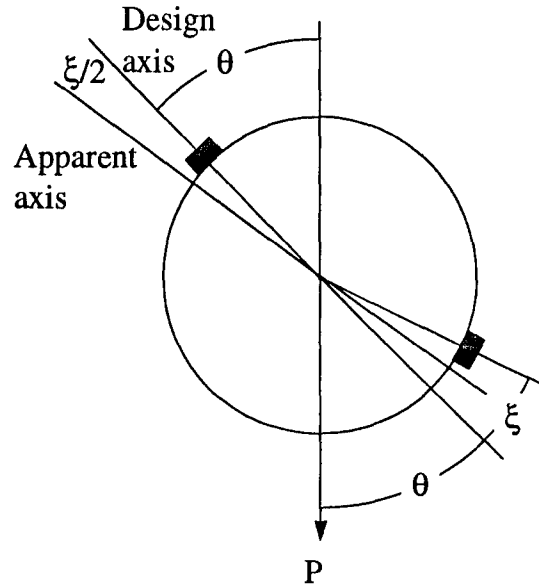


Figure 3-32 Apparent Axis Effect

Substituting the result from Eq (3-150) into Eq (3-148), and again applying small angle approximations, the angle of maximum voltage response is given by

$$V_{L(\max)} = \frac{V_e k_L P L_{s(L)} R \left(1 + \frac{1}{4}\xi^2\right) D_{2L}}{2EI} \quad (3-151)$$

Combining Eqs (3-151) and (3-148), the ratio $V_L/V_{L(\max)}$ is found as

$$\frac{V_L}{V_{L(\max)}} = \frac{\cos\theta - \frac{1}{2}\xi \sin\theta}{1 + \frac{1}{4}\xi^2} \quad (3-152)$$

Expanding the denominator about ξ using Taylor's series, neglecting higher order terms, applying from trigonometric identity, and using small angle approximations, Eq (3-152) becomes

$$V_L = V_{L(\max)} \cos\left(\theta + \frac{1}{2}\xi\right) \quad (3-153)$$

Now, if the angle of rotation is measured from the a position at an angle of $-\xi/2$ as given by Eq (3-392), then the measured angle of rotation is $\theta+\xi/2$. Thus, the vector relation is preserved if an apparent axis is used which is at an angle of $-\xi/2$ from the position of the tension strain gauge.

3.6.1.3. Non-Orthogonal Axes

Ideally, the two axes of maximum sensitivity of the gauge would be perpendicular to each other with one axis coinciding with the gauge alignment marking. In practice, it is difficult to achieve perfect alignment. To compensate for imperfect alignment, the axes of the gauge must be determined through a calibration procedure which will be described more fully in a later section. First, however, the method for calculating the wall shear stress magnitude and direction will be developed.

With axes of the gauge known, the geometry shown in Figure 3-33 will be used. The longitudinal apparent axis is at an angle of α to the design axis, while the transverse apparent axis is aligned at an angle of ζ to the longitudinal apparent axis. The angle ζ will be close to 90° . The wall shear stress measured along the two apparent axes will be denoted τ_1 and τ_2 . In wind tunnel use, τ_1 and τ_2 are known from the voltage response, and the wall shear direction and magnitude must be calculated.

The components of the wall shear stress measured along the two apparent axes can be related to the wall shear stress magnitude by

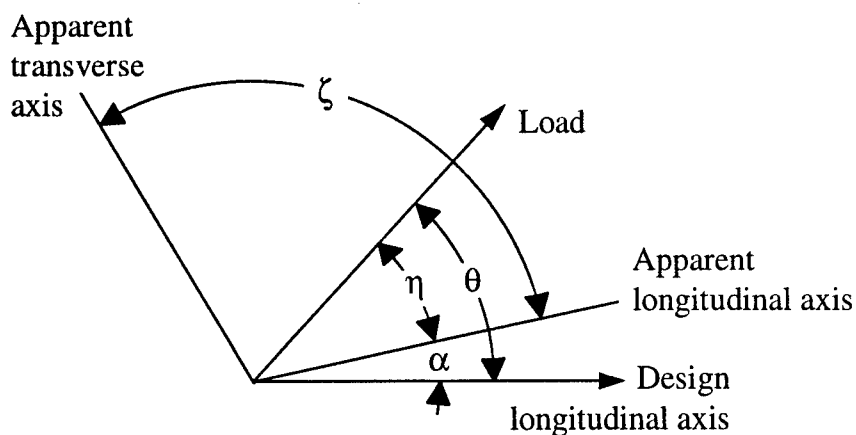


Figure 3-33 Directional Gauge Axes

$$\tau_1 = \tau_w \cos \eta \quad (3-154)$$

$$\tau_2 = \tau_w \cos(\zeta - \eta) = \tau_w \cos \zeta \cos \eta + \tau_w \sin \zeta \sin \eta \quad (3-155)$$

Substituting Eq (3-154) into (3-155) and rearranging results in

$$\eta = \text{Tan}^{-1} \left(\frac{\frac{\tau_2}{\tau_1} - \cos \zeta}{\sin \zeta} \right) \quad (3-156)$$

The wall shear stress magnitude can then be calculated from Eq (3-154).

Equation (3-156) can only be used to calculate an unambiguous flow direction of between -90 and +90 degrees; this is equivalent to τ_1 being positive. When τ_1 is negative, the relation is modified to

$$\eta = \pi - \text{Tan}^{-1} \left(\frac{\tau_2}{\tau_1} \right) \quad \tau_2 > 0 \quad (3-157)$$

$$\eta = -\pi - \text{Tan}^{-1} \left(\frac{\tau_2}{\tau_1} \right) \quad \tau_2 < 0$$

Equivalently, if the calculated η from Eq (3-156) results in a negative shear stress magnitude in Eq (3-154), then the phase of the angle should be changed by 180 degrees.

If the longitudinal apparent axis is misaligned from the design axis at an angle of α , then the angle of the flow relative to the gauge alignment marking is given by

$$\theta = \eta + \alpha \quad (3-158)$$

3.6.2. Calibration

The calibration method resembles the method used for the baseline, one-direction gauge. The gauge is mounted in a vise in a prone position and connected to an amplifier. Weights are then suspended from the sensor head, and the voltage is read with either a voltmeter or data acquisition system. However, for the directional gauge, the calibration must be carried out in several different orientations in order to determine the calibration constants.

There are four unknowns that must be determined in the calibration. These unknowns are the two calibration constants, A_1 and A_2 , and the direction of the axes, α and ζ . These four constants can be determined by taking calibration readings in three orientations. First, the gauge is calibrated along the two design axes; that is, aligned with the strain gauges where the maximum sensitivity is intended to be. The gauge is then turned at an angle of between 30 and 60 degrees with the angle measured as described below. The gauge is then calibrated at this angle with both directions measured. The geometry shown in Figure 3-34 will be used where the transverse apparent axis is misaligned from the design axis by an angle of β , and the angle between the two apparent axes is $\zeta = \pi + \theta - \alpha$.

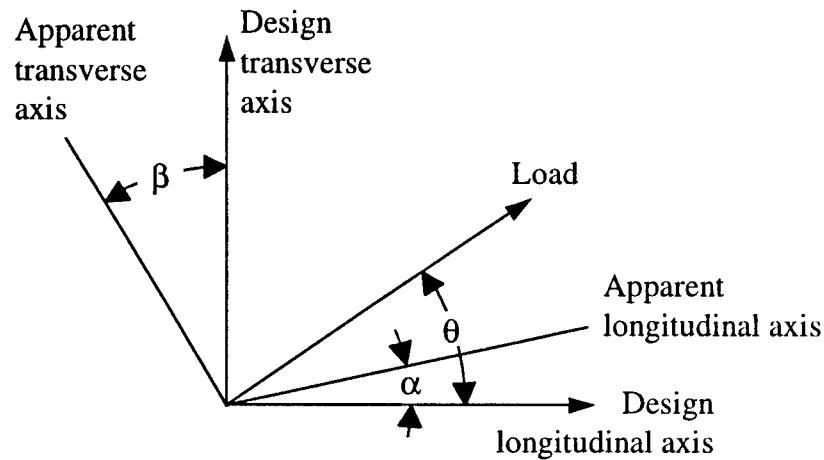


Figure 3-34 Misalignment of Axes

For the longitudinal axis, the voltage slope b_{1d} (V/kg) in the design position is related to the voltage slope b_1 along the apparent axis of maximum sensitivity by

$$b_{1d} = b_1 \cos \alpha \quad (3-159)$$

With θ denoting the angle of rotation from the longitudinal design axis, the measured voltage slope b_{1m} will be

$$b_{1m} = b_1 \cos(\theta - \alpha) \quad (3-160)$$

Substituting Eq (3-160) into (3-159) and expanding using the trigonometric identity $\cos(\theta - \alpha) = \cos\theta\cos\alpha + \sin\theta\sin\alpha$ results in $b_{1m} = b_{1d}(\cos\theta + \sin\theta\tan\alpha)$. This can be rearranged to

$$\alpha = \text{Tan}^{-1} \left(\frac{b_{1m}}{b_{1d} \sin \theta} - \cot \theta \right) \quad (3-161)$$

Since θ , b_{1m} , and b_{1d} have been measured, α can be calculated from Eq (3-161).

Similarly, for the transverse axis, the ideal relations are

$$b_{2d} = b_2 \cos \beta \quad (3-162)$$

and

$$b_{2m} = b_2 \cos \left[\frac{\theta}{2} - (\theta - \beta) \right] = b_2 \sin(\theta - \beta) \quad (3-163)$$

Substituting into Eq (3-163) into (3-162), using the identity $\sin(\theta - \beta) = \sin \theta \cos \beta - \cos \theta \sin \beta$, and rearranging results in

$$\beta = \text{Tan}^{-1} \left(\frac{b_{2m}}{b_{2d} \cos \theta} + \tan \theta \right) \quad (3-164)$$

The voltage slopes for the two axes of maximum sensitivity are calculated from Eqs (3-159) and (3-162). The calibration constants A_1 and A_2 are then calculated from b_1 and b_2 using Eq (2-11) from Chapter 2. The calibration angle ζ is given by

$$\zeta = \frac{\pi}{2} - \alpha + \beta \quad (3-165)$$

Precise positioning of the gauge is necessary for these calibrations. The design longitudinal axis is aligned with the set pin which holds the sensor in the housing. This allows the orientation of the longitudinal axis of the assembled gauge to be determined from the set pin. The orientation of the longitudinal axis is then marked on the surface of the gauge housing. For calibration of the longitudinal axis, a level is used to make sure that the longitudinal axis is exactly vertical. For calibration of the lateral axis, since the lateral axis is aligned to be perpendicular to the longitudinal axis, the level is used to make sure that the longitudinal axis is exactly horizontal. For calibration in angled positions, a protractor is used along with the level in order to measure the angle. The protractor is aligned with the longitudinal axis alignment marks, and the level is aligned with the center mark on the protractor (Figure 3-35). Each position was measured several times to ensure

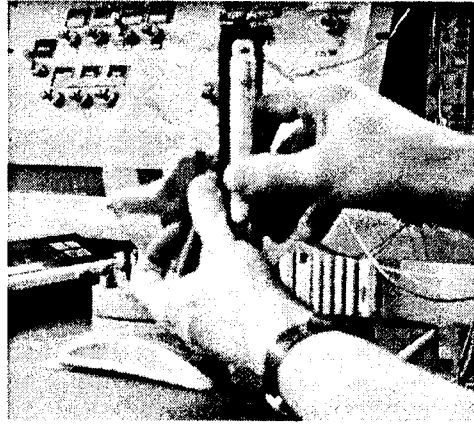


Figure 3-35 Measurement of Alignment Angle

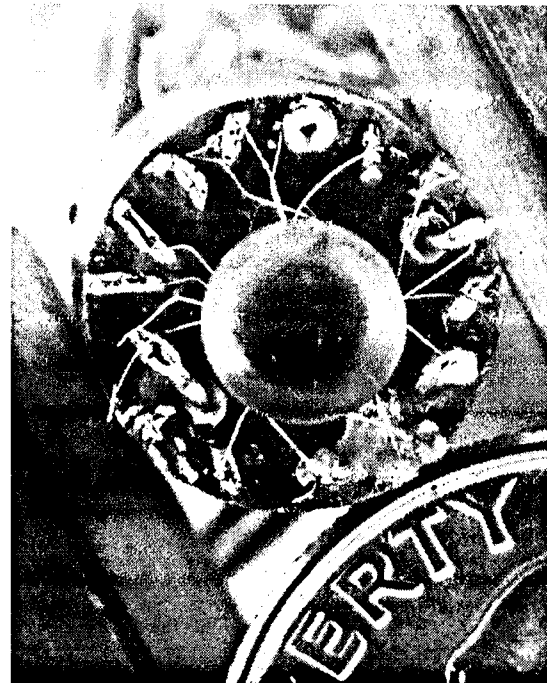
3.6.3. Gauge Evaluation

Three types of directional gauges were constructed. The first was a lower frequency 2 kHz gauge intended for the Wright Lab's Mach 6 test. This gauge was designed so that the cylindrical sensor was slightly flattened on the four surfaces where the strain gauges were to be mounted; alignment of the design axes was thus performed by the machinist. The second type directional gauge was a modified high frequency 10 kHz baseline gauge. The third directional gauge was also a modified 10 kHz baseline sensor but had two pairs of strain gauges (two lower pairs and two upper pairs) to compensate for pressure gradient(Figure (3-36)). The pressure compensation did not work as intended because the upper strain gauges, being closer to the surface, suffered thermal effects, but this third gauge was used successfully as an ordinary directional gauge.

The gauges were powered by Measurements Group 2310 signal conditioning amplifiers. Because each gauge has two sets of strain gauges, two amplifiers were required for each skin friction gauge. The skin friction gauges were calibrated using the Datalab DL1200 data acquisition systems used for high speed data collection in the shock tunnel runs. The amplifiers were set at excitation voltage of 0.5V and gain of 1000. Calibration constants are shown in Table 3-8.



(a) Side View



(b) Top View

**Figure 3-36 10 kHz Directional Gauge #2 with 4 Pairs of Strain Gauges
(dime for perspective)**

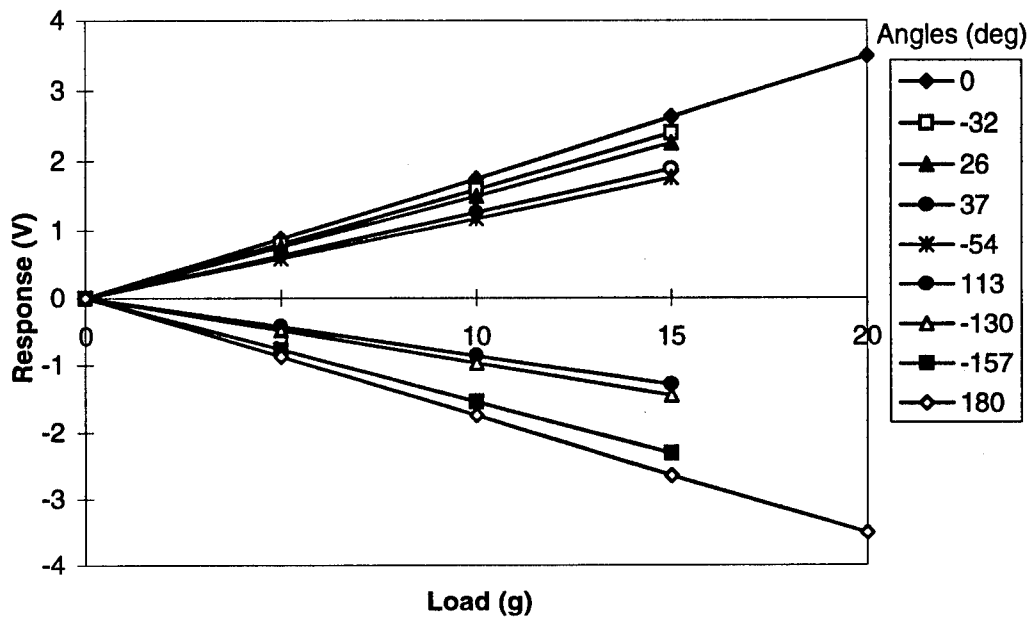
**Table 3-8 Calibration Constants for
Directional Gauges**

	2 kHz	10 kHz #1	10 kHz #2
α (deg)	6.06	-6.91	17.0
ζ (deg)	85.95	94.40	86.16
A_1 (Pa/V)	976.4	3345.0	2919.2
A_2 (Pa/V)	-1096.0*	3087.7	3487.0

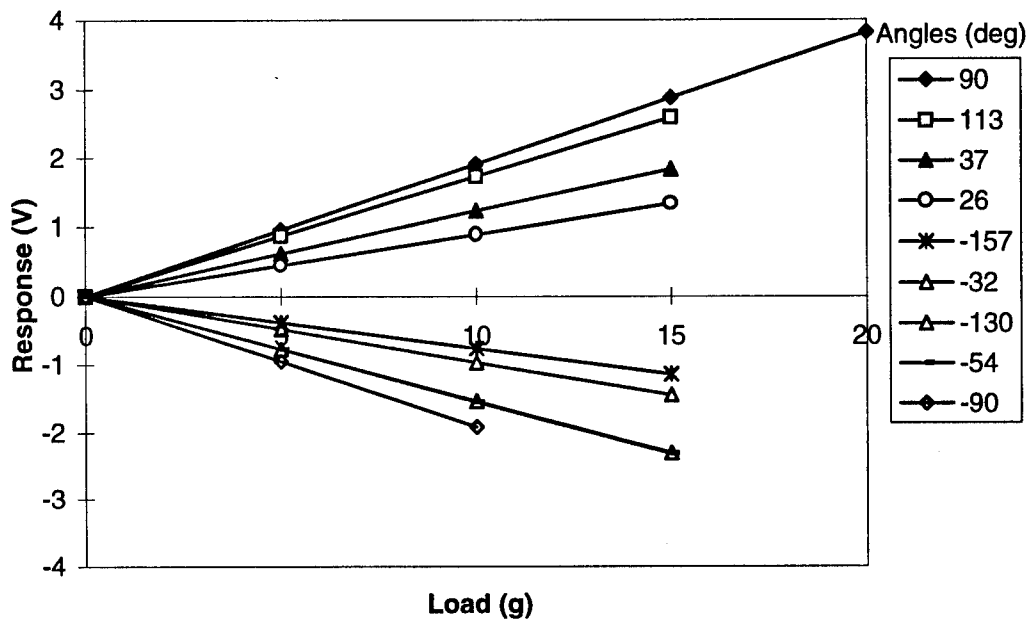
*Negative due to voltage response being in opposite direction to that in Figure 3-4

3.6.3.1. Static Calibration Tests

The directional gauge was tested during calibration by turning the gauge at different angles and verifying that the voltage responses corresponded to theory. The voltage slopes are shown for the various orientations in Figure 3-37. Then using the calculated



(a) Longitudinal Axis



(b) Transverse Axis

Figure 3-37 Calibration Data for 10 kHz Directional Gauge #1

calibration constants, the resolved angles versus the measured angles are summarized in Table 3-9. Also shown in Table 3-9 is the average error in load resolving for each orientation.

Table 3-9 Angle and Load Magnitude Accuracy of 10 kHz Directional Gauge #1 in Static Calibration

Aligned Angle (deg)	Angle measured by directional gauge	Load Magnitude Error (%)
-32	-32.69	0.33%
-54	-55.65	0.78%
26	24.93	0.46%
37	37.38	0.25%
-130	-129.74	1.08%
-157	-158.80	0.85%
113	112.65	0.37%
0	-1.91	0.45%
90	88.38	0.32%
180	-180.98	0.43%
-90	-91.80	0.80%
-9	-8.81	3.57%

One potential source of error discovered in the calibration tests was that when the gauge is turned so that one axis is nearly perpendicular to the load direction, directional error is introduced. This is due to the strain axis being at minimum sensitivity, and is due in part to the data acquisition system. While the amplifier gain could be turned up to compensate, a better approach is to simply avoid situations in the wind tunnel in which the flow direction is aligned with one of the axes (and hence perpendicular to the other axis). From calibration tests, it appears that the sensitivity loss is only of concern when the apparent axis is within 5 degrees of perpendicular. Since the apparent axis itself may be

misaligned by up to 5 degrees, a practical limit then is to place the gauge at a minimum of 10 degrees to the expected flow direction. It should be noted that this effect is limited only to directional sensing. No impact on magnitude sensing was observed, which is to be expected since a near-perpendicular component is small to begin with.

3.6.3.2. Wind Tunnel Gauge Evaluation Tests

The gauge was tested in the shock tunnel by placing the gauge at different angles in the flow. Details of the testing procedure are provided in Chapter 6, so only the results of the gauge evaluation tests will be summarized here.

Two test sections were used for the tests. The first was a simple flat plate attached to the nozzle exit (Figure 3-38). Because the flow is supersonic, the freestream conditions over the length of the plate should be the same as the nozzle exit plane. Two gauges were mounted side by side in the plate for comparison purposes. This arrangement was used primarily in initial tests of the low frequency gauge. The angle of the gauge was measured by first tracing the axis markings of the gauge and the flat plate onto tracing paper and

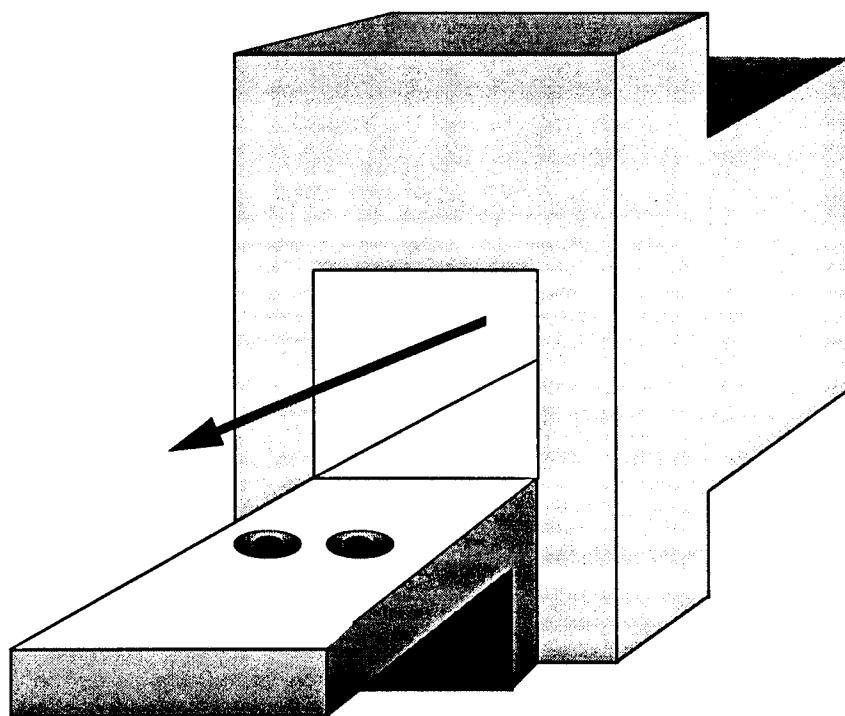


Figure 3-38 Nozzle Floor Extension

extending the markings far enough to allow measuring with a protractor. The resulting directional measurements from the gauge were fairly close to the measured angle. However, it appears that three-dimensional effects may have been present owing to the free-jet nature of the flow. At higher pressures so that the nozzle was underexpanded, these three dimensional effects were eliminated, but when the pressure dropped so that the nozzle was overexpanded, the oblique shocks at the nozzle exit caused the flow direction to change in the location of the gauges. In any event, the agreement was excellent.

The second test section was the duct that was also used to characterize the flow about the sharp fin. This duct was equipped with an instrument wheel mounted in the duct floor (Figure 3-39). The wheel was turned at various flow angles to check the gauge resolution. The alignment of the gauge in the wheel was first measured by turning the wheel so that the gauge was in the center of the duct, and conducting a run. This alignment was considered to have zero angle of crossflow, so the flow angle measured by the gauge was equivalent to the angle of the gauge. The wheel was then turned. The angle of

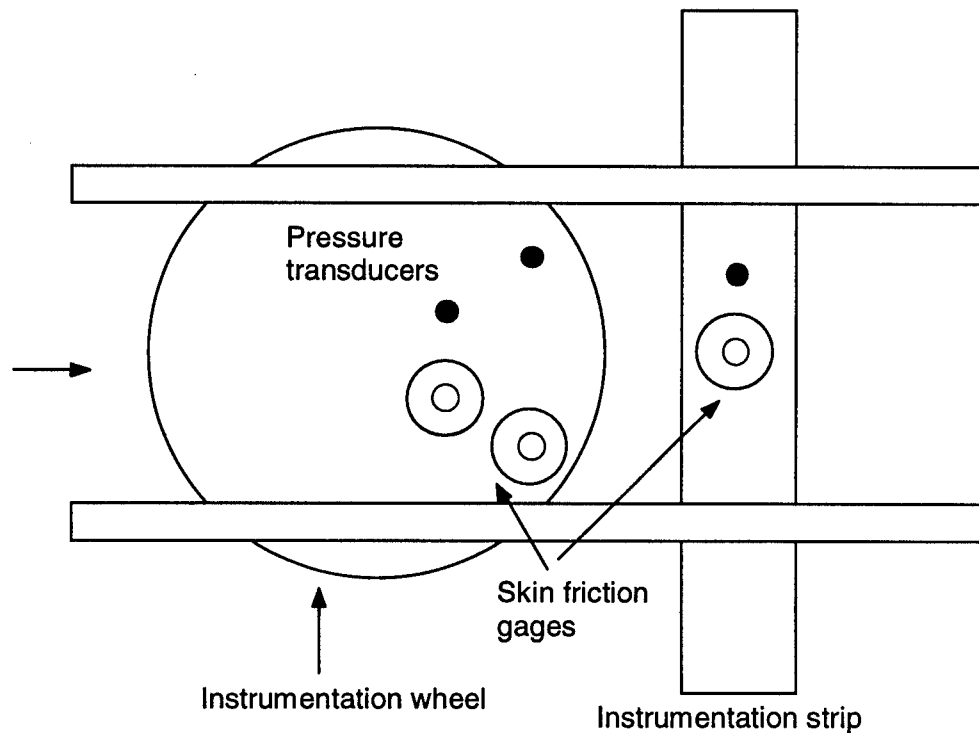


Figure 3-39 Duct Test Section (Top View)

rotation was determined by using micrometers to measure the displacement of locator markings on the wheel. In a run at the turned position, the change in angle measured by the gauge should be the same as the rotation of the wheel.

Summaries of measured versus resolved angles from both test sections are shown in Table 3-10. Wall shear stress direction and magnitude traces for the duct are shown in Figure 3-40.

Table 3-10 Wind Tunnel Directional Tests

Run	Measured Alignment Angle (degrees)	Angle resolved by Skin Friction Gauge (degrees)	Type of Gauge	Type of Test Section
11	40.0	41.3	2 kHz	Nozzle Floor Ext.
12	40.0	40.2	2 kHz	Nozzle Floor Ext.
13	-53.5	-51.4	2 kHz	Nozzle Floor Ext.
14	145.0	147.7	2 kHz	Nozzle Floor Ext.
19/21	80.5	80.7	10 kHz	Duct

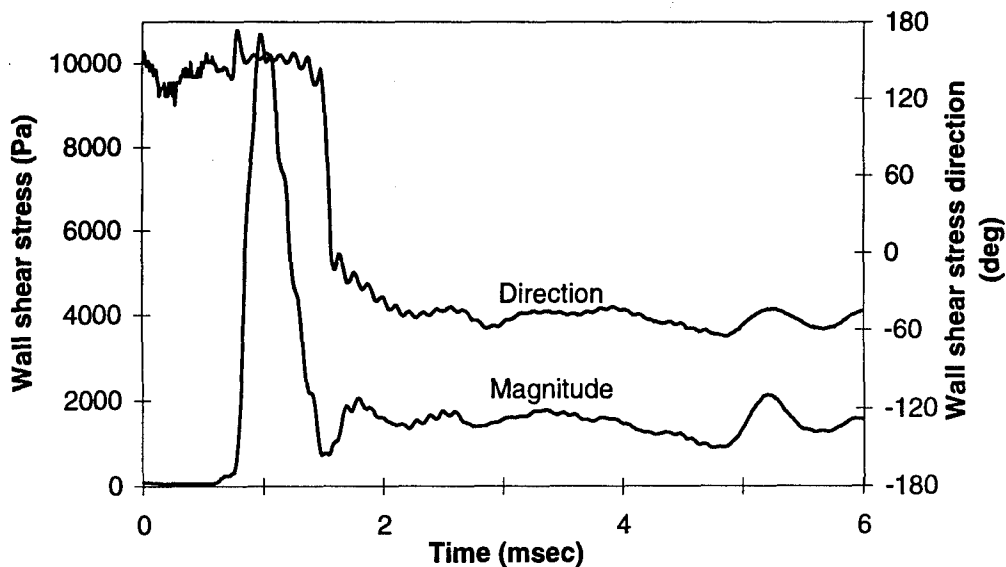


Figure 3-40 Wall Shear Stress Direction and Magnitude Traces, 10 kHz Gauge #1, AFIT Run 21

IV. Skin Friction Gauge Application Issues

Several gauge application issues were examined in the course of this research. These included thermal effects, surface durability, gauge servicing, electrical response, and calibration. All of these factors affected to some extent the gauge's usability, durability, or accuracy. Investigation of these factors was important for improvement of gauge operability, as well as for rigorous assessment of the gauge's accuracy.

4.1. Thermal Effects

Due to the high heat load to which the skin friction gauge is subjected, thermal effects are probably the leading cause for concern with regard to gauge accuracy. The thermal effects were analyzed, and the extent of the temperature rise was investigated by conducting a numerical heat transfer analysis. Several other thermal effects of concern with regard to the gauge accuracy were also investigated, specifically the effects of high rates of heating on the material properties of the sensor and the resistance of the strain gauges, either of which would affect the gauge accuracy.

4.1.1. Heat Transfer Analysis

To determine the temperature distribution in the skin friction gauge during a shock tunnel or wind tunnel run, a one-dimensional heat transfer analysis was developed. This analysis had several purposes: (1) quantify the temperature mismatch between the plastic skin friction sensor surface and the surrounding metal wall; (2) determine thermal effects near the base of the cantilever in order to determine the thermal effects on material properties and the strain gauges; and (3) determine the temperature distribution in the sensor head in order to analyze durability problems.

The heat conduction analysis consisted of analytical and numerical solutions to the one-dimensional heat conduction equation. For the numerical solution, the convection heat transfer from the fluid to the wall was used to determine the surface heat flux. While

a one-dimensional analysis is an approximation, for the plastic sensor for the run times considered, it was found that the temperature change did not penetrate below the lip of the gauge, so the heat conduction problem is, in fact, very nearly one-dimensional.

The analytical solution was developed for a simplified case in order to verify the accuracy of the numerical solution. The one-dimensional heat conduction equation is (Holman, 1981:4)

$$\frac{\partial T}{\partial t} = \alpha \frac{\partial^2 T}{\partial z^2} \quad (4-1)$$

For simple boundary conditions, specifically constant heat flux at the upper surface, this equation can be solved analytically.

The analytical solution was developed using separation of variables, for which a series solution results. The upper boundary condition, constant heat flux, approximates the conditions seen in the shock tunnel. A zero heat flux condition was specified for the boundary condition at the base. The initial condition is a specified uniform temperature throughout the material. The following solution was derived:

$$T(z, t) = T_0 + \frac{\dot{q}}{k} \left[-\frac{h}{6} + \frac{\alpha t}{h} + \frac{z^2}{2h} + \sum_{n=1}^{\infty} \left(-\frac{2h}{n^2 \pi^2} (-1)^n \right) \cos\left(\frac{n\pi z}{h}\right) e^{-\alpha \left(\frac{n\pi}{h}\right)^2 t} \right] \quad (4-2)$$

where h is the thickness of the wall. The derivation of this solution is presented in Appendix B.2.

In a steady flow situation, the surface heat flux decreases as the temperature increases. In order to determine more accurately the change in temperature of the gauge surface, the one-dimensional heat conduction equation was solved numerically. The initial condition was constant room temperature. The boundary condition for the top of the gauge was the heat flux calculated from convection theory for turbulent compressible flow. For the shock tunnel, the heat flux was calculated using Eckert's reference enthalpy method (Kays and Crawford, 1980:304-309). The reference enthalpy method was developed to allow the use of an incompressible correlation for heat transfer and skin friction which is then corrected for compressibility. The Eckert reference enthalpy method is

considered valid up to Mach 20 and was chosen for this application because it allows consideration of high temperature gas effects.

To analyze the thermal effects in the Wright Laboratory's Mach 6 inlet test, the Van Driest II skin friction correlation along with the Reynolds analogy was used to calculate the heat transfer. The Mach 6 wind tunnel is run at cold enough temperatures that the perfect gas assumptions contained in the Van Driest theory are valid. For the AFIT shock tunnel, the measured skin friction along with the Reynolds analogy was used. The bottom of the gauge is normally exposed to stagnant air or vacuum, so the bottom boundary conditions were considered to be zero heat flux.

The one-dimensional heat conduction equation was solved numerically using the Crank-Nicolson scheme as described in Appendix C.1. The solution scheme was verified by running a case that assumed constant heat flux and comparing to the exact solution. Appendix C.1 presents detailed grid convergence and accuracy analyses. The solution was then run for the case of interest, where the heat flux decreases as wall temperature increases. For each time level the heat flux was re-computed as the wall temperature increased. The flow conditions were assumed to consist of an impulsive start followed by steady flow.

For the NASA Ames shock tunnel, the steady flow free-stream conditions were taken to be those of the inlet for Run 2066. The analysis was carried for 6 msec, which was the approximate length of most of the NASA Ames test runs from flow initiation to the end of the averaging period. Temporal and spatial grid clustering was used, and the grids were successively refined until convergence was achieved. At the end of the averaging period, the temperature of the sensor surface was predicted to have reached 895K, compared to 324K for the metal wall surface (Figure 4-1). This analysis also included the oil temperature, since the oil temperature can affect both strain gauges and oil retention.

A thermal analysis was also run for the Wright Laboratory's Mach 6 tests with a 3.5 second run with the flow conditions from Run 57. For an initial temperature of 295K, the surface temperature of the plastic skin friction gauge at the end of the test was estimated to have risen to 471K, compared to 320K for the wall (Figure 4-2).

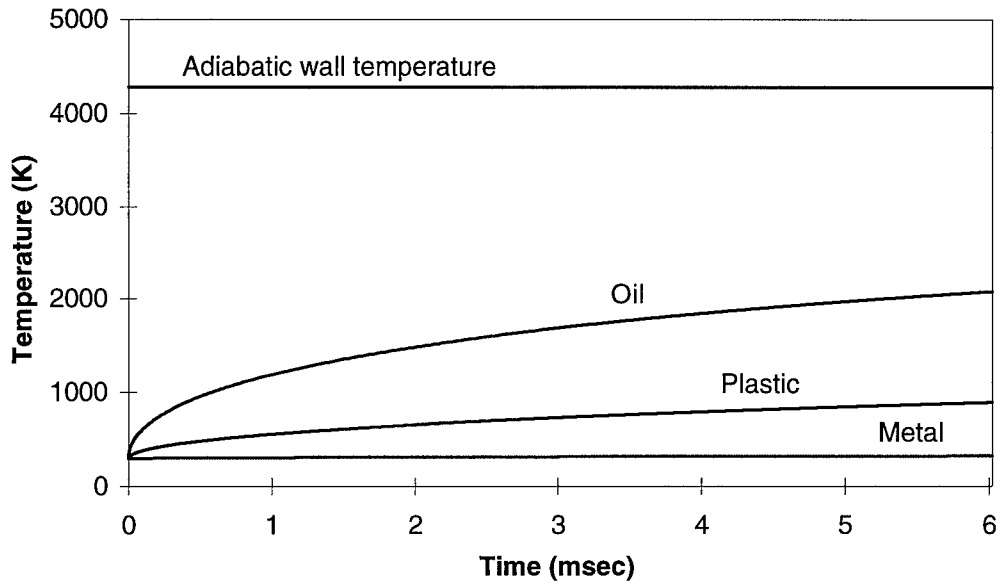


Figure 4-1 Calculated Surface Temperatures for NASA Ames Run 2066 Inlet Conditions

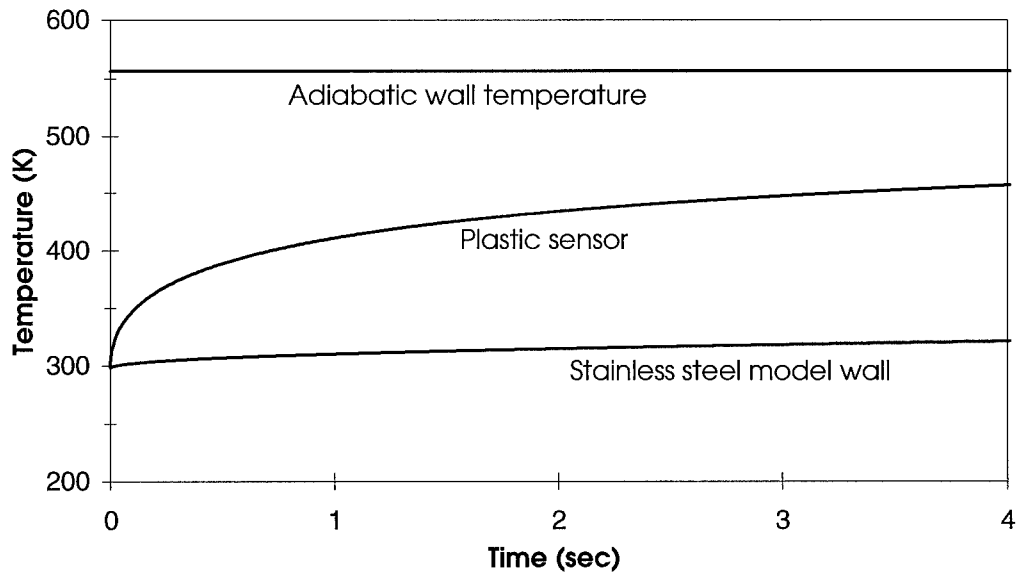


Figure 4-2 Calculated Surface Temperature for Wright Laboratory

4.1.2. Surface Thermal Characteristics

As previously discussed, the current skin friction gauge sensors are made of plastic in order to improve the frequency response and sensitivity, as well as to thermally isolate the strain gauges. However, most shock tunnels and test models are made of either stainless steel or aluminum. The metal absorbs heat faster than the plastic of the skin friction gauge. This gives rise to the question as to whether this difference in thermal characteristics distorts the boundary layer and hence the skin friction measured by the gauge.

4.1.2.1. Effect on Flowfield of Variation in Wall Temperature

In determining the effect on the flowfield of the different material characteristics, the key parameter that needs to be considered is the wall temperature. The wall temperature affects the properties of the air in the boundary layer and thus affects the wall shear. Therefore, if the surface temperature of the plastic gauge is the same as or close to the temperature of the adjacent wall surface, then little or no distortion of the boundary layer would be expected, and hence no distortion of the gauge accuracy. However, since the sensor temperature varies considerably from that of the wall, the next step is to determine the effect of this temperature mismatch.

The previous research on the effect of the presence of a hot spot in the flow is inconclusive. The hot film technique uses a hot spot in the flow with the assumption that the hot spot does not affect the measured skin friction. Pope (1972) in an experimental investigation of the hot film method, concluded that the temperature mismatch was responsible for some of the calibration problems that occur with this technique. Westkaemper (1963) found that the effect of temperature mismatch on the skin friction, when measured with a floating element gauge, was negligible. Voisinet (1978) concluded that the effect of a hot spot on the measured skin friction was significant. Paik (1993), using a combined skin friction/heat flux gauge, found significant differences in the measured skin friction when the gauge was heated. However, a companion computational study by Paik found no change in the skin friction when measured at a hot spot.

4.1.2.2. Analytical Quantification of Gauge/Wall Thermal Mismatch Effect

As an initial estimate, the potential error induced by the temperature difference was quantified by assuming that the presence of the higher temperature sensor could affect the surface skin friction measurement but would not result in a discontinuous change of the boundary layer momentum thickness. The momentum thickness at the point of the gauge was estimated by using the Spalding and Chi skin friction correlation, which can use Reynolds number based on momentum thickness (Re_θ) rather than longitudinal position (Re_x). This allows calculation of momentum thickness for given wall shear, wall temperature, and freestream conditions.

To evaluate the skin friction measurement error, a momentum thickness is first guessed. C_f is then calculated using the estimated sensor temperature. The guessed momentum thickness is then varied until the calculated C_f matches the measured C_f . The momentum thickness thus calculated is then taken as the actual momentum thickness, which is assumed to be equal to the momentum thickness at the location of the skin friction gauge if the gauge were not present. The correct skin friction is then computed using the calculated momentum thickness and the actual wall temperature. The method is described in Appendix B.3.

Using this method, a computer program was developed to estimate the skin friction gauge error due to the temperature mismatch between wall and sensor. For the NASA Ames run 2066, where the measured inlet wall shear stress was 1200 Pa, the momentum thickness was first calculated for the plastic sensor temperature of 895K. Using the calculated momentum thickness with a metal wall temperature of 324K, the Spalding and Chi correlation predicts a wall shear of 1161 Pa. Thus, the actual skin friction is predicted to be slightly less than the measured skin friction; the higher temperature of the sensor potentially overstates the wall shear by 3.4 percent.

Using the Spalding and Chi theory based on Re_x as described in Appendix B.3, the predicted skin friction for Run 2066 was 1174 Pa, which is slightly closer to the measured skin friction of 1200 Pa than the above analysis would suggest.

4.1.2.3. Experimental Analysis of Effect of Gauge/Wall Thermal Mismatch

Given the approximate nature of the above analysis, and the varying results obtained by different researchers into this issue, an experiment was conducted to determine the error, if any, introduced by using the plastic skin friction gauge with its higher surface temperature. The experiment was conducted in the AFIT shock tunnel. A plastic gauge was placed side-by-side or in-line with the hollow-beam gauge with stainless steel head, so that direct comparison could be made of the results. The shock tunnel test procedure is described in Chapter 7. The stainless steel sensor proved to be very sensitive to base vibrations, due to the extra mass of the head, and this, combined with the slow response of the gauge (1 kHz), proved incompatible with the normal shock tunnel operation. However, two runs, in which the shock tunnel was operated in such a way as to increase the run time, produced good data.

The first method used to increase the run time was to pressurize the driver section. This resulted in a weaker shock and longer run time. For Run 9, the driven section was pressurized to 524 kPa. Because of the weaker shock, the stagnation temperature was only 425K. The skin friction traces by the two gauges are shown in Figure 4-3. As can be seen from the trace, the stainless steel gauge does not begin to respond to the flow until midway through the supersonic flow period. Prior to flow initiation, the gauge vibrates due to the diaphragm rupture, which causes vibrations to travel through the metal. After flow initiation, the sensor reacts to the recoil from the nozzle starting dynamics. This run was conducted with a free jet with the gauges mounted in an extension to the nozzle floor, so the recoil effects caused by the initiation of the jet were considerable. The plastic gauge, however, with its less massive head, is not very sensitive to recoil but is sensitive to the traveling pressure gradients associated with the starting dynamics of the nozzle. After approximately 6 msec, the stainless steel sensor began to respond to the wall shear stress, and the responses of the two gauges overlap. From the point where the gauge responses begin to overlap until the nozzle unstarts, the stainless steel gauge measured an average wall shear of 865.02 Pa, while the plastic gauge measured 842.97 Pa. This appears to indicate close agreement. As can be seen from Figure 4-3, the plastic sensor had begun to

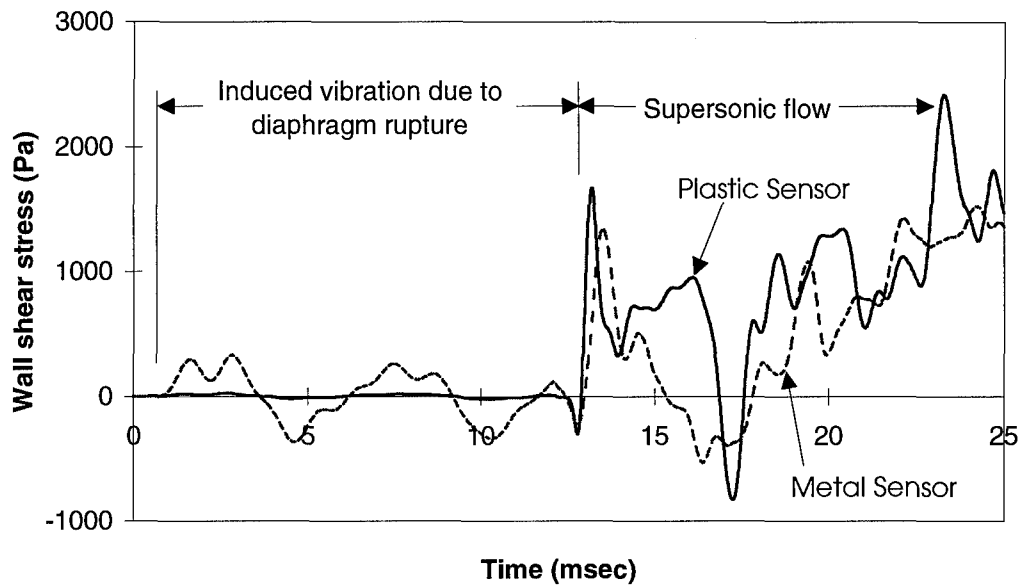


Figure 4-3 Measured Wall Shear Stress by Plastic and Stainless Steel Gauges, AFIT Shock Tunnel Run 9

oscillate during the last part of the supersonic flow, but the oscillation should be centered about the mean, so averaging should give a reasonably accurate estimate of the mean wall shear stress.

The calculated wall temperatures for Run 9 are shown in Figure 4-4. Since the model wall is made of aluminum, while the metal of the gauge is stainless steel, both temperatures were calculated as well as the plastic and oil temperatures. These temperatures were calculated by using one-dimensional numerical heat conduction program described in Appendix C.1. The freestream conditions were computed using the data reduction program described in Chapter 6 and Appendix D.2. The wall heat flux was computed by using the measured wall shear stress along with the Reynolds analogy. It can be seen that even with the lower operating temperature, there is still a large variation in temperature between the plastic and the metal. Using the method described in the previous section to quantify the error, the plastic sensor measurement of 843 Pa along with a surface temperature of 330K was used to predict a momentum thickness of 0.00697 mm. This calculation is based on flow conditions of freestream velocity of 728 m/s, dynamic pressure of 329 kPa, and static pressure of 45.9 kPa. Using the same conditions and momentum

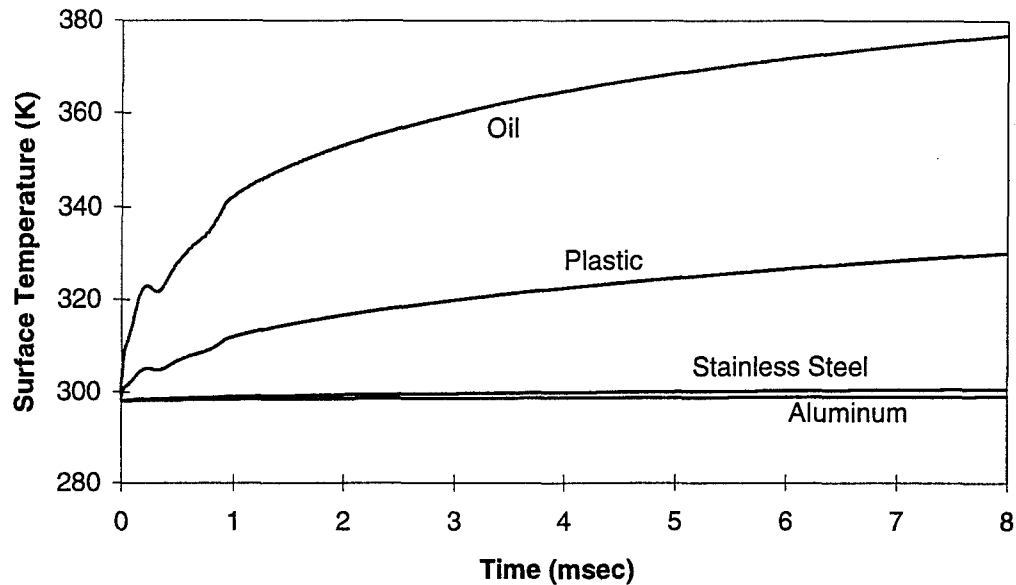


Figure 4-4 Calculated Wall Temperatures for AFIT Shock Tunnel Run 9

thickness, but with the stainless steel temperature of 301K, the predicted wall shear stress is 867 Pa. This agrees closely with the stainless steel gauge measurement of 865 Pa.

The second method by which a longer duration flow was obtained in the shock tunnel was by operating in the tailored condition as described in Chapter 6. In addition, the gauges were filled with a higher viscosity oil (1000 cSt). The run was conducted with the duct test section with dump tank, so recoil effects were lessened. Two directional gauges were used along with the stainless steel headed gauge. The agreement between the gauges was very close (Figure 4-5). The averaged measured skin friction coefficients were 0.0021 for the stainless steel headed gauge, 0.0022 for the 10 kHz directional gauge, and 0.0023 for the 2 kHz directional gauge. At the end of the steady run time, the calculated plastic sensor temperature was 430K versus 305K for the stainless steel. It therefore appears that the thermal effect of using a plastic gauge is minimal.

4.1.3. Strain Gauge Thermal Effects

The resistances of the strain gauges are very sensitive to changes in temperature (Neubert, 1967:83). Provided that the response of the skin friction gauge is linear and the gauge factor does not change with temperature, then as long as both gauges are at the same temperature, the changes of resistance due to temperature changes will electronically

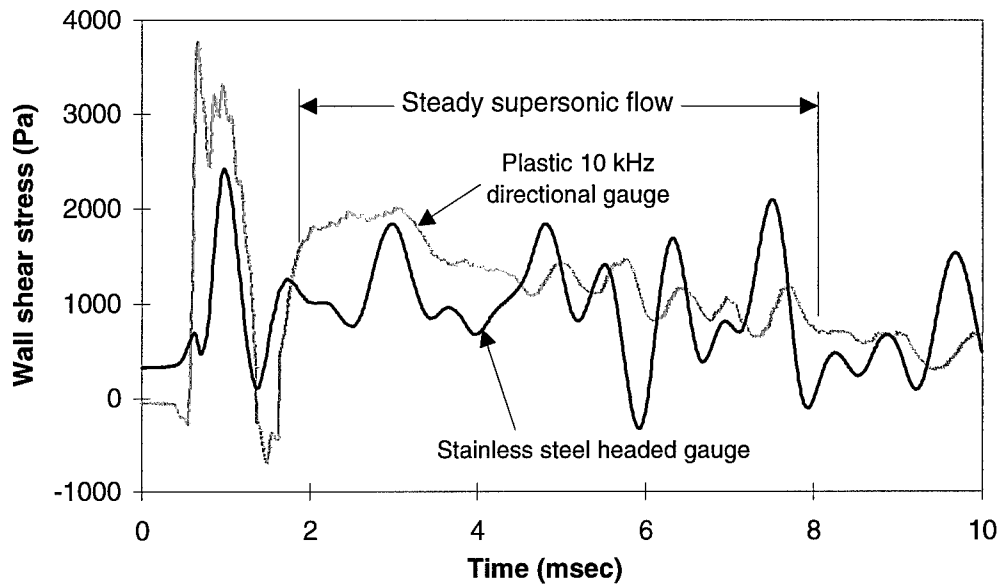


Figure 4-5 Measured Wall Shear Stress by Plastic and Stainless Steel Gauges, AFIT Run 33

cancel. In practice, this means that slow temperature changes, such as those that occur in a room or in the wind tunnel during evacuation, do not affect the gauge accuracy, provided the Wheatstone bridge is re-balanced prior to the test. However, a rapid temperature change during a wind tunnel or shock tunnel run can heat the gauges unevenly, causing resistance changes unrelated to the strain due to sensor deflection, and resulting in an inaccurate response. Such a thermal effect can be seen in the skin friction measurement shown in Figure 4-6, where the rise in the last 5 seconds of the test are believed to have been caused by uneven heating of the strain gauges.

Because thermal effects can destroy the gauge accuracy, the gauge is designed so that the strain gauges are thermally isolated for the duration of the test run. The plastic sensor tends to insulate the strain gauges, while the oil prevents the hot air from entering the gauge cavity. The gauge housing is usually made of plastic, and this further insulates the strain gauges from heat transfer from the model walls.

To investigate the thermal effects on the strain gauges, the numerical model described in Section 4.1.1 was used to determine the change in temperature, due to heat conduction in the plastic, that can be expected in the strain gauge region of the cantilever

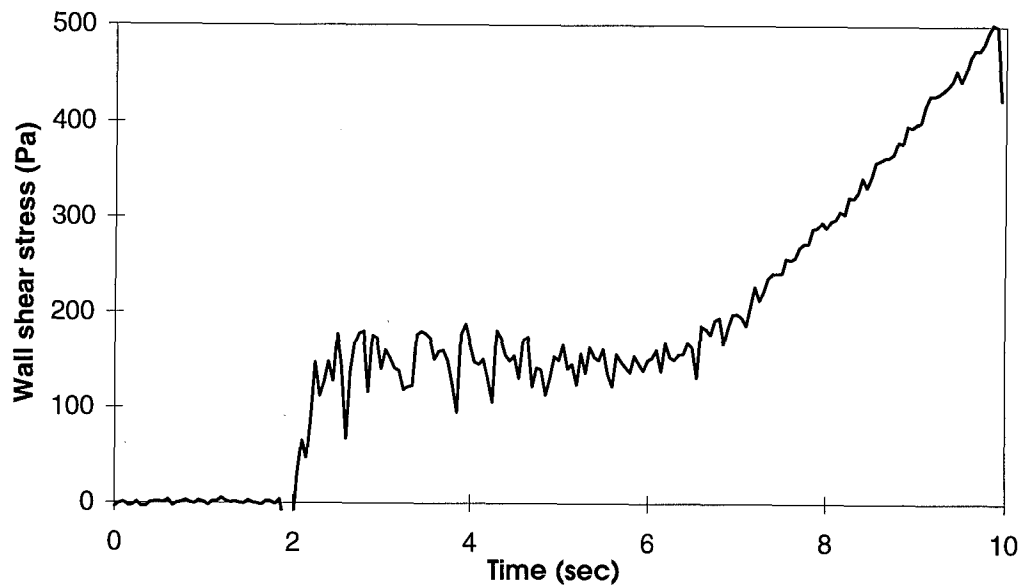


Figure 4-6 Oil Depletion and Resulting Strain Gauge Thermal Effect (Wright Laboratory's Mach 6 Run 19)

during a typical NASA Ames shock tunnel run. It was found that there were no changes in the temperature at the point where the strain gauges are located; as can be seen from the temperature distribution shown in Figure 4-7, the temperature changes were confined to the top 0.4 mm of the gauge. The strain gauges were located approximately 4 mm from the surface. Thus, it is not expected that error was introduced due to heat conduction in the sensor. This analysis was also run for the oil, assuming a full oil cavity, with identical results, that is, no change in temperature at the strain gauges.

When thermal effects have occurred, it is believed that the cause has been oil depletion, and the effect has always been to increase the apparent skin friction. When the sensor is deflected, the strain gauge at the leading edge is stretched, and the resistance increases, while the strain gauge on the trailing edge is compressed with decrease in resistance. An apparent increase in the skin friction due to thermal effects means that the leading edge strain gauge is being heated more than the trailing edge strain gauge. The likely cause is that the strain gauge on the leading edge is exposed to stagnation flow (which has the highest possible heat transfer), while the gauge on the trailing edge is in a wake.

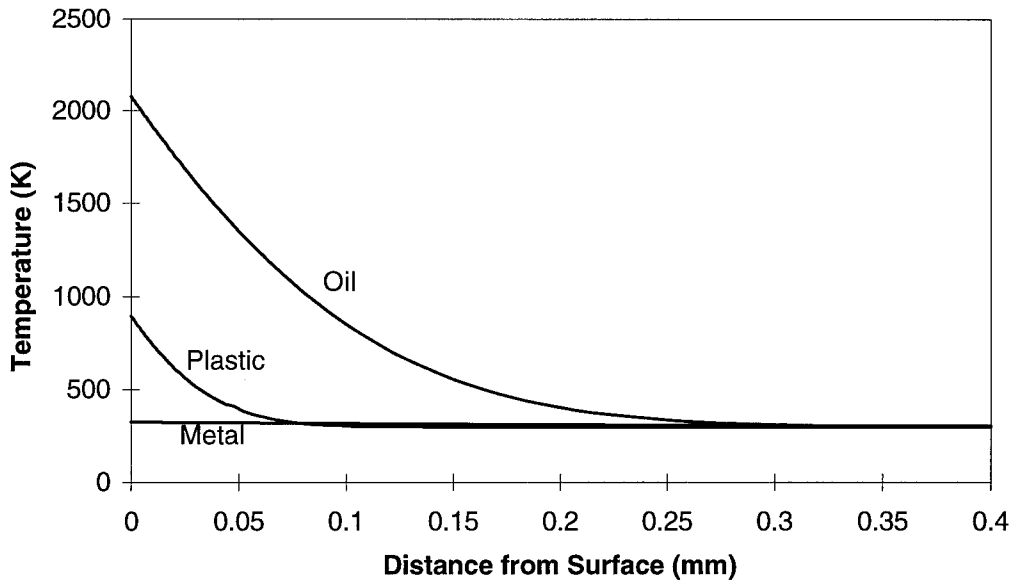


Figure 4-7 Calculated Temperature Distribution in Metal, Plastic, and Oil after 6 msec for NASA Ames Run 2066

It appears that whenever oil depletion occurs, the result has been fairly obvious. It seems unlikely that high temperature air circulating in the oil cavity would have only a moderate effect on the strain gauges (i.e., affect the strain gauges enough to cause error but not enough to be obviously a case of oil depletion). It has also been observed, particularly in the Mach 6 tests, that whenever the thermal effect shown in Figure 4-6 has occurred, re-oiling the gauge has prevented the occurrence in the next run. Conversely, not re-oiling the gauge has resulted in an obvious thermal effect for every run until the gauge was re-oiled. It can, therefore, be concluded that the only thermal effect on the strain gauges that has occurred was caused by oil depletion, and that the effects are easily identified.

4.1.4. Thermal Effects on Material Properties

During a wind tunnel run with high heat transfer, the temperature of the sensor will increase. The increase will largely be confined to the sensor head, but if the heat transfer also affects the sensor stem, then the material properties will change. The specific material property most of interest here is the modulus of elasticity. If the modulus of elasticity

were to decrease due to high temperature, then the gauge would indicate a higher skin friction than is actually present (the deflection of the beam would be greater than it would be at room temperature).

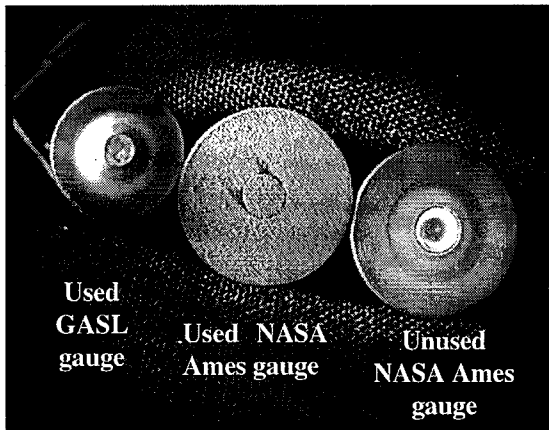
As long as temperature changes are small, the modulus of elasticity will not change. In addition, if large temperature changes are well away from the area where the strain gauges are mounted, then even if the modulus of elasticity does change in the top of the sensor, the forces and moments felt at the bottom of the sensor should be the same. Finally, if temperature changes at the bottom of the gauge are significant, then the thermal effect on the strain gauges would probably be more significant than the thermal effect on the Young's modulus of the plastic sensor.

It can be seen from the temperature distribution in Figure 4-7 that the heat penetration is confined to the sensor head, so no thermal effect on material properties should occur.

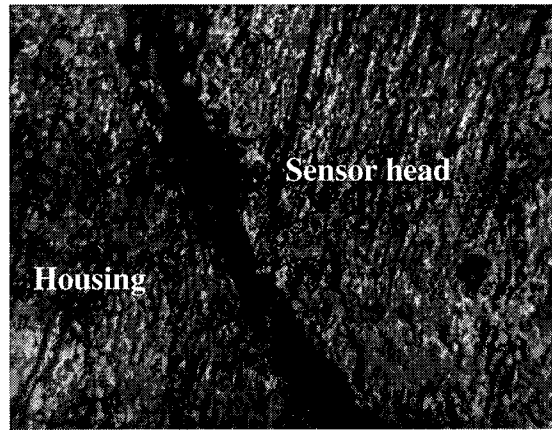
4.2. Surface Durability

The skin friction gauges used in the NASA Ames shock tunnel tests suffered considerable surface erosion after two or three runs (Figure 4-8). Two likely causes of this erosion are the high heat load to which the gauge is subjected and particles in the air flow. Coating the surface of the gauge with metal (through a deposition process called sputtering) improved the durability somewhat; however surface erosion still occurred. The gauges were sputtered by the AFIT Electrical Engineering Department's Cooperative Electronics Laboratory.

Because heat buildup in the top of the sensor could contribute to the surface erosion, the numerical study described in Section 4.1.1 was applied to determine the temperature within the gauge during the wind tunnel tests. For the NASA Ames shock tunnel tests, the gauge surface temperature at the end of the steady flow period was predicted to have reached a temperature of 895K. In the laboratory, during soldering of the strain gauge leads, the plastic has melted at a soldering iron temperature of 700K (this temperature could, in fact, be well beyond the melting point of the plastic). Thus, it appears that



(a) *Used and Unused Gauges*



(b) *Microscope View of Used NASA Ames Gauge*

Figure 4-8 Gauge Surface Erosion

the gauge surface temperature in the shock tunnel is high enough to melt the plastic. Whether the plastic sensor surface actually melts in the shock tunnel is unknown; melting requires a finite amount of energy and time to take place. However, unsteady flow continues for some time past the steady flow interval, with combustion products from the driver tube being exhausted into the test section, so the exposure time and temperature rise for durability considerations are somewhat greater than that predicted by the numerical study.

For the Wright Laboratory's Mach 6 test, the numerical analysis predicted a final temperature of 471K for a typical 5 second run. The exposure time of the gauge to the flow was 3-3.5 seconds. In this sequence of tests, a single skin friction gauge was used for a total of 110 runs, with no discernible degradation of the surface. Comparison of this result to that of the NASA Ames shock tunnel suggests that the surfaces of the shock tunnel gauges do, in fact, melt. If so, metal or ceramic coatings may not greatly improve the surface durability, since the plastic on which the coating is deposited will simply melt beneath the coating. This would cause loss of adhesion, and the coating would be entrained into the air flow. Experience has borne this out; while the surface coatings improve the

gauge's durability by perhaps one run, the coating has generally been completely removed by the end of the first run.

In the other three facilities in which this research was conducted (GASL's Hypulse expansion tube, Wright Laboratory's Mach 6 tunnel, and AFIT's high pressure shock tunnel), surface erosion did not occur (see, for example, the used GASL gauge in Figure 4-8). Although the heat load in both the AFIT and GASL facilities was higher than at NASA Ames, the former two facilities are helium driven, while the NASA Ames shock tunnel is combustion driven. In the helium driven facilities, the high pressure helium is initially at approximately room temperature and then expands to create the shock wave through the driven section. This expansion causes the helium to cool, so in both the AFIT and GASL tunnels, the hot test gas is followed immediately by cold helium, while in the NASA Ames tunnel, the hot test gas is followed by hot combustion gas. Thus, it appears that the length of the heat exposure in the AFIT and GASL tunnels was insufficient to melt the gauge surface, but in the NASA Ames tunnel, the prolonged heat exposure caused the surface to melt.

Though not conclusive, empirical evidence was obtained at NASA Ames concerning gauge surface integrity. For one test case, the gauge set screws were inadvertently left loose. Hence, during the run, the two gauges in the combustor dropped into the instrumentation cavity below the surface. The data trace indicates that this occurred just after the steady test period. The surface of both of these gauges did not show signs of surface erosion. Therefore, it is expected that the relatively long exposure after the run caused erosion.

It has also been suggested that particles in the flow, perhaps as a result of the steel diaphragm rupture, caused the surface erosion in the NASA Ames tests. However, the GASL tests used similar steel diaphragms, without any resulting surface erosion.

4.3. Gauge Servicing

Early wind tunnel and shock tunnel runs conducted with the current gauge design resulted in oil being lost from the gauge after one or two runs. This limited the usefulness

of the gauge because there was not always sufficient time, accessibility, or the necessary equipment to replenish the oil on site at the test facility. In fact, the most common gauge failure observed in both the NASA Ames tests and the Wright Laboratory's Mach 6 tests was caused by thermal effects resulting from oil depletion. In this type of failure, both strain gauges are exposed to circulating air in the oil cavity. The strain gauge on the leading edge of the sensor heats more rapidly than the strain gauge on the trailing edge, which causes a drastic increase in the voltage output. An example of the effect of oil depletion and the resulting thermal effect on the strain gauges was previously shown in Figure 4-6, in which the skin friction gauge provided a reasonable output for the first 5 seconds, followed by linearly increasing output when the strain gauges began to heat unevenly.

The oil insertion and retention problem will first be analyzed, followed by a description of an oil replenishment device that was developed for the Wright Laboratory Mach 6 tests.

4.3.1. Oil Insertion

This section of the research concentrated on identifying the reason for the oil loss and correcting the problem. The goal of this part of the research was to determine the best way to fill, retain, and replenish the oil. The fluid mechanics of the oil filling were analyzed to determine the best way to fill the gauge with oil. The effects of viscosity, surface tension, and gap size were analyzed. In addition, the amount of time to fill the gauge was estimated.

4.3.1.1. Pressure and surface tension effects

For the oil to begin to flow through the gap, the back pressure on the oil must be sufficient to overcome the surface tension at the gap. The surface tension is defined in terms of the surface tension coefficient σ (a material property of the fluid) and the radius of curvature using the following relation (White, 1991:51):

$$p(x, y, \eta) = p_a - \sigma \left(\frac{1}{R_x} + \frac{1}{R_y} \right) \quad (4-3)$$

where p is the pressure in the liquid at the interface, p_a is the air pressure at the interface, η is the elevation of the surface of the interface, σ is the surface tension coefficient, R_x is the radius of curvature in the x -direction, and R_y is the radius of curvature in the y -direction. For these calculations, $R_y \gg R_x$, so the gap can be considered to be two-dimensional. The quantity $1/R_y$ is negligible and can be eliminated from Eq (4-3).

For oil flow to commence through the gap, the tangency condition must be met; that is, the curvature of the interface must be sufficient for the oil to wet the sides of the gap (Hirt, et al., 1986). At the time of flow initiation, the only pressure variation within the oil is due to the varying weight of the oil at different heights. Along the curved leading edge of the oil surface, this variation in height is negligible due to the smallness of the gap. Since the pressure within this part of the oil is constant, then from Eq (4-3), the shape of the oil at the time of flow commencement is circular, with $R_x = -W/2$.

The air pressure at the interface will be assumed to be constant. Since the gap width W and surface tension coefficient are constant, the liquid pressure at the interface is also constant and will be denoted p_o . Equation (4-3) then becomes

$$p_o = p_a + \frac{2\sigma}{W} \quad (4-4)$$

For the air to flow upward, $R_x = W/2$, and

$$p_o = p_a - \frac{2\sigma}{W} \quad (4-5)$$

Three factors contribute to p_o , the oil pressure at the interface. These are the weight of the oil, back pressure above the oil, and the top surface tension. The weight of the oil is given by $F = mg = \rho Ahg$ (Figure 4-9). The pressure resulting from the weight of the oil is then calculated by $p_w = F/A = \rho hg$.

Surface tension at the top surface of the oil decreases the pressure at the oil-air interface, because the surface tension supports part of the weight of the oil. The top surface tension for a fluid in a circular container of diameter D is given by $F_s = \sigma \pi D$ (Roberson

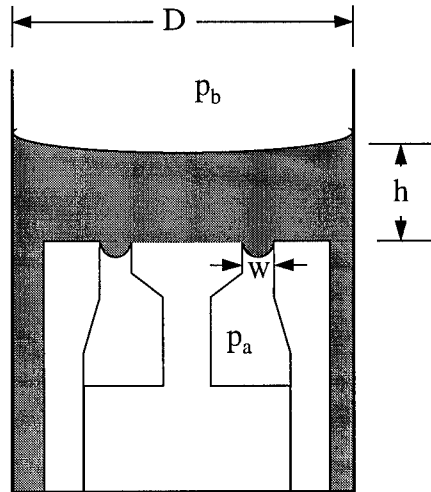


Figure 4-9 Dimensions and Pressures for Gauge in Oil Beaker

and Crowe, 1975:21-22). Taking A as $\pi D^2/2$, the decrease in the pressure at the base of the column is then given by $p_d = F_s/A = 4\sigma/D$. It should be noted that the surface tension force at the top of the oil cannot exceed the weight of the oil, i.e. $4\sigma D \leq \rho h g$.

The total pressure in the fluid at the base of the column is the sum of the back pressure and the pressure resulting from the weight of the oil, less the surface tension effect at the top of the oil:

$$p_t = p_b + p_w - p_d = p_b + \rho h g - \frac{4\sigma}{D} \quad (4-6)$$

In order to force the oil through the gap, the pressure p_t given in Eq (4-6) must be greater than the pressure p_o ; i.e., $p_t > p_o$. From Eqs (4-4) and (4-6), then

$$p_b + \rho h g > p_a + 2\sigma \left(\frac{1}{W} + \frac{2}{D} \right) \quad (4-7)$$

Similarly, for the air to flow upward, from Eqs (4-5) and (4-6),

$$p_a > p_b + \rho h g + 2\sigma \left(\frac{1}{W} - \frac{2}{D} \right) \quad (4-8)$$

The oil used in the skin friction gauge is a silicone oil. Several different viscosities have been tested, but the surface tension coefficient and density were approximately the same for all of the different oils (Dow Corning, 1993). Viscosity affects how long it will take for the oil to flow into or out of the gauge, but the question of whether the oil will

flow in or out of the gauge is governed only by geometry, surface tension, density, and pressure. Thus, increasing viscosity will not affect the ability to get the oil into the gauge (since time is not critical for oil insertion), but may slow the outward oil flow during the run.

4.3.1.2. Oil Insertion Process

In the oil insertion method generally used, the gauge was submerged in oil with in a beaker. The beaker was then placed in a vacuum chamber, and the air was evacuated. The air within the gauge bubbled out through the oil, to be replaced by the oil. The mechanism for this process is shown in Figure 4-10.

In Figure 4-10(a), the oil has been poured over the gauge. Atmospheric air pressure exists over the top of the oil and inside the oil cavity of the gauge. The weight of the oil causes the oil over the cavity to bow downward, but the weight of the oil is insufficient to result in the circular curvature required for the oil to achieve tangential contact with the

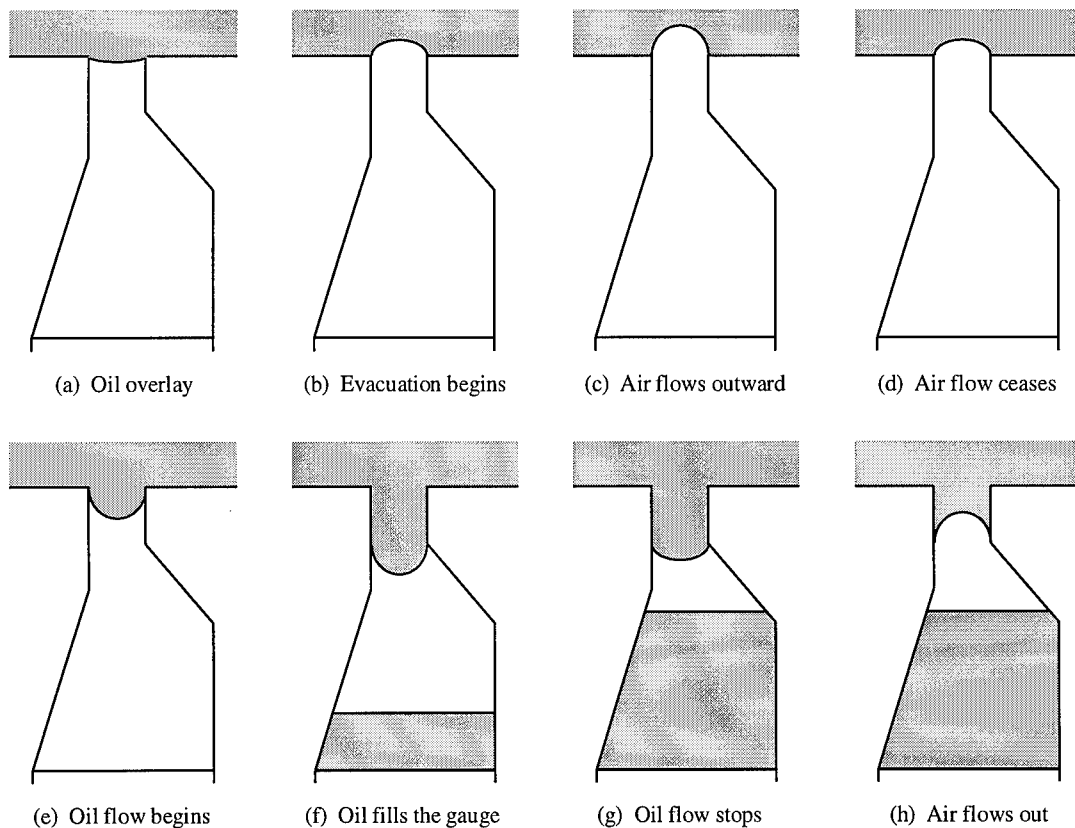


Figure 4-10 Oil Insertion Process

sides of the gap. At this point, the oil does not flow through the gap, and the air does not escape from the cavity.

As shown in Figure 4-10(b), as vacuum is applied, the air pressure inside the cavity causes the oil surface to curve upward. The external vacuum at this point is only partial, and the oil surface has not become sufficiently curved to allow the air to meet the tangency condition. Then, after sufficient external vacuum has been applied, the oil-air interface is fully circular upward as shown in Figure 4-10(c). This allows the air to meet the tangency condition, and air bubbles begin to escape from the oil cavity. From Eq (4-8), this occurs when

$$p_a = p_{br} + \rho hg + 2\sigma \left(\frac{1}{W} - \frac{2}{D} \right) \quad (4-8a)$$

As air escapes from the cavity, a partial vacuum forms inside the cavity. In Figure 4-10(d), enough air has escaped from the oil cavity that the air pressure is no longer sufficient to maintain a circular interface. At this point, the remaining air in the cavity is trapped. From Eq (4-8), this occurs when

$$p_{a0} = p_v + \rho h_0 g + 2\sigma \left(\frac{1}{W} - \frac{2}{D} \right) \quad (4-8b)$$

Then, in Figure 4-10(e), the external vacuum is released, and atmospheric back pressure over the top of the oil causes the oil-air interface to curve downward. The pressure difference is enough that the oil forms a circular profile and flows through the gap.

As shown in Figure 4-10(f), upon reaching the bottom of the gap, the oil forms droplets which detach and fall to the bottom of the oil cavity. As the oil fills the cavity, the remaining air in the cavity is compressed. Then, in Figure 4-10(g), the pressure of the air in the cavity is now high enough that the oil surface in the gap can no longer maintain a circular profile, and oil ceases to enter the oil cavity. At this point, the gap itself is filled with oil, but immediately beneath the gap is an air pocket with air at approximately atmospheric pressure, beneath which the cavity is partially filled with oil. From Eq (4-7), this occurs when

$$p_{af} = p_b + \rho h_f g - 2\sigma \left(\frac{1}{W} + \frac{2}{D} \right) \quad (4-7a)$$

If the exterior air pressure is decreased, then, as shown in Figure 4-10(h), the air pocket expands upward, blowing the oil out of the gap. If this occurs as part of oiling the gauge, then much of the air that was originally trapped will be removed, and re-application of back pressure will result in further filling of the gauge. However, if the reduction of backpressure occurs in preparation for a shock tunnel run, then the bottom part of the oil cavity will contain oil, but the upper part is exposed to circulating air.

Assuming that the air does not change temperature, the volume is inversely proportional to pressure. The volume of the compressed air pocket in Figure 4-10(g) is given by

$$\frac{V_c}{V_t} = \frac{P_{a0}}{P_{af}} = \frac{p_v + \rho h_0 g + 2\sigma \left(\frac{1}{W} - \frac{2}{D} \right)}{p_b + \rho h_f g - 2\sigma \left(\frac{1}{W} + \frac{2}{D} \right)} \quad (4-9)$$

The decrease in the column height can be deduced from the volume of oil that has entered the cavity. If the change can be considered negligible (which would be true if the diameter of the container is much larger than the diameter of the oil cavity), then $h_f \approx h_0 = h$.

The reduced back pressure necessary to cause the compressed air to flow out of the cavity under wind tunnel conditions can be derived from Eq (4-8a) and (4-7a). Setting p_{af} in Eq (4-7a) equal to p_a , substituting into Eq (4-8a), and setting with $h=0$, the following is obtained:

$$p_{br} = p_b + \rho g h_f - 4\sigma \left(\frac{1}{W} + \frac{2}{D} \right) \quad (4-10)$$

It can be seen from Eq (4-10) that, depending on column height and gap width, no reduction in pressure may be necessary to blow the oil out of the gap; this could occur simply because the pressure created by the weight of the oil is removed. In practice, however, the magnitude of the third term in Eq (4-10) tends to be somewhat greater than the second term, so some pressure reduction is necessary. However, both the second and third terms are small compared to the first term, so only a small reduction in pressure is required to blow the oil out of the gap and leave the gauge only partially filled.

As an example of this effect, Table 4-1 shows the amount to which the gauge is emptied if the vacuum pressure during filling was 5000 Pa. The gauge dimensions and the oil properties for this calculation are listed in Appendix A.

Table 4-1 Unfilled Portion of Oil Cavity

		NASA Ames baseline gauge	Wright Labo- ratory Mach 6 gauge
<i>Volume (mm³)</i>	V_{total}	214.3	567.5
	V_{unfilled}	11.6	30.6
<i>Distance to top of oil (mm)</i>	From sensor top	1.4	2.9
	From strain gauge top	1.2	2.8

While, for a given vacuum pressure, it is not possible to change the final pressure of the remaining air bubble in the cavity as given by Eq (4-7a), it is possible to reduce the size of the bubble, and hence fill the cavity more completely with oil, by repeated application of oil and vacuum. With this method, after letting backpressure force the oil into the cavity with resulting compression of the oil bubble, the vacuum is again applied. Since the bubble floats to the top of the cavity while the oil comes into the cavity, when the vacuum is re-applied, the bubble is immediately below the gap (Figure 4-11). The re-application of vacuum causes the bubble to expand upward, and much of the remaining air escapes from the cavity. The vacuum is then released, so that the backpressure forces more oil into the

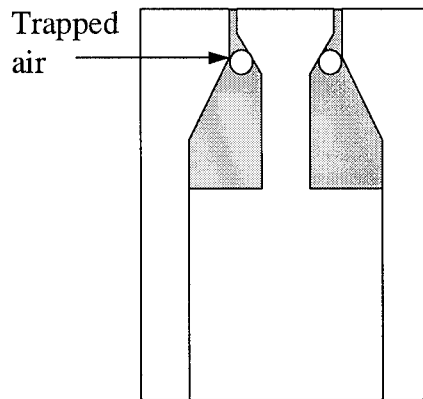


Figure 4-11 Oil Bubble Location (Upright Gauge)

gauge, compressing the remaining air into a smaller bubble. The process can then be repeated, and, from Eq (4-9) the volume of the air bubble is given by

$$\frac{V_c}{V_i} = \left[\frac{p_v + \rho hg + 2\sigma \left(\frac{1}{W} - \frac{2}{D} \right)}{p_b + \rho hg - 2\sigma \left(\frac{1}{W} + \frac{2}{D} \right)} \right]^n \quad (4-9a)$$

where n represents the number of applications and $h_0 \approx h_f = h$. Thus, for the calculations for which the results were shown in Table 4-1, if the oiling process were performed five times, the volume of the air bubble would be 4.6×10^{-5} percent of the total volume of the oil cavity compared to 5.4 percent for the single application. This remaining bubble still has the same pressure as the larger bubble, and reduction of pressure will still cause part of this air to escaped from the gauge with some loss of oil. However, the very small size of this bubble, as compared to the bubble volume calculated for the single application of vacuum, means that the oil loss will be negligible. During this research, after the drawing of a vacuum six times, no more bubbles were observed emerging from the gauge. This was probably due to the trapped air bubble becoming small enough to float out through the gap. If less complete evacuation were performed, then more cycling would be required to fully rid the gauge of air.

The gauge must be in an upright position in order for the repeated application of vacuum to work. If the gauge is not in an upright position, then the bubble floats to the highest part of the oil cavity. Upon re-application of vacuum the bubble then expands downward and to the sides, forcing oil, not air, back out of the gauge (Figure 4-12).

The minimum gap width for oil insertion is given when the back pressure is suffi-

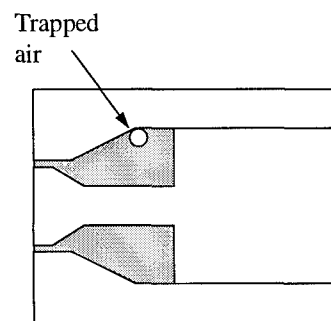


Figure 4-12 Oil Bubble Location (Prone Gauge)

cient only to change the shape of the oil/air interface from convex upward to convex downward, with a circular edge for both, but not to actually initiate flow. This occurs when $p_{a0}=p_{af}$, or, setting Eqs (4-7a) and (4-8a) equal and solving for W

$$W_{\min} = \frac{4\sigma}{p_b - p_v} \quad (4-11)$$

This minimum gap size is generally smaller than the deflection of the sensor beam calculated in Section 3.1.

4.3.1.3. Time requirements for oiling the gauge

In the submerged method, the air evacuation can be observed visually as bubbles form and float to the surface of the oil. This process can take a half hour or longer. The insertion of the oil after release of the back pressure cannot be observed. Therefore, an analysis was undertaken to determine the time required for the oil to flow into the gauge after application of back pressure. Since the pressure inside the gauge increases as the oil flows into the gauge, a closed form solution was not possible, and a numerical procedure was applied. This numerical procedure is described in detail in Appendix C.2, so only an overview will be undertaken here.

The numerical procedure consisted of solving the unsteady Navier-Stokes equations for incompressible flow through a concentric annulus. The entrance length is 0.6 percent of the total length of the annulus, with the remaining 99.4 percent of the length being fully developed flow, so the entire length of the annulus was modeled as fully developed flow. The unsteady Navier-Stokes equations for this situation reduce to a single equation

$$\frac{\partial u_z}{\partial t} - \nu \left(\frac{\partial^2 u_z}{\partial R^2} + \frac{1}{R} \frac{\partial u_z}{\partial R} \right) = -\frac{1}{\rho} \frac{\partial p}{\partial z} + g \quad (4-12)$$

The following boundary and initial conditions apply:

$$u_z(R_H, t) = 0 \quad u_z(R_O, t) = 0 \quad u_z(z, 0) = 0 \quad (4-13)$$

The pressure gradient as a function of time is given by

$$\frac{\partial p}{\partial z} = -\frac{p_b + \rho hg - \frac{p_v V}{V_a} - 2\sigma\left(\frac{1}{W} - \frac{2}{D}\right)}{T_L} \quad (4-14)$$

where

$$V_a = V - \int_0^t Q d\tau \quad (4-15)$$

and

$$Q(t) = \int_{R_H}^{R_o} u_z(2\pi R) dR \quad (4-16)$$

Equation (4-12) was solved using the Crank-Nicolson scheme. The integrals in Eqs (4-15) and (4-16) were evaluated numerically using the trapezoid rule. The numerical method was verified by grid refinement and by comparison with the exact solution for steady flow through an annulus, for which the velocity profile is

$$u_z = \frac{\pi}{8\mu} \left(-\frac{dp}{dz} \right) \left[R_o^4 - R_H^4 - \frac{(R_o^2 - R_H^2)^2}{\ln(R_o/R_H)} \right] \quad (4-17)$$

It was found that filling occurred rapidly ranging from 0.56 second for 200 cSt viscosity oil to 28 seconds for 10,000 cSt oil (Figure 4-13).

For the early NASA Ames tests, the oil was heated in an attempt to more completely fill the gauge by lowering the viscosity. However, the heated oil damaged the strain gauges, so this method is not recommended. In addition, the rapid filling calculated by the numerical procedure illustrates that heating was unnecessary.

4.3.2. Wind Tunnel Response

The reaction of the oil to the wind tunnel environment was examined to determine how the oil is lost and to look for ways to improve the retention of the oil.

4.3.2.1. Pressure Difference Between Top and Bottom of the Gauge

During the wind tunnel run, a pressure difference exists between the top and bottom of the gauge. For the NASA Ames and GASL shock tunnel tests, the pressure at the

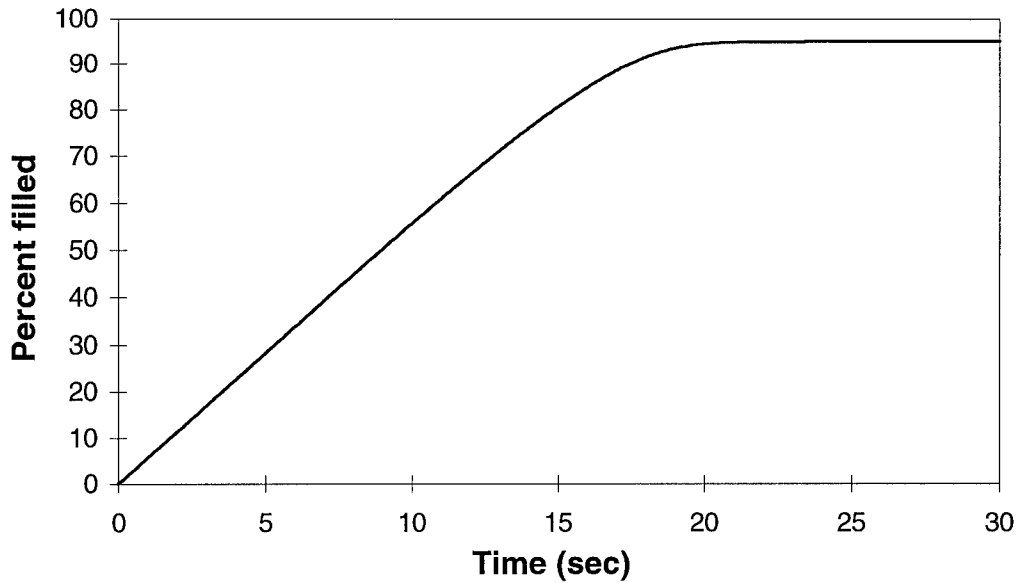


Figure 4-13 Oil Insertion Time for 10,000 cSt Oil

bottom of the gauge is less than the top because the test section is evacuated prior to the run. The higher pressure of the test gas is felt by the top of the gauge first and only later by the bottom of the gauge. This is also true of the Wright Laboratory's Mach 6 tests, where the test section was initially at the Mach 6 freestream pressure and then inserted in the flow. Due to the angle of the plate, an oblique shock reduced the Mach number on the plate to 4.37, so the pressure was again higher on the top than the bottom. If the bottom of the gauge was not perfectly sealed, then this pressure difference could cause oil to run out the bottom of the gauge. However, any leaks would be considerably smaller than the smallest oil gap for which the oil filling time was calculated in Section 4.3.1.4, so the rate of oil loss should be small.

4.3.2.2. Pressure Gradient

A pressure gradient across the sensor surface would cause the oil to flow out as shown in Figure 4-14. The oil flowing out of the gauge is blown down the tunnel. This is consistent with observations of oil smears aft of the gauges following a run. With a shock, the pressure difference would be particularly high. In all of the wind tunnels used in this

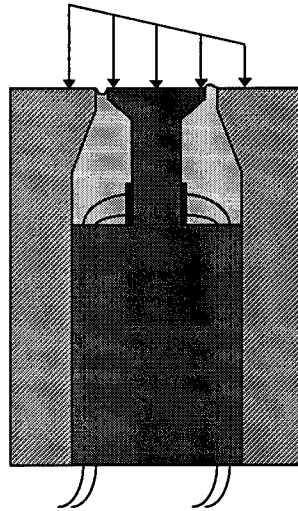


Figure 4-14 Oil Loss Induced by Pressure Gradient

research, the starting dynamics include a transient shock. With a standing shock, the boundary layer would reduce the pressure gradient, but the time exposed would be higher.

However, while it appears that a shock can cause oil loss, the amount would be limited. First of all, as can be seen from the time requirements for oiling the gauge, very little oil could run out in the 2-4 msec duration of a typical shock tunnel run, even with a standing shock. The time for a transient shock is even less, on the order of μsec . Second, once the oil level has dropped below the gap, then the air would simply recirculate through the top of the oil cavity rather than pushing the oil out (Figure 4-15). In the case of a standing shock, this would disrupt the flow pattern and change what is being measured, but for a transient shock, the effect on the measurement would not be significant. Therefore, while a shock can cause initial oil loss in a fully oiled gauge, several runs are required before any substantial oil loss results, and then an equilibrium point is reached where subsequent runs should not result in further oil loss.

4.3.2.3. Oil Loss Due to Evaporation and Heating Effects

In the Wright Laboratory Mach 6 tests, oil was observed on the model surface immediately downwind of the gauge. Even though the Mach 6 tunnel operates at a much lower temperature than the NASA Ames shock tunnel, the thermal conductivity of the oil is low enough that the surface of the oil probably reached a high enough temperature to

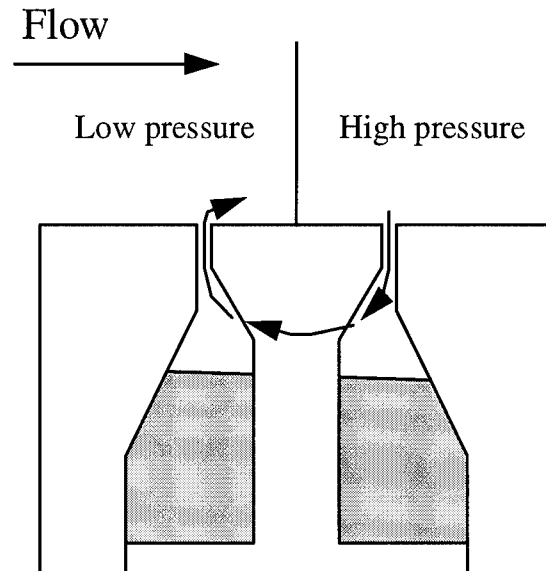


Figure 4-15 Air Circulating through Oil Cavity

boil. If this is the mechanism for the oil loss, then the vaporized oil must have condensed after being swept into the airflow and coming into contact with the colder metal of the model wall.

The thermal heating analysis outlined in Section 4.1.1 with results shown in Figure 4-1 indicates that the oil heats very rapidly. Although the boiling point of the oil is not known, due to the unknown effect of pressure, it appears that the oil does reach the boiling point. In the laboratory, at near vacuum conditions, the oil has boiled at 110°C. This is well below the calculated oil temperature of the gauge during a NASA Ames run. Therefore, this is considered a likely cause of oil loss. The only remedy is to decrease the gap size to decrease the exposed oil surface. Once oil in the gap has been lost, then the exposed oil surface is greater, but a smaller gap size also reduces air circulation in the partially empty cavity, which would also reduce oil loss.

4.3.2.4. Shock Test

It has been postulated that the initial breaking of the shock tunnel diaphragm caused compression of the skin friction gauge, with resulting loss of oil. This hypothesis

was tested by mounting an oiled gauge in a gauge mount. The mount was then struck with a mallet while a sheet of stiff plastic was held approximately 1 mm above the gauge. The shock created by the mallet blow did not cause the oil to splash onto either the plastic or the gauge top or the surrounding mount. Therefore, it appears that compression caused by the opening of the diaphragm is not a cause of oil loss.

4.3.2.5. Operating the Gauge in an Inverted Position

In the scramjet combustor tests at the General Applied Sciences Laboratory (GASL), the skin friction gauges were placed in the top of the combustor in an inverted position. This raised the question of whether the oil would drain out. This question can be answered by using Eq (4-4). If the gauge is inverted, then, for the oil to drain out, the oil surface must bulge outward, requiring higher pressure inside the gauge than on the outside. The pressure inside the gauge at the oil-air interface is the sum of the weight of the oil plus the pressure of the remaining air, which will be taken as atmospheric pressure. Equation (4-4) then becomes

$$\rho gh_c + p_a = p_a + \frac{2\sigma}{W}$$

or, canceling terms and rearranging,

$$h_c = \frac{2\sigma}{\rho g W} \quad (4-18)$$

Using the dimensions and oil properties listed in Appendix A, the minimum oil cavity height required to induce the oil to run out is then 3.5 cm. The oil cavity height is the same as the beam length. Since the longest beam used in this research is 1.3 cm, the oil should not run out.

This relation pre-supposes perfect evacuation of air from the cavity. Any air trapped in the cavity will expand downward during evacuation of the test section, so the volume of oil lost is equal to the volume expansion of the air. This differs from the gauge in the upright position, where only the oil in the gap is lost. In the GASL tests, it was possible to retain enough oil in the gauge to prevent heating effects, but some oil did drip out during the test section evacuation, presumably due to trapped air.

4.3.3. Replenishment Device

For the Wright Laboratory's Mach 6 inlet tests, the design of the model did not allow ready removal of the skin friction gauge for re-oiling. Therefore, a re-oiling device was designed that was successfully used to re-oil the gauge without removing it from the model (Figure 4-16). This device relied on vacuum to create a seal between the re-oiling device and the gauge. In order to maintain the seal, the vacuum is not completely released; rather, the vacuum is partially released, and the resulting pressure of 1/2 atmosphere is sufficient to push the oil through the gap.

While this device was used successfully for the Wright Laboratory tests, one factor made it less useful for other tests. The oil cavity must be perfectly sealed at the bottom, or the suction will pull air into the gauge. This air would then be compressed upon application of back pressure, resulting in incomplete gauge filling. The repeated application of vacuum method, therefore, cannot be used unless a perfect seal around the oil cavity is obtained. In practice, as noted previously, a perfect seal is difficult to obtain, so runs in other wind tunnels used the more rigorous practice of removing the gauges from the tunnel for re-oiling.

4.4. Electrical Response and Calibration

Various factors can potentially cause error in the skin friction gauge's electrical output. Most of these factors can be compensated for through an accurate calibration. This part of the research analyzed the electrical response of the gauge in order to determine which factors can be compensated for through calibration. The actual calibration process was then evaluated in order to eliminate possible sources of error.

The electrical response of the gage was analyzed using circuit theory in order to determine the effect of potential sources of error. The following factors were evaluated:

Effect of the Wheatstone bridge becoming unbalanced prior to the run.

After the Wheatstone bridge has been balanced, temperature effects can cause the response to drift. The Wheatstone bridge then becomes unbalanced prior to the initiation of the run.

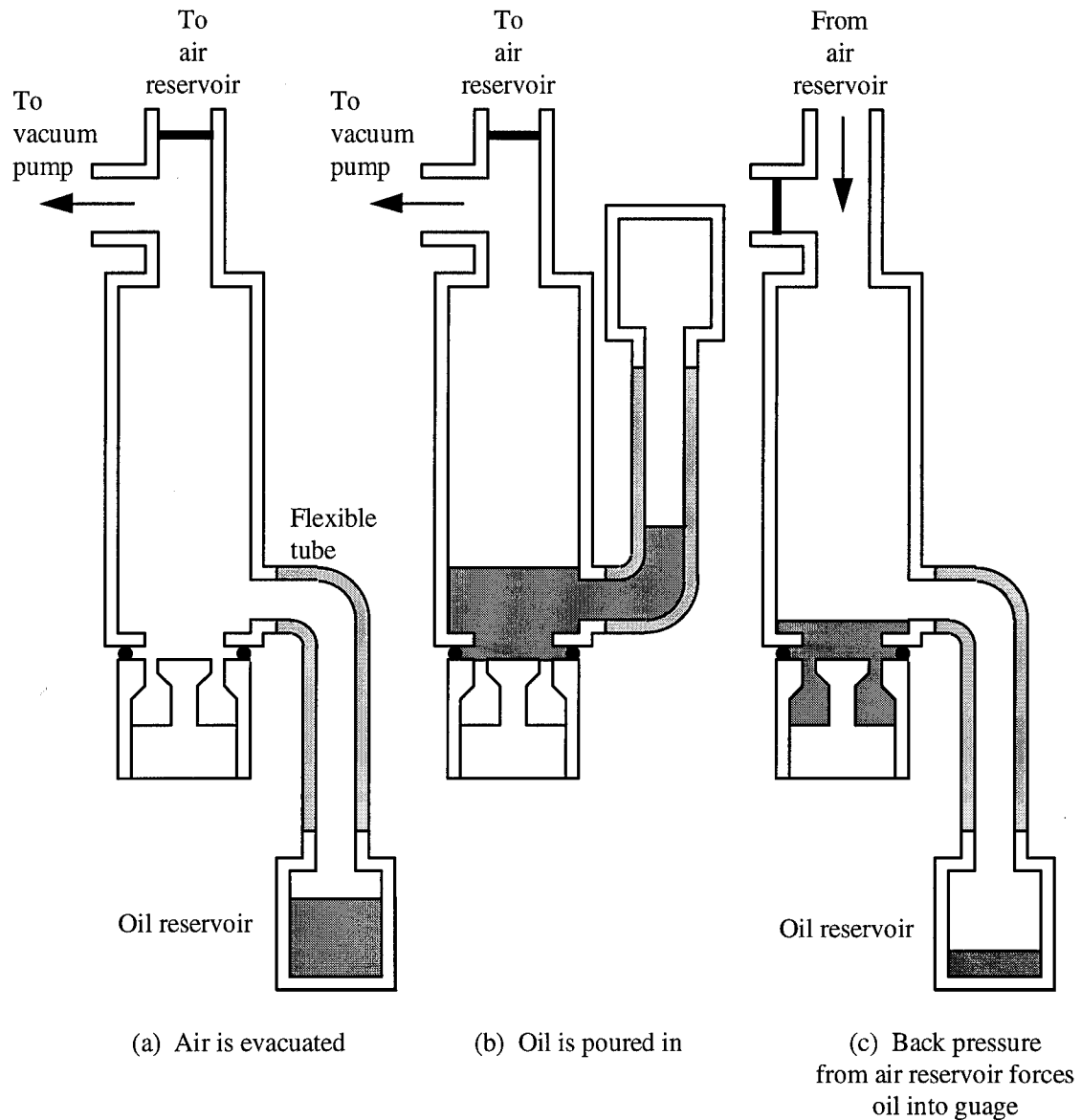


Figure 4-16 Skin Friction Gauge Re-Oiling Device

Tilting the gage. This causes an initial strain as discussed in Section 3.1.4.

Misaligned strain gauges. Strain gauges can be misaligned in three ways: by not being in a completely vertical position on the gage, by not being precisely opposite each other, or by being at different heights on the sensor beam. The effect is that the compression and tension strains are not equal in magnitude.

Differing gauge factors. The strain gauges used for the current research are manufactured to a tolerance of ± 5 percent variation in gauge factor. Thus, the gauge factor of the two strain gauges could differ by as much as 10.5 percent.

Strain gauges not at the same resistance value. There are two possible causes for this. First, the strain gages may not have exactly the same resistance when they come from the factory. Second, the strain gage may be strained upon application to the sensor surface, either because the sensor surface is not completely flat or because the glue is not the same thickness everywhere.

Added resistor. For some skin friction gauges, the difference between the resistances of the two strain gauges is large enough that the internal resistors in the amplifier cannot adjust enough to balance the bridge. For such a case, an external resistor is added to the strain gauge half of the Wheatstone bridge to bring the two halves of the strain gauge circuit into closer agreement.

4.4.1. Electrical Analysis

The Wheatstone bridge circuit diagram was previously shown as Figure 2-10. For the ideal case, the strain gauges have the same initial resistances and gauge factors, and the strain is the same for both strain gauges. Using basic circuit analysis (Appendix B), the voltage response to a given strain can be shown to be

$$V - V_0 = \frac{V_e k (\epsilon - \epsilon_0)}{2} \quad (3-101b)$$

Hence, the change in voltage reading ΔV is a linear function of the change in strain response, $\Delta \epsilon$. The change in strain is linearly related to the wall shear stress as shown in Section 3.1.4. This, it is unnecessary for the bridge to be perfectly balanced at the beginning of the run because the wall shear stress can be measured from the change in voltage. Further, initial strain due to tilt is either balanced out by the bridge or is part of V_0 , so this, too, is eliminated as a source of error by computing wall shear stress from the change in voltage.

For the general case encompassing the other four factors, the variations were represented by small disturbance parameters δ , such that

$$\varepsilon_c = -(1 + \delta_e)\varepsilon_t = -(1 + \delta_e)\varepsilon \quad (3-142)$$

$$k_c = (1 + \delta_k)k_t = (1 + \delta_k)k \quad (3-112)$$

$$R_{c0} = (1 + \delta_R)R_{t0} \quad (4-19)$$

$$R_B = \delta_B R_{t0} \quad (4-20)$$

Then using basic circuit analysis along with series expansions, the voltage response is

$$V - V_0 = \frac{V_e k (\varepsilon - \varepsilon_0) D}{2} \left[1 + \frac{Bk(\varepsilon + \varepsilon_0)}{2 + \delta_R + \delta_B} + O(\varepsilon^2 \delta^2 k^2) \right] \quad (3-101c)$$

where

$$D = \frac{2(2 + \delta_R + B)}{(2 + \delta_R + \delta_B)^2} \quad (3-141a)$$

and

$$B = (1 + \delta_R)(1 + \delta_k)(1 + \delta_e) - 1 \quad (4-21)$$

The value of D is constant so long as all of the δ terms are constant, which would generally be the case. The non-linear part of the response is then given by the term in brackets in Eq (3-101c), which is a function of the four δ terms and ε_0 , but not of the initial voltage. The leading order non-linear term in Eq (3-101c) disappears if B goes to zero. B contains the factors δ_R , δ_k , and δ_e ; the non-linear effect is of the order $\varepsilon \delta k$ because B is of order δ . Since B is of order δ , the degree of non-linearity is determined by the largest δ term, excepting δ_B , which is not part of B but is contained in the denominator of the leading order term. If all four δ terms are zero, then both D and the nonlinear bracketed term have values of 1, and the design case given by Eq (3-101b) is recovered.

The δ factors do not have to be small in order for the non-linearity to be small. Even if all of the δ factors were of order 1, a strain of 2×10^{-5} would result in an error of less than 1 percent. However, if one of the strain gauges is not completely bonded to the beam, then this can be considered as a decrease in the effective gauge factor. In this case,

δ_k can be quite large and introduce non-linearity into the response. In fact, the only instances of significant non-linearity observed during the course of this research were traceable to incomplete bonding. (If a gauge had a non-linear response, additional glue was applied, which cured the problem.)

The presence of the added resistor does not affect the non-linearity. It can be seen from Eq (3-141a), however, that δ_B is contained in D which is considered to be constant for calibration purposes. If a resistor is added or changed after calibration, D is changed, which causes a shift in the calibration value. The error can be minimized by keeping the added resistance or change of resistance as small as possible. The Measurements Group 2310 signal conditioning amplifier used in this research will not balance if the resistances of the tension and compression strain gauges differ by more than 30Ω ; the worst error that could be introduced by changing resistors would be approximately 9.7 percent (Appendix B).

4.4.2. Calibration

If the non-linearity in Eq (3-101b) is considered negligible, and the signal is amplified by a gain factor of F_G , then

$$V - V_0 = \frac{F_G V_c k(\epsilon - \epsilon_0) D}{2} \quad (3-101c)$$

Further, if the strains are linear, then, as discussed in Section 3.1.1.4, the strain due to the end loading can be superimposed on any existing strain in the beam. Thus, Eq (3-5) can be written

$$\epsilon - \epsilon_0 = \frac{\tau_w A_H \left(L - \frac{1}{2} L_{sgt} \right) R}{EI} \quad (3-5a)$$

Since the difference in voltage can be used to compute the wall shear stress, the gauge calibration factor can be defined through the relation

$$\tau_w = A(V - V_0) \quad (2-11a)$$

Substituting Eqs (3-5a) and (2-11a) into Eq (3-101c), the calibration factor is given by

$$A = \frac{2EI}{F_G V_e k A_H \left(L - \frac{1}{2} L_{sgt} \right) RD} \quad (3-6b)$$

This is the design calibration value when $D=1$. If the strain gauges are not at the base of the cantilever, then the calibration constant becomes

$$A = \frac{2EI}{F_G V_e k A_H L_s RD} \quad (3-6c)$$

Factors affecting the beam stiffness can be factored into I , while strain gauge misalignment effects enter into k and D .

If the gain factor or the excitation voltage is changed, then the new calibration constant can be calculated from Eq (3-6c) as

$$A_{new} = A_{cal} \frac{F_{G(cal)} V_{e(cal)}}{F_{G(new)} V_{e(new)}} \quad (2-13)$$

To ensure that the calibration constant was accurately measured, the following procedures were developed in the course of this research:

Calibration over entire range of expected wall shear values. The weights used to calibrate the gauge must exceed the equivalent maximum wall shear stress expected for the gauge's expected application. If this criterion is not applied, then the skin friction determination is an extrapolation. Since the response of semiconductor strain gauges is linear only for small strains (Neubert, 1967:81-83), extrapolation can lead to an incorrect result if the strain is large enough to cause a non-linear response from the strain gage. The non-linear terms in Eq (3-101c) can also become important at larger strains.

Measurement of sensor head. Calculation of wall shear stress from calibration involving end-loaded weights requires accurate knowledge of the sensor head area. Since the sensor head area may differ from the design specifications, the sensor head should be measured to ensure the wall shear stress is accurately calculated.

Calibration in both directions. If the skin friction gauge is not precisely aligned, then an error factor of $\sin\alpha$ is introduced, where α is the misalignment angle. By calibrating in both directions, misalignment can be detected since different voltage slopes would result.

Determination of effective axis. If a single axis gauge is to be used in a situation where a cross flow exists, and if it is desired to measure the longitudinal component of the flow, then, as described in Section 3.6, the effective axis, not the design axis must be aligned in the longitudinal direction. The effective axis can be determined by calibrating in several directions.

Calibration of amplifier. The Measurements Group 2310 signal conditioning amplifier can be set for several different excitation voltages and has a dial-set gain factor. It has been found that both the excitation voltage and the gain factor can vary between different amplifiers set at the same settings (Appendix A). Thus, it is best to calibrate a gauge on the same amplifier that will power it in the wind tunnel. This is not always practical, however, so the amplifier must be calibrated and the skin friction gauge calibration factor adjusted using Eq (2-11). The maximum variation in excitation voltages among the five amplifiers used during this research was 0.6 percent, while the maximum variation in gain factor was 5.78 percent. These variations could result in a maximum error of 6.4 percent if a gauge were switched between amplifiers without correction of the calibration constant.

Ensure maximum voltage output of amplifier is not exceeded. The Measurements Group 2310 amplifier has a maximum linear output voltage of 10V. If the gain is set so that the output voltage would exceed 10V, a nonlinear response results.

Allow strain gauge glue to set fully prior to calibrating. It has been found on a few occasions that if the skin friction gauge was calibrated immediately after being built that the calibration factor would change over the next few days. The probable cause of this is that the strain gauge glue had not fully set at the time of initial calibration.

V. Skin Friction Gauge Application in Scramjet Tests

This chapter discusses the skin friction measurements taken in three sequences of scramjet tests sponsored by NASA and the Air Force. The tests were conducted at the NASA Ames 16 inch shock tunnel, the Wright Laboratory's Mach 6 blow-down tunnel, and GASL's Hypulse expansion tube facility. The skin friction measurements in these tests were used by the engine developers to evaluate and improve the efficiency of their designs. In addition, these tests provided valuable information on how to improve the skin friction gauges.

In order to compare the results obtained in these tests to the results predicted by theory, several common skin friction correlations were adapted to high temperature applications. These correlations are discussed in Appendix B.

5.1. NASA Ames Scramjet Shock Tunnel Tests

The NASA Ames 16 inch shock tunnel is a large scale facility that was constructed in the 1950s. The driver section is made from a 16-inch naval gun from which the facility takes its name (Figure 5-1). The shock tunnel was renovated in the 1980s to support scramjet testing. The shock tunnel operates in reflected shock mode and uses a hydrogen

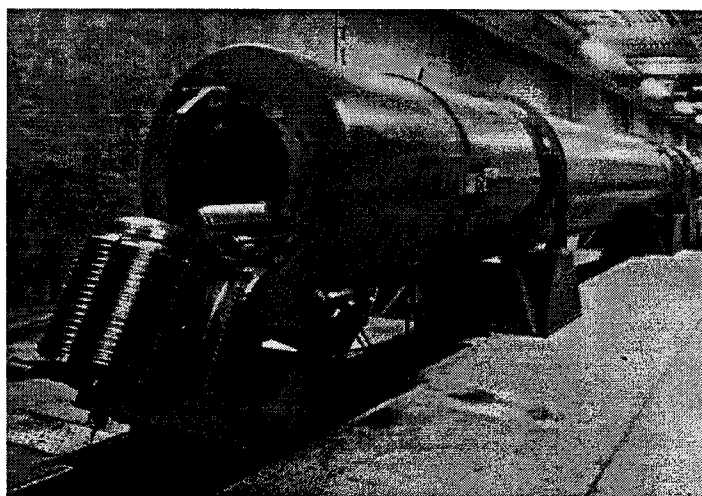


Figure 5-1 NASA Ames 16 Inch Shock Tunnel

fueled combustion driver section. Skin friction gauges designed and built as part of this dissertation research were used in scramjet tests during 1994. The model, as shown in Figure 5-2, was a full-scale scramjet with inlet, combustor, and nozzle (Deiwert, Cavolowsky, and Loomis, 1994). The stagnation enthalpy corresponded to a flight Mach number of 12-14 (stagnation temperature of 6000K) with an actual free stream Mach number of 6. The steady run time, which NASA Ames called the "averaging period," was 2 milliseconds. For all of the runs, the averaging period was provided by NASA. Four skin friction ports were available, two in the inlet and two in the combustor. The two ports in the combustor were side-by-side (one centerline, one off-center), while the two in the inlet were in-line (Figure 5-3).

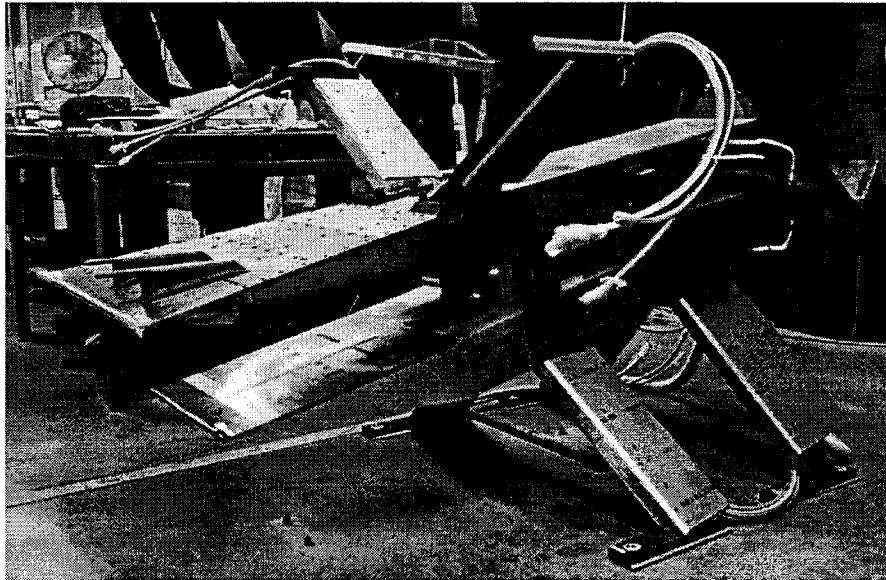


Figure 5-2 NASA Ames Scramjet Model

Two types of gauges were used in the NASA Ames tests. The first used a sensor with a circular cross section similar to the "baseline" gauge developed by Drs. Bowersox and Schetz. This gauge has a nominal natural frequency of 10 kHz. The second gauge used an I-beam cross section and a lightweight sensor head to provide a natural frequency of 30 kHz. A total of 17 gauges was provided for 15 runs. In addition, in a parallel effort, Virginia Tech researchers provided gauges of other designs, some with hollow cores, in an effort to increase the frequency response. The researchers at Virginia Tech also investi-

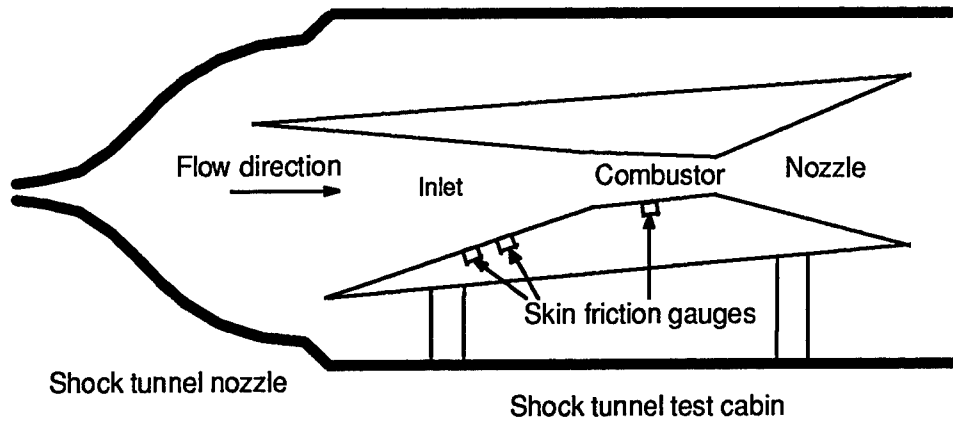


Figure 5-3 Scramjet model in NASA Ames Shock Tunnel

gated replacing the oil with silicon rubber. All gauges were powered by the Measurements Group 2310 Signal Conditioning Amplifiers, and data was collected by the NASA Ames data acquisition system.

5.1.1. Application of Measurements

The skin friction measurements were used by the engine designers to assess the efficiency of their designs. As an example of how the skin friction measurements were used, a combustor skin friction trace from Run 2089 is shown in Figure 5-4. This meas-

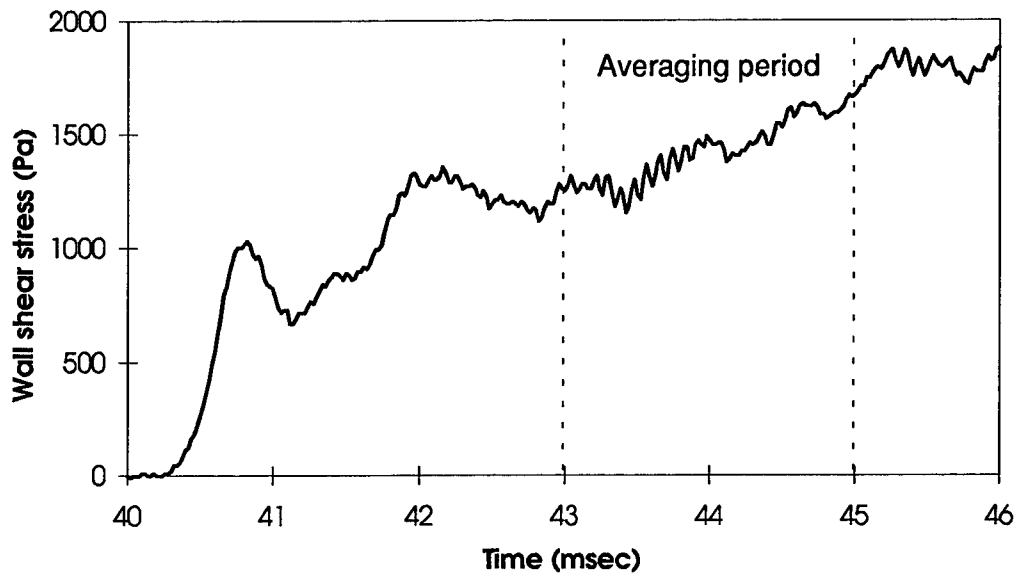


Figure 5-4 NASA Ames Run 2089 Combustor Wall Shear Stress

urement was made with an AFIT baseline gauge. The response is fairly steady with a slight rise that probably reflects increasing pressure. Shown in Figure 5-5 is a numerical analysis of this run condition performed by engineers at NASA Langley Research Center using a parabolized Navier-Stokes solver. The abscissa of the plot is a non-dimensionalized distance from the combustor entrance. The different lines represent different combustor efficiencies. The averaged skin friction measurement from Figure 5-4 was also plotted by the NASA Langley engineers. As can be seen, the skin friction measurement agrees well with the computational result. In addition, the measurement was used by the engineers to pinpoint at what efficiency the scramjet was operating.

5.1.2. Gauge Analysis

Most of the skin friction measurements were taken in the combustor, because this is the most complicated part of the flowfield, and the skin friction measurements can help to determine the combustor efficiency. However, a few measurements were taken in the

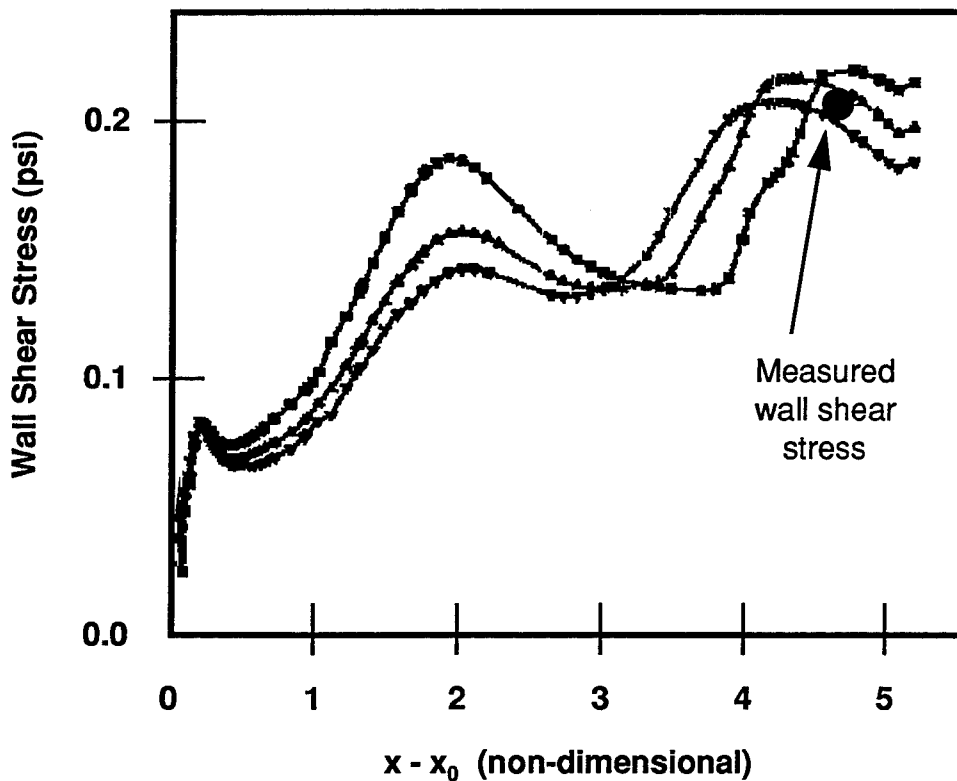


Figure 5-5 CFD Data Analysis of NASA Ames Run 2089 (NASA Langley)

inlet, and these were particularly useful from the gauge development aspect. The inlet is a planar ramp, so for the position of the skin friction gauge, the flat plate skin friction correlations can be applied. In addition, the thermal analysis described in Chapter 4 was applied to the inlet data, and a frequency analysis was also conducted.

The problem with comparing the measured data to what any of the common skin friction correlations would predict is that most skin friction correlations were developed using perfect gas assumptions. Therefore, several of the common skin friction correlations, including the Van Driest II and Spalding and Chi, were analyzed to determine the conditions under which they may be applied to high temperature flow. These are discussed in Appendix B.

Shown in Figure 5-6 is the inlet skin friction trace for Run 2066 made by an AFIT baseline gauge. The gauge's natural frequency of 10 kHz appears plainly in this trace along with a lower frequency base vibration. Applying the skin friction correlations from Appendix B, it was found that the Spalding and Chi theory agreed the best with the measured skin friction (Figure 5-7). The Spalding and Chi theory predicted a skin friction of 1174 Pa, as compared to the measured 1200 Pa. The greater accuracy of the Spalding and Chi theory, as compared to the Van Driest II and other theories, is not surprising because

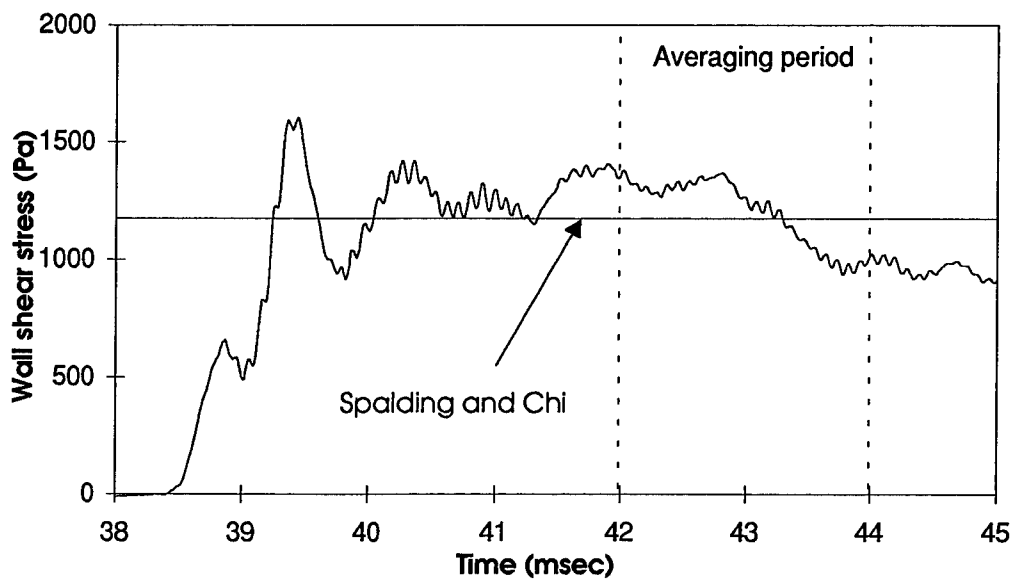


Figure 5-6 NASA Ames Run 2066 Inlet Wall Shear Stress

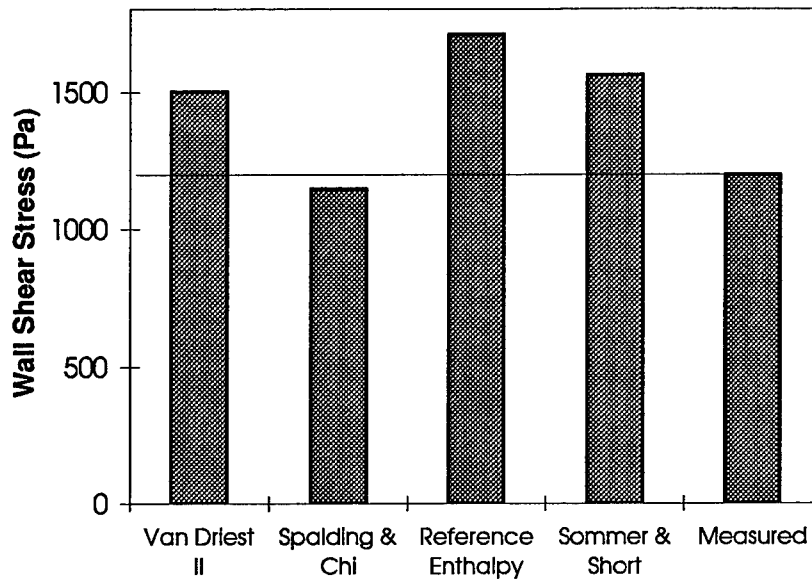


Figure 5-7 Comparison of Skin Friction Theories with Average Measured Wall Shear Stress for NASA Ames Run 2066

previous researchers (Hopkins and Inouye, 1971) have also found that the Spalding and Chi formula more accurately predicts the skin friction for a cold wall, and for this particular run the wall was very cold ($T_w/T_e=0.15$)

The thermal analysis described in Section 4.1.1 was also applied to the NASA Ames Run 2066 inlet data. It was found that for this run, the gauge surfaces would have heated to approximately 895K by the end of the 2 msec averaging period, compared to 324K for the metal wall surface. However, as described in Section 4.1.2.3, the estimated error caused by this temperature mismatch between gauge and wall surface is only 3.4 percent.

The data for several of the runs were analyzed to determine whether the frequency of the gauge response followed that predicted from vibration theory. These analyses were applied primarily to the earlier runs, which were conducted at a sampling rate of 100 kHz.

To analyze the frequency response, a fast Fourier transform (FFT) was applied using the DADiSP software along with Hamming window as described in Section 3.2. In general, the natural frequency of the gauge was preserved in the signal from the model, although as noted in Section 3.2, some variation of natural frequency exists between

models of the same design. Shown in Figure 5-8 is the FFT analysis for Run 2066. The natural frequency of the gauge during the run was 10.9 kHz. In addition, a base vibration of 1.25 kHz was found. Both of these effects can be seen in the trace for the run (Figure 5-6). The base vibration exists in most of the NASA Ames traces. The effects of a base vibration are discussed in Section 3.2.

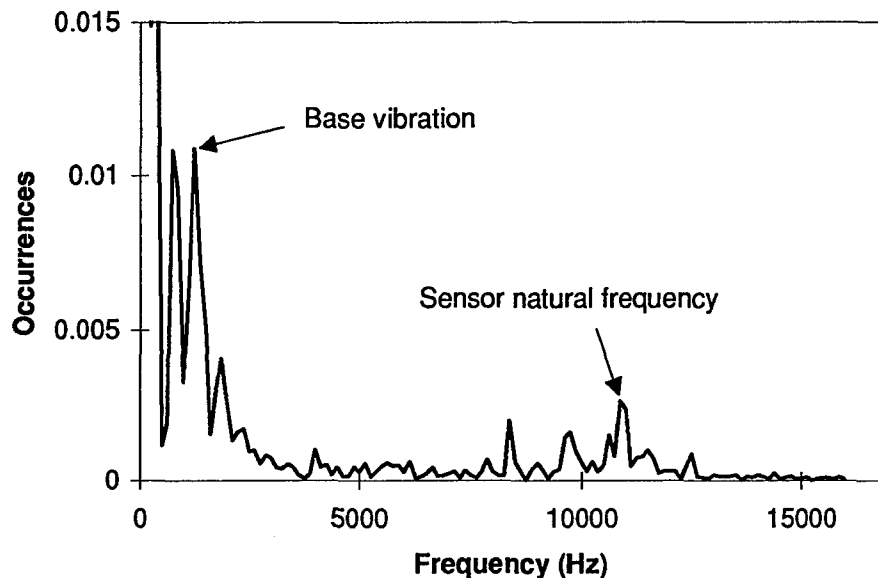


Figure 5-8 Spectrum Analysis for Run 2066

5.1.3. Reported Data and Discussion of Traces

The measurements from the NASA Ames runs were reported by Novean, Schetz, Hazelton, and Bowersox (1995). The data for the AFIT gauges are summarized in Table 5-1. It should be noted that the data are for varying conditions, some with film cooling and others without (however, that information has not been cleared for public release). Thus, the wide variations in the results are a largely function of flow conditions.

A combustor skin friction trace for Run 2060 is shown in figure 5-9. This was the first successful combustor skin friction measurement obtained at NASA Ames. The measurement was obtained with an AFIT baseline gauge, as were all of the other runs that will be discussed here except for Run 2082. The sharp increase in the skin friction midway through the averaging period is very similar to the effects of a traveling shock as seen in

Table 5-1 Summary of NASA Ames Wall Shear Stress Measurements

Run	Wall Shear stress (Pa)	Standard Deviation	Run	Wall Shear stress (Pa)	Standard Deviation
2060 C2	1872	183	2083 C2	1292	316
2060 I2	1910	532	2086	1402	96
2061 C2	1692	222	2087 C1	205	199
2062 C2	1908	150	2088 C1	3036	316
2066 I1	1200	141	2088 C2	1694	199
2079 C2	2671	375	2089 C1	1423	138
2080 C2	1613	119	2089 C2	292	139
2082 C1	912	118			

the GASL measurements. An inlet trace for the same run is shown in Figure 5-10. It can be seen that this trace also has a spike in the middle of the averaging period. The spike is more pronounced for the inlet trace, so it appears that a shock may have passed through the tunnel and was then attenuated as it traveled through the scramjet.

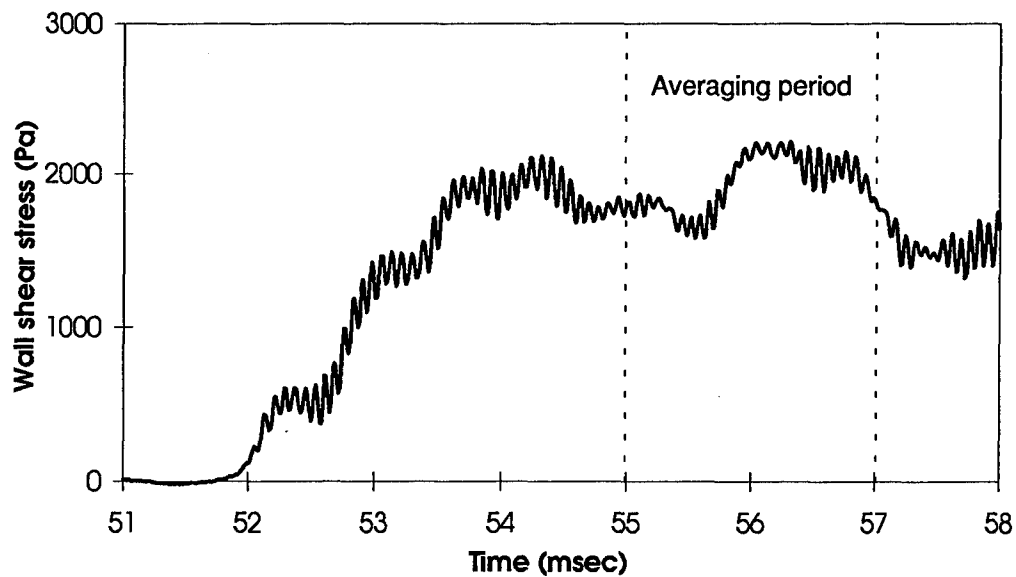


Figure 5-9 NASA Ames Run 2060 Combustor Wall Shear Stress

A combustor skin friction trace for Run 2061 is shown in Figure 5-11. This trace is fairly steady with a slight increase throughout the run as is characteristic of many of the combustor traces. Shown in Figure 5-12 is another combustor trace, this one for Run 2062. This trace appears remarkably similar to the previous trace, although the magnitude

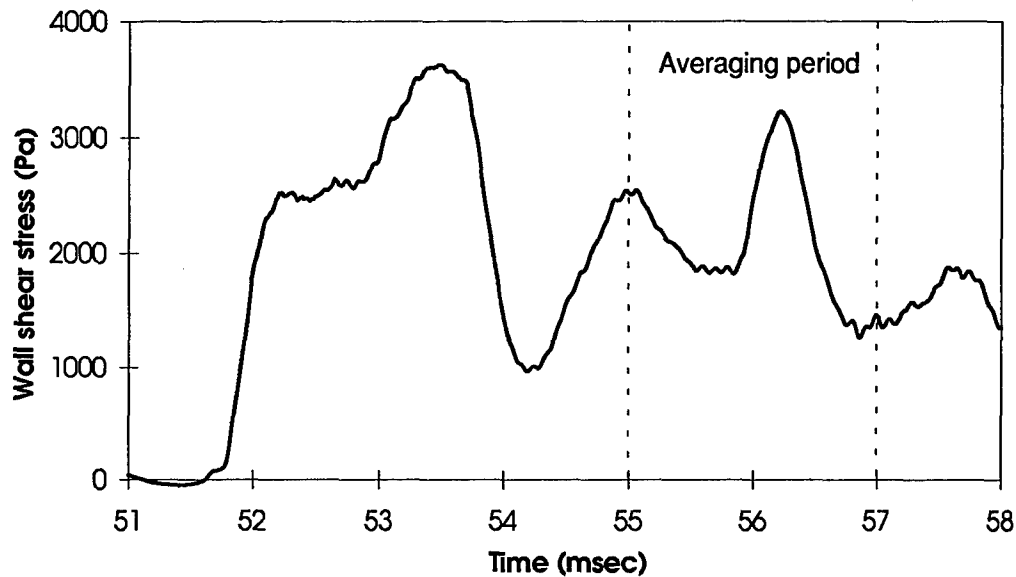


Figure 5-10 NASA Ames Run 2060 Inlet Wall Shear Stress

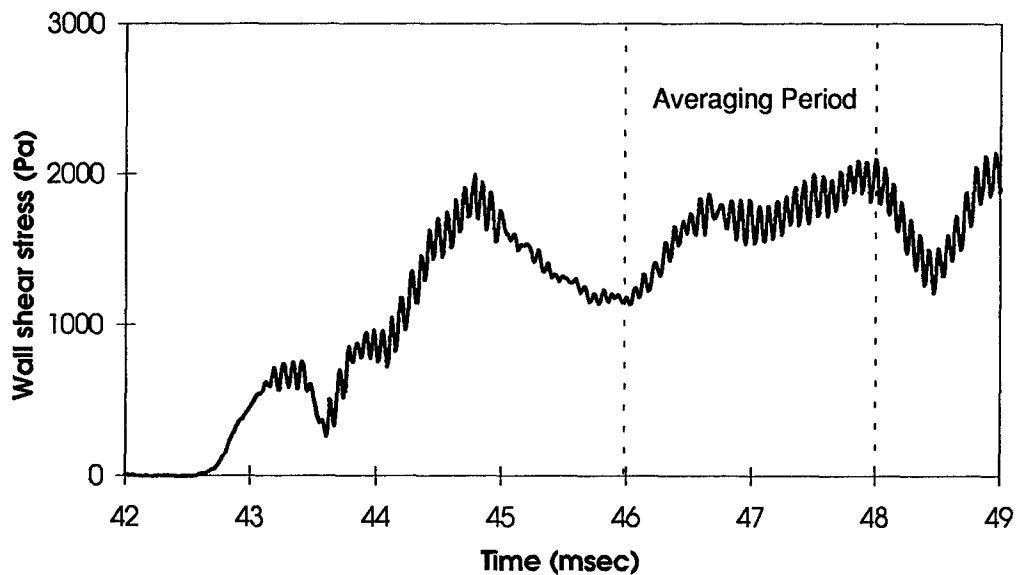


Figure 5-11 NASA Ames Run 2061 Combustor Wall Shear Stress

is somewhat higher.

In Figure 5-13, two combustor traces are shown for Run 2082. This is a very interesting run because two different types of gauges were used, one an AFIT baseline gauge and the other a Virginia Tech 14 kHz gauge. Both gauges gave reasonable responses during the averaging period with fairly close results. The shear stress in this loca-

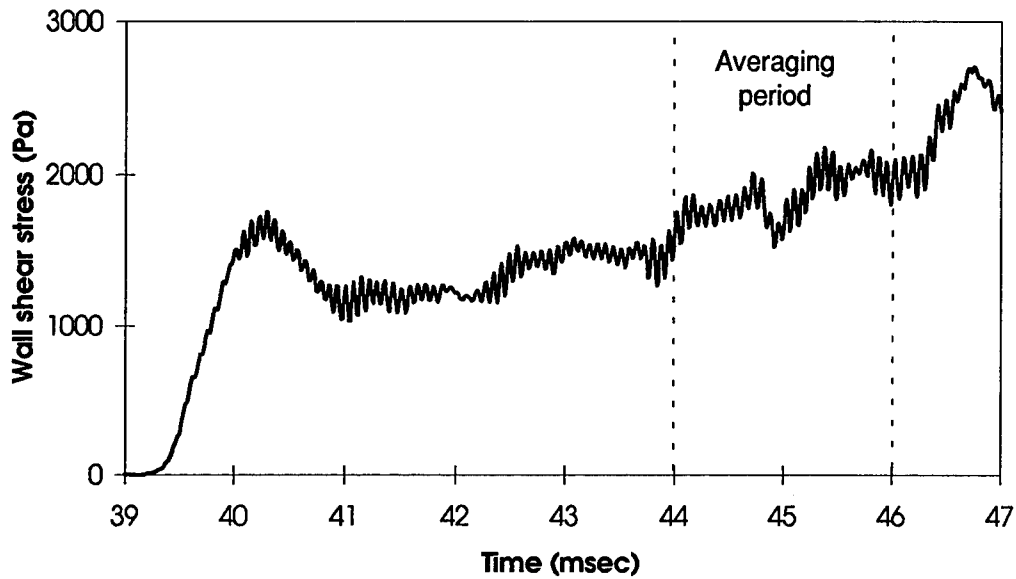


Figure 5-12 NASA Ames Run 2062 Combustor Wall Shear Stress

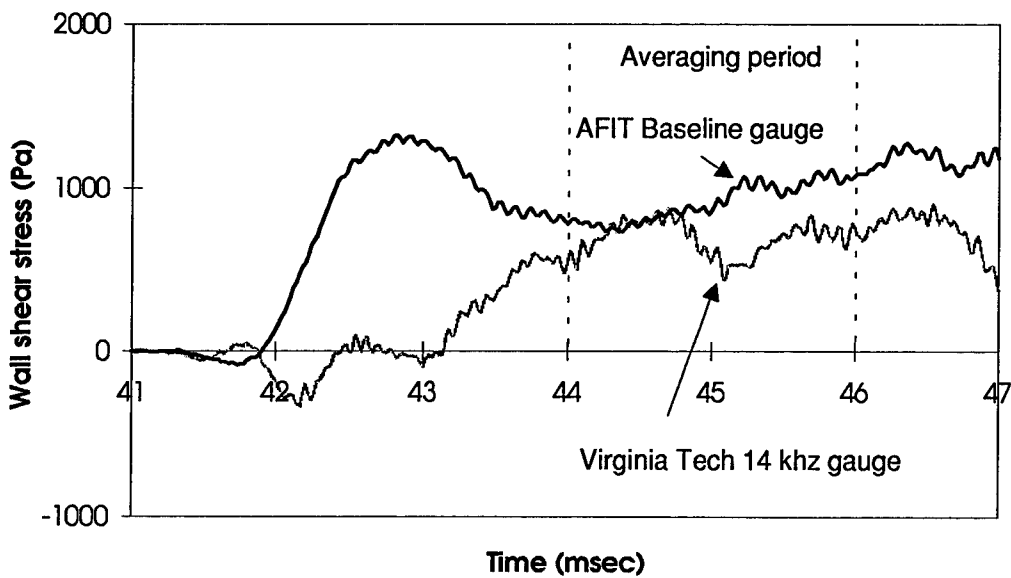


Figure 5-13 NASA Ames Run 2082 Combustor Wall Shear Stress

tion is not expected to be the same for both ports because one is closer to the wall. The flow patterns from the injectors also play a role in varying the measurements. Shown in Figure 5-14 are the combustor skin friction traces from Run 2089. Both of the gauges for this run were AFIT baseline gauges. The traces show a similar effect at the beginning as appeared in the previous run; the second gauge response remains around zero for about 3 msec while the first gauge responds more quickly. Since these were different gauges, it appears to be a flow condition and not a problem with the gauges.

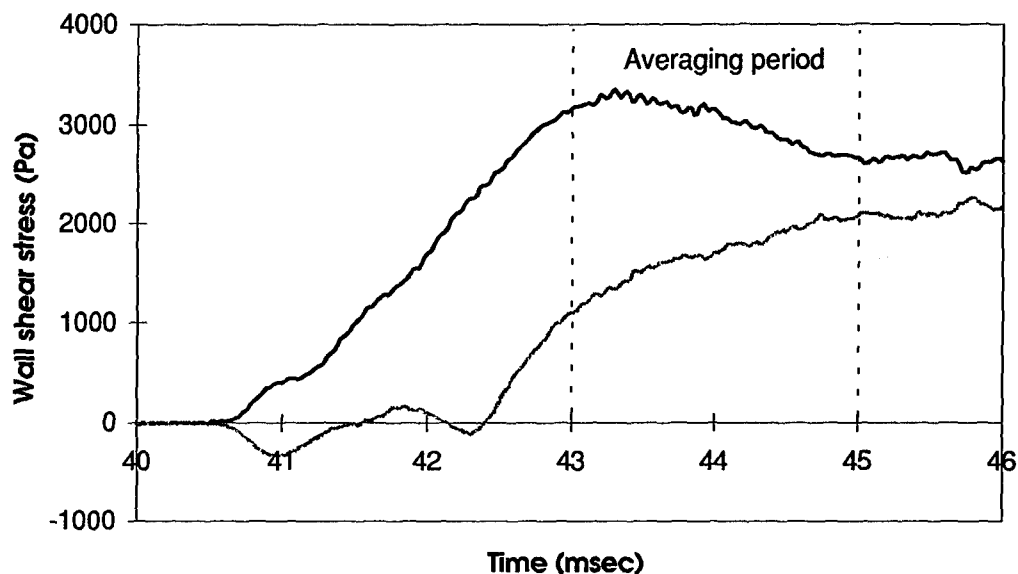


Figure 5-14 NASA Ames Run 2088 Combustor Wall Shear Stress

5.2. Wright Laboratory Mach 6 Tests

A gauge developed as part of this dissertation research was used to measure skin friction in a scramjet inlet test in the Wright Laboratory's Mach 6 blow-down wind tunnel. This test sequence was for the purpose of measuring heat transfer in a scramjet inlet configuration. However, one skin friction gauge port was made available. The number of test runs totaled 110, all with a skin friction gauge present.

The Mach 6 blow-down tunnel is a large free-jet facility operated at a stagnation temperature of 620K. The run is initiated with the model lowered out of the flow region. After flow is established in the nozzle (approximately 2 seconds), the model is raised (injected) into the free-jet test flow (Figure 5-15). Most of the runs lasted for 5 seconds, including the 2 second start time; however, a few of the runs were carried for 10 seconds.

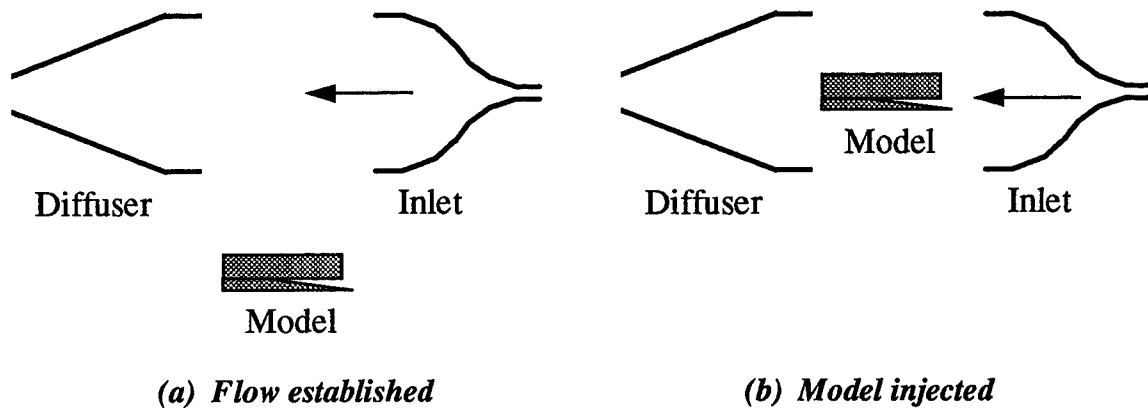


Figure 5-15 Mach 6 Wind Tunnel Model Injection

The model simulated part of a scramjet inlet, with the base simulating the side of the inlet and the sharp fin an adjustable cowl lip (Figure 5-16). The base measured 45.7 cm long by 30.5 cm wide. The front part of the base was at an angle of 5 degrees to the flow. The skin friction gauge was located 25.4 cm from the leading edge (25.5 cm if

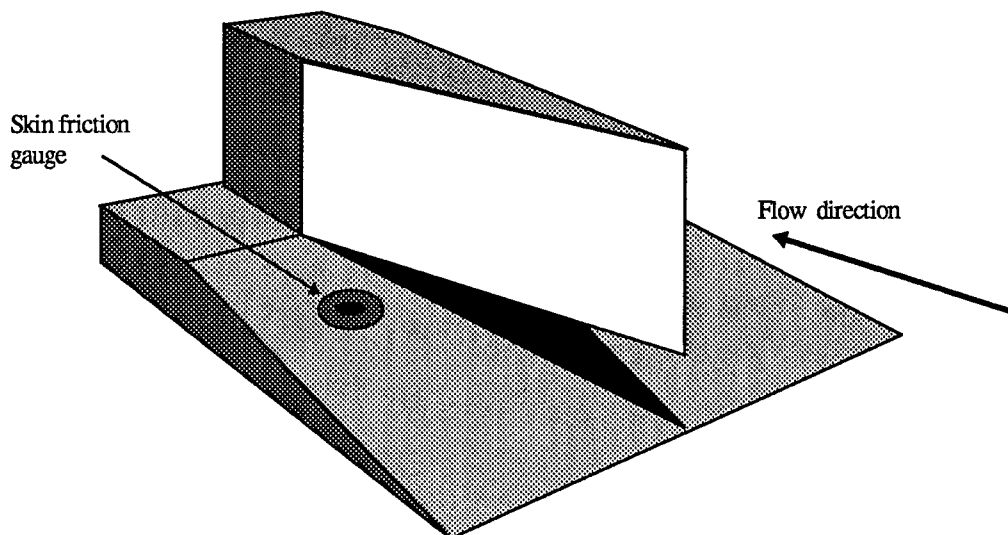


Figure 5-16 Wright Laboratory Mach 6 Inlet Model

measured along the surface). The skin friction gauge was offset 7.62 cm from the centerline. Two different configurations were used for the base, the first, a round leading edge and the second a sharp leading edge. The fin was 48.3 cm long and 10.2 cm high with a 5 degree nose angle. The fin was yawed to different angles and the gap height between the fin and the base was varied to measure heat transfer under different flow conditions.

Based on the dynamic pressure and the Van Driest II correlation, the expected skin friction for this test was somewhat lower than for the NASA Ames tests, so a nominal 100 Pa gauge was designed with natural frequency of 2.5 kHz. Due to the design of the test model, the gauge could not be removed from the model for re-oiling, so the re-oiling device discussed in Chapter 4 was developed to re-oil the gauge in the tunnel.

5.2.1. Skin Friction Correlations and Data Analysis

Several of the runs were flat plate runs, which allowed use of the Van Driest II theory to compare to the measured data. In addition, wall temperature and pressure measurements were taken at the location of the skin friction gauge, which allowed for further analysis of the flow field and comparison with the Reynolds analogy for skin friction prediction.

Coaxial thermocouples were mounted in multiple locations in the model. The one closest to the skin friction gauge (and in the same x-location) was used to compute the Reynolds analogy. The heat flux was first calculated from the measured temperatures using the Crank-Nicolson numerical method described in Appendix C. The freestream conditions over the surface of the plate were calculated using the measured pressure to compute the shock angle, and then applying oblique shock relations to the nozzle exit conditions which were calculated from measured stagnation conditions. The enthalpy conductance was then calculated from the heat flux, the measured wall conditions, and the calculated freestream conditions. The enthalpy conductance is given by (Kays & Crawford, 1980:304-305)

$$\dot{q}_w = g_h (h_w - h_{aw}) \quad (5-1)$$

where the adiabatic wall enthalpy is given by

$$h_{aw} = h_e + \frac{1}{2}rU_e^2 \quad (5-2)$$

and the flat plate recovery factor is given by $r = \sqrt[3]{Pr}$ for turbulent flow. The Stanton number then follows from the enthalpy conductance:

$$St = \frac{g_h}{\rho_e u_e} \quad (5-3)$$

and then the skin friction coefficient from the Reynolds analogy

$$St = 1.16 \frac{C_f}{2} \quad (5-4)$$

The Reynolds analogy was computed at each data point; so the result shows fluctuations as a result of the fluctuations in measured temperature.

The Van Driest calculation was implemented as described in Appendix B. The Van Driest correlation contains wall temperature as one of the variables, so the measured wall temperature was used, and the Van Driest correlation was calculated at each data point. As with the Reynolds analogy, the measured pressure was used to calculate the freestream conditions. The Van Driest correlation was also calculated using the adiabatic wall temperature condition by using the adiabatic wall enthalpy given in Eq (5-2).

5.2.2. Discussion of Results

Figure 5-17 shows the skin friction measurements and correlated data for Run 57, which was a flat plate run with the sharp nose. From Figure 5-17, it appears that the skin friction gauge is tracking more closely to the adiabatic wall temperature correlation than to the cold wall correlation or to the Reynolds analogy. This could be due to the plastic surface being hotter than the surrounding metal. The thermal analysis described in Section 4.1.1 was used to calculate the increase in temperature of the skin friction gauge. It was found that for this run, the gauge surface would have heated to approximately 471K by the end the test, compared to the measured 320K for the wall. However, this does not approach the adiabatic wall temperature of 560K. In addition, this can be considered a cold wall situation; consequently, the same scatter occurs among the various skin friction correlations as described in Section 5.1.2. For example, the Spalding and Chi correlation

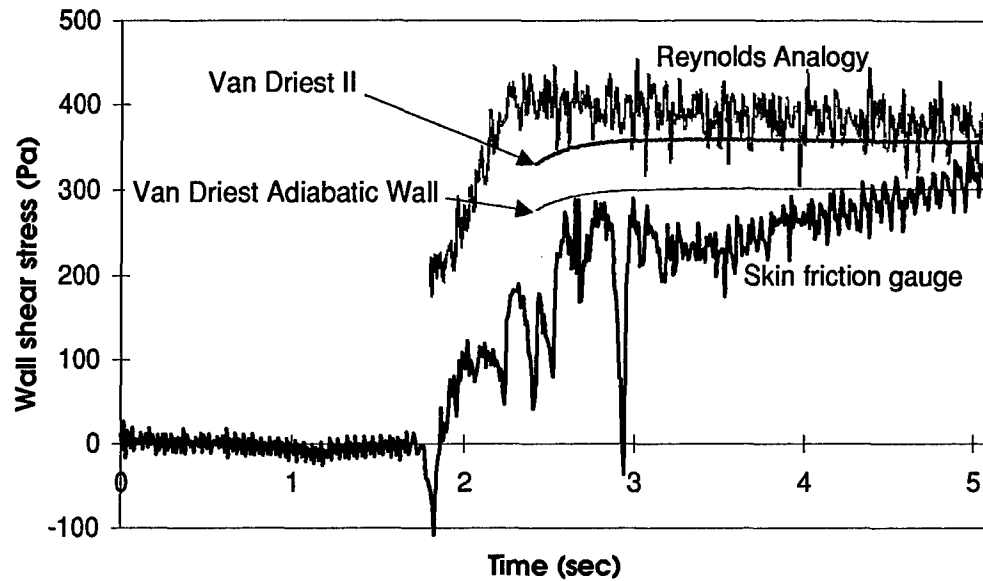


**Figure 5-17 Wright Laboratory Run 57 Wall Shear Stress
(Flat Plate, Sharp Nose, $p_t=11$ MPa)**

would predict a nominal steady state value of about 309 Pa, which is in good agreement with the averaged measured value of 291 Pa.

The Reynolds analogy also shows a great deal of scatter at higher Mach numbers. Above Mach 5, the Reynolds analogy factor has ranged from 0.8 to 1.4 (Cebeci and Bradshaw, 1988:349). The Reynolds analogy factor used in the calculation in Figure 5-17 was 1.16. For the skin friction measurement shown in Figure 5-17, the Reynolds analogy factor would be approximately 0.90, which is well within the range of the reported scatter.

Two other effects could cause the difference between the measured wall shear stress and the Reynolds analogy. First, the skin friction gauge was offset from the centerline of the plate by 7.62 cm. At this point, there could be a three-dimensional effect with a cross flow component present. Since the skin friction gauge is aligned with the longitudinal axis of the plate, the skin friction gauge would measure only the longitudinal component of the wall shear. Second, the skin friction gauge was outboard of the thermocouple. The turbulent transition point may vary across the width of the plate, so the wall shear stress may not be the same at the skin friction gauge as at the thermocouple.

As can be seen in Figure 5-17, the wall shear stress tends to increase throughout the run. The increase appeared at first to be a viscoelastic effect. However, the viscoelasticity analysis undertaken in Chapter 3 indicates that the increase should not be this great. The increase in wall shear stress could be a result of a shift in the turbulent transition point over time due to the wall heating.

Several other of the flat plate skin friction traces are shown in Figures 5-18 through 5-21. Three runs were conducted with the sharp-nosed flat plate; for these the Reynolds analogy and Van Driest correlations were calculated. Figure 5-18 shows the skin friction trace for Run 55, which was the first run conducted with the sharp leading edge. The gauge response was somewhat erratic for this run. The gauge had been oiled immediately prior to the run, so the erratic response may be due to the dynamic effects of initial oil loss. The small shock near the beginning of the run is due to the injection of the model, which disrupts the flow. This shock shows up on many of the runs, although not always so clearly.

For Run 56 (Figure 5-19), the gauge provided a fairly stable response. Again, as for Run 57, the measurement tracks more closely to the adiabatic wall prediction than to the Van Driest cold wall correlation.

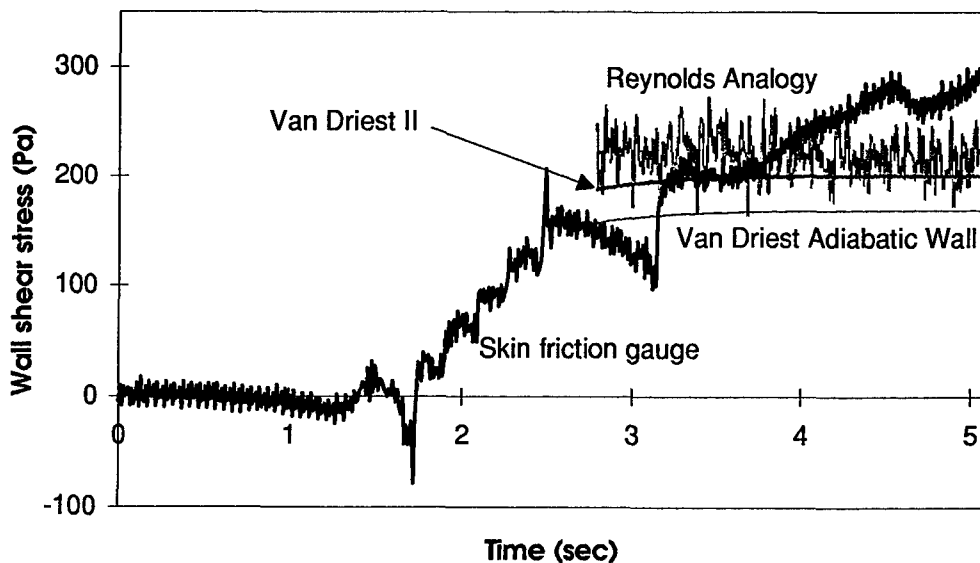


**Figure 5-18 Wright Laboratory Run 55 Wall Shear Stress
(Flat Plate, Sharp Nose, $p_t=5.5$ MPa)**

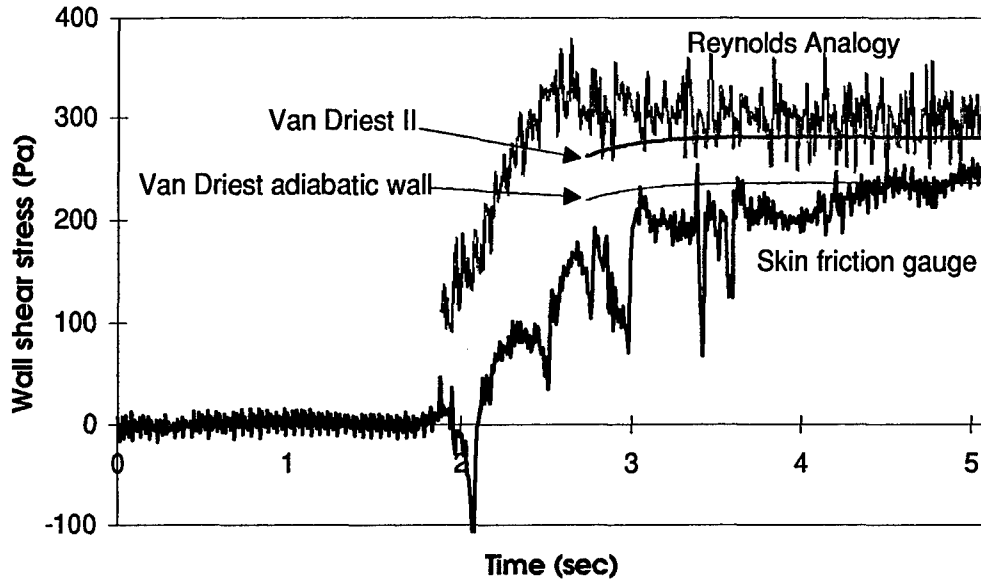


**Figure 5-19 Wright Laboratory Run 56 Wall Shear Stress
(Flat Plate, Sharp Nose, $p_t=8.3$ MPa)**

The next two runs shown were conducted with the blunt nose. For these runs, the wall shear stress was lower due to the delay of turbulent transition; the wall shear stress was either completely laminar or in the transition phase. Figure 5-20 shows the trace for

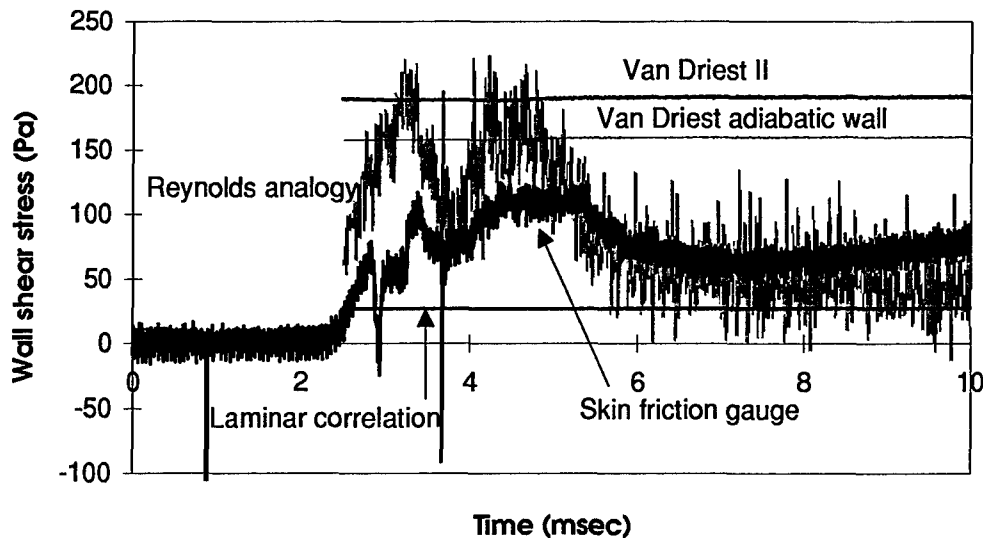


**Figure 5-20 Wright Laboratory Run 2 Wall Shear Stress
(Flat Plate, Blunt Nose, $p_t=5.5$ MPa)**

Run 2, which was conducted at a stagnation pressure of 5.5 MPa, the lowest pressure at the runs were conducted. At this condition, the skin friction appears to be representative of a completely laminar boundary layer. The laminar skin friction correlation shown was computed using Eckert's reference enthalpy method as described in Appendix C but with the laminar recovery factor $r = \sqrt{Pr}$. The Reynolds analogy also used $r = \sqrt{Pr}$ to compute the adiabatic wall enthalpy. For this run, the measured skin friction agreed closely with the Reynolds analogy.

Figure 5-21 shows the results from Run 19, another run with the blunt nose. The response for this run was very stable. This run was conducted at a higher stagnation pressure than most of the other runs, but even at this pressure, the wall shear stress is still somewhat lower than for the runs with the sharp nose. The Reynolds analogy is not shown for this run because the result appeared to be in the transition region between laminar and turbulent. Calculation of the Reynolds analogy requires determination of the adiabatic wall enthalpy, which in turn depends on the recovery factor. Since the recovery factor is different for laminar than for turbulent flow, the recovery factor for the transition region is not well defined. The trace for Run 19 appears a little different from the others because the wind tunnel data acquisition system for this run was set to store only 20 points

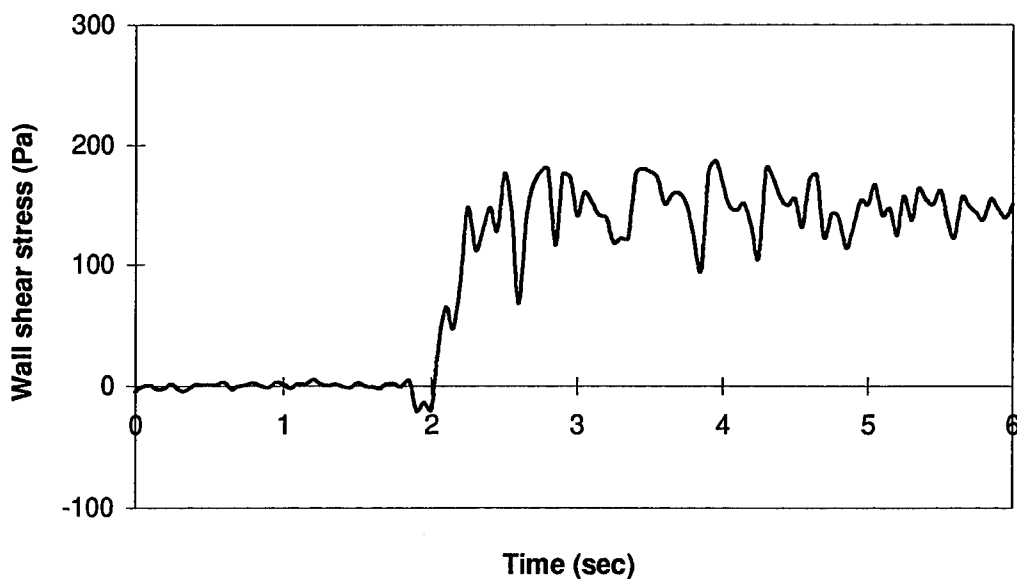


**Figure 5-21 Wright Laboratory Run 19 Wall Shear Stress
(Flat Plate, Blunt Nose, $p_t=13.8$ MPa)**

per second rather than 100 as for the other runs.

5.3.1. Re-Calibration and Pressure Test

After all runs were completed, the gauge was removed from the model and recalibrated. It was found that the calibration had not changed. In addition, the re-oiling device was used to test the pressure sensitivity of the gauge as described in Chapter 3. Again, there was no measurable pressure sensitivity. In fact, this was the only gauge tested that did not show some pressure sensitivity. This may be due to the fact that different strain gauges were used on this sensor than on the high frequency gauges. The strain gauges used with the Mach 6 sensors were provided by the same manufacturer, but the length was 6.35 mm instead of the 2.03 mm strain gauges normally used. This change was due to the manufacturer being unable to provide any of the shorter strain gauges at the time required; in addition, the longer sensor beam of the Mach 6 gauge could accommodate the longer strain gauge.

5.4. Hypulse Scramjet Combustor Tests

Skin friction gauges built as part of this research effort were used in a series of scramjet combustor tests at the General Applied Science Laboratories' Hypulse Test Facility (Figures 5-22 and 5-23). The tests were sponsored by NASA Langley Research Center.

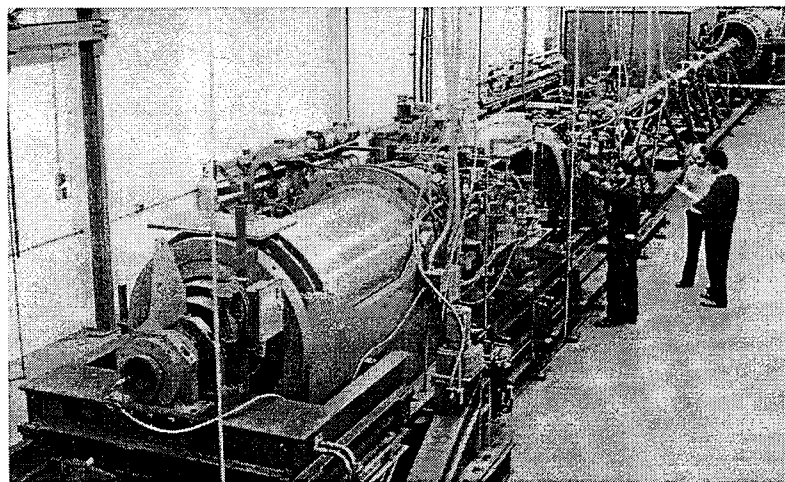


Figure 5-22 Hypulse Test Facility

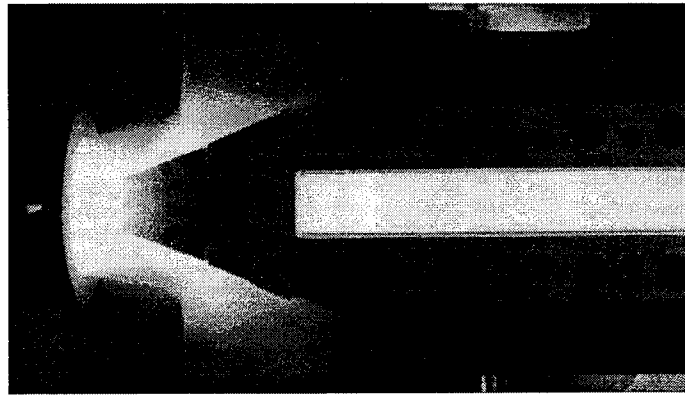


Figure 5-23 Hypulse Scramjet Combustor Model

5.4.1. Overview of the Tests

The Hypulse facility is a type of shock tube test facility known as an expansion tube. An expansion tube is similar to a conventional shock tunnel. However, instead of using a nozzle to achieve acceleration of the driven gas, the acceleration is achieved by expanding the driven gas in a constant diameter tube (Calleja and Tamagno, 1993). This is accomplished by separating the driven gas by a plastic diaphragm from a lower pressure "expansion gas." After the initial shock passes through the driven gas, rather than being reflected, the shock passes breaks the second diaphragm and passes on through the expansion gas (Figure 5-24). Since the expansion gas is initially at a lower pressure than the driven gas (and often a different composition), the expansion gas remains at lower pressure after the shock passes through. This lower pressure results in the driver gas expanding and accelerating. The pressures and the composition of the expansion gas are adjusted to achieve a desired acceleration. At the end of the expansion tube, the gases pass into a test cabin where the test model is mounted.

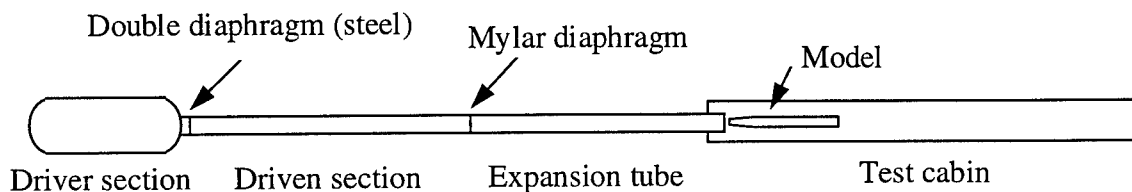


Figure 5-24 Expansion Tube

Because the initial shock is not reflected but passes straight through into the expansion gas, the test times in the Hypulse facility are very short, on the order of 0.4 msec. In addition, since a reflected shock is not used, the initial shock must be strong enough to generate the high enthalpy desired for the test. This requires very high driver pressures, on the order of 400 MPa. The driver gas for the Hypulse facility is helium and the driven gas air. The composition of the driven gas varies depending on the desired test condition, but for the tests using the AFIT skin friction gauges, the expansion gas was pure nitrogen. The tests were conducted at Mach 14 enthalpies.

The Hypulse tests supported by the AFIT gauges were conducted in late 1995. Two gauges were supplied by AFIT as part of the present research effort. The first was a baseline gauge and the second was an I-beam gauge. Virginia Tech also supplied skin friction gauges (Novean, Schetz, and Bowersox, 1996:75-81). Five skin friction gauge ports were available in the model (Figure 5-25). The skin friction gauges were powered by Measurements Group 2310 signal conditioning amplifiers.

5.3.2. Oil Problem

A particularly challenging aspect of the GASL test was that the gauges were mounted in the roof of the combustor model in an inverted position. The inverted position poses a problem because the oil tends to drain out. However, by applying the repeated application of vacuum method discussed in Chapter 4, and also by using a high viscosity oil (10,000 cSt), the gauges retained enough oil to function.

The oil problem was not completely solved, because the test cabin was evacuated

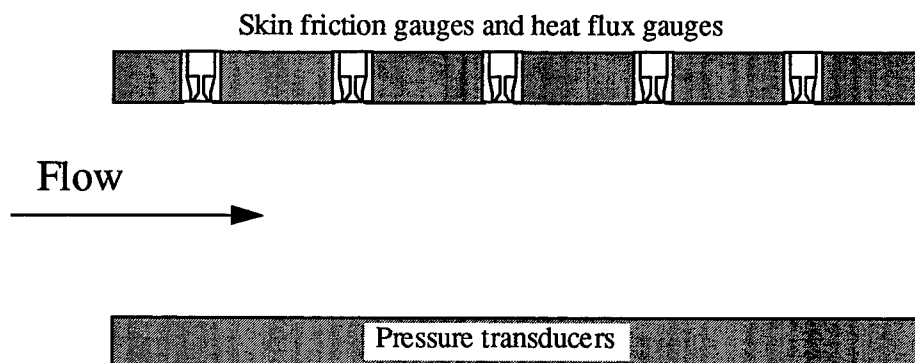


Figure 5-25 Hypulse Skin Friction Gauge Locations

to a lower pressure prior to the run than the vacuum chamber was able to attain. This resulted in some oil dripping out during the evacuation. The functioning of the gauges was not affected by this loss, possibly because of the short run time, but concerns over possible fouling of the pressure transducers, which were located on the floor of the model, led to the oil filled gauges being limited to the aft two pressure ports, where damage from oil fouling would be minimized.

5.3.3. Results

Several good skin friction traces were obtained by both AFIT gauges in the Hypulse tests. In the first run in which these gauges were used (Run 37), the baseline gauge was not adequately tightened down and was blown out of the model during the run, but appeared to provide a reasonable response until then (Figure 5-26). As can be seen, the trace approaches a stable point of about 8.2 kPa during the first part of the averaging period. Then, prior to the arrival of the shock, the measurement begins to oscillate wildly. This appears to the point at which the gauge was blown out of the model. The baseline gauge was located in the fourth port, which is the next to last.

The I-beam gauge appears to have provided a reasonable response for Run 37

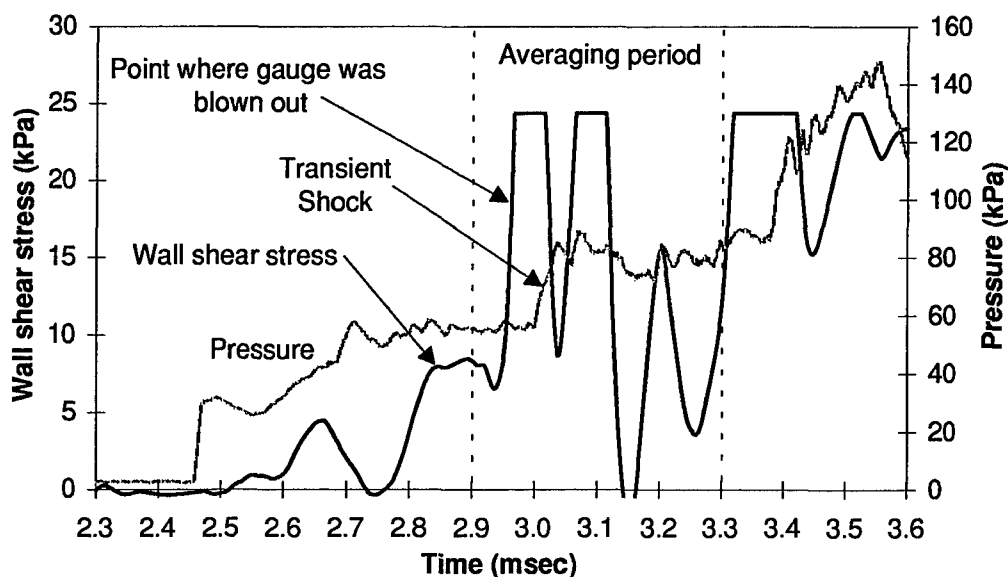


Figure 5-26 GASL Run A37 Skin Friction and Pressure Traces, Port #4 (AFIT Baseline Gauge)

(Figure 5-27); however, the magnitude of the wall shear stress is somewhat higher than expected. The response reaches a stable point of approximately 13.6 kPa before the transient shock causes a spike in the output. However, the response quickly returns to approximately the same stable point. After the steady flow period, another pressure jump causes the response to oscillate again. The I-beam gauge was located in the fifth port which is the farthest aft. Although the wall shear stress for this gauge is high, the shear stress for this run was also high for the baseline gauge. The I-beam gauge recorded a higher skin friction than the baseline gauge, but the combustor model has a constant cross-sectional area, so the pressure of the air increases as it travels through the combustor. Thus, the pressure is higher at the number 5 port (66.7 kPa versus 55.3 kPa), so this accounts for some of the increase in wall shear stress.

The jumps in the the skin friction trace which are attributed to the pressure effects actually occur prior to the pressure effect being recorded by the pressure transducer. This can be due to three effects. First, the shock is probably not one-dimensional but may be slanted across the combustor. The shock could therefore strike the skin friction gauges on the upper surface prior to corresponding pressure transducer on the lower surface. Second, the pressure transducers are not precisely collocated axially with the skin friction

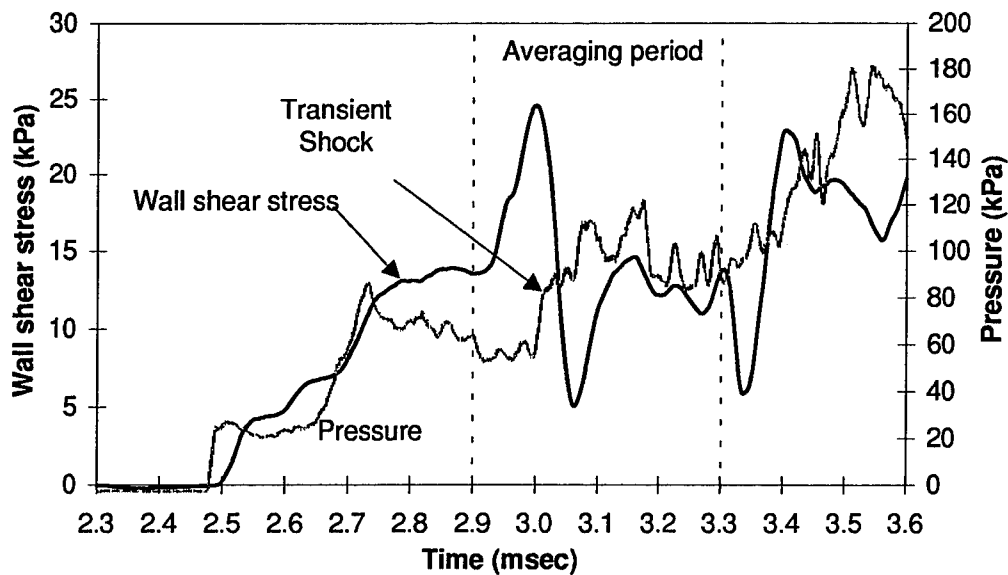


Figure 5-27 GASL Run A37 Skin Friction and Pressure Traces, Port #5 (AFIT I-Beam Gauge)

gauge. Third, as noted in Chapter 3, the gauge responds to a transient shock when the shock strikes the oil, while a pressure transducer may take longer to respond. The skin friction gauge head is also somewhat larger than the pressure transducer, so even if the two were precisely collocated axially and the shock were one-dimensional, the skin friction gauge would still be affected by the shock before the pressure transducer.

The I-beam gauge also provided a good response in Run A38 (Figure 5-28), with the magnitude this time being closer to what would be expected. The wall shear trace reaches a stable point this time of approximately 4.04 kPa, before again being deflected by a transient shock. However, the response again returns very quickly to the stable point. The static pressure was somewhat lower for this run than for the previous run (43.5 kPa versus 66.7 kPa). In addition Run 37 used air as the test gas, while Run 38 used nitrogen. Since oxygen dissociates and ionizes at lower temperatures than does nitrogen (see Figure 2-2), the real gas effects would be much greater for Run 37 than for Run 38. This could also account for part of the difference in the measured wall shear stress between the two runs.

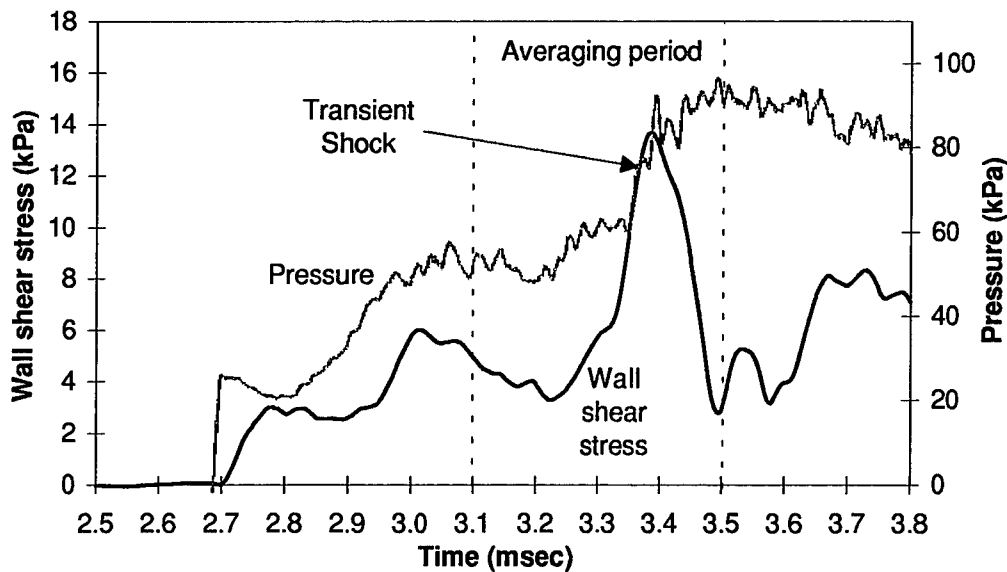


Figure 5-28 GASL Run A38 Skin Friction and Pressure Traces, Port #5 (AFIT I-Beam Gauge)

VI. Shock Tunnel Characterization

This chapter presents the theoretical and experimental characterization of the AFIT high pressure shock tunnel. The theoretical characterization uses inviscid one-dimensional flow theory to predict the performance of the shock tunnel. The actual performance differs somewhat due to viscous and three-dimensional effects, but the theoretical characterization is important in understanding the flow phenomena in the shock tunnel, as well in improving the performance of the shock tunnel. The theoretical characterization also formed the basis of the data reduction program which was developed to compute freestream and stagnation properties from the measured pressures.

6.1. Theoretical Characterization

A shock tunnel consists of a shock tube with a nozzle attached (Figure 6-1). Shock tubes have been fairly well characterized, and most gas dynamics textbooks discuss the basic calculations for shock tubes. However, closed-form solutions are only possible if perfect gas assumptions are made. Since the operation of the AFIT shock tunnel involves high temperatures and real gas effects, a numerical procedure must be employed. However, the perfect gas calculations can be used as the initial guess for the iteration procedure.

6.1.1. Shock Tunnel Description

A shock tube is made up of a driver section with high pressure gas and a driven section with lower pressure gas. The two sections are initially separated by a diaphragm

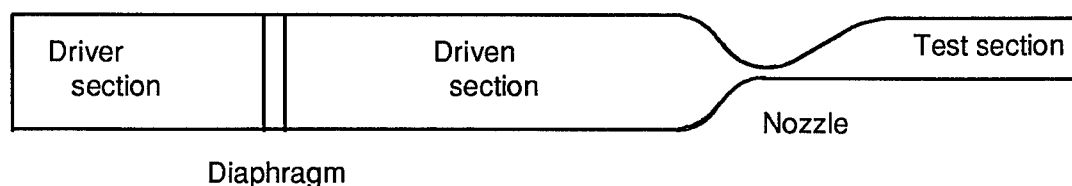


Figure 6-1 AFIT High-Pressure Shock Tunnel

(Figure 6-2). The diaphragm is then caused to rupture, and the high pressure gas expands into the low pressure section. This sudden expansion of the high pressure gas causes a shock wave to travel through the low pressure section (Figure 6-3). This shock wave sets the low pressure gas into motion and increases the pressure. Behind the shock wave, the pressure of the driven gas is equal to the pressure of the expanding driver gas. This sudden increase in pressure without a corresponding increase in density causes a temperature rise in the driven gas behind the shock. The high pressure driver section is set into motion by an expansion wave. The four regions in the shock tube at this stage can be characterized as follows:

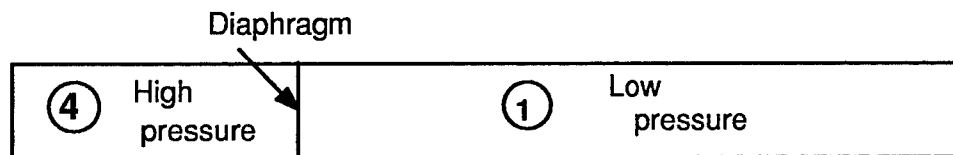


Figure 0-2 Shock Tube Before Diaphragm Rupture

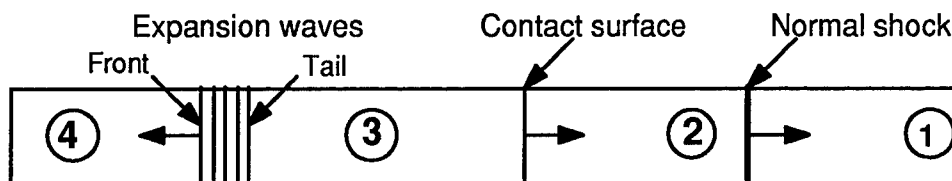


Figure 6-3 Shock Tube After Diaphragm Rupture

Region 1. Low temperature, low pressure gas from the driven section which has not yet been set into motion by the moving shock.

Region 2. High temperature, high pressure, low density gas from the driven section which has been set into motion by the shock. The velocity of the gas is to the right. The velocity and pressure in region 2 are equal to the velocity and pressure of region 3 but a temperature discontinuity exists between regions 2 and 3. This discontinuity is called the "contact surface," which is where the expanding driver gas (region 3) contacts the high temperature driven gas. The conditions in region 2 (velocity, temperature, and pressure) are constant until the shock is reflected from the end of the shock tube.

Region 3. Expanding high pressure, low temperature driver gas. The velocity of the gas is to the right. Because the gas in region 3 has expanded, the pressure is lower than the initial pressure in the driver section. Region 3 is separated from region 4 by an unsteady expansion wave. The left edge (head) of the expansion wave travels to the left, while the right edge (tail) may travel right or left, depending on conditions, but the head and tail of the expansion waves separate. The conditions in region 3 are constant until the expansion wave is reflected from the left end of the shock tube.

Region 4. High pressure, low temperature, driver gas which has not yet been set into motion by the moving shock.

The shock is reflected from the right end of the shock tube and travels to the left (Figure 6-4). The effect of the reflected shock is to cause a further increase in temperature and pressure in the gas behind (to the right of) the reflected shock. The high temperature, high pressure gas behind the reflected shock is initially left motionless by the reflected shock. In a shock tunnel operating in reflected mode, it is this gas which is exhausted through the nozzle to form a high enthalpy flow. The conditions in this region (Region 5) are steady until the reflected shock is reflected by the contact surface.

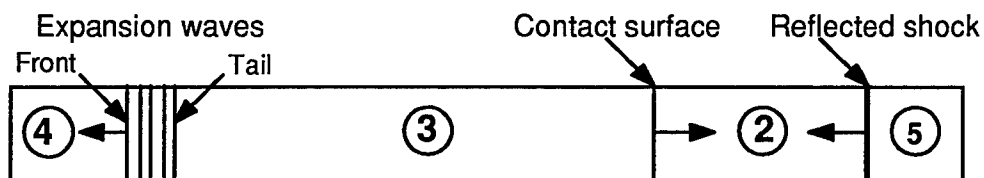


Figure 6-4 Shock Tube with Reflected Shock

6.1.2. Shock Tunnel Calculations

The shock tunnel calculations will be broken up to consider first the initial shock, or incident shock, which can be calculated knowing only the initial conditions of the driver and driven gases. Next, the reflected shock and converging nozzle will be considered together, because the strength of the reflected shock depends on the geometry of the converging part of the nozzle. Then, the steady flow period, which depends on the strength

of the two shocks, will be evaluated. Then the diverging part of the nozzle and the test section calculations will be developed.

6.1.2.1. Incident Shock

The incident shock characteristics depend only on the initial conditions of the driver and driven gases. Because of the high temperatures in the driven gas, the perfect gas assumptions are not valid but can be used to provide an initial guess for the high temperature iterative procedure. The helium, however, is not subjected to heating, so perfect gas relations can be used.

For an inviscid gas in one dimensional steady flow (with no cross-sectional area change) the equations of motion reduce to the following (Anderson, 1989:507):

$$\text{Continuity} \quad \rho_u u_u = \rho_d u_d \quad (6-1)$$

$$\text{Momentum} \quad p_u + \rho_u u_u^2 = p_d + \rho_d u_d^2 \quad (6-2)$$

$$\text{Energy} \quad h_u + \frac{u_u^2}{2} = h_d + \frac{u_d^2}{2} \quad (6-3)$$

The subscripts u and d represent the upstream and downstream conditions relative to the shock. Although the shocks in a shock tunnel are moving, and hence unsteady, the steady flow equations can be applied by considering the shock to be fixed in space, and adjusting the gas velocities by adding or subtracting the shock velocity as appropriate. For a shock moving with velocity u_s into a stagnant gas, the relations become (Figure 6-5):

$$\text{Continuity} \quad \rho_1 u_s = \rho_2 (u_s - u_2) \quad (6-1a)$$

$$\text{Momentum} \quad p_1 + \rho_1 u_s^2 = p_2 + \rho_2 (u_s - u_2)^2 \quad (6-2a)$$

$$\text{Energy} \quad h_1 + \frac{u_s^2}{2} = h_2 + \frac{(u_s - u_2)^2}{2} \quad (6-3a)$$

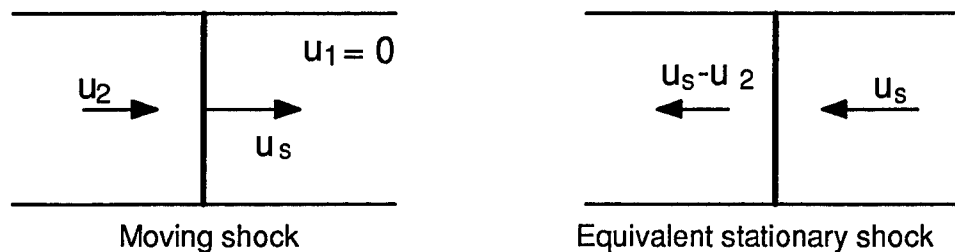


Figure 6-5 Moving Shock and Equivalent Stationary Shock

The above equations contain five unknowns. The system is resolved by using a thermodynamic relation $h=h(p,\rho)$ and the following perfect gas equation for the helium:

$$u_3 = \frac{2a_4}{\gamma_4 - 1} \left[1 - \left(\frac{p_3}{p_4} \right)^{(\gamma_4 - 1)/2\gamma_4} \right] \quad (6-4)$$

At the contact surface, $p_2=p_3$ and $u_2=u_3$. For high temperature calculations, an iterative process was implemented to solve the system of equations and to provide the conditions behind the incident shock. An equilibrium thermochemistry polynomial curve fit (Tannehill and Mugge, 1974) was used to provide $h=h(p,\rho)$. The iterative procedure required an initial guess for p_2 which is given by the perfect gas relation (Anderson, 1990:237):

$$\frac{p_4}{p_1} = \frac{p_2}{p_1} \left\{ 1 - \frac{(\gamma_4 - 1)(a_1 / a_4)(p_2 / p_1 - 1)}{\sqrt{2\gamma_1[2\gamma_1 + (\gamma_1 + 1)(p_2 / p_1 - 1)]}} \right\}^{-2\gamma_4/(\gamma_4 - 1)} \quad (6-5)$$

Since p_4 and p_1 are known, p_2 must be calculated iteratively. Alternatively, p_2/p_1 can be specified and p_4/p_1 calculated directly.

Although it is not readily apparent from Eq (6-20), for a given ratio of p_4/p_1 , the shock strength p_2/p_1 can be increased by decreasing the ratio a_1/a_4 . This can be accomplished by using a light gas such as helium in the driver section (Region 4). However, for given a_1 , a_2 , γ_1 , and γ_2 , there is a maximum value of p_2/p_1 that causes the quantity in the brackets to go to zero. The ratio p_4/p_1 can be increased without bound, but p_2/p_1 asymptotically approaches this maximum value.

To facilitate the iterative procedure Eq (3-1a) is substituted into (3-2a) to eliminate ρ_2 . The following form of the momentum equation results:

$$u_s = \frac{p_2 - p_1}{\rho_1 u_2} \quad (6-6)$$

The result is a system of five equations with five unknowns which can be solved using an iterative process as described in Appendix D.

6.1.2.2. Reflected Shock and Nozzle

The reflected shock is calculated in a similar manner to the initial shock. The equations of motion are

$$\text{Continuity} \quad \rho_5(u_{sr} + u_5) = \rho_2(u_{sr} + u_2) \quad (6-1b)$$

$$\text{Momentum} \quad p_5 + \rho_5(u_{sr} + u_5)^2 = p_2 + \rho_2(u_{sr} + u_2)^2 \quad (6-2b)$$

$$\text{Energy} \quad h_5 + \frac{(u_{sr} + u_5)^2}{2} = h_2 + \frac{(u_{sr} + u_2)^2}{2} \quad (6-3b)$$

where u_{sr} is the speed of the reflected shock and u_5 is the speed of the air behind the reflected shock. In a shock tube (with the end closed), u_5 is zero, but in a shock tunnel, an induced flow into the nozzle weakens the shock (Nagamatsu, 1961b:97). With the relation $h=h(p,\rho)$, the result is four equations with five unknowns. To solve the system requires bring in the conditions for the converging part of the nozzle.

The flow through the nozzle will be considered a quasi-one-dimensional flow. For steady flow, the continuity equation is then (Anderson, 1990:148)

$$\rho u A = \text{constan t} \quad (6-7)$$

$$h + \frac{u^2}{2} = h_t = \text{constan t} \quad (6-3c)$$

The steady nozzle flow is isentropic. For high temperature flows in chemical equilibrium, the assumption of sonic flow at the nozzle throat remains valid (Anderson, 1989:522). Instead of the perfect gas relations, polynomial curve fits for high temperature air in chemical equilibrium will be used (Tannehill and Mugge, 1974). The polynomial curve fits used for this calculation can be summarized as $h=h(p,\rho)$, $\rho=\rho(p,s)$, and $a=a(p,s)$. When the nozzle equations are combined with the region 5 equations, a system of 12 equations and 12 unknowns results which is solved iteratively as described in Appendix D. The iterative procedure involves guessing u_5 , calculating the region 5 conditions, and then calculating the throat conditions. If the throat conditions do not result in the correct throat area, then a new value of u_5 is guessed. Implementing this iterative scheme also requires guessing u_{sr} and p_{th} . Several perfect gas relations are used to provide initial guesses.

Since the strongest reflected shock is obtained with $u_5 = 0$, this case will first be considered as the limiting case for the shock tunnel. Substituting the perfect gas relation $p = \rho RT$ into both sides of Eq (6-2b) to eliminate p and then substituting Eq (6-1b) to eliminate ρ_5 , the following relation is obtained

$$(R_1 T_2 + u_2^2)u_{sr} + u_2 u_{sr}^2 = R_1 T_5 (u_{sr} + u_2) \quad (6-8)$$

Letting $h = c_p T$ in the energy equation, substituting into Eq (6-8), and rearranging results in

$$u_2 u_{sr} + u_{sr}^2 = R_1 T_2 + \frac{R_1}{c_{p1}} \left(\frac{1}{2} u_2^2 + \frac{3}{2} u_2 u_{sr} + u_{sr}^2 \right) \quad (6-9)$$

Then using the perfect gas relations $RT = a^2/\gamma$ and $R/c_p = (\gamma-1)/\gamma$, rearranging, and solving for u_{sr} using the quadratic equation results in the following relation:

$$u_{sr} = \frac{1}{4} \left[\sqrt{(\gamma_1 + 1)^2 u_2^2 + 16a_2^2} - (3 - \gamma_1)u_2 \right] \quad (6-10)$$

The iterative solution also requires a guess for the throat pressure for given region 5 conditions. This guess can be generated from the perfect gas equation (Anderson, 1989:155):

$$\left(\frac{A}{A^*} \right)^2 = \frac{1}{M^2} \left[\frac{2}{\gamma + 1} \left(1 + \frac{\gamma - 1}{2} M^2 \right) \right]^{(\gamma + 1)/(\gamma - 1)} \quad (6-11)$$

along with equation (Anderson, 1989:155):

$$\frac{p_t}{p} = \left(1 + \frac{\gamma - 1}{2} M^2 \right)^{\gamma/(\gamma - 1)} \quad (6-12)$$

6.1.2.3. Diverging Nozzle

Once the throat conditions are known, the diverging part of the nozzle may be calculated. This calculation uses Eqs (6-7) and (6-3c) along with the constant entropy requirement and $\rho = \rho(p, s)$. An iterative procedure is then implemented as described in Appendix D to solve for the four unknowns, p_6 , ρ_6 , h_6 , and u_6 . An initial guess is required for p_6 , which can be generated by using the supersonic case for Eq (6-11) along with Eq (6-12). The nozzle exit temperature, which is important for determination of transport properties, can be calculated from a polynomial curve fit $T = T(p, \rho)$ (Tannehill and Mugge,

1974). The Mach number can be computed by calculating the speed of sound from and $a=a(p,s)$.

6.1.2.4. Test Section Stagnation Conditions

From the nozzle exit conditions, the stagnation properties can be calculated. Since the entropy s and total enthalpy h_t are known, the calculation makes use of the polynomial curve fits $h_t=h(p_t,r)$ and $\rho_t=\rho(p_t,s)$. The system consists of two equations with two unknowns, which are solved using the iterative procedure in Appendix D. The curve fit $T=T(p,\rho)$ then provides the stagnation temperature.

6.1.3. Steady Flow Time

The steady flow time is affected by two factors: the steady flow time in region 5 of the shock tube and the starting dynamics of the nozzle. Both of these will be examined.

The steady flow time in the shock tube begins when the incident shock is reflected from the nozzle entrance. When the reflected shock strikes the contact surface separating the hot air from the helium, the shock continues into the helium but a reflection back toward the nozzle also occurs. This second reflection can be either a shock wave or an expansion wave. The steady flow time in the shock tube ends when this second reflected shock wave or expansion wave arrives at the nozzle entrance. Determining the steady flow time in the shock tube thus requires calculating first the time for the reflected shock to reach the contact surface, and then the type and speed of the second reflection from the contact surface. The type of reflection is governed by a bifurcation point known as the tailored condition.

The steady flow time in the shock tunnel test section is shorter than that in the shock tube because of the starting dynamics. This will be examined in Section 6.1.3.3.

6.1.3.1. Time for Reflected Shock to Reach the Contact Surface

The time from when the shock is reflected to when the reflected shock intersects the contact surface can be computed from the shock speeds and gas velocities previously calculated (Figure 6-6).

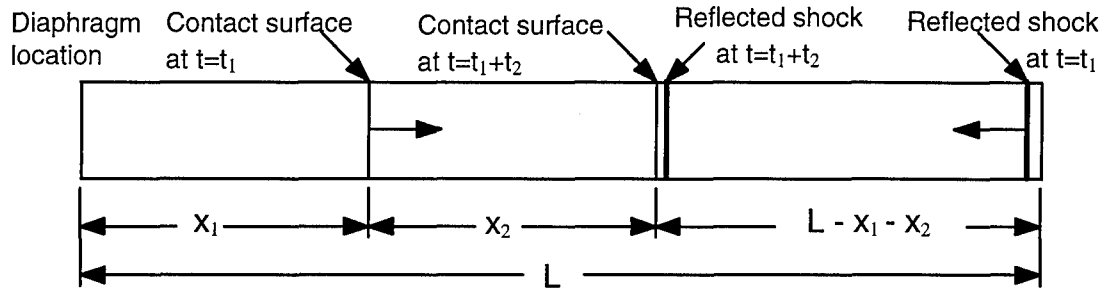


Figure 6-6 Duration of Steady Flow in Shock Tube

The time interval from the initial diaphragm rupture to the shock reaching the end of the shock tube will be denoted t_1 , while the time interval required for the reflected shock to reach the contact surface will be denoted t_2 . Then, since $u_s t_1 = L$ and $x_1 = u_2 t_1$,

$$x_1 = \frac{u_2 L}{u_s} \quad (6-13)$$

Since the reflected shock travels a distance $L - (x_1 + x_2)$ during time t_2 , $L - (x_1 + x_2) = u_{sr} t_2$. Substituting Eq (6-13) for x_1 and rearranging results in

$$t_2 = \frac{L - \left(\frac{u_2 L}{u_s} + x_2 \right)}{u_{sr}} \quad (6-14)$$

Further,

$$x_2 = u_2 t_2 \quad (6-15)$$

Equations (6-14) and (6-15) can be combined to eliminate t_2 with the result

$$x_2 = \frac{u_2 L \left(1 - \frac{u_2}{u_s} \right)}{u_{sr} + u_2} \quad (6-16)$$

Substituting this result into Eq (6-14) results in

$$t_2 = \frac{L \left(1 - \frac{u_2}{u_s} \right)}{u_{sr} + u_2} \quad (6-17)$$

The time t_2 is the first part of the steady flow time. As can be seen from Eq (6-17), the steady flow time can be increased by increasing L .

6.1.3.2. Tailored Condition and Type and Speed of Second Reflection

When the reflected shock strikes the contact surface separating the hot air from the helium, the shock continues into the helium but a reflection back toward the nozzle also occurs. Whether this second reflection is a shock or an expansion depends on the conditions in region 5 and region 3. The two phenomena are separated by a point at which neither a second reflected shock nor expansion wave occurs. This point is called the tailored condition because it is the time at which the longest steady flow time is attained (Wittliff, Wilson, and Hertzberg, 1959). While the AFIT shock tunnel was not operated at the tailored condition, determining whether the region 5 pressure is above or below the tailored condition determines what type of second reflection from the contact surface occurs.

If the shock is reflected from the contact surface as a shock, then the situation shown in Figure 6-7 applies. The relevant equations of motion are, for the helium

$$\rho_3(u_{sH} + u_3) = \rho_7(u_{sH} + u_5) \quad (6-1d)$$

$$p_3 + \rho_3(u_{sH} + u_3)^2 = p_5 + \rho_7(u_{sH} + u_5)^2 \quad (6-2d)$$

$$\frac{\gamma_4}{\gamma_4 - 1} \left(\frac{p_3}{\rho_3} \right) + \frac{1}{2} (u_{sH} + u_3)^2 = \frac{\gamma_4}{\gamma_4 - 1} \left(\frac{p_5}{\rho_7} \right) + \frac{1}{2} (u_{sH} + u_5)^2 \quad (6-3d)$$

In Eqs (3-1f) - (3-3f), the substitutions $u_7=u_5$ and $p_7=p_5$ have been made. In addition, since the helium remains at low temperature, the perfect gas relation $h=(\gamma/\gamma-1)(p/\rho)$ (Anderson, 1990:57) has been used. Equations (3-1f) - (3-3f) constitute a system of three

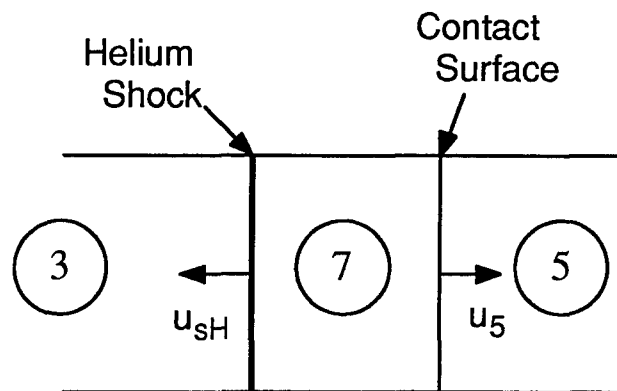


Figure 6-7 Tailored Interface

equations with three unknowns (p_5 , ρ_7 , u_{sH}) which can be solved using the iterative technique shown in Appendix D. In this procedure, the u_5 calculated from the shock tunnel equations is used to calculate the required p_{5t} for the tailored condition. Comparing p_{5t} to the p_5 calculated from the shock tunnel equations then determines whether the shock is reflected as a shock or an expansion:

$p_5 < p_{5t}$	Shock is reflected as shock
$p_5 = p_{5t}$	Shock is not reflected
$p_5 > p_{5t}$	Shock is reflected as expansion wave

If the shock is reflected as an expansion, then speed of the expansion wave is $u_{er} = u_5 + a_5$, since an expansion wave travels at the speed of sound relative to the medium. If the shock is reflected as a shock, then equations of motion for the passing through the air must be included (Figure 6-8). The resulting system of seven equations and seven unknowns and the solution procedure is shown in Appendix D.

The distance traveled by this second reflection is given by Eq (6-14). Denoting the speed of the second reflection as u_{2r} , where the reflection can be either a shock or expansion, the time for the second reflection to reach the nozzle entrance is given by

$$t_3 = \frac{L - (x_1 + x_2)}{u_{2r}} = \frac{u_{sr} t_2}{u_{2r}} \quad (6-19)$$

The total steady flow time of the shock tube is then

$$t_{st} = t_2 + t_3 \quad (6-20)$$

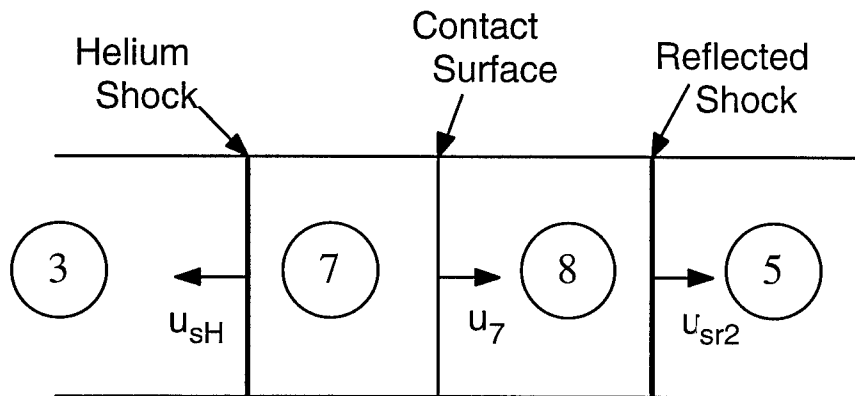


Figure 6-8 Second Reflected Shock

6.1.3.3. Test Section Starting Dynamics

The shock tunnel nozzle can be considered as a second shock tube. The driven section of the shock tube is now the driver for the nozzle. As the high pressure test gas expands into the nozzle, a shock passes through the stagnant air in the nozzle ahead of the expanding test gas. The only difference between this situation and the shock tube is that the area is variable in the nozzle.

With low backpressure, the starting dynamics as shown in Figure 6-9 apply. As described by Alpher and White (1958), the flow through a converging-diverging nozzle in a shock tube consists of the following:

Region 5. High temperature, high pressure, low density, stagnant gas behind the reflected shock.

Region 6. Steady nozzle flow of the test gas.

Region 9. Steady flow of test gas separated from region 6 (the nozzle exit) by an unsteady expansion. In effect, this means that the test gas undergoes further expansion after leaving the nozzle and will flow at a higher velocity (and Mach number) than the nozzle area ratio would cause. The expansion moves to the right.

Region 10. High temperature, high pressure, low density gas (room air, for the proposed research) which has been set into motion by the leading shock. The velocity of the gas is to the right. The velocity and pressure in region 10 are equal to the velocity and pressure of region 9 but a temperature discontinuity (contact surface) exists between re-

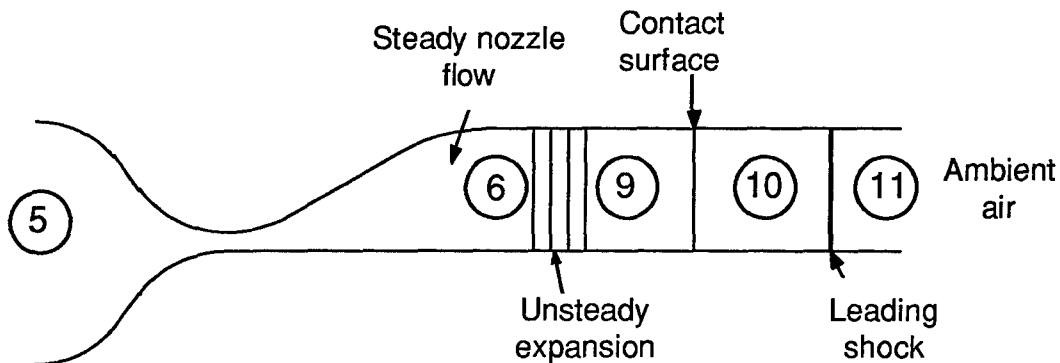


Figure 6-9 Shock Tunnel Nozzle with Low Backpressure

gions 9 and 10. This contact surface is where the expanding test gas (region 7) contacts the high temperature room air. The conditions in region 8 (velocity, temperature, and pressure) are constant.

Region 11. Low temperature, low pressure gas (room air) which has not yet been set into motion by the moving leading shock.

The expansion at the nozzle exit can not exist in the presence of a moderate back pressure. The reason is that if the back pressure is high enough, the pressure ratio for the leading shock is insufficient to result in a gas velocity behind the shock to match the velocity coming out of the nozzle. The mechanism to account for the nozzle exit conditions is to separate region 6 from region 9 by a rightward moving trailing shock as shown in Figure 6-10 (C.E. Smith, 1965). Although the shock moves to the right, it moves at a lower velocity than the test gas. The shock does not move into the test gas; rather, the test gas moves into the shock. The test gas to the right of the shock is thus at a higher pressure and lower velocity than the gas exiting the nozzle. This provides a high enough p_{11} for the leading shock to induce a velocity in the quiescent room air to match the velocity of the contact surface.

For the double shock system, the normal shock equations must be written for both shocks. The contact surface conditions $u_9 = u_{10}$ and $p_9 = p_{10}$ apply. The resulting system of 8 equations and 8 unknowns is shown in Appendix D along with the solution procedure.

The velocity of the trailing shock is then used to calculate the decrease in steady

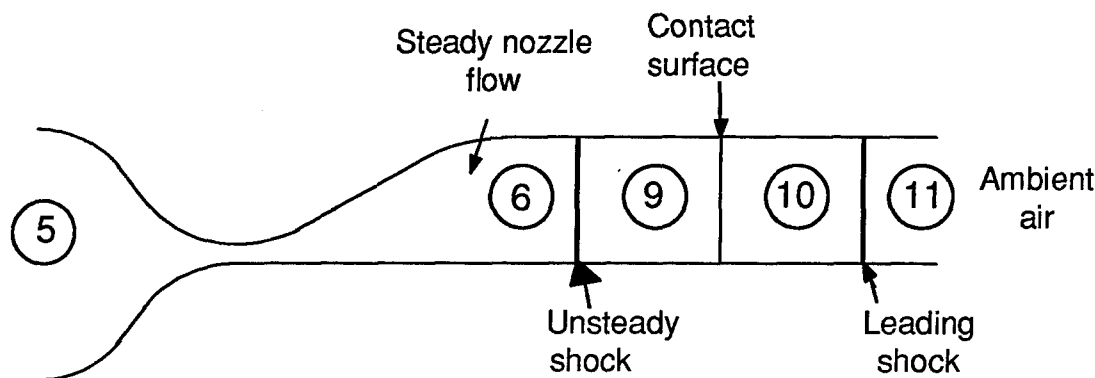


Figure 6-10 Shock Tunnel Underexpanded Nozzle with Moderately High Backpressure

flow time which occurs because of the nozzle starting dynamics. The steady flow time calculated for the shock tube represents the amount of time that the steady flow of the test gas occurs in the nozzle. Because the trailing shock moves more slowly than the steady flow of the test gas, which occurs behind the trailing shock, the part of the test gas which has entered the shock by the time the test object is reached represents the decrease in the test time. This decrease can be calculated by

$$t_d = \frac{L_n}{u_g - u_{ST}} \quad (6-21)$$

Here, L_n represents the distance from the nozzle throat to the trailing edge of the test model (Figure 6-11). Equation (6-21) is an approximation because it contains the assumption that the difference between the gas velocity and the trailing shock is constant through the nozzle.

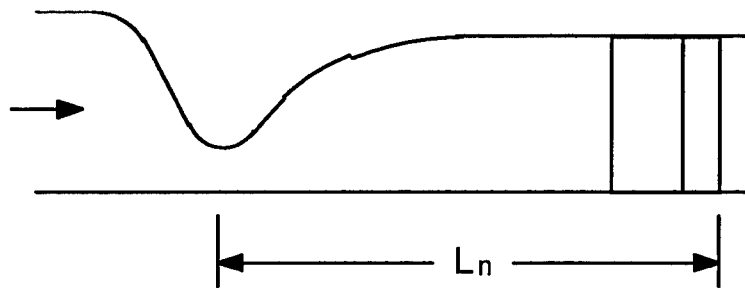


Figure 6-11 Test Section Length

The total steady test time is now calculated by combining Eqs (6-37) and (6-58)

$$t_s = t_{st} - t_d \quad (6-22)$$

It can be seen that as the distance from the nozzle increases, the steady flow time decreases.

6.1.3.4. Test Section Evacuation

The driven section can be initiated at a different pressure than the test section by placing a second diaphragm at the nozzle exit. This allows the driven section to be maintained at a desired pressure to produce a specific flow condition, but the nozzle and test

section can be evacuated. Lower pressure in the test section causes the starting shock to pass more quickly so that less of the steady flow time is lost. This is done, for example, in the NASA Ames shock tunnel. However, the diaphragm at the nozzle creates additional problems in that the diaphragm must not be allowed to contaminate the test gas, which could happen if parts of the ruptured diaphragm are blown through the nozzle; also, the requirement to put in a new diaphragm for each test will slow the turn-around time for the shock tunnel operation. In addition, in the present research, test section evacuation would have been difficult due to the instrumentation set-up. Finally, the length of the test section along with the adequate steady flow time produced by the shock tube and the high natural frequency of the skin friction gauges made the nozzle diaphragm along with test section evacuation unnecessary and undesirable.

6.1.4. Helium

The previous calculations have dealt only with the initial expansion of the helium. However, two other factors regarding the driver gas need to be considered. First, because the driver is not evacuated prior to filling with helium, the driver gas is actually a mixture of helium and air, which affects the gas properties which are used to calculate the helium expansion. The properties of the helium/air mixture can be calculated as shown in Appendix B. Second, the expansion of the helium reflects from the back of the driver tube, and then passes back through the helium and then through the air. Since the initial shock moves at subsonic speed relative to the air behind it, the expansion, which travels at sonic speed relative to the air, can catch the shock and weaken it. The expansion reflection was calculated using the method of characteristics as described in Appendix C.

Calculations using this method showed, with the original configuration of the shock tunnel with 1.62 m driver, that at lower driver pressures, the reflected expansion moved past the contact surface into the air prior to the reflected shock meeting the contact surface. This results in decrease of the steady flow period. At higher pressures, the shock, in theory, moves fast enough that the expansion does not decrease the steady flow period. However, the shock strength and speed attenuate, so in practice, this may not be

the case. Therefore, an extra 1.62 m length of tube was added to the driver section. This means that the expansion must travel farther both before and after reflection, and so does not enter the air until after the shock reflection from the contact surface.

6.1.5. Expansion at Nozzle Exit

The possibility of operating the shock tunnel in a free jet mode was evaluated as an alternative to using an enclosed test section. In a free jet mode, the flow is allowed to expand as it exits the nozzle. If the proposed tests were conducted in a free jet mode, only a test section floor would be used. In a free jet mode, the core of the flow remains in steady flow for a certain distance past the nozzle exit. Because the expansion angle increases as Mach number decreases, a free jet mode would normally only be used at higher Mach numbers. A free jet mode is desirable because flow visualization procedures are facilitated and test model access is improved. However, as will be seen in the following analysis, the expansion angle for Mach 3 is too high to test anything except a very small model.

With a high pressure driver, the nozzle will be underexpanded; that is, the pressure at the nozzle exit will be greater than the backpressure of the outside air. To equalize the pressure between the nozzle free jet and the ambient atmosphere, the free jet undergoes expansion at the nozzle exit on three sides as shown in Figure 6-12. This expansion places limits on the region in which uniform flow is expected. The fourth side (bottom) of the

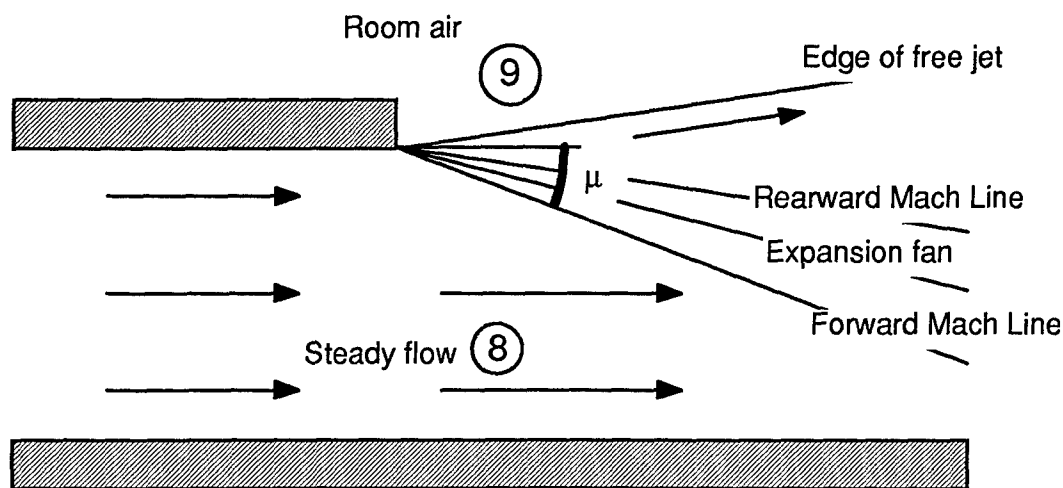


Figure 6-12 Nozzle Exit Jet

nozzle is bounded by a flat plate, so expansion does not occur here.

As shown in Figure 6-12, the expansion fan centered at the top edge of the nozzle is bounded by a forward Mach line and a rearward Mach line (Anderson, 1990:131). For the shock tunnel operation, the rearward Mach line is not of interest, but the forward Mach line (mathematically a characteristic) is the limit of the steady flow region: within the region delineated by the forward Mach line, the flow is steady.

The angle of the forward Mach line is given by (Anderson, 1990:131)

$$\mu = \sin^{-1}(1/M_6) \quad (6-23)$$

where M_6 is the exit Mach number. For Mach 3, the angle is 19.5 degrees. The forward Mach lines also bound the sides of the steady test area. Placement of the test model is then dictated by the principles that (1) the test model must be within the steady flow section delineated by the forward Mach lines, and (2) shocks and expansions from the test model, when reflected from the expansion beginning at the forward Mach line, should not strike the test model.

Because this expansion severely limits the size and length of the test model, the shock tunnel was not be operated in a free jet mode for the fin tests. Instead, a test section duct of the same cross section dimensions as the nozzle exit was constructed to enclose the fin as described in Chapter 7.

6.1.6. Results of Shock Tunnel Characterization Studies

The methodology developed in this section was incorporated into a computer program which was used to analyze the expected performance of the AFIT shock tunnel. The results are summarized in Appendix F.

There are several limitations to the above analysis which will cause the actual results to differ somewhat from the calculated results. First, the flow is assumed to be inviscid. The presence of viscous effects in the actual shock tunnel operation can have several effects. First, the boundary layer displacement thickness in the nozzle can cause the nozzle to produce a lower Mach number than predicted. While the nozzle was designed to correct for the effects of the displacement thickness, this correction is accurate only for

the design condition. Second, the presence of growing boundary layers as the gas moves through the shock tube makes the flow less steady than predicted by inviscid analysis. Third, shocks have finite thickness due to viscosity and have some curvature. Fourth, walls heating due to viscous effects, particularly in the nozzle throat, cause the enthalpies to differ somewhat from the calculated values. Finally, viscous effects both within the shock and on the wall cause the shock to attenuate as it travels down the shock tube. As discussed in Section 6.3, this is the most important variation of actual performance from predicted performance.

The assumption of flow in chemical equilibrium is an improvement over perfect gas calculations but neglects finite-rate effects. The effects of non-equilibrium will probably be the greatest in the diverging section of the nozzle (Anderson, 1989:570). While dissociation occurs almost instantaneously, re-association (which occurs in the diverging nozzle) is a more time-dependent process.

The quasi-one dimensional flow assumption used in the nozzle analysis neglects the lateral component of the velocity. This may have an effect on flow uniformity at the nozzle exit plane.

Another possible source of error may be the double diaphragm used to separate the driver and driven sections of the AFIT shock tunnel. The double diaphragm setup uses two diaphragms in-line (see Figure 6-13). The space between the two diaphragms is pressurized at an intermediate pressure. To start the run, the pressure is released; the resulting pressure difference causes diaphragm A to break, allowing the driver gas to contact diaphragm B. Diaphragm B then breaks, resulting in the shock and expansion described in the beginning of this chapter. However, a shock and expansion also occur with the breaking of the first diaphragm, which is not included in the calculations. The use of the double diaphragm allows precise starting of the shock tube at the desired pressures, but degrades the shock quality.

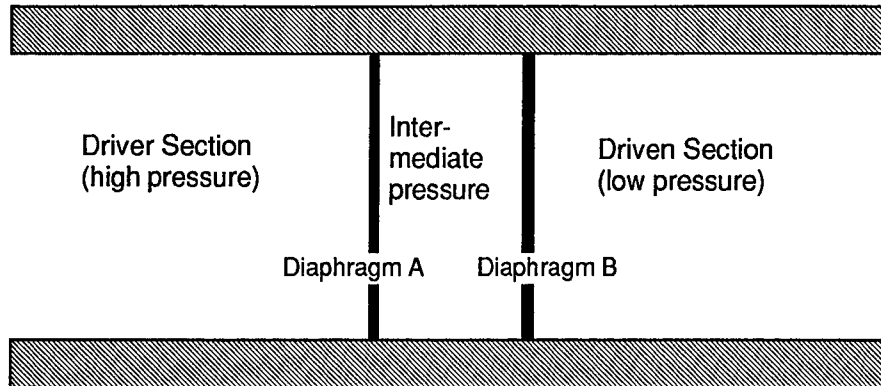


Figure 6-13 Shock Tube Double Diaphragm

6.1.7. Data Reduction

Characterization of the measurements which will be described in Chapter 7 require knowledge of the freestream conditions. The only freestream property that can be measured directly is the pressure. Other freestream properties were calculated based on pressure measurements as described in this section.

For calculation of the free stream properties, the measured conditions p_1 , p_5 , p_6 (nozzle exit) and T_1 are available. In addition, an approximate value of the shock speed u_s is known. Because of the varying nature of the flow and the shock attenuation described in Section 6.3, the pressure p_2 is not known. The procedure is to guess a value for p_2 , calculate the value for p_5 , and compare to the measured p_5 . An iterative process determines the correct value of p_2 , and the region 5 conditions are then calculated. Using the region 5 conditions and the measured nozzle exit pressures, the freestream conditions are calculated. This process is carried out for every data point in the steady flow part of the run. Because approximately 320 data points must be calculated for each run, computational efficiency is important.

The calculation procedure is similar to that for the theoretical shock tunnel analysis previously performed. For the theoretical case, however, p_5 was unknown. The region 2 conditions (behind the incident shock) were calculated by matching to knowledge of the

helium driver expansion. The region 5 conditions were then calculated from the region 2 conditions. For data analysis purposes, the helium conditions will be considered unknown, while p_5 is known. (The helium pressure is known, but due to shock attenuation and other viscous effects, the stagnation conditions in region 5 cannot be calculated directly from the initial pressures unless empirical correlations are used. These empirical correlations represent an average of previously measured flow results and are useful for predicting shock tunnel performance, but may not match the measured region 5 pressure for a particular run, particularly since p_5 varies throughout the run.)

Similarly, in the theoretical analysis, the nozzle exit pressure is unknown while the nozzle exit area is known. For data analysis, the effective nozzle exit area is unknown (due to the boundary layer displacement thickness being unknown), but the pressure is known.

Because of the varying flow conditions, nozzle entrance pressures must be offset to account for the time required for the air to pass through the nozzle. The amount of offset is determined by aligning the second shock reflection (the reflection of the reflected shock from the contact surface).

A data reduction program was written in FORTRAN for use with the AFIT shock tunnel. As described in Section 6.3, the DADiSP software is used to download the data files from the DL1200 to the computer. The offset of the nozzle entrance pressure is accomplished using DADiSP. In addition, a moving average of the pressures is accomplished, and the steady flow time extracted. These pressure data files (averaged, offset, and parsed) are then exported from DADiSP to a data file. The data reduction program calculates freestream and stagnation properties and writes these to data files. These files can then be imported into DADiSP for data analysis. The data reduction program is described more fully in Appendix D.

6.2. The AFIT Shock Tunnel Facility

This section describes the AFIT high pressure shock tunnel and the shock tunnel instrumentation and operation.

6.2.1. Description of Facility

The shock tunnel consists of a shock tube to which a nozzle and test section were fitted for the present research. The shock tube is constructed of stainless steel tubing of 5.26 cm inner diameter with wall thickness of 2.54 cm. The tube is constructed of sections that are 1.524 m long and are bolted together using flanges that are screwed onto threaded ends of each section. In its final configuration, two sections of tubing were used for the driver section and five for the driven (Figure 6-14). Early runs used only one section for the driver. Instrument flanges for pressure transducers and thermocouples can be added between the tube sections. Each tube section is mounted on a wheeled stand. To allow access to the diaphragm section, the entire driver section is moved by a pneumatic piston which is bolted to the floor (Figure 6-15).

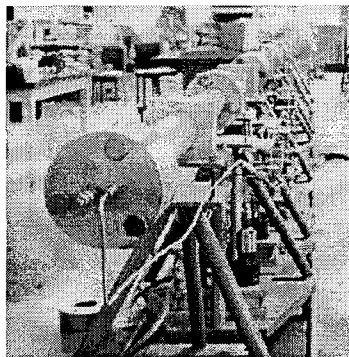


Figure 6-14 AFIT High Pressure Shock Tunnel

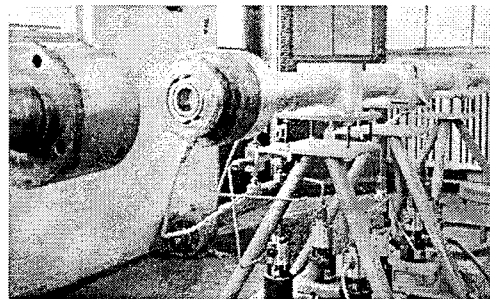


Figure 6-15 Breech Section for Diaphragm Access

The diaphragms are mounted in a holder that can be removed from the tube. A double diaphragm arrangement is used in which the space between the two diaphragms is pressurized at an intermediate pressure. The diaphragms are selected to burst when the full driver pressure is applied. Venting the intermediate section then applies the full driver pressure to the rear diaphragm, which bursts. High pressure helium then expands into the intermediate section, bursting the forward diaphragm and starting the run.

The driver section uses helium supplied by a bottle farm (Figure 6-16). The bottle farm is equipped with a pressure regulator that limits the maximum helium pressure to 10.4 MPa. The maximum pressure at which the driver section was operated in the present

research was 9.06 MPa. The driver section is also attached to the Building 19 air compressor, which can supply air at pressure of 0.79 MPa. The valves controlling the flow of helium and air are pneumatically activated using electrical switches from a remote control panel (Figure 6-17).

The shock tunnel is fitted with a Mach 3 converging/diverging nozzle. The nozzle is of two-dimensional (constant width) half nozzle design. The nozzle is constructed of aluminum and is bolted onto the flange of the shock tube section. Two test sections were

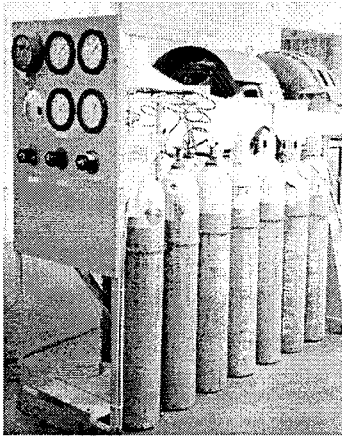


Figure 6-16 Helium Bottle Farm

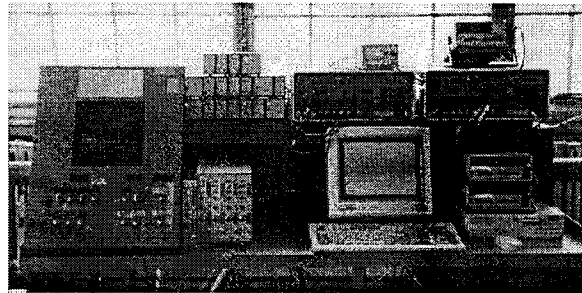


Figure 6-17 Shock Tunnel Control Panel

used in the present research. The first was a simple flat plate extension to the nozzle floor to allow two skin friction gauges to be mounted side by side. The second was a rectangular duct that could be operated with or without a sharp fin (Figure 6-18).

A dump tank was used with the duct test section in order to lessen the recoil from the gas exhaust (Figure 6-19). The initial shocks expand and diminish in strength upon

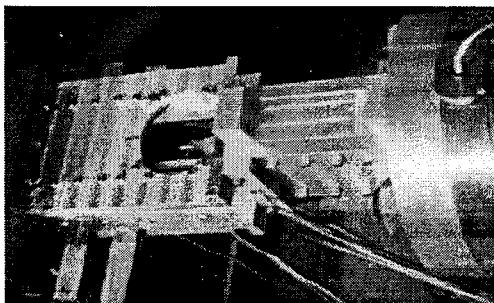


Figure 6-18 Duct Test Section with Fin

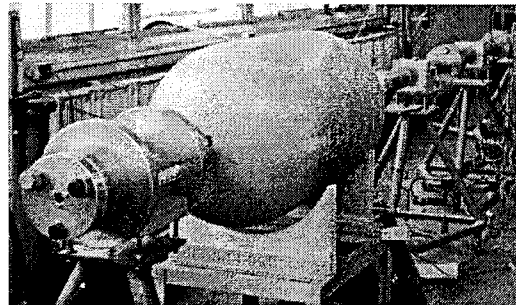


Figure 6-19 Dump Tank

entering the dump tank, preventing reflection of shocks into the test section during the steady flow. In addition, an old shock tube test section was bolted onto the end of exhaust end of the dump tank to add additional mass in order to diminish base vibrations.

6.2.1. Instrumentation

The instrumentation used in the research included pressure transducers, thermocouples, and skin friction gauges. Data was collected by a high speed data acquisition system and downloaded to a computer.

6.2.1.1. Data Acquisition System

The data acquisition system was a Datalab DL1200 waveform generator. The DL 1200 is an 8 channel recorder that can be set for sampling rates of 50 Hz to 200 kHz. Each channel records data 4096 samples. For the present research, a sampling rate of 100 kHz was used for the shock tunnel runs, resulting in a 40.96 msec data collection period. Lower sampling rates were used for skin friction gauge calibrations to obtain a longer data collection period. The DL1200 divides the assigned data range into 4096 parts. Thus, if a range of 20 volts is assigned to a particular channel, the resolution is 0.004883 volts. The range is separately assigned for each channel.

The DL1200 operates in 2 modes. In the armed mode, the DL1200 samples data continuously, and old data is replaced by new data as to remain within the 4096 sample limit. When the DL1200 is triggered, it collects data for a specified period of time which is equal to or less than the maximum sampling period. The user is allowed to specify a certain number of points to be retained prior to the trigger which were collected in the armed mode. For the shock tunnel runs, 10 percent of the points (496) were retained prior to the trigger. The trigger is set to a specified voltage change in one of the channels. For the shock tunnel, the trigger is the first pressure transducer after the diaphragm.

The DL1200 has some error associated with the digitizing process. This error is different for each channel, so each channel must be calibrated. The calibration is carried out by using a power source to apply a set voltage to the channel input. The voltage is monitored using a voltmeter. The DL1200 is then armed and triggered. The channel rec-

ord is downloaded to the computer, and the difference between the voltmeter-measured voltage and the DL1200 measured voltage is calculated. It was found that the error took the form of

$$\text{Error} = mV + b \quad (6-24)$$

where m and b are constant. The voltage is corrected using the formula $V = V_{DL} + \text{Error}$.

Substituting into Eq (6-24)

$$V = V_{DL} + mV_{DL} + b = (1 + m)V_{DL} + b \quad (6-25)$$

For correcting the data reading, only the slope m is needed, because the voltages used from the shock tunnel are always the difference between an initial voltage and voltage during the run: $\Delta V = V - V_0$. Substituting Eq (6-25) into this relation,

$$\Delta V = (1 + m)V_{DL} + b - [(1 + m)V_{DL0} + b] = (1 + m)(V_{DL} - V_{DL0}) \quad (6-26)$$

Early shock tunnel runs used a single DL1200. Later runs required 15 channels of data, so two DL1200s were used. The same pressure transducer was used to trigger both DL1200s; this pressure transducer trace was then used to synchronize the data between the two DL1200s. The data was downloaded and analyzed using Data Analysis and Display (DADiSP) software.

6.2.1.2. Pressure Transducers

Pressure transducers were used in the driver section, driven section, nozzle exit, and test section. The driven section pressure transducer was a Viatran model 104 with a rated maximum pressure of 13.78 MPa. Three Endevco 8510B 500 psig (3.45 MPa) transducers were used in the driven tube. An Endevco 8510B 100 psig (0.69 MPa) transducer was used in the nozzle exit. Three other 8510B 100 psig transducers were used in the duct test section along with one 8510B 500 psig transducers. All pressure transducers were powered by Endevco amplifiers. The pressure transducers were calibrated using a dead-weight technique with an Ametek HK-500 pneumatic tester. The calibration used the same amplifiers and wiring as in the shock tunnel. The calibration is linear according to the relation $p_{\text{gauge}} = AV$.

Rather than zeroing the amplifier voltages at the beginning of each run, the pressure was calculated by taking the voltage difference between readings during the run and the readings prior to shock arrival. The readings prior to the shock arrival correspond to atmospheric pressure, which was measured using a mercury barometer. The absolute pressure is then given by

$$P_{\text{absolute}} = A(V - V_0) + P_{\text{atmosphere}} \quad (6-27)$$

6.2.1.3. Thermocouple

Temperature measurements were made in the settling portion of the shock tube with an Omega T-type thermocouple. The thermocouple was mounted in the shock tube as shown in Figure 6-20. The primary purpose of the thermocouple was to measure the stagnant air temperature prior to the run. A secondary purpose was to detect the passage of the contact surface. The time response of the thermocouple is not fast enough to allow capture of the stagnation temperature. However, the hot air will cause the thermocouple-measured temperature to increase, while the arrival of the cold helium will cause a decrease in the measured temperature.

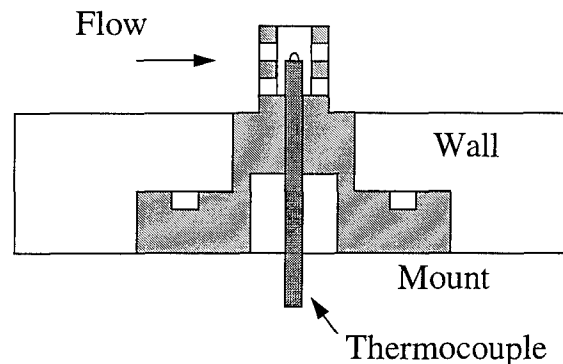


Figure 6-20 Gas Temperature Thermocouple

The temperature versus voltage response for a thermocouple is non-linear. For the T-type thermocouple, voltage as a function of temperature is expressed as 8th order polynomial over the range 0-450°C. Using Lagrange interpolation polynomials, a fourth order inverse polynomial was developed for the range 20 to 200°C. The inverse function was

used to calculate the thermocouple temperature from the voltage readings. The inverse function is of the form

$$T = a_4 V^4 + a_3 V^3 + a_2 V^2 + a_1 V + a_0 \quad (6-28)$$

The calibration factors are shown in Appendix A.

6.2.1.4. Skin Friction Gauges

The operation and calibration of the skin friction gauges are described in Chapters 2 and 3. The skin friction gauges were powered by Measurements Group model 2310 Signal Conditioner/Amplifiers. All of the skin friction gauges used in the AFIT shock tunnel were calibrated using the DL1200 data acquisition system. The calibration used the same amplifiers and wiring as in the shock tunnel. Because the voltages were read through the DL1200, there was no need for calibration of the channels that the skin friction gauges were connected to; the factor m is part of the calibration constant for the skin friction gauge. The skin friction gauges used in the AFIT shock tunnel were of 1.27 cm outer diameter.

6.2.2. Shock Tunnel Operation

The shock tunnel firing procedure commences by setting up the DL1200s to the desired operating parameters. The diaphragms are next placed in the diaphragm holder and placed in the shock tube. The pneumatic piston is then used to close the shock tube. The driver section is pressurized with air to test the seal of the double diaphragm. The air is then vented.

At this point, the atmospheric pressure is noted, and a zero run is conducted on the driver section pressure transducer (the zero run consists of measuring the voltage at zero gauge pressure through the DL1200). The DL1200 is then armed and the skin friction gauge amplifiers are zeroed. The temperature in the shock tube is noted from a voltmeter connected to the thermocouple at the nozzle entrance.

The vents to the driver section are now closed. The helium valves are opened, and then the tank valves are manually controlled to pressurize the diaphragm intermediate sec-

tion. The intermediate section pressurization valve is then closed, and the driver section is pressurized to full pressure. The helium valve is then closed.

At this point, the vent to the diaphragm intermediate section is opened. The diaphragms burst, triggering the DL1200. The DADiSP software is then used to download the data. Valves are opened to the compressor air to blow air through the shock tube to eliminate helium from the driven section prior to the next run.

The shock tunnel can use either metal or Mylar plastic diaphragms. Generally, plastic is used for lower pressures and metal (stainless steel or aluminum) for higher pressures. However, the metal diaphragms were found to produce inconsistent bursts. Testing showed that a layer of three sheets of 0.014 inch Mylar burst at driver pressures of 5.5-8.25 MPa. For the selected operating driver pressure of 9.06 MPa, each diaphragm consisted of the three sheet layer with the intermediate pressure approximately 4.58 MPa.

6.3. Experimental Characterization of the Shock Tunnel

This section discusses the experimental results from initial operation of the shock tunnel. These results were used to guide the development of the data reduction programs and the design of the flow about the sharp fin experiment. Results from the sharp fin experiment are discussed in Chapter 7, while skin friction gauge test results were described in Chapters 3 and 4.

6.3.1. Pressure and Temperature Traces

The pressures recorded in the shock tunnel operation do not approach the steady pressures predicted by inviscid one-dimensional shock tube theory. Pressure traces from the driven section of the shock tube are shown in Figure 6-21. From these traces, it can be seen that the incident shock attenuates considerably as it travels down the tube. This in turn causes considerable variation in the pressure after the shock is reflected during the steady flow period.

Figure 6-22 shows the pressure at the nozzle entrance for two different runs. The second reflection of the shock from the contact surface is seen in the Run 15 trace. Run 20 was conducted with a lower driver pressure, and hence the shock did not reflect from

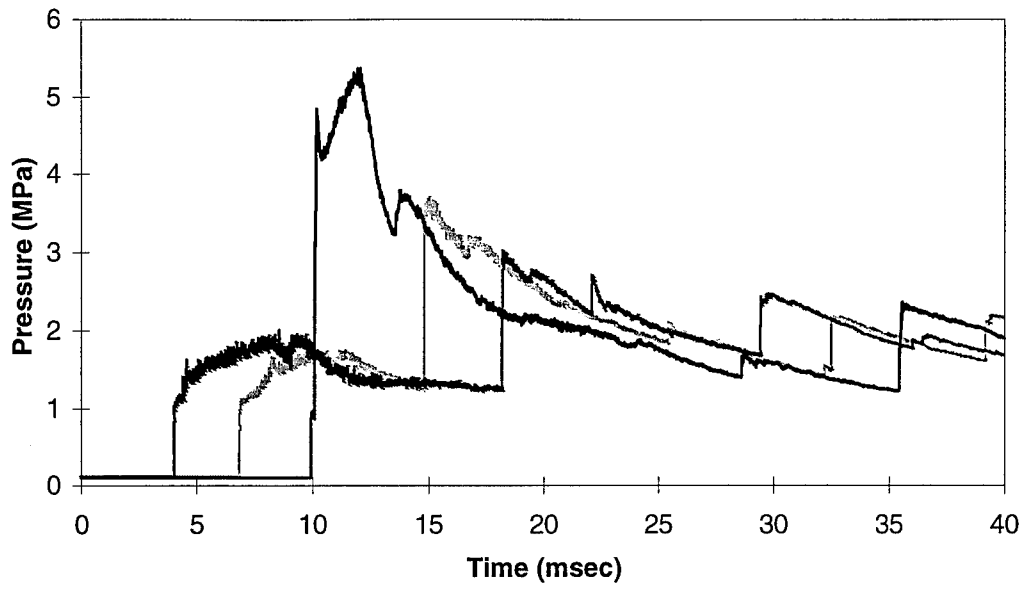


Figure 6-21 Shock Tube Pressure Traces

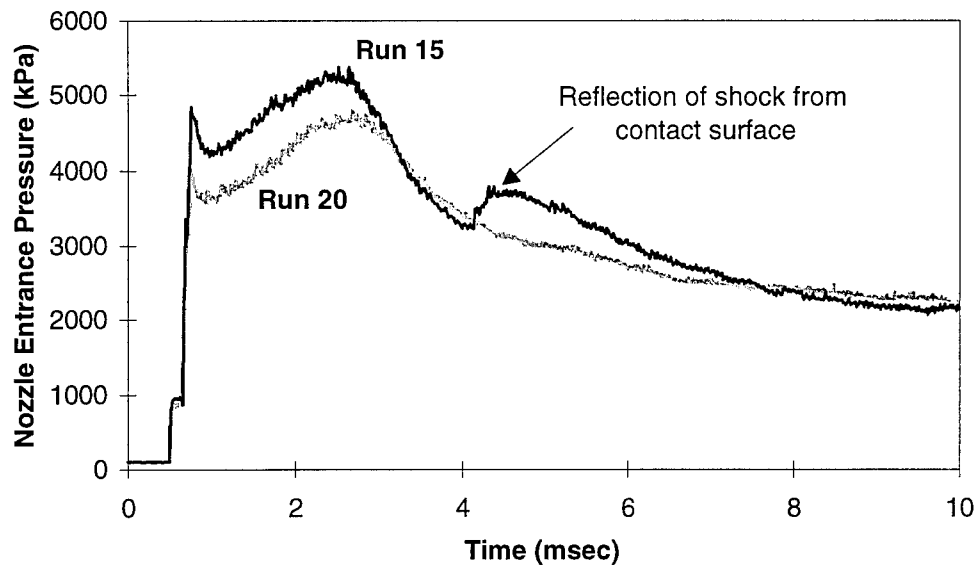


Figure 6-22 Reflection of Shock from Contact Surface

the contact surface. Run 20 was the highest driver pressure at which the shock did not reflect, and hence can be considered to be approximately the tailored condition. The driver pressure for Run 20 was 8.63 MPa. In Run 15, the arrival of the second reflection

of the shock from the contact surface occurs approximately 3.2 msec after the arrival of the incident shock. This marks the end of the steady flow period.

In Figure 6-23, the temperature trace overlaying the pressure trace shows the arrival time of the contact surface. The air has been heated by shocks, while the helium has been cooled by expansion, so the arrival of the helium at the nozzle entrance is marked by a decrease in temperature. It should be noted that the temperature is the temperature recorded by the nozzle entrance thermocouple. As discussed previously, the response time of this thermocouple is too slow to allow capture of the air temperature, which is approximately 1100K.

6.3.2. Shock Attenuation

The shock strength p_2/p_1 attenuates due to viscous effects as the shock progresses through the tube. The shock attenuation can be described by the following relation (Bleakney and Emrich, 1961:631):

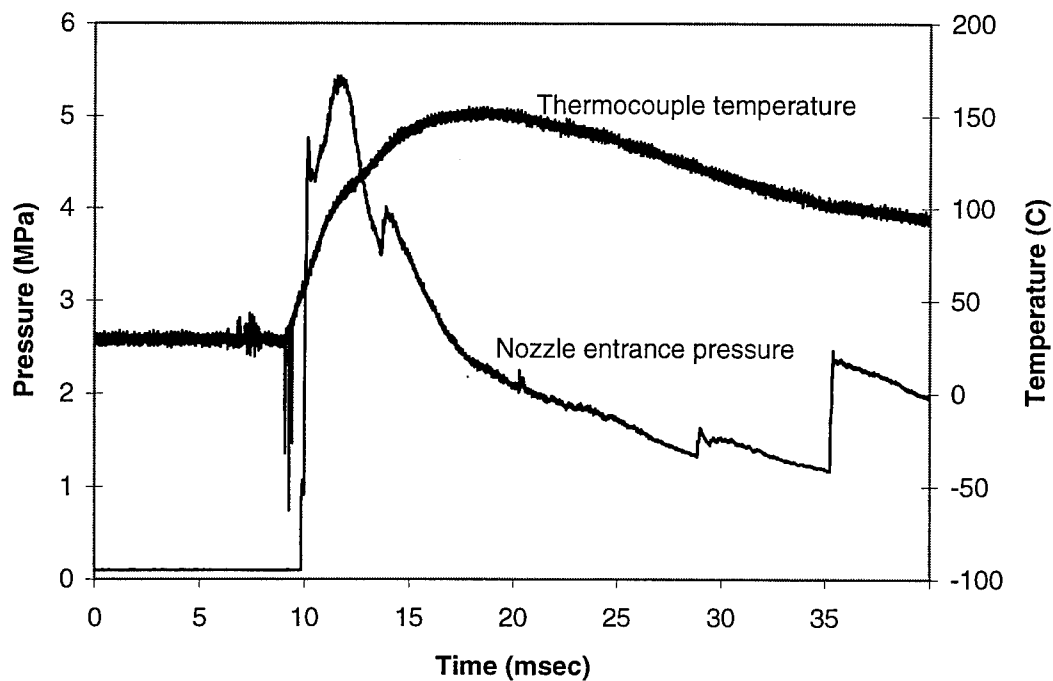


Figure 6-23 Pressure and Thermocouple Traces

$$A = -\frac{R}{P_{21} - 1} \frac{dP_{21}}{dx} \quad (6-29)$$

where A is a dimensionless attenuation coefficient, R is the hydraulic radius, and P_{21} is the pressure ratio shock pressure ratio: $P_{21}=p_2/p_1$. The coefficient A is empirically derived and depends on both shock strength and tube diameter. The attenuation relation, Eq (6-29) can be integrated as follows:

$$\int A dx = -\int \frac{R}{P_{21} - 1} dP_{21} = -R \ln(P_{21} - 1) + C \quad (6-30)$$

At $x=0$, let $P_{21}=P_0$, where P_0 is the initial shock strength. With this boundary condition, the constant in Eq (6-30) can be evaluated as $C=R \ln(P_0-1)$. Substituting into Eq (6-30) and rearranging,

$$P_{21} - 1 = (P_0 - 1)e^{-Ax/R} \quad (6-31)$$

There are two unknowns in Eq (6-31): the initial shock strength P_0 and the attenuation constant A. If the shock strength is known at two locations, then these unknowns can be resolved. Starting with Eq (6-31),

$$\frac{Ax_1}{R} = -\ln(P_1 - 1) + \ln(P_0 - 1) \quad (6-32a)$$

$$\frac{Ax_2}{R} = -\ln(P_2 - 1) + \ln(P_0 - 1) \quad (6-32b)$$

Subtracting Eq (6-32a) from Eq (6-32b)

$$A = \frac{R}{x_2 - x_1} \ln \left(\frac{P_1 - 1}{P_2 - 1} \right) \quad (6-33)$$

Substituting this result into Eq (6-32a),

$$P_0 - 1 = \frac{(P_1 - 1)^{x_2/(x_2 - x_1)}}{(P_2 - 1)^{x_1/(x_2 - x_1)}} \quad (6-34)$$

Equation (6-33) is used to calculate the attenuation constant for the shock and Eq (6-34) the initial shock strength, which is not measured. Using this method, the attenuation factor for the AFIT shock tunnel operating with driver pressure of 9 MPa is approximately 5×10^{-3} . This is consistent with a survey undertaken by Bleakney and Emrich

(1961:632), in which shock tubes of approximately the same diameter as the AFIT shock tube had attenuation factors ranging from 4×10^{-4} to 8×10^{-4} . Two factors should be noted however. The attenuation factor is not constant but increases as the shock strength increases. In addition, if the helium expansion wave catches the shock (which would happen for weaker shocks), then further attenuation would occur beyond that predicted by the attenuation factor.

Figure 6-24 compares the actual performance of the AFIT shock tunnel to the predicted performance over a range of driver pressures. In general, a single diaphragm resulted in a stronger shock than the double diaphragm. A single diaphragm was used to determine the breaking strength of various combinations of Mylar; at the driver pressures of around 6 MPa, the higher p_4 pressures were for the single diaphragm in the diaphragm test, while the lower p_4 pressures were in the double diaphragm runs.

6.3.3. Pressure variation

The variation of the pressure trace behind the incident shock is caused by several effects. The increase in pressure immediately following the shock could be caused by the

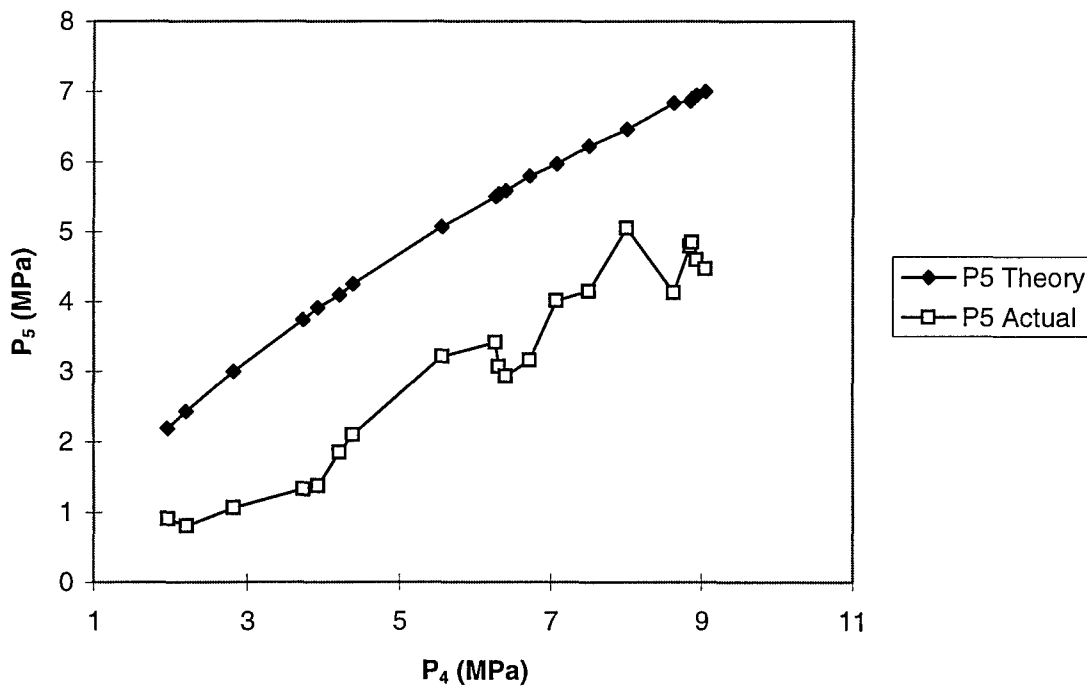


Figure 6-24 Predicted vs. Actual Performance of AFIT Shock Tunnel

shock attenuation. The shock is weaker by the time it has passed through the gas immediately behind the shock, while the air farther behind the shock was affected by a stronger shock. Thus, the air immediately behind the shock is at lower pressure than the air farther behind the shock.

A second factor that could cause the rise in pressure is that the compression waves resulting from the diaphragm opening may not coalesce into a single shock but rather consists of a main shock followed by either compression waves or small shocks.

A third factor that could cause the pressure rise is shock curvature, where the edges of the shock trail the center. At the wall location of the pressure transducers, the full pressure rise associated with the shock would not be felt until the trailing edge of the shock passes.

The decrease in pressure following the peak pressure is probably due to viscous effects. The air behind the shock is traveling at subsonic speed, so viscous effects cause the pressure to decrease. Initially, the boundary layers grow, causing a decrease in the effective cross sectional area of the tube. This causes a converging nozzle effect, which results in pressure decrease. Farther down the tube, the boundary layers may merge to result in fully developed duct flow, with the wall frictional forces manifesting as pressure losses. The air close behind the shock has not traveled very far, so boundary layers are thin and viscous losses small. The air farther behind the shock has traveled farther; boundary layers are thicker and viscous losses are larger.

6.3.4. Helium temperature

The initial shock strength is affected by the temperature of the driver gas through the effect on the speed of sound, which increases with temperature. A cold driver gas thus results in a weaker shock. The helium expands as it flows from the high pressure helium bottles at room temperature into the lower pressure of the driver section, and this expansion causes the temperature to decrease. The temperature change for an isentropic expansion is governed by (John, 1984:20)

$$\frac{T_2}{T_1} = \left(\frac{P_2}{P_1} \right)^{(\gamma-1)/\gamma} \quad (6-35)$$

Thus for a decrease in pressure by 1/2, the decrease in absolute temperature is about 24 percent, corresponding to a decrease from room temperature to about 226K (γ for helium is 1.67).

In reality, the expansion is not isentropic, and convection heating occurs both in the feed tubes going into the driver section and in the driver section itself. However, the driver gas temperature could still be somewhat cooler than room temperature, so an experiment was run to the helium condition. The driver section was filled to a pressure of 0.86 MPa from a full helium bottle (thus at highest pressure) at a pressure of 17.4 MPa. Rather than modifying the driver section to accommodate a thermocouple, the pressure was monitored. Since volume is constant, pressure should vary with temperature. The time response of the pressure was recorded using the DL1200. The pressure was monitored for 10 minutes with no change in pressure. It can thus be concluded that convection heating returns the helium to room temperature during the filling process, so no time delay is required prior to firing the tunnel to allow the helium to heat in the driver tube.

6.4. Analysis of Representative Flight Conditions

The nozzle exit conditions that the shock tunnel generates might typically be encountered in the inlet of a scramjet combustor after the air in the free stream has already undergone compression. This can be seen in the pressures and temperatures, both of which are higher than would be found in the atmosphere. To determine the atmospheric conditions that would result in these nozzle exit conditions, a nominal shock compression system typical of a scramjet inlet will be used (Figure 6-25).

The nominal inlet shown in Figure 6-25 uses the vehicle forebody to create a series of oblique shock waves to slow and compress the air. This is a typical configuration for hypersonic vehicles currently under consideration, although the number and arrangement of shocks vary (Heiser and Pratt, 1994:214). For the arrangement shown, the flow is de-

flected by the same angle for each shock. The angle θ is the deflection angle, while β is the initial shock angle.

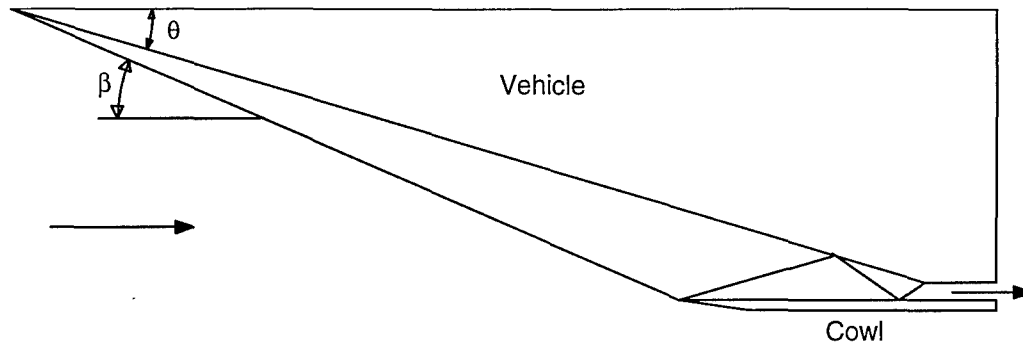


Figure 6-25 Scramjet Compression System with Four Oblique Shocks

6.4.1. Equivalent Mach Number

The velocity of the vehicle through the atmosphere is calculated from the total enthalpy calculated for the nozzle exit in Chapter 6 using Eq (6-3c). Since the total enthalpy is preserved through a shock, Eq (6-3c) can be re-written using the relation $h_o = c_p T_o$ as

$$u_o = \sqrt{2(h_t - c_p T_o)} \quad (6-36)$$

where the subscript o refers to atmospheric freestream conditions. The Mach number can then be calculated by dividing Eq (6-36) by the speed of sound $a = \sqrt{\gamma RT}$ together with the definition $M=u/a$, to give

$$M_o = \sqrt{\frac{2(h_t - c_p T_o)}{\gamma RT_o}} \quad (6-37)$$

Using the relation $c_p/R = \gamma/(\gamma - 1)$, Eq (6-37) can be re-written as

$$M_o = \sqrt{2 \left(\frac{h_t}{\gamma RT_o} - \frac{1}{\gamma - 1} \right)} \quad (6-38)$$

From Eq (6-38), it can be seen that the equivalent free-stream Mach number varies only with temperature. Since the temperature does not vary greatly in the atmosphere, it was

determined that the calculated shock tube nozzle exit conditions correspond to Mach 6-7 enthalpies, while the actual conditions correspond to Mach 5 enthalpies.

6.4.2. Equivalent Altitude

To conduct the analysis to determine which flight conditions match the shock tunnel conditions, an altitude and deflection angle are selected. The velocity is then calculated from the total enthalpy equation. The conditions through the four shocks in the typical scramjet inlet are then calculated. The resulting temperature after the four shocks is compared to the exit temperature of the shock tunnel nozzle. The deflection angle is then varied until the temperature after the four shocks matches the shock tunnel exit temperature. The pressure after the four shocks is then compared to the exit pressure for the shock tunnel nozzle exit. The whole process is repeated for various altitudes until both the temperature and pressure after the four shocks of the nominal inlet match the nozzle exit conditions for the shock tunnel. If equilibrium chemistry is assumed for high temperature dissociation, once the temperature and pressure match, then all other conditions such as density, dynamic pressure, and Mach number also match.

Determining the conditions through the four shocks requires high temperature gas effects to be taken into consideration. For oblique shocks, the same equations apply as for normal shocks, but the equations are only applied to the component of the velocity normal to the shock (Figure 6-26) (Anderson, 1990:515). Re-written for the oblique shock, these equations are

$$\textit{Continuity} \quad \rho_1 u_{1n} = \rho_2 u_{2n} \quad (6-1d)$$

$$\textit{Momentum} \quad p_1 + \rho_1 u_{1n}^2 = p_2 + \rho_2 u_{2n}^2 \quad (6-2d)$$

$$\textit{Energy} \quad h_1 + \frac{u_{1n}^2}{2} = h_2 + \frac{u_{2n}^2}{2} \quad (6-3d)$$

The normal component can be calculated from $u_{1n} = U_1 \sin \beta$, while the tangential component is $u_{1t} = U_1 \cos \beta$. The tangential component of velocity is unchanged across the shock: $u_{1t} = u_{2t}$.

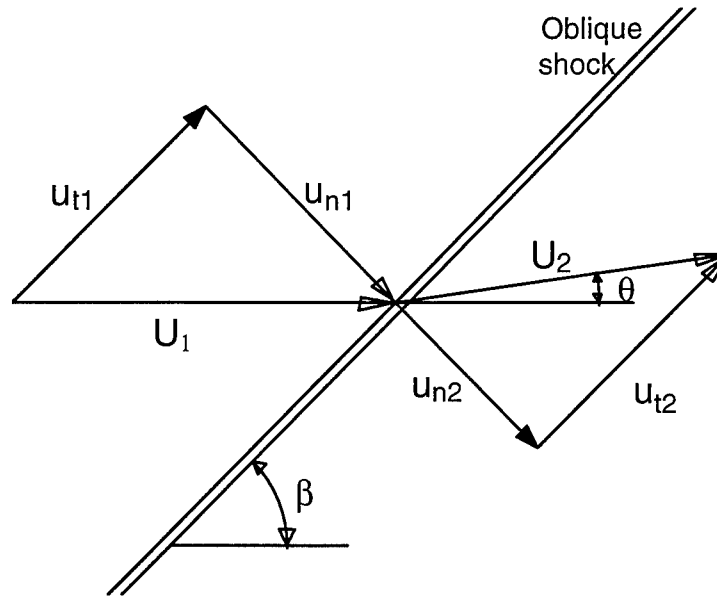


Figure 6-26 Oblique shock geometry

The high temperature analysis makes use of the Tannehill and Muggge (1974) polynomial curve fit $h=h(p,\rho)$. The iterative procedure for calculating the oblique shock properties is described in Appendix D. The deflection angle θ is calculated from the geometric relation (Anderson, 1990:516)

$$\tan(\beta - \theta) = \frac{u_{2n}}{u_{2t}} \quad (6-39)$$

The initial guess for ρ_2 can be improved by using the ideal gas relation (Anderson, 1989:106)

$$\frac{\rho_2}{\rho_1} = \frac{(\gamma - 1)M_{1n}^2}{(\gamma - 1)M_{1n}^2 + 1} \quad (6-40)$$

where M_{1n} is defined by $M_{1n} = u_{1n}/a_1 = M_1 \sin \beta$.

For the calculation of interest (the four oblique shock compression system), θ is known and β is unknown. Since β is an implicit function of θ , an iterative procedure must be used in which a value of β is guessed and θ calculated and compared to the known θ . As an initial guess, the following ideal gas relation can be used (Anderson, 1989:107):

$$\tan \theta = 2 \cot \beta \left[\frac{M_1^2 \sin^2 \beta - 1}{M_1^2 (\gamma + \cos 2\beta)} + 2 \right] \quad (6-41)$$

In Eq (6-41), β is an implicit function of θ , so an iterative procedure is still required, but this procedure is much faster than solving the high temperature equations. In the presence of real gas effects, equilibrium chemistry calculations result in a shock angle less than the ideal gas shock angle, so the ideal β from Eq (6-41) can also be used as the maximum shock angle for a given deflection angle. For the conditions calculated, the first two shocks were equivalent to the perfect gas calculations, while the last two shocks showed real gas effects.

VII. Application of Directional Skin Friction Gauge in a Flow About a Sharp Fin Mounted on a Flat Plate

The primary purpose of this part of the research was to demonstrate the directional gauge in a flow with a cross flow component. The sharp fin on a flat plate (Figure 7-1) was chosen because it could be investigated using the existing Mach 3 nozzle. In addition, this flow has been studied extensively but few skin friction measurements have been undertaken.

The fin is similar to a strut, fuel injector, or sidewall compression plate that might be encountered in a scramjet. The geometry is also similar to that of a fin (wing-body junction) on a high-speed vehicle. In supersonic flow, the fin generates a swept shock which disrupts the established boundary layer on the flat plate. This problem of swept-shock-wave/boundary-layer interactions has been studied extensively in the literature. However, the development of the directional skin friction gage suitable for shock tunnel testing allowed direct measurements of, not only wall shear magnitude, but also direction, which has not been done in this type of flow. In addition, the effects of the wake from the blunt trailing edge on the flat plate surface skin friction were measured. Wakes and boundary layers have also been a subject of extensive research; however, a combined wake/boundary layer interaction flow has not been studied. Aside from skin friction gauge

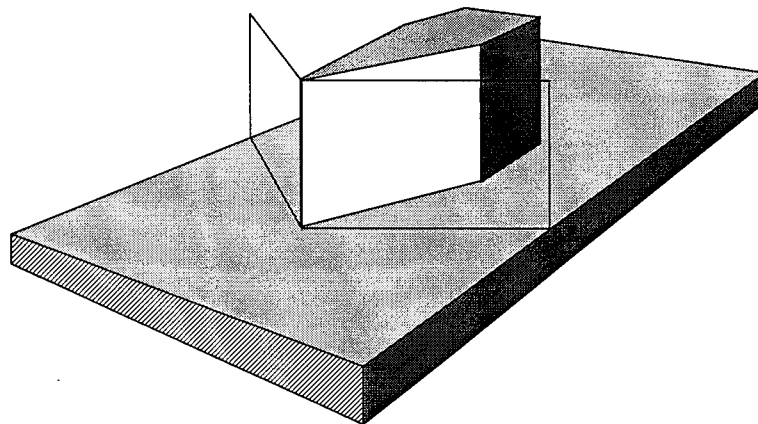


Figure 7-1 Test Model (Wedge-Shaped Fin on Flat Plate)

demonstration, the data have the added benefit of contributing to both drag assessment of scramjet engines and to CFD turbulence model development for this class of combined viscous flows. The test runs simulated the conditions that might occur in a scramjet compression section after the flow has been slowed to Mach 3.0.

7.1. Nature of the Flowfield

The investigation measured the wall shear in the interaction between the swept shock, caused by the fin, and the existing boundary layer on the flat plate. This situation is somewhat similar to a shock reflection from solid boundary. When a shock wave impinges on an existing boundary layer, the shock causes the boundary layer to separate in the area of the shock and then reattach downstream of the shock (Anderson, 1989:323). The reflected shock/boundary layer interaction is depicted in Figure 7-2. Due to viscous interactions, the boundary layer actually begins to separate ahead of the shock impingement point. Beneath the separated boundary layer, flow recirculation exists. Two shocks are generated by the separated boundary layer. The first, the induced separation shock wave, occurs at the boundary layer separation point. This shock results from the compression in the outer flow which is caused by the bending of the boundary layer upward. Expansion waves exist across the top of the separated boundary layer as the boundary layer bends back toward the solid surface. At the reattachment point, the curvature of the boundary

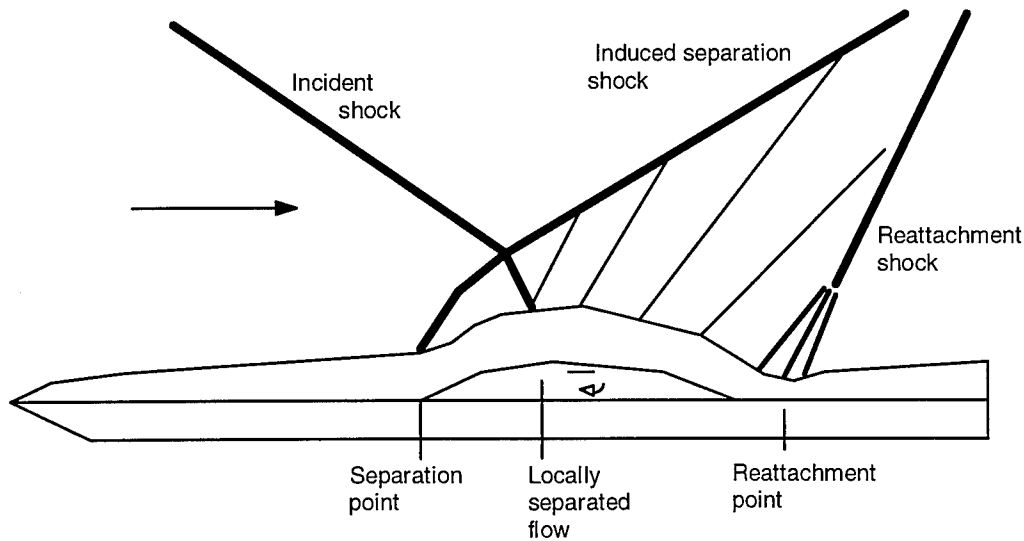


Figure 7-2 Reflected Shock/Boundary Layer Interaction

layer reverses, causing compression in the outer flow, with another shock wave resulting. The induced separation shock wave and the reattachment shock wave merge to form the reflected shock predicted by inviscid shock theory.

A swept shock crossing a boundary layer has similar effects, as shown in Figure 7-3 (Settles and Dolling, 1986:310). Again, the separation occurs ahead of the shock. For this case, however, the shock is normal to the surface and is not reflected, although the separated boundary layer causes secondary shocks which merge with the main shock away from the boundary layer. Due to the shock being swept, this interaction is three-dimensional, although some researchers have demonstrated that the interaction region possesses either conical symmetry (Settles and Lu, 1985) (Figure 7-4) or cylindrical symmetry (Wang and Bogdonoff, 1986).

The boundary layer separation with flow recirculation beneath has been a subject of some dispute in the literature (Settles and Dolling, 1984:306-307,310). Horstman (1986), in a numerical study, predicted that the separation bubble would consist of a helical vortex. Settles and Kimmel (1986) used a local vapor technique to visualize the boundary layer separation but found no evidence of a vortex core. Behind the shock,

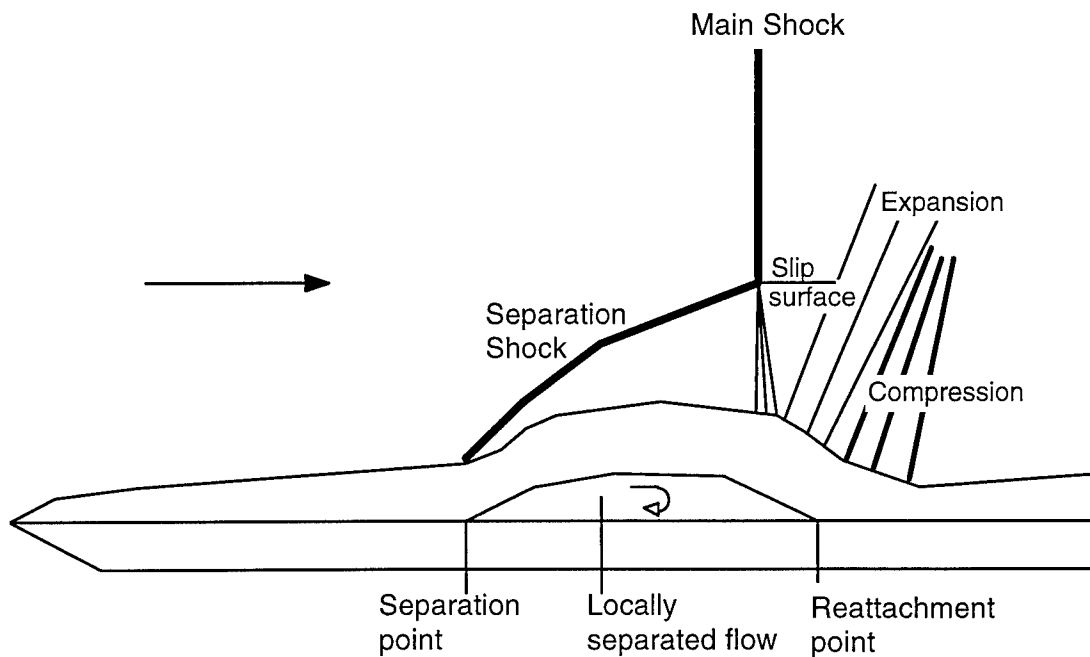


Figure 7-3 Side View of Swept Shock/Boundary Layer Interaction

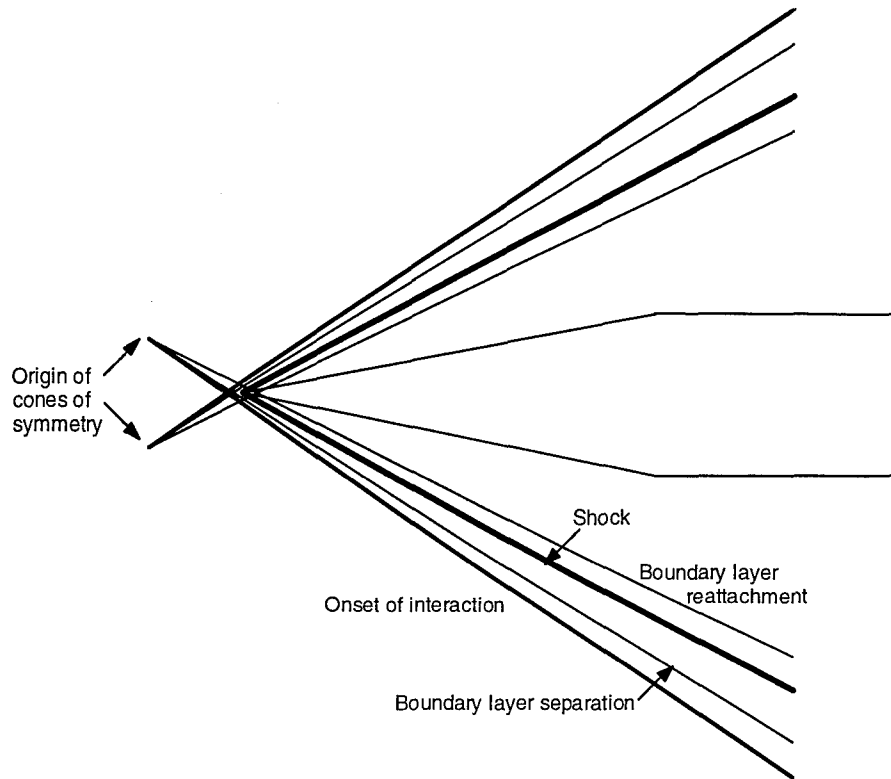


Figure 7-4 Top View of Shock/Boundary Layer Interaction Showing Conical Similarity

away from the interaction region, the flow at the surface aligns with the freestream. Hence, for a 10 degree flow deflection, the yaw angle of the flow relative to the freestream would be 10 degrees.

In the interaction, from both surface oil flow visualization and CFD calculations, the boundary layer separation line in Figure 7-4 is characterized by a line of coalescence while the reattachment point is characterized by a line of divergence (Figure 7-5) (Knight, Horstman, Shapey, and Bogdonoff, 1987:1335). As can be seen in Figure 7-4, the line of coalescence (boundary layer separation) is at a greater angle than the shock, while at the line of coalescence, as can be seen in Figure 7-5, the surface flow is at an even greater angle than the line of coalescence. Thus, a 10 degree deflection, which has a shock angle of about 28.5 degrees, has a line of separation at about 32 degrees (Alvi and Settles, 1992:2254) and can produce surface flow yaw in excess of 32 degrees. As described by Settles and Dolling (1992:512-513) some researchers have considered separation to occur

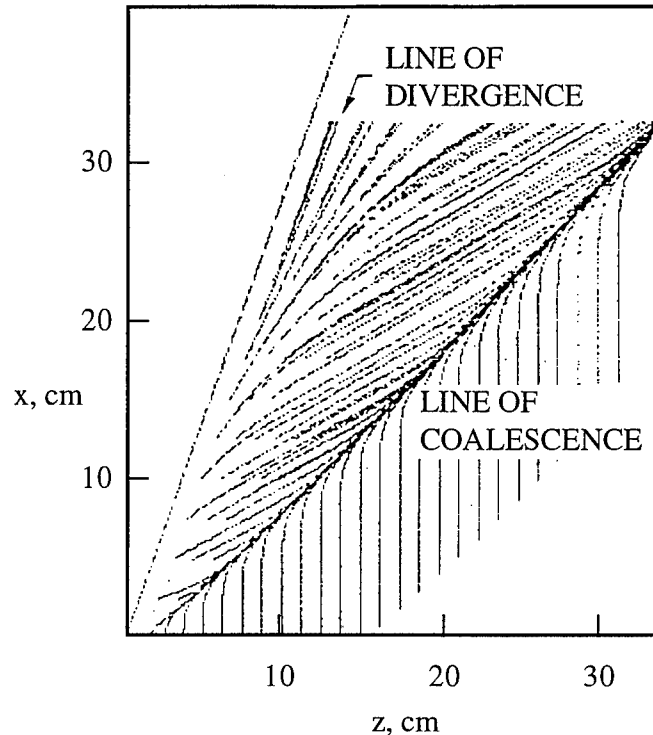


Figure 7-5 Computed Surface Skin Friction Lines (Knight, et al., 1987)

when the surface flow yaw angle aligns with the shock (the Korkegi criterion, which will be discussed in Section 7.3 uses this definition) although other researchers have shown that separation can occur well before the yaw angle aligns with the shock.

Because the shock wave/boundary layer interaction can occur in a wide variety of flows, this phenomenon has been a subject of extensive study, both experimental and numerical. Settles and Dolling (1992) conducted a systematic review of research on the swept shock/boundary layer interaction in 1992. The Settles and Dolling paper surveyed 187 papers published between 1940 and 1984 that dealt with the swept-shock/boundary layer interaction. The only reported skin friction measurements that have been made in the swept-shock/boundary-layer interaction have been by laser interferometer (oil coating). Kim and Settles (1990) measured swept shock/boundary layer skin friction generated by a sharp fin. Garrison, Settles, Narayanswami, and Knight (1994) measured skin friction in a crossing shock situation.

Skin friction measurements have not been previously undertaken for the swept-shock/boundary layer interaction problem for high enthalpy flows. In addition, directional skin friction measurements have not been undertaken for the interaction under any flow condition, although the surface oil coating does show, to some extent, the surface flow direction.

The other unique feature of the flowfield is the wake/boundary layer interaction. Although wakes have been subjected to extensive research, no literature has been found regarding the interaction with an established boundary layer.

7.2. Overview of the Experiment

The measurements were conducted in the AFIT high pressure shock tunnel which is described in Chapter 6. A total of 20 runs was conducted.

The tests used a sharp fin within the shock tunnel test section duct (Figure 7-6). The fin extended from top to bottom of the test section. The duct has a square cross-section, 3.81 cm by 3.81 cm. The fin width was 6.35 mm, and the fin half angle was 10.3 degrees.

The measurements were taken on the test section floor using an "instrument

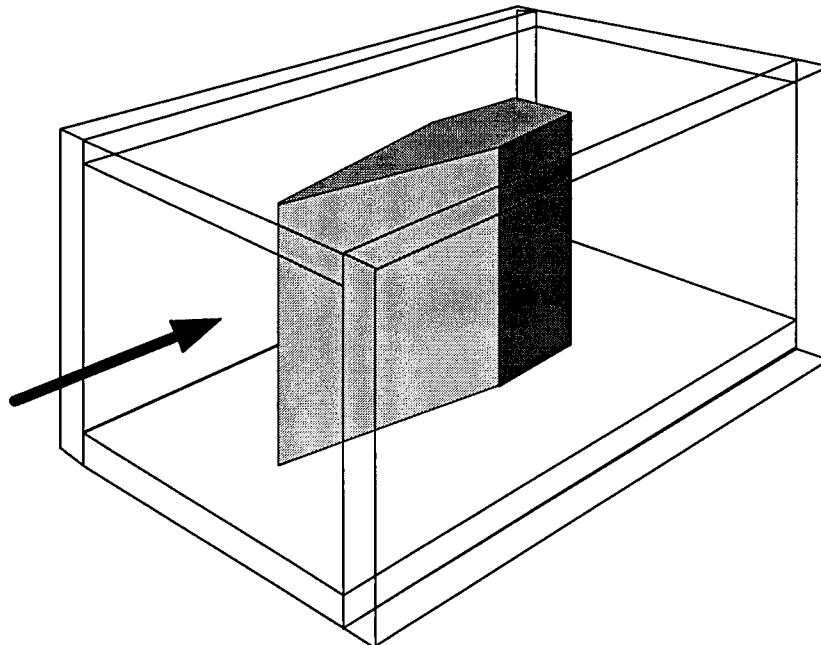


Figure 7-6 Test Section with Fin

wheel" and "instrument strip" as shown in Figure 7-7. Since the shock/boundary-layer interaction takes place near the oblique shock, which radiates from the wedge vertex (Figure 7-4), the instrument wheel has the instrumentation arranged on radials with the center of the wheel at the wedge vertex. By rotating the wheel between runs, different areas of the flow field were mapped. At certain points, some of the instruments were beneath the tunnel wall. The centerpoint of the skin friction gauges were located 7.94 mm and 22.22 mm from the center of the wheel. The wheel pressure transducers were located symmetric to the skin friction gauges on a radial at an angle of 100 degrees to the skin friction gauges.

The instrument strip was used to map the wake area. The midpoint of the skin friction gauge was 9.525 mm (i.e., 1.5 fin widths) behind the back of the fin. The separation distance between the centerpoints of the pressure transducer and the skin friction gauge was 3.175 cm.

For the fin measurements, the shock tunnel was operated at driver pressure of 9.06 MPa with driven section at atmospheric pressure. This condition, which is slightly

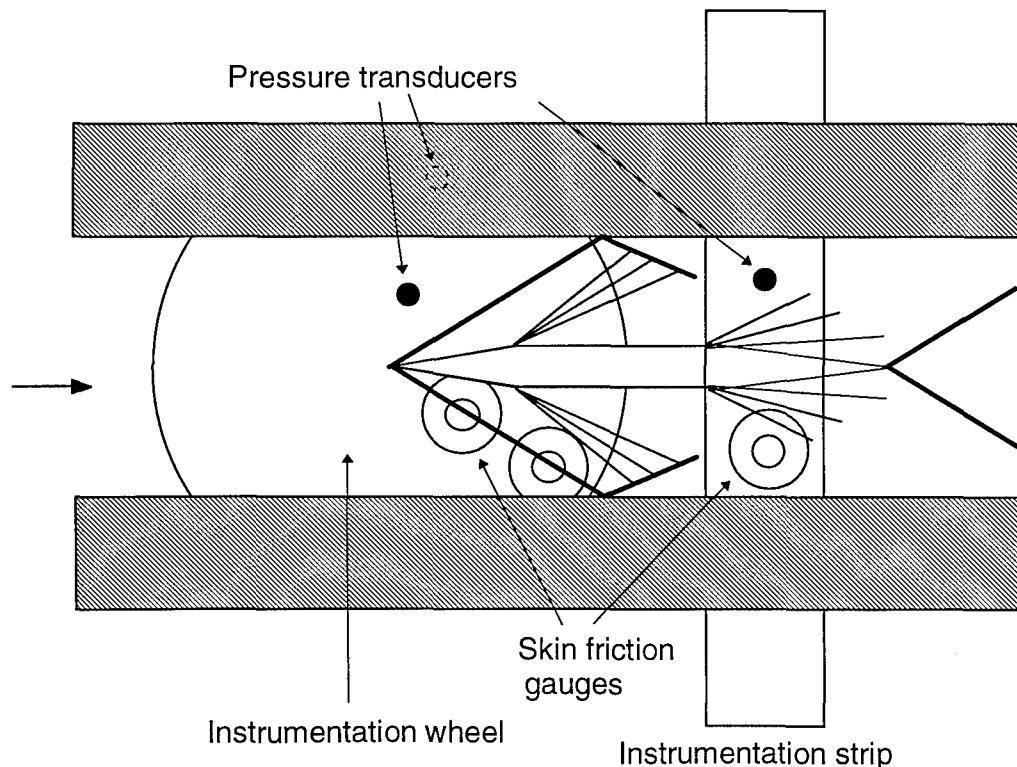


Figure 7-7 Top View of Test Section

higher than the tailored condition, was selected because it provides a high temperature flow (stagnation temperature of 1200K) with adequate run time. In addition, the minor flow disturbance produced by reflection of the shock from the contact surface provides a useful demarcation point for aligning flow conditions for normalization purposes. Finally, this condition produces flow at slightly higher than atmospheric pressure, which means that any duct leakage would not significantly affect the accuracy of the results. In addition, any skin friction gauge normal pressure sensitivity would not be an issue since the gauges are balanced at atmospheric pressure.

The mean flow conditions were pressure of 1.13 atmospheres (115 kPa), density of 0.973 kg/m^3 , velocity of 1,174 m/sec (2,627 mph), and Mach number of 2.89. Using the equivalent flight conditions calculation as described in Section 6.3, this equates to Mach 4.7 flight at an altitude of 14.5 km.

7.3. Analysis of Flowfield

This section presents the calculations for the flow field about the fin in the shock tunnel. An inviscid analysis will first be performed to determine the location and strengths of shock waves and expansion fans, as well as freestream pressure, density, and velocity. Correlations from the literature will then be used to determine peak heating and pressures associated with the shock/boundary layer interaction.

7.3.1. Inviscid analysis

When boundary layer effects are neglected, the inviscid analysis is two dimensional, with no variation in the z-direction. The flow field is shown in Figure 7-7. The salient features of the flow field are the two oblique, attached shocks off the sharp leading edge of the fin, which are reflected from the tunnel walls; the expansion fans at the shoulders of the fin, which intersect and weaken the reflected shocks, and the wake region. Prior to the leading shocks, the flow is the uniform flow from the shock tunnel nozzle exit which has previously been calculated.

The initial shock waves, reflected shock waves, expansion fans, and the base pressure in the wake region will be calculated using inviscid shock/expansion theory. The interaction of the reflected shock and the expansion fan will not be analyzed, since this region occurs downstream of area being measured and the interaction does not directly affect the forces and moments on the fin.

7.3.1.1. Shock Waves

Calculation procedures for high temperature oblique shocks were developed in Chapter 6 for calculating the flow conditions for the nominal scramjet inlet with four oblique shocks. The same procedure will be used here. For the test section calculation, the initial flow deflection is the wedge half angle. At the tunnel wall the flow is deflected to be once again parallel to the tunnel wall, resulting in a reflected shock. The wall deflection angle is the same as the initial deflection angle.

7.3.1.2. Expansion Fans

The expansion fan turns the flow to be parallel with the shoulder (Figure 7-8). This process is isentropic and is governed by the relation, derived from geometry (Anderson, 1990:133)

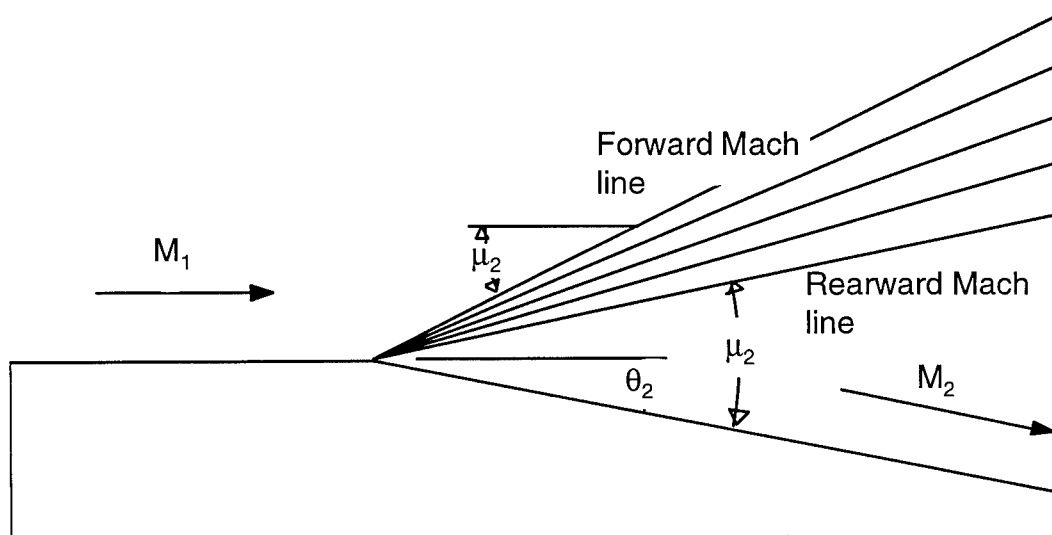


Figure 7-8 Expansion Fan

$$\int_{\theta_1}^{\theta_2} d\theta = \int_{M_1}^{M_2} \sqrt{M^2 - 1} \frac{dU}{U} \quad (7-1)$$

where θ represents the angle of inclination, M the Mach number, and U the magnitude of the velocity. The subscript 1 designates conditions before the expansion and the subscript 2 designates conditions after the expansion.

For a perfect gas, with $\theta_1 = 0$, Eq (7-1) reduces to

$$\theta_2 = v(M_2) - v(M_1) \quad (7-2)$$

where $v(M)$ is the Prandtl-Meyer function (Anderson, 1990:134)

$$v(M) = \sqrt{\frac{\gamma+1}{\gamma-1}} \tan^{-1} \sqrt{\frac{\gamma+1}{\gamma-1} (M^2 - 1)} - \tan^{-1} \sqrt{M^2 - 1} \quad (7-3)$$

For given Mach numbers before and after the expansion fan, the expansion angle θ_2 can be calculated from Eqs (7-2) and (7-3). However, for most applications, the angle θ_2 and M_1 are known and M_2 is unknown. The calculation of $v(M_1)$ and $v(M_2)$ is straightforward, but M_2 must be calculated through an iterative procedure or the use of tables. The forward and rear Mach lines can be calculated from

$$\mu = \sin^{-1}(1/M) \quad (7-4)$$

Since the expansion is isentropic, total pressure, temperature, and density are preserved. Thus, pressure, temperature, and density after the expansion can be calculated by using the perfect gas equations for total properties. A maximum value exists for the Prandtl-Meyer function which can be derived by letting M go to infinity. The maximum value is given by

$$\lim_{M \rightarrow \infty} v(M) = \left(\sqrt{\frac{\gamma+1}{\gamma-1}} - 1 \right) \frac{\pi}{2} \quad (7-5)$$

The maximum turning angle can then be derived from Eq (7-2)

$$\theta_{2(\max)} = \left(\sqrt{\frac{\gamma+1}{\gamma-1}} - 1 \right) \frac{\pi}{2} - v(M_1) \quad (7-6)$$

For high temperatures, Eq (7-1) must be solved numerically. If equilibrium chemistry is used, the relevant polynomial curve fits are represented by

$$h = h(p, \rho) \quad (7-7)$$

$$T = T(p, \rho) \quad (7-8)$$

$$\rho = \rho(p, s) \quad (7-9)$$

$$a = a(p, s) \quad (7-10)$$

In addition, the following definition of total enthalpy is used:

$$h_t = h + \frac{U^2}{2} = \text{const} \quad (6-3c)$$

where U is the magnitude of the velocity vector. Equation (7-1) is evaluated numerically by using Simpson's 1/3 rule in the following form, which is derived from Eq (7-1):

$$\begin{aligned} \theta_2 = & \sum_{i=1}^{n-1} \frac{\Delta U_1}{6} \left(\frac{\sqrt{M_i^2 - 1}}{U_i} + \frac{\sqrt{M_{i+1/2}^2 - 1}}{U_{i+1/2}} + \frac{\sqrt{M_{i+1}^2 - 1}}{U_{i+1}} \right) \\ & + \frac{\Delta U_2}{6} \left(\frac{\sqrt{M_n^2 - 1}}{U_n} + \frac{\sqrt{M_{n+1/2}^2 - 1}}{U_{n+1/2}} + \frac{\sqrt{M_{n+1}^2 - 1}}{U_{n+1}} \right) \end{aligned} \quad (7-11)$$

Equation (7-11) uses n increments of width ΔU_1 and one smaller increment of width ΔU_2 . For a given expansion angle θ_2 , the interval width ΔU_1 is specified. The number of increments, n , is initially unknown, but can be estimated using the perfect gas solution. The integration is carried out until the summation exceeds the specified angle θ_2 . The summation is then backed up to the previous spatial step, and an iterative process is carried out to determine the proper value of ΔU_2 that will match the specified value of θ_2 . Details of the iterative procedure are given in Appendix D. The temperature can be evaluated from the polynomial curve fit represented by Eq (7-8).

7.3.1.3. Wake Region

The wake flow will be approximated by an expansion fan at the corner followed by an oblique shock to turn the flow back parallel to the tunnel wall. Although a 90 degree turn with an expansion fan is theoretically possible using Eq (7-6) up to a Mach number of 2.56, a 90 degree deflection by an oblique shock is not possible (the maximum compression turning angle increases as Mach number increases but approaches a maximum value of 46 degrees as the Mach number goes to infinity). In addition, the boundary layer on the

shoulder cannot be turned by as great an angle as inviscid theory would predict for the freestream. Therefore, a region of stagnant or recirculating air exists immediately behind the body (Krieger and Vukelich, 1986:398-399) (Figure 7-9). The pressure in this stagnation region can be predicted by an empirical correlation (Stoney, 1961), which predicts the base pressure coefficient to be

$$C_p = -.12 \quad (7-12)$$

where the pressure coefficient is defined as

$$C_p = \frac{p - p_\infty}{\frac{1}{2} \rho_\infty U_\infty^2} \quad (7-13)$$

The inviscid wake the uses an iterative procedure to match the base pressure predicted by Eq (7-12).

7.3.2. Swept Shock/Boundary Layer Interaction

The separation of the boundary layer occurs only when the sweep angle is high enough. An empirical relation to predict separation was developed by Korkegi (1973):

$$M_\infty \alpha_i = 0.364 \quad (7-14)$$

where α_i is the sweep angle in radians. For the shock tunnel, with $M=2.89$, Eq (7-14)

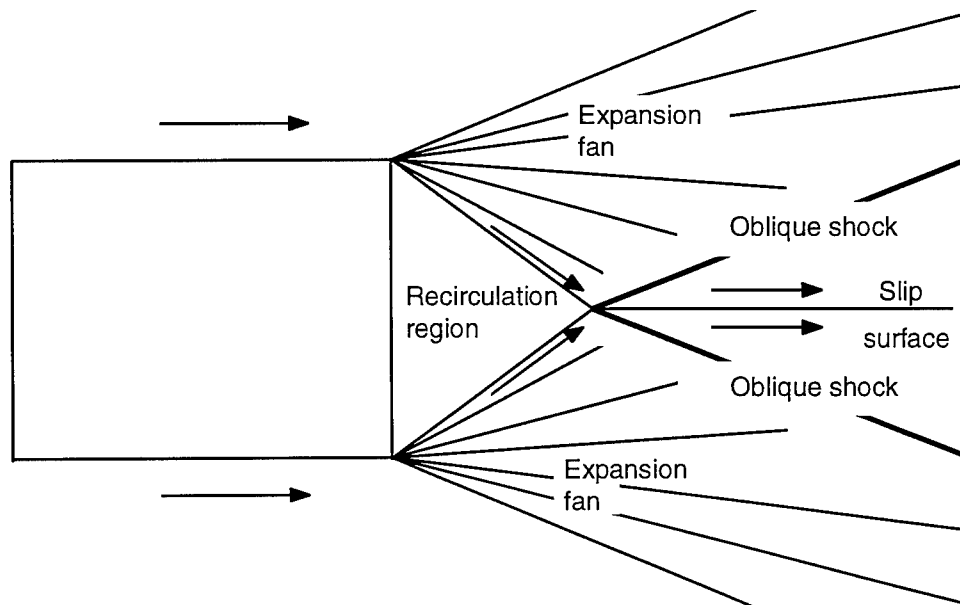


Figure 7-9 Wake Region

predicts the minimum sweep angle for boundary layer separation as 7.22 degrees.

Peak pressure and heating on the flat plate in the region of the shock are given by two empirical correlations developed by Hayes (1977):

$$\frac{P_{pk}}{P_{fp}} = (M_{\infty} \sin \theta)^{n_p} \quad (7-15)$$

$$\frac{St_{pk}}{St_{fp}} = (M_{\infty} \sin \theta - 1)n_{St} + 0.75 \quad (7-16)$$

The subscript pk denotes the peak value, while fp denotes the undisturbed flat plate value. The Stanton number is represented by St, and θ represents the shock angle. The constants n_p and n_{St} are empirical values derived from experimental values. For Mach 2.95, the closest Mach number for which the constants were reported, $n_p=2.7$ and $n_{St}=4.3$. The Stanton number is used to derive the heat flux using the equation (see Chapter 2)

$$\dot{q}_w = St_p u_e (h_{aw} - h_w) \quad (7-17)$$

The Stanton number can be derived from the skin friction coefficient using the Reynolds analogy (Cebeci and Bradshaw, 1984:349):

$$St = 1.16 \frac{C_f}{2} \quad (2-7a)$$

The factor 1.16 is called the Reynolds analogy factor, which is sometimes taken as unity.

Equation (7-15) were used to determine what maximum pressure to expect the pressure transducers to measure, while Eqs (7-16), (7-17), and (2-7a) were used to evaluate heating rates to ensure the plastic skin friction gages did not melt.

7.3.3. Design Factors

Two design factors were applied to the design and positioning of the fin. The objective of the first design factor is to ensure that the interaction of the reflected shocks do not propagate forward through the subsonic region of the boundary layer to affect the forces on the fin. For a two dimensional object, Allen and Spiegel (1961:674) state that the intersection point should be at least 1/2 the chord length aft of the object. Allen and

Spiegel calculate the distance in terms of the Mach angle, with the following equation given for the intersection point (Allen and Spiegel, 1961:673):

$$x_w = y_w \sqrt{M_\infty^2 - 1} \quad (7-19)$$

Here, x_w is the distance from the leading edge of the object to the intersection of the reflected Mach waves, and y_w is the width of the tunnel test section. Using the actual shocks instead of the Mach waves is a more stringent criteria because the shock angle is greater than the angle of the Mach waves.

The object of the second design criterion given by Allen and Spiegel is to prevent the tunnel from choking due to the obstruction created by the model. For air with $\gamma=1.4$, this criterion is stated as

$$\frac{A_m}{A_w} \leq \frac{M_\infty}{\left[1 + \frac{M_\infty^2 - 1}{6}\right]^3} \quad (7-20)$$

Here A_m is the unobstructed area of the tunnel (tunnel cross-sectional area less the effective frontal area of the model, to included boundary layer effects) and A_w is the cross-sectional area of the test section. If a Mach number of 2.5 is used (in case the actual Mach number is somewhat lower than the predicted Mach number), the ratio A_m/A_w is 0.379. With a 3.81 cm wide tunnel test section, the maximum width of the model is then 1.44 cm. For Mach 3, the ratio $A_m/A_w = 0.236$, and the maximum model width is 0.9 cm. Equation (7-20) is actually more critical for transonic flow; for supersonic flow, if the first design factor (that the reflected shocks should not intersect less than 1/2 the chord length aft of the body) is met, then the criterion expressed by Eq (7-21) will almost certainly be met. However, for the fin used, the first design criteria was only barely met, so Eq (7-20) was also used to verify that the test section would start.

7.3.4. Results of Flowfield Analysis

The results of the flowfield analysis for the fin are summarized in Table 7-1. The peak pressures and heat flux for shock/boundary layer interaction are shown in Table 7-2. As can be seen, the peak pressures in the interaction area are somewhat higher than the

pressure behind the shock. The calculated heat fluxes, even for the freestream, are the same order of magnitude as the inlet heat flux for the NASA Ames shock tunnel runs. While the NASA Ames runs had higher total enthalpy, the AFIT tests used higher density gas; the heat flux is directly proportional to the density if other factors are held constant.

Table 7-1 Calculated Flow Conditions

	Pressure (kPa)	Density (kg/m ³)	Temp (K)	Velocity (m/s)	Mach No.	Deflection angle (deg)	Shock angle (deg)	Mach angle (deg)	Dynamic Pressure (kPa)
Freestream	114.7	0.973	410.6	1173.9	2.89				670.4
Leading shock						10.3	28.4		
Wedge	234.8	1.608	508.8	1086.2	2.42			24.4	948.7
Shoulder	116.4	0.977	415.1	1169.6	2.87	10.3		20.4	668.5
Wake exp.	36.2	0.435	290.1	1272.4	3.71	14.9		15.6	
Wake shock						28.1	43.3		
Wake	271.7	1.506	628.6	960.0	1.95				
Reflected shock						10.3	32.8		
After re- flected shock	433.7	2.501	604.1	988.3	2.02				

**Table 7-2 Peak heat flux and pressure for the swept-shock/
boundary layer interaction**

	Pressures (kPa)		Peak heating	
	Peak	Post-shock	Stanton No.	Heat flux (W/m ²)
Freestream	114.7		.001451	2,165,000
10° deflection	267.2	234.8	.003236	4,828,000

7.4. Experimental Setup

This section describes the starting dynamics of the test section, the instrumentation, and the data collection and processing for the experiment.

7.4.1. Starting Dynamics

The starting dynamics with the fin required more time to stabilize than without the fin, apparently due to transient shock reflections. Figure 7-10 shows a plot of the pressure trace immediately in front of the swept shock overlaid on the nozzle exit pressure trace. The high pressure in the location in front of the shock is part of the starting dynamics. At the point that the test section pressure dips and matches the nozzle exit pressure, the steady flow has started. Because of the longer starting dynamics, it was necessary to use some of the measurements after the second shock reflection. From the overlaid temperature trace (Figure 7-11), it can be seen that approximately 4 msec of steady, high temperature flow are available after the second shock reflection, so the measurements were taken from this "steady" region of the flow rather than the initial steady flow.

7.4.2. Instrumentation

The test section instrumentation consisted of two skin friction gauges and four pressure transducer, along with the nozzle exit pressure transducer. In addition, the shock tube was equipped with four pressure transducers and a thermocouple as described in

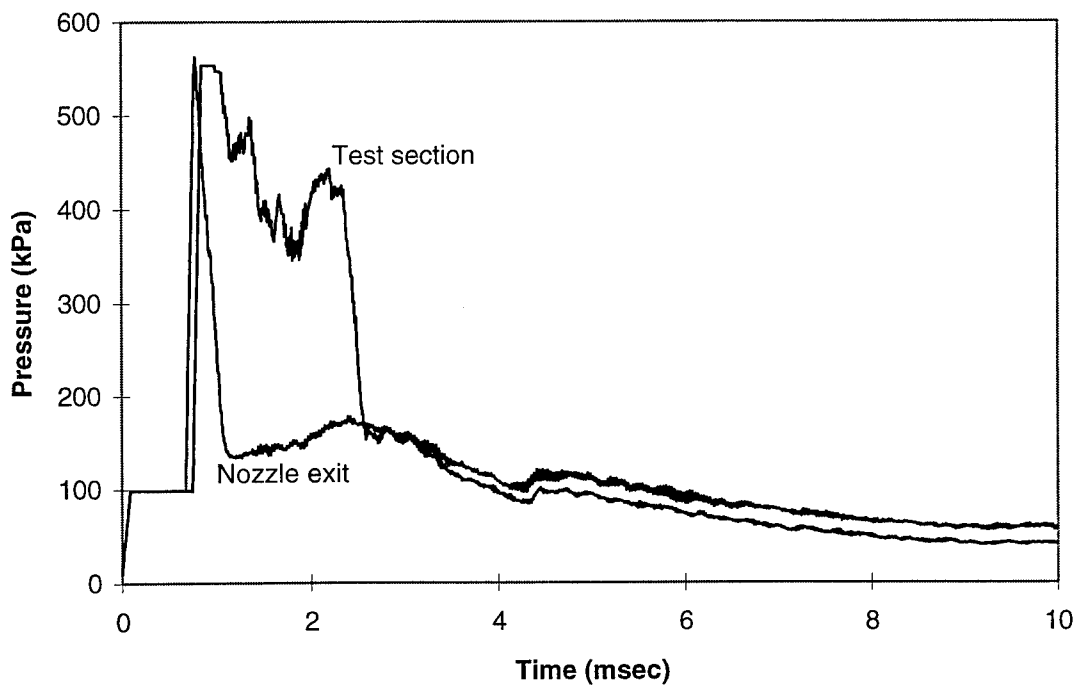


Figure 7-10 Test Section Pressures with Fin, Run 24

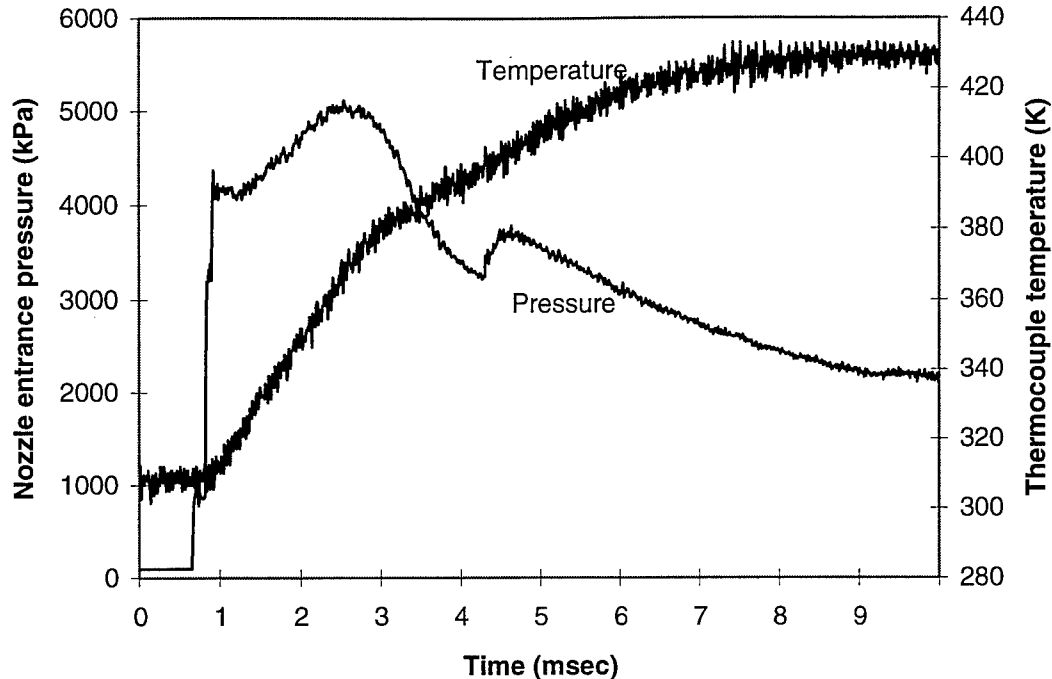


Figure 7-11 Nozzle Entrance Pressure vs. Thermocouple Temperature, Run 24

Chapter 6. Not all of the test section pressure transducers were in the flow for all runs. Some of the runs were conducted with the pressure gradient-compensated skin friction sensor described in Chapter 3. This sensor used four amplifiers, so no other skin friction gauges were used when the combination gauge was in use. Although the pressure gradient part of the gauge failed to work due to strain gauge thermal effects, the lower strain gauges functioned properly and allowed the gauge to be treated as an ordinary directional gauge.

The locations at which measurements were made are shown in Figure 7-12. The exact position of the stations are listed in Table 7-3. The angle of the wheel for station 1a was only 1.6 degrees different than for station 1. For stations 1 and 2, the wheel was turned so that the leading skin friction gauge sensor head was immediately adjacent to the fin (26.9 degrees) while for station 1a, the sensors were centered under the shock at an angle of 28.5 degrees.

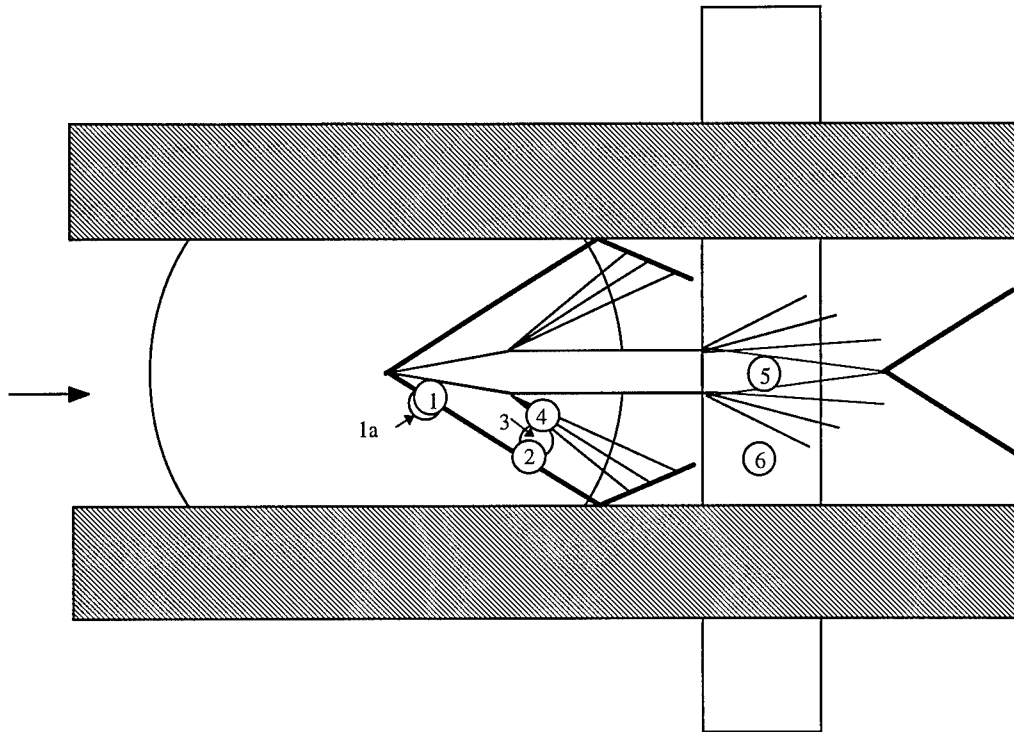


Figure 7-12 Measurement Stations

Table 7-3 Station Positions

Station	Angle (deg)	Distance from vertex (mm)
1	26.9	7.94
1a	28.5	7.94
2	26.9	22.22
3	22.5	22.22
4	14.5	22.22
Station	Distance from centerline (mm)	Distance behind fin (mm)
5	0.	9.52
6	15.87	9.52

The skin friction gauge alignment was measured by conducting an alignment run in which the measurements were taken without the fin. The duct flow is assumed to be without crossflow component, so the flow direction measured by the gauge represents the gauge's alignment angle. The angle of the instrument wheel was set by using calipers along with a micrometer to measure chord length. The micrometer and calipers were also used to measure the position of the instrument strip.

Three directional gauges were used. The combination gauge was used in the instrument wheel for measurements at Station 1a. The 10 kHz directional gauge was used in the instrument wheel for measurements at Stations 1, 3 and 4. The 2 kHz directional gauge was used in the instrument wheel for measurements at Station 2 and in the instrument strip for measurements at Stations 5 and 6. During some of the flat plate alignment runs, the I-beam and stainless steel headed gauges were used in addition to the directional gauges.

7.4.3. Data Reduction and Analysis

Prior to and after each run, atmospheric pressure was measured using a mercury barometer. The ambient air temperature in the driven section was measured prior to the run using a type K thermocouple. Data was collected with two Datalab DL1200 waveform analyzers set at a sampling rate of 100 kHz. The digitized voltages were then downloaded to a computer using DADiSP software. The calibration factors were applied using the DADiSP spreadsheet to calculate skin friction magnitude and direction, pressures, and temperatures. The nozzle entrance and exit pressure traces were smoothed using a DADiSP moving average algorithm (10 point average). These traces were then written to an ASCII file for processing by the shock tunnel data reduction program described in Chapter 6. This program calculated the freestream dynamic pressure, Mach number, velocity, adiabatic wall enthalpy, stagnation temperature, and Reynolds number per meter. This data was then uploaded to DADiSP. The wall shear stress was then normalized by the nozzle exit dynamic pressure, while the pressures were normalized by the nozzle exit pressure.

Because of the unsteady nature of the flow, offsets were used to temporally align the traces. The number of offset points was calculated by matching the second shock reflection in the various pressure traces. The offset for nozzle entrance to nozzle exit was 15-19 points, nozzle exit to Stations 1 and 1a, 4-5 points, nozzle exit to Stations 2, 3, and 4, 7-8 points, and to Stations 5 and 6, 11-12 points. The offset was also performed with the DADiSP software. Reported measurements are averages over 2-4 msec.

7.5. Experimental Results

The measured skin friction coefficients, directions, and normalized pressures for each station are summarized in Table 7-4. For the flow angles, a negative angle represents deflection away from the fin, while a positive angle is deflection toward the fin. The size of the sensor head in the present research is large enough compared to the interaction region that the measurements in Table 7-4 represent an integrated value of the skin friction, rather than a point value.

7.5.1. Shock (Stations 1, 1a, 2, and 2a)

The shock measurements, particularly at Stations 1 and 1a, appear somewhat erratic. However, all of the measurements appear to be consistent with previous measurements and calculations of the swept shock/boundary layer interaction. The erratic nature of the measurements appear to be a function primarily of the unsteady nature of the flow produced by the shock tunnel. While the shock tunnel produces a somewhat steady flow, the Mach number varies slightly throughout the run. This is due primarily to the freestream high temperature effects and the fact that the ratio of specific heats γ is no longer constant. A secondary cause is the varying thickness of the boundary layer in the nozzle due to both the varying freestream pressures and temperatures, as well as the heating of the nozzle walls. All of these effects combine to cause a slight increase in the Mach number during the course of the run.

Table 7-4 Measured Skin Friction and Pressure

Station	Run	Gauge	C_f	$C_f/C_{f\infty}$ (=0.0032)	Yaw (deg)	p/p_∞
1	16	10 kHz	0.0057	1.8	-13.2	
1	17	10 kHz	0.0051	1.6	-27.2	
1	18	10 kHz	0.0040	1.3	0.0	
2	16	2 kHz	0.0071	2.2	-36.2	
2	17	2 kHz	0.0030	0.94	-34.3	
2	18	2 kHz	0.0082	2.6	-36.6	
1a	24	Combination	0.0011	0.34	-62.3/- 19.9	
1a	25	Combination	0.0063	2.0	-25.3	
1a	26	Combination	0.0062	1.9	-51.6	
3	29	10 kHz	0.0039	1.2	-7.9	
4	30	10 kHz	0.0048	1.5	-17.7	
5	29	2 kHz	0.0042	1.3	-0.1	
	24					1.14
	25					1.14
	26					1.15
6	30	2 kHz	0.0026	0.81	17.2	1.17
Flat Plate	21	10 kHz	0.0030	0.94		
		2 kHz	0.0033	1.03		
	32	10 kHz	0.0034	1.06		
		2 kHz	0.0031	0.97		
		I-beam	0.0030	0.94		
	33	10 kHz	0.0022			
		2 kHz	0.0023			
		Stainless Steel	0.0021			

For Mach 3 flow with a deflection of 10 degrees, the separation is marginal. This has been found by other researchers (e.g., Alvi and Settles, 1992), and is also reflected in the Korkegi criterion, Eq (7-15). Thus, small variations in Mach number for this flow can cause the boundary layer to be at various times separated or not separated. Since the Mach number also affects the shock angle, and since the measurement represents an integrated value of the skin friction, rather than a point value, a shift in the shock angle along with a shift in separation and reattachment points, affect the integrated value of both the magnitude and the direction. Figure 7-13 shows the skin friction direction overlaid by the Mach number for Run 24. In this trace, the sudden shift of the direction from -62.3 degrees to -19.9 degrees can be seen as the Mach number passes through 2.92.

Figure 7-14, from a paper by Alvi and Settles (1992), shows skin friction measurements taken by Kim, et al. (1991) in the shock interaction region using the laser interferometer skin friction (LISF) technique. It can be seen that the ratio of $C_f/C_{f\infty}$ varies between 1 and 2.5. This is consistent with the measurements at Stations 1, 1a, 2, and 2a in the present research.

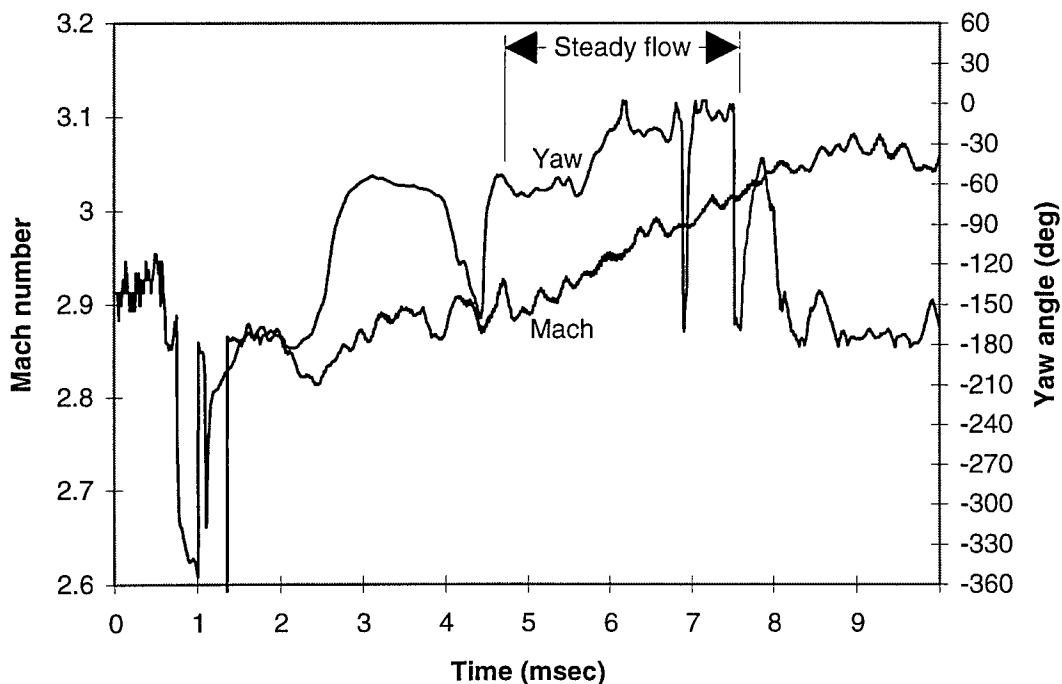


Figure 7-13 Yaw Angle vs. Mach Number, Run 24

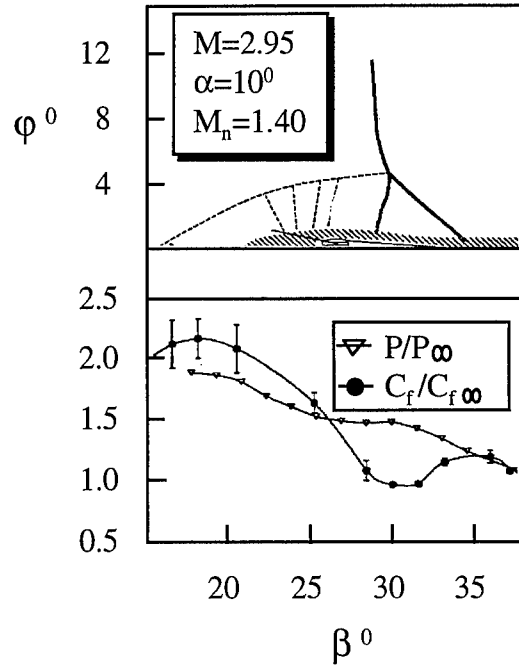


Figure 7-14 Flowfield Map
(Mach 2.9, $\alpha=10$ deg) (Alvi and Settles)

The shear stress directions are also consistent with the directions predicted from CFD analyses and oil flow visualization. The more extreme directions at Station 1 in Runs 24 and 26 (-51.6 degrees and -62.3 degrees) probably are a result of flow recirculation under the separation bubble. Flow recirculation perpendicular to the shock would have an angle of -188.5 degrees; however, the flow recirculation is not perpendicular to the shock, and the effect is muted somewhat by the surrounding flow. In particular, the very low C_f for Run 24, coupled with the extreme angle of -62.3 degrees suggests flow recirculation.

One final factor that may account for the erratic nature of these results is that the shock wave/boundary layer interaction is inherently unsteady (Alvi and Settles, 1992). With a shock tunnel, only a few msec are captured, and, due to the unsteady nature of the interaction, results may differ even if the operating conditions were exactly the same between runs.

The analysis of pressure gradient sensitivity in Chapter 3 indicated that the 2 kHz gauge could have some sensitivity to a large pressure gradient such as a shock. Since the 2 kHz gauge was used under the shock in Runs 16-18, a pressure gradient compensation

was calculated. For the location at which the gauge was used, the head covered an arc about 16 degrees wide. From Figure 7-14, it can be seen that the pressure difference across a 16 degree arc is about 80 percent of the total pressure difference induced by the shock. A linear pressure gradient was calculated using this pressure difference divided by the width of the sensor head. The pressure gradient sensitivity factor from Chapter 3 was then used to calculate the indicated wall shear stress that this would cause. The calculated false wall shear was taken to be perpendicular to the shock and was then resolved into vector components and subtracted out of the measurement. It was found that this correction did not noticeably affect the magnitude of the result but did decrease the yaw angle 8-12 degrees. If this is an accurate correction, then it would indicate that the flow is not separated in this region because the yaw angle would be slightly less than the shock angle.

The large dip in the directional trace in Figure 7-13 ($t=4.4$ msec) coincides with the second shock reflection. The effect of this and other transient shocks is dramatic compared to that of standing shocks. This may be due to the transient shock not being diffused by a boundary layer.

7.5.2. Flow between shock and expansion (Station 3)

An angle of -7.9 degrees was measured compared to the expected value of -10.3 degrees. This may be due to inaccuracy of the gauge; however, the boundary layer effects of both the shock and the expansion impinged somewhat on the sensor, so the value could represent simply the integrated effect for this region. The expansion, in particular, turns the flow back to an angle of zero, so the impingement of the expansion could lessen the flow angle. The shear stress magnitude appears reasonable.

7.5.3. Expansion (Station 4)

This station is centered under the expansion, which because of its narrow width, is a very sudden change in pressure almost akin to a shock (but with the direction reversed). The measured skin friction appears reasonable, but the direction does not. Based on the inviscid analysis, the surface flow direction for this station should be between -10.3 degrees and zero. The measured direction is -17.7 degrees. However, recall that at Stations

1 and 2, the surface flow angles away from the fin were also much greater than would be expected from the inviscid analysis. Hence, the likely reason for the high angle is that the flow deep in the boundary layer has not had sufficient space to recover to the expected value.

If this is a pressure gradient induced effect, then the likely cause for the expansion to result in a pressure gradient effect, but not the shock, is that the expansion probably does not separate the boundary layer and diffuse the surface pressure as the shock does.

A third possibility is that the expansion does separate the boundary layer, and that the odd angle is due to flow recirculation. While expansions normally do not result in boundary layer separation, this is a three-dimensional interaction with the expansion perpendicular to the boundary layer. The expansion turns the flow almost as rapidly as a shock would, and it may not be possible for the viscous boundary layer be turned at an angle of 10.3 degrees in the space of 4 mm without separating.

7.5.4. Wake (Stations 5 and 6)

Both the direction and the magnitude of the wake measurements appear reasonable. The pressure measurements in the wake region show that there are no large pressure gradients, so these measurements should be unaffected by pressure gradients. At Station 6, the turning of the flow toward the center is expected due to the lower pressure in the center. The slightly increased magnitude along the center (Station 5) as compared to the flat plate data is somewhat surprising. However, the flow field is significantly more complicated than Figure 7-12 implies. For example, the wave structure off of the base recirculation is uncharacterized here. The data at Station 6 show that the duct flow C_f is reasonably recovered downstream of the shock and expansion waves.

7.5.5. Flat Plate

The flat plate measurements show the undisturbed skin friction coefficient to be approximately 0.0030 to 0.00335. The results in Run 33 are somewhat low; however, this run was not at the test condition. A premature diaphragm burst occurred for this run. As happened on several occasions for premature bursts, the shock was stronger, resulting in

higher nozzle entrance pressure, higher dynamic pressure and consequently lower C_f . However, although not representative of the test condition, this run is interesting because of the consistency of the results between the three skin friction gauges, particularly the stainless steel headed hollow-beam gauge, which closely matched the two plastic gauges. The success of the stainless steel gauge in this run is apparently due to the addition of the dump tank, which lessened the starting recoil, and the high viscosity oil used (1000 cSt vs. 350 cSt for earlier runs) which provided greater damping.

VIII. Conclusions and Recommendations

This chapter presents the conclusions that can be drawn from the overall research effort, as well as recommended avenues for future research and lessons learned regarding the design and construction of cantilever skin friction gauges.

8.1. Conclusions

The cantilever skin friction gauge has proven to be a valuable and robust tool for characterizing viscous effects in high enthalpy flows. Further, the new gauge designs developed through this research effort have improved the capability of resolving the skin friction force in complex flowfields. The I-beam gauge has made it possible to measure skin friction in very short duration facilities such as the GASL Hypulse facility, while the directional gauge has made it possible to resolve not only wall shear stress but also direction in high enthalpy tests. This may be particularly useful in combustor tests. In addition, the directional gauge technology can be transferred to other flow conditions not requiring high frequency response. Finally, the analysis of the skin friction gauge design has increased the confidence in these designs and provided a way to quantify the uncertainty associated with the measurements.

The measurements undertaken in various scramjet tests as part of this research have aided in understanding the complex flowfields and wall shear stresses in scramjet inlets and combustors. These measurements have been used by the scramjet designers in analyzing test data to determine the efficiency of their designs. Gauge usability was enhanced by the analysis of the oil and damping effects undertaken in this research. This analysis made possible the skin friction measurements in the GASL test, where the gauges were operated in an inverted position.

The directional gauge successfully resolved the wall shear stress magnitude and direction in the flow about the sharp fin. These measurements have provided the aerospace technical community with increased visibility into the complex viscous interactions

associated with a shock impinging on a boundary layer. Due to the size of the sensor relative to the flow area, the measurements represent an integrated valued of the skin friction over the surface of the gauge. Given this proviso, the directional skin friction gauges appear to have provided accurate measurements of the skin friction in all locations.

In addition to these general observations, a few specific observations are offered:

8.1.1. Pressure Gradient Sensitivity

The cantilever skin friction gauge appears to be relatively insensitive to pressure gradients. While insensitivity to mild pressure gradients was expected, it was initially thought that large pressure gradients such as shock waves would impart a bending moment to the sensor that would affect the accuracy of the result. This does not appear to be the case. Transient shocks, particularly those associated with the shock tunnel start, cause a large deflection but in the opposite direction from what the pressure gradient would cause. The reason appears to be that the large deflection is either a large wall shear stress value associated with high pressure and low Reynolds number, or a more complicated interaction involving the pressure gradient being transmitted through the oil.

Sensitivity to the pressure gradient associated with a swept shock was not observed. While some error may be present in the measurement due to pressure gradient, the error is less than the magnitude of the expected skin friction and thus is not readily discernible. Skin friction measurements in the swept shock region are rare, and comparison with the few that do exist indicate that the measurements described in Chapter 7 are reasonable.

The relative insensitivity to the pressure gradient has been observed by other researchers, including Novean (1996:92-105) and Hirt, et al. (1986). Hirt et al. believed that surface tension effects of the oil would completely compensate for the pressure gradient effect. Novean, who measured skin friction with the cantilever gauge in a shock impingement/boundary layer interaction, found that the oil-filled gauge proved less sensitive to a pressure gradient than a rubber filled gauge. Novean found, however, that the oil-filled gauge was somewhat sensitive to the pressure gradient, but not to the extent pre-

dicted by a bending moment. The swept shock/boundary layer interaction, however, diffuses the pressure gradient to a greater extent than the shock impingement, and therefore the pressure gradient effect may be insignificant.

From the mechanism described in Chapter 3 for pressure gradient effects, it appears that the gauge geometry can be designed to avoid pressure gradient sensitivity, at least for a linear pressure distribution. In fact, the baseline gauge met the criteria for pressure gradient insensitivity. This could explain why the gauges proved relatively insensitive to even the large pressure gradient associated with a shock.

It has been suggested that a second set of strain gauges mounted higher on the beam would allow compensation for pressure gradient by measuring the pure bending moment imparted by the pressure differences across the sensor head. However, a pressure gradient appears to cause, not just a pure bending moment, but also a significant lateral force due to the pressure imbalance on the edge of the head. The lateral force is an end-loading just as the wall shear stress is and cannot be compensated for by strain measurements. Since the lateral force is in the opposite direction to the bending moment, eliminating the bending moment but not the lateral force would magnify the error. In addition, a pressure mismatch between the upper and lower surfaces of the sensor head could cause a compressive effect. Compression can cause a change in the voltage reading if the strain gauges are not perfectly aligned or have slightly different gauge factors. For a constant diameter beam, any compression should be constant along the length, so the compressive effect could be measured by another set of strain gauges.

8.1.2. Gauge Performance

It appears that the best way to improve the gauge performance without otherwise coming up with a radical design is to make the head thinner. This was done with both the I-beam gauge and the 2 kHz directional gauge and has not affected durability. The thinner head has two advantages: it increases frequency response with no loss of sensitivity, and it also improves the oil damping by decreasing the mass.

If future gauges are to be continued to be oil filled, then two recommendations are made: use the highest viscosity oil possible and use the repeated application of vacuum method to fill. The higher viscosity improves oil retention and damping, while the repeated application of vacuum ensures that the gauge is more completely filled.

8.1.3. Error Analysis

No significant sources of error were discovered in the analysis of the gauge response. The largest potential sources of error were the thermal differences between the gauge and the wall and the normal pressure sensitivity; however, both of these effects were relatively small. A summary of the potential errors discussed in this dissertation is presented in Appendix G.

8.1.4. AFIT Shock Tunnel

The AFIT high pressure shock tunnel has proven to be a valuable research tool. Once the initial difficulties associated with inconsistent diaphragm bursts were overcome, the shock tunnel provided consistent, repeatable performance. In addition, the data reduction program that was developed as part of this research effort will provide future researchers with a useful tool to compute test section freestream data from the measured pressures. However, a few factors need to be looked at by future researchers who use this facility. First, the driven section may be too long. The purpose of a long driver is to obtain longer test times. However, with the shock attenuation, the shock slows down and eventually moves no faster than the contact surface (Mirels, 1964). Additional length beyond this point provides further attenuation of the shock with no increase in test time.

One other factor that needs to be looked at is how to decrease the vibrational effects, perhaps by bolting the shock tunnel to the floor.

8.2. Recommended Further Research

Two variations to the cantilever skin friction gauge are worthy of further study. These are an aluminum skin friction gauge and a variation on the rubber filled gauge

8.2.1. Aluminum Gauge

Metal gauges have not been used in the field of high enthalpy skin friction sensing because of the lower frequency response. However, the introduction of the I-beam gauge will not only allow measurement of skin friction in short duration facilities, but it will also allow construction of a 10 kHz aluminum gauge. Although the aluminum gauge will have a lower natural frequency than the plastic I-beam gauge, the aluminum gauge will have the advantage of being more durable. The aluminum gauge can, therefore, be used in situations where the steady flow is of long enough duration to allow the use of the lower natural frequency. In the case of facilities with very short test times (i.e., on the order of microseconds), or in which driver combustion products are not exhausted into the test section, durability of the plastic gauge will probably not be a concern because the heating effect, though intense, is too short in duration to melt the plastic.

The numerical heat transfer analysis described in Section 3.6.3 was used to predict the depth of heat penetration for the aluminum skin friction gauge. It was found that, for the thermal load predicted for the NASA Ames shock tunnel tests, the heat did not penetrate to the strain gauges. It can be concluded, therefore, that an aluminum gauge is practical from the heat transfer aspects

8.2.2. Rubber-Filled Gauge

As an alternative to an oil-filled gauge, a gauge in which the strain gauges are encased in rubber should be evaluated. Researchers at Virginia Tech, under the supervision of Dr. Schetz, have evaluated a skin friction gauge with the oil cavity completely filled with rubber (Novean, 1996). A liquid rubber is used which is mixed with a catalyst to solidify under vacuum. Several of these gauges were used with satisfactory results in the NASA Ames scramjet tests (Novean, Schetz, Hazelton, and Bowersox, 1995). However, this arrangement has the disadvantage of decreasing the gauge sensitivity, as well as introducing possible sensitivity to normal pressure variations due to air bubbles or cavities in the rubber. A method in which the strain gauges are encased in rubber, but the cavity is not filled completely with rubber (Figure 8-1), might alleviate these problems. With such

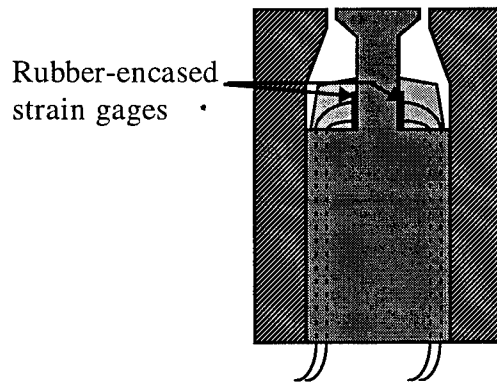


Figure 8-1 Skin friction gauge with rubber-encased strain gauges

a method, the rubber would serve to thermally isolate the strain gauges without greatly affecting the sensitivity.

The rubber encasing could be used in conjunction with oil filling, provided the oil does not cause the rubber to deteriorate, but another method of operation may be to simply let the air circulate in the cavity. The gap around the sensor head is small enough that it would not affect the air flow, much as a pressure port does not affect the air flow. Although encasing the strain gauges in rubber would have the disadvantage of removing the damping property of the oil, the damping is thought to be of only secondary importance; internal friction and viscoelasticity provide some damping, and even a vibration with very little damping tends to die out after several oscillations. When the skin friction gauge in the Wright Lab's Mach 6 test was used without oil, the only difference in the response appeared to be due to uneven heating of the strain gauges.

This type of gauge design used without oil may be more sensitive to pressure gradient effects, since some researchers believe the oil prevents pressure gradient effects. However, one way to compensate for this would be to fill the gap with oil but not the cavity. This method was used by Hirt, et al.; the surface tension alone is sufficient to retain the oil in the gap. To prevent pressure differences from blowing the oil out of the gap, Hirt et al. used a vent hole connected to the flow aft of the gauge. This could also be used with the skin friction gauge with rubber encased strain gauges.

8.3. Lessons Learned

In the three years the present researcher spent improving the cantilever skin friction gauge and developing variations there-on, much of a practical nature was learned regarding construction of the gauges. The following are offered as advice to future researchers who use this method of skin friction measurement.

8.3.1. Sensor base diameter

The larger the diameter of the sensor base, the more room for soldering. This is particularly important with the directional gauge, for which 8 solder points are required, or the combination gauge, with 16 solder points. Use as large a sensor base as the external diameter of the housing allows.

8.3.2. Metal versus plastic housing

Stainless steel housings were used on the Mach 6 gauges with plastic on the other gauges. The metal has the advantage of being a closer thermal match to the model surface (so only the sensor head itself is a mismatch). A metal housing is also stiffer, so that oil will not be squeezed out when the gauge is tightened into the model. Finally the metal housing will not suffer surface degradation. One potential disadvantage of the metal housing is lack of thermal isolation; however, the oil should thermally isolate the strain gauges from the metal. A larger problem is electrical isolation of the strain gauge leads. If the leads, part of the wire, or the solder comes into contact with the metal housing, then an electrical short occurs and the gauge will not function. Even if the gauge functions properly initially, the space in the gauge is limited, and the strain gauge leads move when the sensor is deflected, when oil is inserted, and when wind tunnel air blows through the gauge after oil loss. This can cause shorting. Of the five Mach 6 gauges constructed with stainless steel housings, only two functioned properly after assembly.

8.3.3. Wires

For a directional gauge, eight wires must be run through the sensor base to the strain gauge location. It is difficult to place eight wire holes in the sensor base because of

its small size. Two techniques can make this easier. First, the insulation can be stripped from the wire at the point that it enters the sensor base. This allows smaller holes to be used and also allows a better seal to prevent air leaks. Second, two or more wires can be passed through the same hole. One of these can have the insulation stripped to allow for a smaller bore.

The wires going from the outside of the skin friction gauge to the strain gauge leads need to be immobilized to prevent any wire motion on the outside of the assembled gauge from being transmitted to the solder joint and possibly pulling the solder loose or breaking the strain gauge leads. The best technique is to superglue the wires in the holes.

To facilitate soldering of the strain gauge leads, a single strand copper wire was used to pass through the sensor base. The single strand wire was soldered to stronger braided wire at the base of the sensor.

8.3.4. Gluing the strain gauges

Measurements Group M-bond 200 strain gauge glue was used in the present research. A glue package comes with the glue itself and a catalyst, which is applied prior to the glue. The glue is a commercial variety cyanoacrylate-base superglue, but use of the catalyst is essential because the glue will not harden quickly otherwise. Since the strain gauge must be held in place with tweezers by the leads, quick hardening is necessary. Commercial superglues will not work without the catalyst. A spray catalyst was also successfully used on some of the sensors.

The expiration date on the glue needs to be observed; gauges that were constructed in the last part of this research with expired glue (due to the unavailability of unexpired glue) often did not completely bond the strain gauge to the sensor, resulting in reduced sensitivity or non-linear response (if one strain gauge was completely bonded and the other not). This did not happen with unexpired glue, so the age of the glue (or catalyst) was apparently the cause. Glue can also be placed over the back of the strain gauge; this improves adherence but lowers the sensitivity of the sensor by as much as a factor of 2. However, an incompletely bonded sensor can fall off, become partially unglued and

shift the calibration factor, cause a non-linear response, or cause a loss of sensitivity of a factor of 5 or more.

8.3.5. Soldering

Use a soldering iron with a fine point in order to place it more precisely. Pre-tin the wire tips but not the gold leads of the strain gauges (cannot be done without melting the lead). If the heat is adjustable, set the heat on the maximum setting. Pull the lead onto the wire tip, hold it down with another piece of solder, and apply heat. The object is to melt the solder as quickly as possible before something else is accidentally destroyed. A second technique was used in which the solder was melted and the lead was drawn into the melted solder. This was not as durable, however, and the leads tended to pull out of the solder later on after the gauge was assembled.

8.3.6. Assembly of the gauge

The sensor is secured in the housing by a press-fit set pin. To prevent air leaks, the sensor was also glued into the housing with a silicon rubber glue. Epoxy was used on the bottom of the assembled gauge to further immobilize the wires.

Since the sensor surface needs to be absolutely level with the housing surface (not protruding and not being below the sensor surface, the alignment should be performed before the set pin is inserted and before the glue has dried; make sure that the sensor is at the right angle to align with the set pin hole. After the alignment is completed, the set pin can be hammered in using a punch to complete the insertion. If the set pin hole is slightly misaligned, hammering the set pin in will usually enlarge the hole without causing the surface alignment to be altered. Simply inserting the set pin by hand, however, will preserve the original set pin hole and cause the sensor surface to be misaligned.

If the epoxy on the base of the gauge does not extend onto the housing, then the gauge can be more easily disassembled for repairs. If epoxy is placed over the entire base of the sensor, a more secure seal is obtained, but any disassembly for repairs could break the strain gauge leads.

8.3.7. Balancing resistor

If a balancing resistor is added before calibrating, use the resistance that will bring the two resistances closest together. This is so that when the gauge is canted during calibration, the imbalance will not exceed the ability of the amplifier to balance. If a balancing resistor is added after calibrating, use the smallest resistance necessary in order to minimize the error introduced. The Measurements Group 2310 amplifier has a hard time balancing any bridge that has resistors above 350Ω , so use of higher resistance resistors is not recommended if the 2310 amplifier is used. It has also been suggested that the balancing resistor be added in parallel rather than in series to the strain gauge. This could reduce the error associated with changing the resistance of the balancing resistor.

8.3.8. Oiling

The plastic gauges float, even when full of oil, so weights are required to pull the gauges to the bottom of the oil. The gauges need to be in an upright position so that the air can escape through the gap and not be trapped inside the gauge. The best way to weight the gauge and maintain it in an upright position is to use a bolt large enough to fit around the gauge. With the wires looped through the bottom, the gauge will stay in an upright position. Use the highest viscosity oil obtainable; the high viscosity will not prevent the oil from flowing into the gauge, and the critical damping level is at least one order of magnitude higher than the highest viscosity oil commercially available. Use the repeated application of vacuum method to fill the gauge more completely. Each application of vacuum will need to be maintained for some time (often an hour or longer); watch for the bubbles coming out of the oil to stop before releasing vacuum. Upon release of vacuum, the oil flows into the gauge fairly quickly; 10-15 minutes was sufficient for the I-beam gauge at GASL (smallest gap size and highest viscosity oil).

8.3.9. Inserting into model

The skin friction gauges are usually secured in the gauge port with set screws. When the set screws are tightened, the housing is compressed, and oil comes out of the gap. The gauge surface should therefore be cleaned prior to the run.

8.4. Summary

This dissertation has presented a thorough review of the skin friction gauge development and analysis effort undertaken for the purpose of measuring wall shear stress in high enthalpy impulse facilities. While scramjet testing requirements initiated the development of the cantilever skin friction gauge, the improved skin friction gauge can be applied to any short duration measurements.

In the course of this research, skin friction measurements were undertaken in three series of scramjet tests conducted by NASA and the Air Force. The measurements aided the engine designers in understanding the flow conditions in the engine and in assessing the efficiency of their designs. The measurements also contributed to the improvement of the skin friction gauge.

A rigorous analysis of the skin friction gauge was undertaken to assess the accuracy of the gauge, improve durability and usability, and to improve the frequency response. A 30 kHz gauge was developed that successfully measured the wall shear stress in the 0.4 msec GASL tests. A directional gauge was developed to measure both direction and magnitude of the wall shear stress. The directional gauge was demonstrated by measuring the flow about a sharp fin on a flat plate. In support of these measurements, the AFIT shock tunnel was characterized, and a data reduction program was developed.

This further development of the miniature cantilever skin friction gauge has extended the utility of the gauge to more complex flowfields. In addition, the measurements in the scramjet tests have furthered the development of hypersonic airbreathing propulsion systems. Moreover, the accuracy and design considerations of the gauge are now better understood. Finally, a previously uncharacterized flowfield has been measured.

Appendix A - Dimensions and Calibrations

A.1. Skin Friction Gauges

This appendix presents the dimensions and calibration constants for the skin friction gauges. Section A.1.1 presents the sensor dimensions. Section A.1.2 presents the oil cavity volume calculations. Section A.1.3 lists the calibration constants.

A.1.1. Gauge Dimensions

The dimensions of the sensors used in this research are presented in Table A-1. Explanation of nomenclature is shown in Figures A-1 and A-2. The outside dimensions of the housing are shown in Table A-2.

Table A-1 Dimensions of Skin Friction Gauge Sensors

	Baseline	I-beam	Mach 6	Stainless steel head	Directional
Beam length (mm)	6.400	5.000	13.335	13.335	13.500
Beam outer diameter (mm)	2.540	2.000	3.175	3.175	2.500
Beam inner diameter (mm)				1.587	
Flange length (mm)		2.000			
Web length (mm)		1.600			
Flange thickness (mm)		.200			
Web thickness (mm)		.200			
Head diameter (mm)	4.600	3.476	6.350	6.350	6.350
Head tip thickness (mm)	.254	.100	1.270	1.270	.500
Head root thickness (mm)	.762	.200	1.270	1.270	1.000
Sensor head area (mm ²)	16.619	9.490	31.669	31.669	31.669
Sensor base length	12.700	14.100	6.985	6.985	6.820
Sensor base width	9.525	9.525	9.525	9.525	11.100
Elastic modulus (GPa)	3.3	3.3	3.3	3.3	2.6
Moment of Inertia (mm ⁴)	2.04	0.72	4.99	4.99	1.92
Natural frequency (kHz)	10.09	32.14	2.43	1.03	1.63

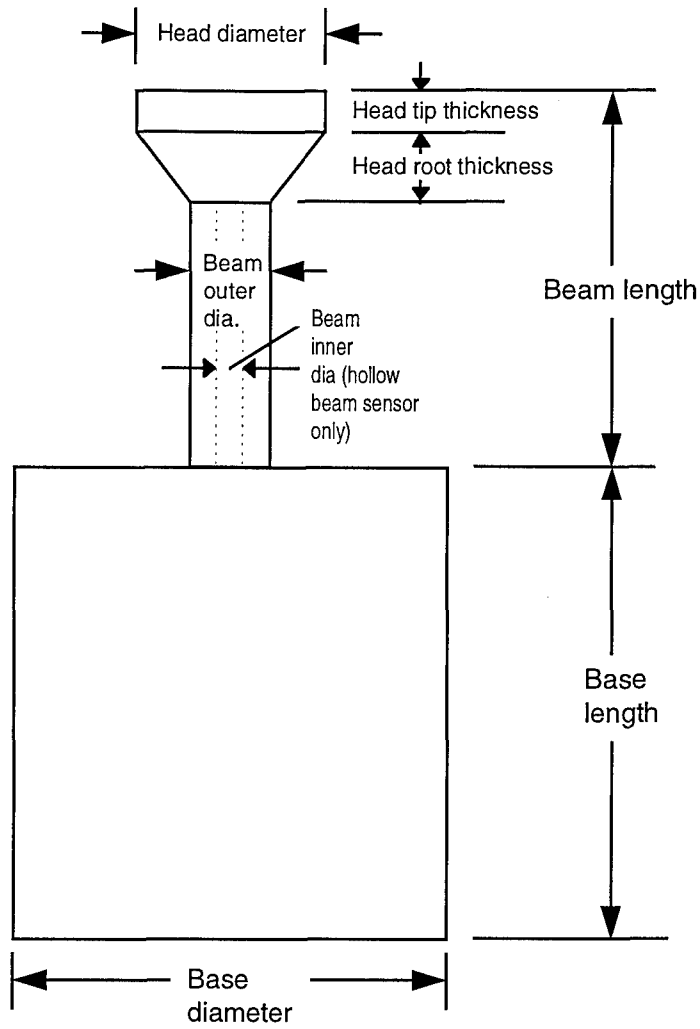


Figure A-1 Sensor Dimension Nomenclature

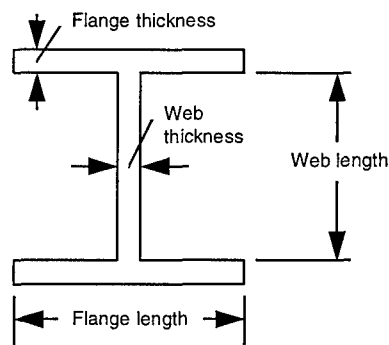


Figure A-2 I-Beam Nomenclature

Table A-2 Skin Friction Gauge Housing Dimensions

	Outer diameter (mm)	Length (mm)	Gap width (mm)
NASA Ames baseline	19.05	19.10	0.127
NASA Ames I-beam	19.05	19.10	0.063
Mach 6	12.70	20.32	0.127
GASL baseline	15.24	19.10	0.127
GASL I-beam	15.24	19.10	0.063
AFIT 2 kHz directional	12.70	20.32	0.127
AFIT 10 kHz directional	12.70	19.10	0.127
AFIT I-beam	12.70	19.10	0.063
AFIT Stainless steel head	12.70	20.32	0.127

A.1.2. Oil Cavity Dimensions and Volume

This appendix presents the calculations for the volume of the oil cavity for the different skin friction gauge designs. This information is used in calculations presented in Section 4.3. The volume of the oil cavity is calculated using the dimensional notation shown in Figure A-3

For the circular regions where the boundaries are vertical, the volume is given by the cross-sectional area times the height. Hence, the volume of the gap (Region G) is given by

$$\begin{aligned} V_G &= T_L (\pi R_O^2 - \pi R_H^2) \\ &= T_L \pi (R_O^2 - R_H^2) \end{aligned} \quad (A-1)$$

The volume of the regions with sloping sides can be calculated by considering the region to be a sum of a sub-region with vertical sides and a second region with triangular shaped side view (Figure A-3). The equation of the sloping side in Figure A-3 can be stated as

$$R = R_1 + \left(\frac{R_2 - R_1}{h} \right) z \quad (A-2)$$

The volume is then given by

$$V = \pi \int_0^h (R_2^2 - R^2) dz \quad (A-3)$$

Substituting Eq (A-2) into Eq (A-3) and integrating results in

$$V = \pi h \left(\frac{2}{3} R_2^2 - \frac{1}{3} R_1 R_2 - \frac{1}{3} R_1^2 \right) \quad (A-4)$$

Using this equation, the volumes of the different regions in Figure A-3 can be calculated as follows:

$$V_G = \pi T_L (R_O^2 - R_H^2)$$

$$V_S = \pi T_S \left[(R_O^2 - R_H^2) + \left(\frac{2}{3} R_H^2 - \frac{1}{3} R_H R_B - \frac{1}{3} R_B^2 \right) \right]$$

$$= \pi T_S \left(R_O^2 - \frac{1}{3} R_H^2 - \frac{1}{3} R_H R_B - \frac{1}{3} R_B^2 \right)$$

$$V_N = \pi T_L (R_O^2 - R_H^2) (h_T - T_S - T_L)$$

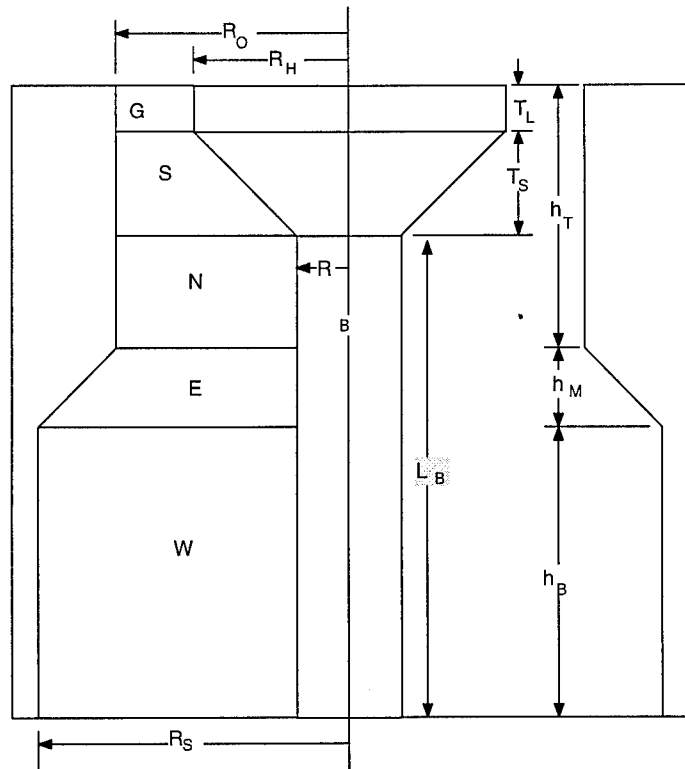


Figure A-3 Oil Cavity Dimension

$$\begin{aligned}
 V_E &= \pi h_M \left[(R_O^2 - R_B^2) + \left(\frac{2}{3} R_S^2 - \frac{1}{3} R_S R_O - \frac{1}{3} R_O^2 \right) \right] \\
 &= \pi h_M \left(\frac{2}{3} R_O^2 - R_B^2 + \frac{2}{3} R_S^2 - \frac{1}{3} R_S R_O \right) \\
 V_W &= \pi h_B (R_S^2 - R_B^2)
 \end{aligned}$$

The total volume of the oil cavity is then given by

$$V = V_G + V_S + V_N + V_E + V_W \quad (\text{A-5})$$

Using these volume equations, the volumes for two typical gages are calculated as shown in Table A-3.

Table A-3 Oil Cavity Volumes

		Ames baseline gauge	Wright Laboratory Mach 6 gauge
<i>Lengths (mm)</i>	R_H	2.30	3.18
	R_B	1.27	1.59
	T_L	0.25	1.27
	T_S	0.76	1.27
	L_B	5.38	10.80
	R_O	2.43	3.30
	R_S	4.76	4.76
	h_T	2.79	5.72
	h_M	2.34	1.27
	h_B	1.27	6.35
<i>Volumes (mm³)</i>	V_G	0.5	3.3
	V_S	6.2	20.0
	V_N	23.9	83.6
	V_E	99.6	58.3
	V_W	84.1	402.1
	V_{tot}	214.3	567.5

A.1.3. Skin Friction Gauge Calibration Constants

Table A-4 lists the calibration values for the single axis skin friction gauges used in this research. Table A-5 lists the directional gauges. Gauge numbers beginning in A were used at NASA Ames, CF were used at GASL, Gauge 4 was used in the Wright Labora-

tory Mach 6 test, and all others were used in the AFIT shock tunnel. The combination skin friction/pressure gradient sensor was used as a directional gauge after the failure of the upper axis; the directional calibration values appear in Table A-5. All calibrations used the Measurements Group 2310 signal conditioning amplifier, set at excitation voltage of 0.5V and gain of 1000.

Table A-4 Skin Friction Gauge Calibration Values

Gauge	Type	A _{actual} (Pa/V)	Gauge	Type	A _{actual} (Pa/V)
A1	Baseline	3964	A11	Baseline	4531
A2	Baseline	4266	A12	Baseline	3323
A3	Baseline	4273	A13	Baseline	3818
A4	Baseline	3362	CFU4	Baseline	4759
A5	Baseline	2654	A14	I-beam	3069
A6	Baseline	2708	A15	I-beam	4168
A7	Baseline	2950	CFU5	I-beam	4930
A8	Baseline	3072	AFIT I-beam	I-beam	18753
A9	Baseline	2921	Gauge 4	Mach 6	2248
A10	Baseline	5701	Gauge 5	Stainless steel	2204
A11	Baseline	4531			

Table A-5 Directional Gauge Calibration Values

	A ₁ (Pa/V)	A ₂ (Pa/V)	α (deg)	ζ (deg)
2 kHz	976.4	-1096.0*	6.06	85.95
10 kHz #1	3345.0	3087.7	-6.91	94.40
10 kHz #2	2919.2	3487.0	17.0	86.1624

*Negative due to voltage response being in opposite direction to that in Figure 3-4

A.2. Instrument Calibration Values

Table A-6 lists the measured gain and excitation voltage for the five Measurements Group 2310 Signal Conditioning Amplifiers used at AFIT. These amplifiers were used to

power the skin friction gauges. The amplifiers were set at a gain of 1000 with excitation of 0.5 volts. The product gain times the voltage is also listed because this product can be used in Eq (2-13) to correct the calibration factors for the skin friction gauges when switching between amplifiers.

Table A-6 Amplifier Gain and Excitation Voltage

Amplifier	Gain	Excitation (Volts)	Gain* Excitation (Volts)
1	1018.505	0.503	512.3078
2	1016.783	0.504	512.4586
3	1009.583	0.501	505.8011
4	997.8057	0.502	500.8985
5	965.0165	0.502	484.4383

Table A-7 lists the calibration factors for the two Datalab DL1200 waveform recorders used with the AFIT high pressure shock tunnel. These factors are for use with the formula

$$\Delta V = (1 + m)(V_{DL} - V_{DL0})$$

For the thermocouple, the inverse function is of the form

$$T = a_4 V^4 + a_3 V^3 + a_2 V^2 + a_1 V + a_0$$

For T in degrees C and V in volts, the coefficients are

$$a_4 = -1.1759424528401E + 09$$

$$a_3 = 4.1412052127580E + 07$$

$$a_2 = -7.6086790508306E + 05$$

$$a_1 = 2.5975680471471E + 04$$

$$a_0 = -5.6239215638161E - 02$$

Table A-7 DL1200 Waveform Recorder Correction Factors

Instrument	Channel	m	Use before Run 16	Use after Run 16
DL 1200 #1	1	-.006245	Pressure	Pressure
	2	.002824	Pressure	Pressure
	3	.000020	Pressure	Pressure
	4	.005479	Pressure	Pressure
	5	.004276	Skin friction	Pressure
	6	.005522	Skin friction	Pressure
	7	.004017	Skin friction	Pressure
	8	.010948	Pressure	Pressure
DL 1200 #2	1	-.001775		Pressure
	2			Pressure
	3	-.003643		Skin friction
	4	-.004641		Skin friction
	5	-.010851		Skin friction
	6	-.003333		Skin friction
	7	-.003272		Skin friction
	8	.003366		Temperature

A.3. Material Properties

A.3.1. Silicone Oil

The oil used in the skin friction gauges was a Dow-Corning Silicone 200 Fluid. Runs at NASA Ames used viscosities of 200 and 350 cSt, GASL 10,000 cSt, and the AFIT measurements about the sharp fin 1,000 cSt. Earlier tests at AFIT used lower viscosities (200 and 350 cSt), while an oiling test run at AFIT in preparation for the GASL tests (Run 14) used 10,000 cSt oil. Other properties of the oil are listed in Table A-8

(Dow-Corning, 1992:2). This table also lists the dimensions used in example calculations in Section 4.3.

Table A-8 Oil Properties and Typical Dimensions for Oil Filling

<i>Oil properties</i>	Viscosity	200, 350, 1000, 10000 cSt
	Surface tension coefficient	21 dynes/cm (0.021 N/m)
	Density	964 kg/m ³
	Thermal Conductivity	0.159 W/m-K
	Thermal Diffusivity	0.1212x10 ⁻⁵ m ² /s
<i>Dimensions used in Chapter 4 example calculations</i>	Acceleration of gravity g	9.81 m/sec ²
	Gap width W	0.000127 m
	Container width D	0.0127 m
	Oil column height h	0.0127
	Back pressure p _b	101300 N/m ²
	Vacuum pressure p _v	5000 N/m ²

A.3.2. Plastic

Two plastics were used to manufacture the skin friction gauges. Most of the gauges were made of Ultem plastic, manufactured by General Electric. The 2 kHz directional gauge was made of Victrex plastic, manufactured by Westlake Plastics. Relevant properties are listed in Table A-9.

Table A-9 Plastic Material Properties

	Ultem	Victrex
Elastic Modulus (GPa)	3.3	2.6
Density (kg/m ³)	1270	1370
Yield strength (MPa)	105	
Thermal conductivity (W/m-K)	0.22	
Thermal diffusivity (m ² /s)	.01533x10 ⁻⁵	

A.3.3. Strain Gauges

Strain gauges were manufactured by Micro Gage. For all of the skin friction gauges except those constructed for the Mach 6 test, a 2.03 mm strain gauge was used (manufacturer's model number 919). The strain gauges used with the Mach 6 sensor were provided by the same manufacturer, but the length was 6.35 mm (model 920). This change was due to the manufacturer being unable to provide any of the shorter strain gauges at the time required; in addition, the longer sensor beam of the Mach 6 gauge could accommodate the longer strain gauge. Strain gauge properties are listed in Table A-110.

Table A-10 Strain Gauge Properties

	Model 919	Model 920
Length (mm)	2.03	6.35
Width (mm)	0.2286	0.2286
Thickness (mm)	0.01016	0.01016
Sensing length (mm)	1.27	4.06
Gauge factor	135	120
Resistance (Ω)	350	350
Elastic Modulus (GPa)	107	107
Type	P	P

A.4. Model and Nozzle

Drawings of the AFIT shock tunnel test section are shown in Figures A-4 through A-7. The nozzle coordinates are shown in Table A-11.

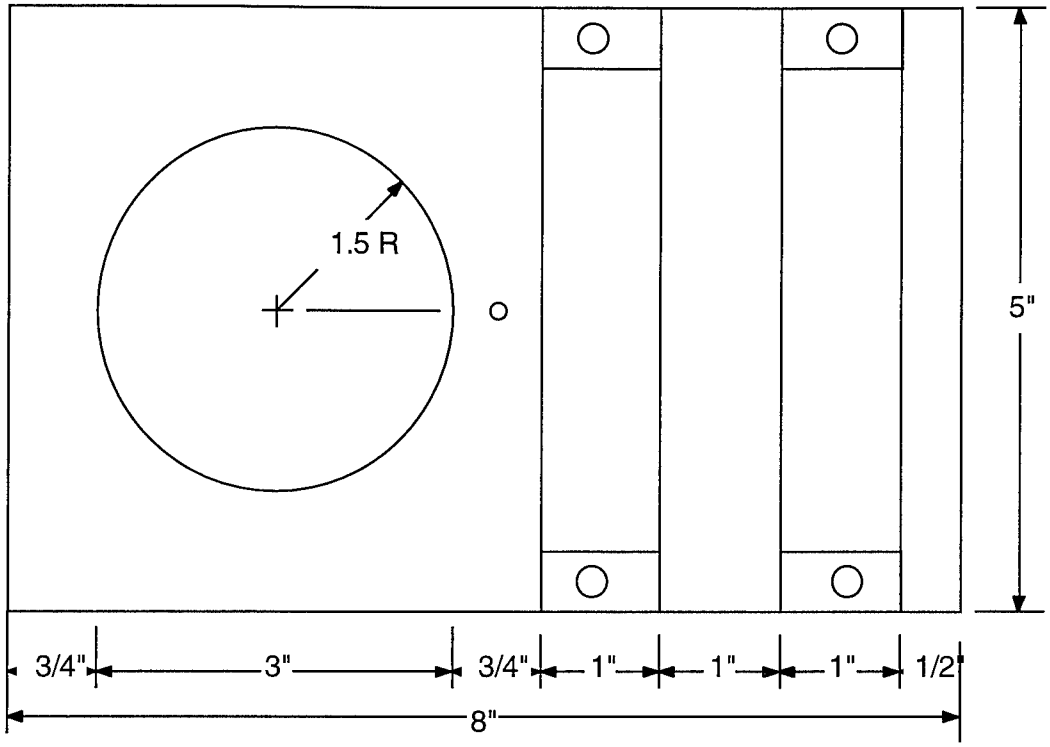


Figure A-4 AFIT Shock Tunnel Test Section Floor (dimensions in inches)

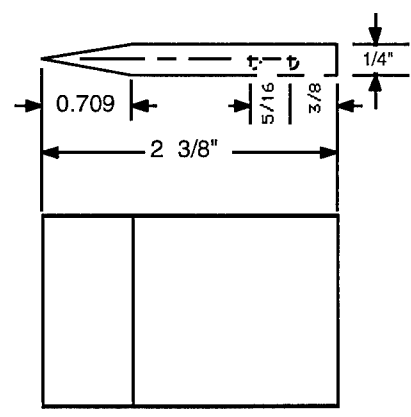


Figure A-5 AFIT Shock Tunnel Test Section Fin (dimensions in inches)

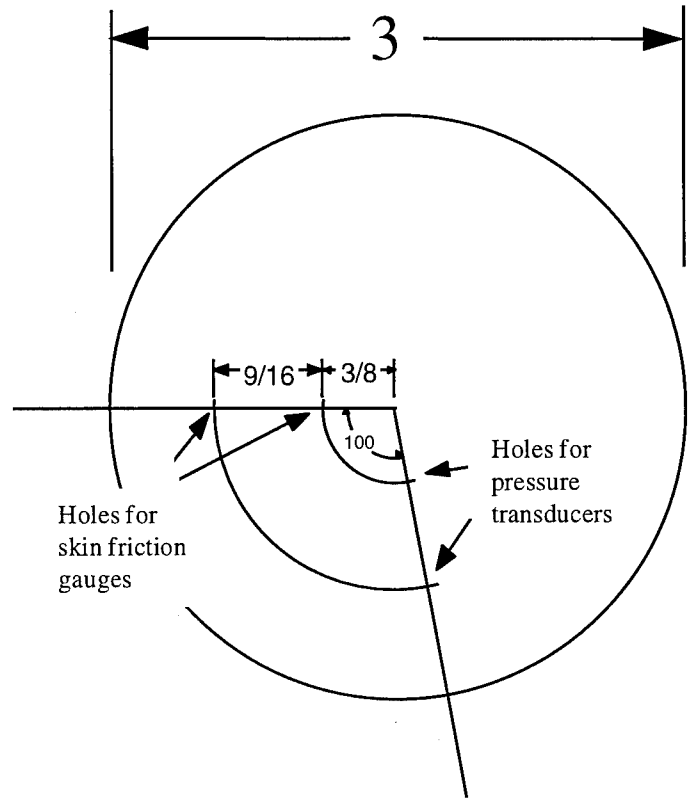


Figure A-6 Instrument Wheel (dimensions in inches)

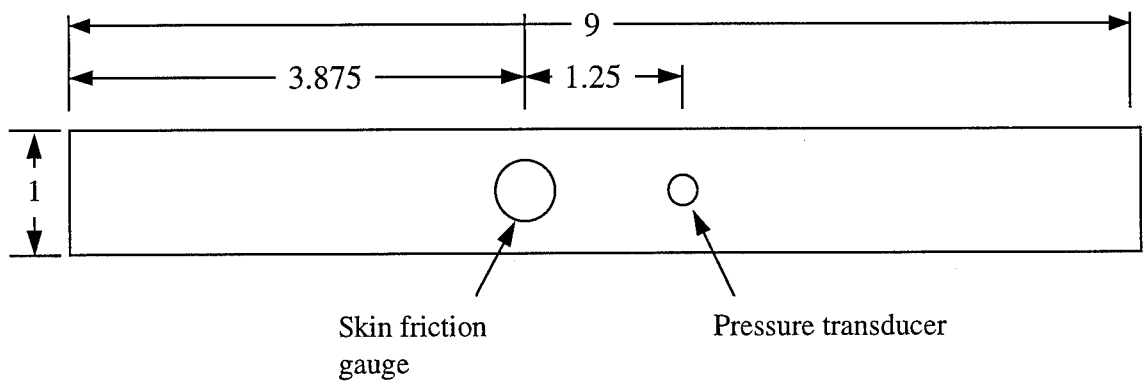


Figure A-7 Instrument Strip (dimensions in inches)

Table A-11 Mach 3 Nozzle Contour

	x (in)	y (in)		x (in)	y (in)		x (in)	y (in)
1	0.0000	0.3479	28	0.1736	0.3752	55	1.5990	0.9325
2	0.0025	0.3479	29	0.1806	0.3773	56	1.6990	0.9615
3	0.0089	0.3481	30	0.1876	0.3795	57	1.8020	0.9904
4	0.0153	0.3483	31	0.1947	0.3820	58	1.9090	1.0190
5	0.0217	0.3485	32	0.2019	0.3844	59	2.0200	1.0480
6	0.0281	0.3489	33	0.2090	0.3871	60	2.1360	1.0760
7	0.0345	0.3492	34	0.2163	0.3897	61	2.2570	1.1050
8	0.0409	0.3497	35	0.2236	0.3926	62	2.3830	1.1320
9	0.0474	0.3502	36	0.2310	0.3955	63	2.5140	1.1610
10	0.0538	0.3509	37	0.2384	0.3986	64	2.6520	1.1870
11	0.0603	0.3515	38	0.2459	0.4017	65	2.7950	1.2150
12	0.0667	0.3523	39	0.2535	0.4050	66	2.9450	1.2420
13	0.0732	0.3531	40	0.2612	0.4085	67	3.1030	1.2670
14	0.0797	0.3541	41	0.2689	0.4120	68	3.2670	1.2930
15	0.0862	0.3550	42	0.3485	0.4495	69	3.4400	1.3170
16	0.0928	0.3560	43	0.5301	0.5329	70	3.6210	1.3410
17	0.0993	0.3572	44	0.6374	0.5805	71	3.8100	1.3640
18	0.1059	0.3584	45	0.7296	0.6202	72	4.0090	1.3860
19	0.1126	0.3597	46	0.8156	0.6560	73	4.2180	1.4050
20	0.1192	0.3610	47	0.8989	0.6897	74	4.4370	1.4240
21	0.1259	0.3626	48	0.9813	0.7221	75	4.6670	1.4420
22	0.1326	0.3640	49	1.0640	0.7533	76	4.9100	1.4580
23	0.1393	0.3656	50	1.1480	0.7841	77	5.1640	1.4710
24	0.1461	0.3674	51	1.2330	0.8143	78	5.4320	1.4830
25	0.1529	0.3692	52	1.3210	0.8442	79	5.7140	1.4910
26	0.1598	0.3711	53	1.4110	0.8738	80	6.0100	1.4970
27	0.1667	0.3730	54	1.5040	0.9032	81	6.3230	1.5000

Appendix B - Mathematical Derivations

B.1. Viscoelastic Cantilever Beam

This section presents the viscoelastic solution to the end-loaded beam. This solution is used in Chapter 3 to analyze the potential error introduced to the skin friction measurement due to the viscoelastic response of the beam. This solution was developed using the elastic-viscoelastic analogy.

As stated by Findley, Lai, and Onaran (1989:115), the elastic-viscoelastic analogy for a linearly viscoelastic beam can be stated as follows:

- (1) Solve the corresponding elastic problem
- (2) Take the Laplace transform of the of the elastic solution
- (3) Replace the elastic modulus E with the Laplace transform of the viscoelastic relaxation modulus, $sE(s)$
- (4) Take the inverse Laplace transform.

The Laplace transform is defined (Findley, Lai, and Onaran, 1989:326):

$$\mathcal{L}\{f(t)\} = F(s) = \int_0^{\infty} e^{-st} f(t) dt \quad (\text{B-1})$$

Laplace transforms of several common functions, which will be used in this analysis, are as follows (Findley, Lai, and Onaran, 1989:331):

<u>f(t)</u>	<u>Laplace transform F(s)</u>	
$H(t)$	$\frac{1}{s}$	(B-2)

$H(t-a)$	$\frac{e^{-as}}{s}$	(B-3)
----------	---------------------	-------

$\delta(t-a)$	e^{-as}	(B-4)
---------------	-----------	-------

$\int_0^t f(\xi)g(t-\xi)d\xi$	$F(s)G(s)$	(B-5)
-------------------------------	------------	-------

In the above equations, the function H is the heaviside function defined by (Stakgold, 1979:47)

$$H(t) = \begin{cases} 0 & t < 0 \\ 1 & t > 0 \end{cases} \quad (\text{B-6})$$

while δ is the Dirac delta function defined by (Stakgold, 1979:53):

$$\int_a^b \delta(x) dx = \begin{cases} 1 & \text{if } (a, b) \text{ contains the origin} \\ 0 & \text{otherwise} \end{cases} \quad (\text{B-7})$$

The last of the transforms, Eq (B-5), is also known as the convolution theorem.

The elastic solution for the beam under end-loading was provided in Section 3.1:

$$\varepsilon_{11} = \frac{P(L - x_1)R}{EI} \quad (\text{B-8})$$

The loading P will now be considered as a step function of time:

$$P(t) = P_0 [H(t) - H(t - t_1)] \quad (\text{B-9})$$

This loading represents a constant load which is abruptly applied at time $t=0$ and abruptly removed at time $t=t_1$. Using this load function, the elastic solution becomes

$$\varepsilon(t) = \frac{P_0 [H(t) - H(t - t_1)] (L - x_1) R}{EI} \quad (\text{B-10})$$

Taking the Laplace transform

$$\varepsilon(s) = \frac{P_0 \left[\frac{1}{s} - \frac{e^{-t_1 s}}{s} \right] (L - x_1) R}{EI} \quad (\text{B-11})$$

The elastic modulus E is now replaced by the Laplace transform of the relaxation modulus, $sE(s)$:

$$\varepsilon(s) = \frac{P_0 \left[\frac{1}{s} - \frac{e^{-t_1 s}}{s} \right] (L - x_1) R}{sE(s)I} \quad (\text{B-12})$$

The following identity is then applied (Findley, Lai, and Onaran, 1989:85):

$$sE(s) = \frac{1}{sJ(s)} \quad (\text{B-13})$$

where $J(s)$ is the Laplace transform of the creep compliance, where the creep compliance is a function that depends on the viscoelastic model. Substituting Eq (B-19) into Eq (B-18),

$$\varepsilon(s) = \left[\frac{P_0(L-x_1)R}{I} \right] [J(s) - e^{-t_1s}J(s)] \quad (\text{B-14})$$

The inverse Laplace transform is now applied, with the convolution theorem used to evaluate the inverse transform of the second term in the second set of brackets:

$$\varepsilon(t) = \left[\frac{P_0(L-x_1)R}{I} \right] \left[J(t) - \int_0^t \delta(\xi - t_1)J(t - \xi)d\xi \right] \quad (\text{B-15})$$

In Eq (B-19), the term $\delta(\xi - t_1)$ represents the inverse Laplace transform of e^{-t_1s} , as shown in Eq (B-11). To evaluate the integral in Eq (B-15), the sifting property of the Dirac delta function is used (Stakgold, 1979:54):

$$\int_a^b \delta(\xi - x)\phi(\xi)d\xi = \begin{cases} \phi(x) & \text{if } a < x < b \\ 0 & \text{if } x < a \text{ or } x > b \end{cases} \quad (\text{B-16})$$

In terms of the integral in Eq (B-15), the sifting property can be stated as

$$\int_0^t \delta(\xi - t_1)J(t - \xi)d\xi = \begin{cases} J(t - t_1) & \text{if } 0 < t_1 < t \\ 0 & \text{if } t_1 > t \end{cases} \quad (\text{B-17})$$

This result can be restated in terms of the heaviside function as

$$\int_0^t \delta(\xi - t_1)J(t - \xi)d\xi = H(t - t_1)J(t - t_1) \quad (\text{B-18})$$

Substituting this result into Eq (B-15),

$$\varepsilon(t) = \left[\frac{P_0(L-x_1)R}{I} \right] [J(t) - H(t - t_1)J(t - t_1)] \quad (\text{B-19})$$

The above solution represents the strain that would be encountered during calibration of the skin friction gauge, when a weight is abruptly applied and then removed. This solution can be extended to a load function consisting of several incremental step loadings such as

could be encountered in a shock tunnel run or in a calibration series in which weights are added incrementally. This type of load function could be represented by

$$P(t) = H(t)P_1 + H(t-t_1)P_2 + H(t-t_2)P_3 - H(t-t_3)(P_1 + P_2 + P_3) \quad (\text{B-20})$$

For this loading, the strain solution is

$$\begin{aligned} \varepsilon(t) = \left[\frac{(L-x_1)R}{I} \right] & \left[J(t)P_1 + H(t-t_1)J(t-t_1)P_2 \right. \\ & \left. + H(t-t_2)J(t-t_2)P_3 - H(t-t_3)J(t-t_3)(P_1 + P_2 + P_3) \right] \end{aligned} \quad (\text{B-21})$$

B.2. Unsteady One Dimensional Heat Conduction with Constant Surface Heat Flux

A solution to the unsteady heat conduction problem was sought in order to evaluate thermal effects on the skin friction gauges. The application of this solution is discussed in Section 4.1. This analytical solution is for the case of constant wall heat flux and was used to verify the numerical solution which is developed in Appendix C.1.

The one-dimensional heat conduction equation is (Holman, 1981:4)

$$\frac{\partial T}{\partial t} = \alpha \frac{\partial^2 T}{\partial x^2} \quad (\text{B-22})$$

where T is temperature, t represents time, and α is the thermal conductivity. For simple boundary conditions, specifically constant heat flux at the upper surface, this equation can be solved analytically. The solution will serve as a means of validating the numerical scheme that will be used to analyze the more complicated case of varying heat flux at the sensor surface.

The analytical solution was developed using separation of variables, for which a series solution results. The upper boundary condition, constant heat flux, approximates the conditions seen in the shock tunnel. A zero heat flux condition was specified for the boundary condition at the base. The initial condition is a specified uniform temperature throughout the material.

The geometry used for the solution is shown in Figure (3-1) where the symbol q represents the magnitude of the heat flux into the material. The heat flux is given by Fourier's Law (Holman, 1981:21)

$$\dot{q} = k \frac{\partial T}{\partial z}$$

where k is the thermal conductivity. The mathematical formulation of the problem consists then of the partial differential equation:

$$\frac{\partial T}{\partial t} = \alpha \frac{\partial^2 T}{\partial z^2} \quad (\text{B-23})$$

which will be solved with the following initial condition

$$T(z,0) = T_0 \quad (\text{B-23a})$$

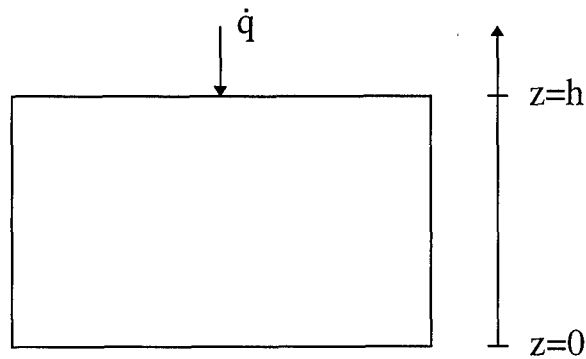


Figure B-1 Geometry for 1-D Heat Transfer

and with the following boundary conditions:

$$\frac{\partial T}{\partial z}(0, t) = 0 \quad (\text{B-23b})$$

$$\frac{\partial T}{\partial z}(h, t) = Q \quad (\text{B-23c})$$

where Q is shorthand notation for $\frac{\dot{q}}{k}$

$$Q \equiv \frac{\dot{q}}{k} \quad (\text{B-24})$$

The solution is assumed to be of the form

$$T(z, t) = U(z, t) + F(t) + G(z) \quad (\text{B-25})$$

The boundary conditions become

$$U_z(0, t) + G'(0) = 0 \quad (\text{B-25b})$$

$$U_z(h, t) + G'(h) = Q \quad (\text{B-25c})$$

Now let

$$G'(h) = Q$$

$$G'(0) = 0$$

which means that

$$U_z(0, t) = 0 \quad (\text{B-26b})$$

$$U_z(h, t) = 0 \quad (\text{B-26c})$$

One solution to G is $G' = \frac{Qz}{h}$

Then, integrating

$$G(z) = \frac{Qz^2}{2h} \quad (\text{B-27})$$

The expression for T, Eq (B-25) then becomes

$$T(z, t) = U(z, t) + F(t) + \frac{Qz^2}{2h} \quad (\text{B-28})$$

Substituting this equation into the partial differential equation, Equation (B-23),

$$\frac{\partial U}{\partial t} + F' = \alpha \frac{\partial^2 U}{\partial z^2} + \alpha \frac{Q}{h} \quad (\text{B-29})$$

Now, let $F' = \alpha \frac{Q}{h}$, or, integrating,

$$F(t) = \frac{\alpha Qt}{h} \quad (\text{B-30})$$

so that

$$\frac{\partial U}{\partial t} = \alpha \frac{\partial^2 U}{\partial z^2} \quad (\text{B-31})$$

with the boundary conditions given by Equations (B-26b) and (B-26c):

$$U_z(0, t) = 0 \quad (\text{B-26b})$$

$$U_z(h, t) = 0 \quad (\text{B-26c})$$

Now, from Eq (B-28),

$$T(z, t) = U(z, t) + F(t) + \frac{Qz^2}{2h} \quad (\text{B-28})$$

and since, from Eq (B-30),

$$F(t) = \frac{\alpha Q t}{h} \quad (\text{B-30})$$

the expression for T becomes

$$T(z, t) = U(z, t) + \frac{\alpha Q t}{h} + \frac{Q z^2}{2h} \quad (\text{B-32})$$

Looking at the initial condition from Eq (B-23a),

$$T(z, 0) = T_0 \quad (\text{B-23a})$$

and using the result from Eq (B-32), the new initial condition becomes

$$T(z, 0) = U(z, 0) + \frac{Q z^2}{2h} = T_0 \quad (\text{B-33})$$

The initial condition for U then becomes

$$U(z, 0) = T_0 - \frac{Q z^2}{2h} \quad (\text{B-33a})$$

The partial differential equation to be solved is then

$$\frac{\partial U}{\partial t} = \alpha \frac{\partial^2 U}{\partial z^2} \quad (\text{B-31})$$

$$U_z(0, t) = 0 \quad (\text{B-26b})$$

$$U_z(h, t) = 0 \quad (\text{B-26c})$$

$$U(z, 0) = T_0 - \frac{Q z^2}{2h} \quad (\text{B-33a})$$

Now, applying the separation of variables technique, let

$$U(z, t) = Z(z)\tau(t)$$

Substituting into the partial differential equation, Equation (B-31),

$$Z\tau' = \alpha Z''\tau$$

Dividing through by $\alpha Z\tau$,

$$\frac{\tau'}{\alpha\tau} = \frac{Z''}{Z} = -\lambda^2 \quad (\text{B-34})$$

where the parameter $-\lambda^2$ is yet to be determined.

Now, considering the Z variable,

$$Z'' - \lambda^2 Z = 0 \quad (\text{B-35})$$

with the boundary conditions deduced from Eqs (B-26b) and (B-26c),

$$Z'(0) = 0 \quad (\text{B-35b})$$

$$Z'(h) = 0 \quad (\text{B-35c})$$

Now, let

$$Z = e^{\Lambda z} \quad (\text{B-36})$$

Substituting into Eq (B-35), $\Lambda^2 e^{\Lambda z} - \lambda^2 e^{\Lambda z} = 0$, or, $(\Lambda^2 - \lambda^2)e^{\Lambda z} = 0$, and since $e^{\Lambda z} = 0$ yields only the trivial solution, the following characteristic equation is obtained:

$$\Lambda^2 - \lambda^2 = 0$$

and so,

$$\Lambda^2 = \lambda^2 \quad (\text{B-37})$$

Three cases will be considered for λ^2 :

Case 1 $\lambda^2 < 0$

For this case,

$$\Lambda = \pm i\lambda \quad \text{where } i \equiv \sqrt{-1}$$

Substituting into Equation (B-36),

$$Z = C_1 e^{i\lambda z} + C_2 e^{-i\lambda z}$$

Now, applying the Euler formulas (Kreyszig, 1979:76)

$$e^{i\theta} = \cos\theta + i\sin\theta \quad e^{-i\theta} = \cos\theta - i\sin\theta$$

results in

$$Z = A\cos\lambda z + B\sin\lambda z \quad (\text{B-38})$$

where A and B are undetermined constants derived from

$$A = C_1 + C_2 \quad \text{and} \quad B = i(C_1 - C_2)$$

Applying the boundary conditions, Eq (B-35b) and (B-35c)

$$Z'(0) = 0 \quad (\text{B-35b})$$

$$Z'(h) = 0 \quad (\text{B-35c})$$

results in

$$Z' = -A\lambda\sin\lambda z + B\lambda\cos\lambda z$$

$$Z'(0) = -A\lambda\sin(0) + B\lambda\cos(0) = 0$$

or, since $\lambda \neq 0$ (since the case is being considered where $\lambda^2 < 0$), $B = 0$ and

$$Z' = -A\lambda\sin\lambda z.$$

Then,

$$Z'(h) = -A\lambda\sin\lambda h = 0$$

so $Z=0$, and, therefore

$$\lambda h = n\pi \quad n = 1, 2, 3, \dots$$

Thus,

$$\lambda = \frac{n\pi}{h} \quad (\text{B-39})$$

For Case 1, then, from Equation (B-39),

$$Z = A\cos\left(\frac{n\pi z}{h}\right) \quad (\text{B-40})$$

Case 2 $\lambda = 0$

Returning to Equation (B-35), and using $\lambda = 0$,

$$Z'' = 0$$

Integrating

$$Z' = C_3$$

Applying the boundary condition from Eq (B-35b),

$$Z'(0) = C_3 = 0$$

or,

$$Z' = 0$$

Integrating once more,

$$Z = C_4 \quad (\text{B-41})$$

Case 3 $\lambda^2 > 0$

For this case, $\Lambda = \pm \lambda$

Substituting into Eq (B-36),

$$Z = C_5 e^{\lambda z} + C_6 e^{-\lambda z} \quad (\text{B-42})$$

Applying the boundary condition from Eq (B-35b),

$$Z'(0) = C_5 \lambda e^0 - C_6 \lambda e^0 = 0$$

$$(C_5 - C_6) \lambda = 0$$

Since for this case $\lambda \neq 0$, $C_5 - C_6 = 0$, so, $C_5 = C_6$. Substituting into Equation (B-42),

$$Z' = C_5 \lambda (e^{\lambda z} - e^{-\lambda z})$$

Applying the boundary condition from Eq (B-35c),

$$Z'(h) = C_5 \lambda (e^{\lambda h} - e^{-\lambda h}) = 0$$

Since $\lambda \neq 0$, either $C_5 = 0$ or $e^{\lambda h} - e^{-\lambda h} = 0$. The second possibility would imply that

$$e^{\lambda h} = e^{-\lambda h}$$

which can only be true if $\lambda = 0$. Therefore, $C_5 = 0$, so $Z = 0$. Thus, only a trivial result is obtained for this case.

Now, the variable τ will be considered, which from Equation (B-34) satisfies the ordinary differential equation

$$\frac{\tau'}{\alpha \tau} = -\lambda^2$$

From the solutions to Cases 1 and 2 for the variable Z , it is known that

$$\lambda = \frac{n\pi}{h} \quad (\text{B-39})$$

where $n = 0, 1, 2, 3, \dots$ (Letting $n=0$ incorporates the result of Case 2, where $\lambda = 0$). Substituting into Equation (B-34),

$$\frac{\tau'}{\tau} = -\alpha \left(\frac{n\pi}{h} \right)^2$$

Integrating,

$$\ln \tau = -\alpha \left(\frac{n\pi}{h} \right)^2 \tau + C_5$$

$$\tau = C_6 e^{-\alpha \left(\frac{n\pi}{h}\right)^2 t} \quad (\text{B-43})$$

Now, from the results of Eqs (B-40), (B-41), and (B-43),

$$U(z, t) = Z(z)\tau(t)$$

$$U_n(z, t) = A_n \cos\left(\frac{n\pi z}{h}\right) e^{-\alpha \left(\frac{n\pi}{h}\right)^2 t} \quad n = 0, 1, 2, 3, \dots$$

where $A_n = AC_6$. Forming a series solution,

$$U(z, t) = \sum_{n=0}^{\infty} \left[A_n \cos\left(\frac{n\pi z}{h}\right) e^{-\alpha \left(\frac{n\pi}{h}\right)^2 t} \right] \quad (\text{B-44})$$

The initial condition is given by Equation (B-33a), $U(z, 0) = T_0 - \frac{Qz^2}{2h}$, so

$$U(z, t) = \sum_{n=0}^{\infty} \left[A_n \cos\left(\frac{n\pi z}{h}\right) \right] = T_0 - \frac{Qz^2}{2h} \quad (\text{B-45})$$

This is a Fourier cosine series, the coefficients of which are (Kovach, 1984:65)

$$A_0 = \frac{1}{h} \int_0^h f(s) ds \quad A_n = \frac{2}{h} \int_0^h f(s) \cos\left(\frac{n\pi s}{h}\right) ds \quad (\text{B-46})$$

Then,

$$A_0 = \frac{1}{h} \int_0^h \left(T_0 s - \frac{Qs^2}{2h} \right) ds = T_0 - \frac{Qh}{6} \quad (\text{B-47})$$

$$A_n = \frac{2}{h} \int_0^h \left(T_0 - \frac{Qs^2}{2h} \right) \cos\left(\frac{n\pi s}{h}\right) ds \quad (\text{B-48})$$

This second integral can be integrated by parts to result in (Weast, 1973:A-143)

$$A_n = -\frac{2Qh}{n^2 \pi^2} (-1)^n \quad (\text{B-49})$$

Now, the results of Eq (B-49) and Eq (B-47) are substituted into Equation (B-44) to obtain the solution

$$U(z, t) = T_0 - \frac{Qh}{6} + \sum_{n=1}^{\infty} \left(-\frac{2Qh}{n^2 \pi^2} (-1)^n \right) \cos\left(\frac{n\pi z}{h}\right) e^{-\alpha \left(\frac{n\pi}{h}\right)^2 t} \quad (\text{B-50})$$

Then from Eq (B-32), the general solution is

$$\begin{aligned}
T(z,t) &= U(z,t) + \frac{\alpha Q t}{h} + \frac{Q z^2}{2h} \\
&= T_0 - \frac{Qh}{6} + \frac{\alpha Q t}{h} + \frac{Q z^2}{2h} + \sum_{n=1}^{\infty} \left(-\frac{2Qh}{n^2 \pi^2} (-1)^n \right) \cos\left(\frac{n\pi z}{h}\right) e^{-\alpha \left(\frac{n\pi}{h}\right)^2 t} \quad (B-51)
\end{aligned}$$

The quantity Q was defined as $Q \equiv \frac{\dot{q}}{k}$. Substituting this result into Eq (B-51) provides the final form of the general solution:

$$T(z,t) = T_0 + \frac{\dot{q}}{k} \left[-\frac{h}{6} + \frac{\alpha t}{h} + \frac{z^2}{2h} + \sum_{n=1}^{\infty} \left(-\frac{2h}{n^2 \pi^2} (-1)^n \right) \cos\left(\frac{n\pi z}{h}\right) e^{-\alpha \left(\frac{n\pi}{h}\right)^2 t} \right] \quad (B-52)$$

At the surface, $z = h$, so the surface temperature is given by

$$T(h,t) = T_0 + \frac{\dot{q}}{k} \left[\frac{h}{3} + \frac{\alpha t}{h} - \sum_{n=1}^{\infty} \left(\frac{2h}{n^2 \pi^2} \right) e^{-\alpha \left(\frac{n\pi}{h}\right)^2 t} \right] \quad (B-53)$$

B.3. Application of Common Skin Friction Correlations to High Temperatures

The common skin friction correlations for a compressible turbulent boundary layer on a flat plate are based on the perfect gas assumptions. This appendix adapts several of these correlations to high temperature use.

B.3.1. Van Driest II

This derivation follows Van Driest's derivation as described in his 1951 paper. However, where possible, the perfect gas assumptions used by Van Driest are avoided. The details of the derivation are shown only when necessary for the derivation of the general formulation.

The Van Driest II skin friction correlation is based on the integration of the momentum equation using the von Karman mixing length. In his 1951 paper, Van Driest used the Prandtl mixing length, and the correlation thus derived is referred to as Van Driest I. The von Karman mixing length was used by Van Driest in a 1956 paper; this skin friction formula is Van Driest II. Some of the derivation of this general formulation is therefore taken from the 1956 paper.

In the boundary layer, the density is considered inversely proportional to temperature (since pressure is constant). Temperature is related to velocity in the boundary layer through the Crocco temperature equation (Van Driest, 1951:151)

$$\frac{\bar{T}}{T_w} = 1 + B \frac{\bar{u}}{u_e} - A^2 \left(\frac{\bar{u}}{u_e} \right)^2 \quad (\text{B-54})$$

where the variables with bars represent time averaged components. The constants A and B are defined in terms of Mach number, wall and edge temperature, γ , and recovery factor. The constants A and B appear in several of the skin friction correlations, including the Van Driest, Spalding and Chi, and White and Christoph. To adapt these skin friction correlations to high temperatures, then, an equivalent Crocco enthalpy equation will be developed, of the form

$$\frac{\bar{h}}{h_w} = 1 + B \frac{\bar{u}}{u_e} - A^2 \left(\frac{\bar{u}}{u_e} \right)^2 \quad (\text{B-55})$$

It should be noted that when the constant specific heat assumption can be made, then $h=c_p T$, and Eq (B-58) reduces to (B-57). However, the constants in Eq (B-55) will be developed in general form without invoking a constant specific heat or γ .

Following the development of Van Driest, the Reynolds averaged energy equation can be rendered (Van Driest, 1951:149)

$$\bar{\rho} u \frac{\partial \bar{h}}{\partial x} + \bar{\rho} v \frac{\partial \bar{h}}{\partial y} = \frac{\partial}{\partial y} \left[-\overline{(\rho v)' h'} \right] - \overline{(\rho v)' u'} \frac{\partial \bar{u}}{\partial y} \quad (\text{B-56})$$

Now, letting

$$-\overline{(\rho v)' u'} = \varepsilon \frac{\partial \bar{u}}{\partial y} \quad -\overline{(\rho v)' h'} = \xi \frac{\partial \bar{h}}{\partial y} \quad (\text{B-57})$$

the energy equation can be rendered

$$\bar{\rho} u \frac{\partial \bar{h}}{\partial x} + \bar{\rho} v \frac{\partial \bar{h}}{\partial y} = \frac{\partial}{\partial y} \left(\xi \frac{\partial \bar{h}}{\partial y} \right) - \varepsilon \left(\frac{\partial \bar{u}}{\partial y} \right)^2 \quad (\text{B-58})$$

The eddy quantity ξ for constant c_p could be written

$$\xi = \frac{k_T}{c_p} \quad (\text{B-59})$$

This defines the units of ξ .

Similarly, the Reynolds averaged momentum equation can be written (Van Driest, 1951:147)

$$\bar{\rho} \bar{u} \frac{\partial \bar{u}}{\partial x} + \bar{\rho} \bar{v} \frac{\partial \bar{u}}{\partial y} = \frac{\partial}{\partial y} \left(\varepsilon \frac{\partial \bar{u}}{\partial y} \right) \quad (\text{B-60})$$

Next, the enthalpy in the boundary layer is assumed to be a function of \bar{u} :

$$\bar{h} = f(\bar{u}) \quad (\text{B-61})$$

Substituting into the energy equation and rearranging, the following is obtained:

$$\frac{df(\bar{u})}{d\bar{u}} \left[\bar{\rho} \bar{u} \frac{\partial \bar{u}}{\partial x} + \bar{\rho} \bar{v} \frac{\partial \bar{u}}{\partial y} - \frac{\partial}{\partial y} \left(\varepsilon \frac{\partial \bar{u}}{\partial y} \right) \right] = \varepsilon \left[\frac{d^2 f(\bar{u})}{d\bar{u}^2} + 1 \right] \left(\frac{\partial \bar{u}}{\partial y} \right)^2 \quad (\text{B-62})$$

The term in the brackets on the left hand side is identical to the momentum equation, and therefore must be zero. Thus, the right hand side must be zero, which implies:

$$\frac{d^2 f(\bar{u})}{d\bar{u}^2} + 1 = 0$$

Rearranging,

$$d^2 f(\bar{u}) = -d\bar{u}^2$$

Integrating

$$f(\bar{u}) = \bar{h} = A_1 + B_1 \bar{u} - \frac{\bar{u}^2}{2} \quad (\text{B-63})$$

where A_1 and B_1 are constants of integration. The boundary conditions are

$$\bar{h} = h_w \quad \text{at} \quad \bar{u} = 0$$

$$\bar{h} = h_e \quad \text{at} \quad \bar{u} = u_e$$

from which the constants of integration are determined as

$$A_1 = h_w \quad B_1 = \frac{h_e - h_w}{u_e} + \frac{1}{2} u_e$$

Substituting into Eq (B-63),

$$\bar{h} = h_w + (h_e - h_w) \frac{\bar{u}}{u_e} + \frac{1}{2} u_e \bar{u} - \frac{1}{2} \bar{u}^2$$

Now, dividing through by h_w ,

$$\frac{\bar{h}}{h_w} = 1 + \left[\left(1 + \frac{1}{2} \frac{u_e^2}{h_e} \right) \frac{h_e}{h_w} - 1 \right] \frac{\bar{u}}{u_e} - \frac{1}{2} \frac{u_e^2}{h_e} \frac{h_e}{h_w} \left(\frac{\bar{u}}{u_e} \right)^2 \quad (\text{B-64})$$

This equation is the desired enthalpy form of the Crocco temperature equation. In comparison to Eq (B-55), it can be seen that the constants A and B are

$$B = \frac{1 + \frac{1}{2} \frac{u_e^2}{h_e}}{\left(\frac{h_w}{h_e} \right)} - 1 \quad A^2 = \frac{\frac{1}{2} \frac{u_e^2}{h_e}}{\left(\frac{h_w}{h_e} \right)} \quad (\text{B-65})$$

If c_p were constant, then $h_w/h_e = c_p T_w / c_p T_e = T_w/T_e$, and

$$\frac{1}{2} \frac{u_e^2}{h_e} = \frac{1}{2} \frac{u_e^2}{c_p T_e} = \frac{1}{2} \frac{u_e^2}{\left(\frac{c_p}{\gamma R} \right) a_e^2} = \frac{1}{2} \frac{\gamma R}{c_p} M_e^2 = \frac{\gamma - 1}{2} M_e^2 \quad (\text{B-66})$$

The constants A and B would then reduce to the familiar form derived by Van Driest (1951:151):

$$B = \frac{1 + \frac{\gamma - 1}{2} M_e^2}{\left(\frac{T_w}{T_e} \right)} - 1 \quad A^2 = \frac{\frac{\gamma - 1}{2} M_e^2}{\left(\frac{T_w}{T_e} \right)} \quad (\text{B-67})$$

Van Driest, in deriving the skin friction correlation, assumed that the Prandtl number and turbulent Prandtl number were both equal to 1. He then corrected for the variation of these numbers from 1 by incorporating an effective Mach number into Eqs (B-67) with the value $M_{\text{eff}}^2 = rM^2$, where r is the flat plate recovery factor (Van Driest, 1951:160). Since u^2/h_e in Eq (B-66) is analogous to M^2 , the factors A and B in Eqs (B-70) are modified to include the recovery factor as follows:

$$B = \frac{1 + \frac{1}{2} \frac{ru_e^2}{h_e}}{\left(\frac{h_w}{h_e}\right)} - 1 \quad A^2 = \frac{\frac{1}{2} \frac{ru_e^2}{h_e}}{\left(\frac{h_w}{h_e}\right)} \quad (\text{B-68})$$

The flat plate recovery factor for turbulent flow is generally taken as (Schetz, 1984:268)

$$r = \sqrt[3]{\text{Pr}} \quad (\text{B-69})$$

where Pr represents the Prandtl number.

Van Driest obtained his skin friction formula by integrating Prandtl's mixing length equation

$$\tau = -\bar{\rho} \ell^2 \left(\frac{d\bar{u}}{dy} \right)^2 \quad (\text{B-70})$$

along with the von Karman mixing length

$$\ell = \kappa \left(\frac{d\bar{u}/dy}{d^2\bar{u}/dy^2} \right) \quad (\text{B-71})$$

Since pressure is constant in the y-direction in the boundary layer, Van Driest assumed that density was inversely proportional to temperature

$$\frac{\bar{\rho}}{\rho_w} = \frac{T_w}{T} \quad (\text{B-72})$$

and then used Eq (B-54) to write density as a function of velocity. This allowed Eq (B-70) to be written in terms of u and integrated to result in

$$\frac{1}{A} \sin^{-1} \frac{2A^2 \left(\frac{\bar{u}}{u_e} \right) - B}{\sqrt{B^2 + 4A^2}} + \frac{1}{A} \sin^{-1} \frac{2B}{\sqrt{B^2 + 4A^2}} = \frac{1}{u_e} \sqrt{\frac{\tau_w}{\rho_w}} \left(F + \frac{1}{\kappa} \sqrt{\frac{\tau_w}{\rho_w}} \frac{y}{v_w} \right) \quad (\text{B-73})$$

This has been referred to as Van Driest's effective velocity concept and has been used to extend the law of the wall to compressible flows (Bradshaw, 1977).

The perfect gas assumption that temperature is inversely proportional to density is what makes the Van Driest II and some of the other skin friction correlations less valid for high temperature flows. The freestream temperature is often cold enough to be within perfect gas range, but the hotter temperatures in the boundary layer result in molecular

vibrational effects and dissociation that result in the perfect gas assumptions no longer being valid. However, the only way to obtain a closed form solution is to make such an assumption, and depending on wall temperature, the high temperature effects in the boundary layer may not result in excessive departure from the perfect gas assumptions.

Van Driest next used the flat plate momentum equation $d\theta/dx=C_f/2$ in the form

$$\tau_w = \frac{d}{dx} \int_0^{\delta} \bar{\rho} \bar{u} (u_e - \bar{u}) dy \quad (\text{B-74})$$

to solve for wall shear stress. Equation (B-78) was differentiated to obtain dy , substituted into Eq (B-74), and then integrated, with the integral approximated by a series to result in

$$\frac{\sin^{-1} \alpha + \sin^{-1} \beta}{\sqrt{\frac{1}{2} A^2 c_{fw}}} = \text{Const} + \frac{1}{\kappa} \ln(c_{fw} \text{Re}_w) \quad (\text{B-75})$$

where

$$\alpha = \frac{2A^2 - B}{\sqrt{B^2 + 4A^2}} \quad \beta = \frac{B}{\sqrt{B^2 + 4A^2}} \quad (\text{B-76})$$

and c_f and Re are expressed in terms of wall values

$$c_{fw} = \frac{\tau_w}{\frac{1}{2} \rho_w u_e^2}$$

$$\text{Re}_w = \frac{\rho_w u_e x}{\mu_w}$$

These can be converted to the more familiar freestream forms by use of

$$c_{fw} \text{Re}_w = \frac{\tau_w}{\frac{1}{2} \rho_w u_e^2} \frac{\rho_w u_e x}{\mu_w} = \frac{\tau_w}{\frac{1}{2} \rho_e u_e^2} \frac{\rho_e u_e x}{\mu_e} \frac{\mu_e}{\mu_w} = c_f \text{Re}_e \frac{\mu_e}{\mu_w}$$

$$c_{fw} = \frac{\tau_w}{\frac{1}{2} \rho_w u_e^2} = \frac{\tau_w}{\frac{1}{2} \rho_e u_e^2} \frac{\rho_e}{\rho_w} = c_f \frac{\rho_e}{\rho_w}$$

Equation (B-75) then becomes

$$\frac{\sin^{-1} \alpha + \sin^{-1} \beta}{\sqrt{\frac{1}{2} A^2 c_f \frac{\rho_e}{\rho_w}}} = \text{Const} + \frac{1}{\kappa} \ln \left(c_f \text{Re}_e \frac{\mu_e}{\mu_w} \right) \quad (\text{B-77})$$

The constant is then calculated by letting $M=0$ and $T_w=T_e$ and matching to the Karman-Schoenherr incompressible skin friction formula

$$\frac{1}{\sqrt{c_f}} = 1.70 + 4.15 \log_{10} (c_f \text{Re}_e) \quad (\text{B-78})$$

The final form of the Van Driest II skin friction formula is then

$$\frac{0.242(\sin^{-1} \alpha + \sin^{-1} \beta)}{\sqrt{A^2 c_f \frac{\rho_e}{\rho_w}}} = 0.41 + \log_{10} \left(c_f \text{Re}_e \frac{\mu_e}{\mu_w} \right) \quad (\text{B-79})$$

The primary difference between this form of the Van Driest formula and the usual form is that the usual formulation renders viscosity and density in terms of temperature so that only temperature and Reynolds number appear as dependent variables, along with Mach number in the definition of A and B. In addition, A and B have been written in general form in order to eliminate the adiabatic wall temperature formulation which can introduce error into high temperature calculations.

B.3.2. Spalding and Chi

The Spalding and Chi skin friction correlation is an empirical correlation. In the usual form of the Van Driest equation, as shown in Chapter 4, the ratios T_w/T_e and T_{aw}/T_e , so Spalding and Chi derived a curve fit to existing data to obtain a correlation as a function of T_w/T_e and T_{aw}/T_e . In the high temperature version, T_w/T_e and T_{aw}/T_e are replaced by h_w/h_e and h_{aw}/h_e .

The Spalding and Chi theory was used in two forms, one with the Reynolds number based on distance from the leading edge (Re_x), and the other on momentum thickness (Re_θ). The Re_x version was used to calculate the skin friction for specific runs for comparison with the measured data, while the Re_θ version was used to estimate the effects of the thermal mismatch between the plastic sensor and metal wall.

B.3.2.1. Skin Friction Correlation

The Spalding and Chi correlation will be stated in a canonical form in which the compressible skin friction coefficient is based on an equivalent incompressible skin friction coefficient. This canonical form will be also be used for several of the other skin friction correlations. The method is outlined as follows (Cebeci and Bradshaw, 1984:345):

$$C_{fi} = F_c C_f \quad (\text{B-80})$$

where C_f is the compressible skin friction coefficient and C_{fi} is the equivalent incompressible skin friction coefficient. The value for C_{fi} is calculated using an equivalent Reynolds number given by

$$\text{Re}_{xi} = F_{rx} \text{Re}_x \quad (\text{B-81})$$

where Re_{xi} is the equivalent Reynolds based on x for incompressible flow and Re_x is the actual compressible Reynolds number defined by

$$\text{Re}_x = \frac{\rho_e u_e x}{\mu_e} \quad (\text{B-82})$$

For the Spalding and Chi equation, which was used in both Re_x and Re_θ form, the factor F_{rx} is defined by

$$F_{rx} = \frac{F_{r\theta}}{F_c} \quad (\text{B-83})$$

For high temperature flows where the calorically perfect gas assumption becomes unrealistic, the functions F_c and $F_{r\theta}$ are more appropriately defined in terms of enthalpies

$$F_c = \frac{\frac{h_{aw}}{h_e} - 1}{(\sin^{-1} \alpha + \sin^{-1} \beta)^2} \quad (\text{B-84})$$

$$F_{r\theta} = \left(\frac{h_{aw}}{h_e} \right)^{0.772} \left(\frac{h_w}{h_e} \right)^{-1.474} \quad (\text{B-85})$$

where h represents specific enthalpy, the subscript aw denotes the adiabatic wall condition, and the subscript w represents the actual wall condition. The adiabatic wall enthalpy is calculated by

The factors α and β are the same factors that are used in the Van Driest skin friction correlations, Eqs (B-81). The incompressible skin friction correlation that was used for the NASA Ames run 2066 analysis was (White, 1991:432)

$$C_{fi} = \frac{0.455}{\ln^2(0.06 Re_{xi})} \quad (B-87)$$

The Spalding and Chi formulation based on momentum thickness also uses $C_{fi} = F_c C_f$, but C_{fi} is calculated based on an equivalent Reynolds number given by

$$Re_{\theta_i} = F_{r\theta} Re_{\theta} \quad (B-88)$$

where Re_{θ_i} is the equivalent Reynolds based on the momentum thickness for incompressible flow and Re_{θ} is the actual compressible Reynolds number defined by

$$Re_{\theta} = \frac{\rho_e U_e \theta}{\mu_e} \quad (B-89)$$

The equivalent incompressible skin friction coefficient C_{fi} can be calculated from the Spalding-Chi formula (Spalding and Chi, 1964):

$$Re_{\theta_i} = \frac{(u_e^+)^2}{6} + \frac{\left[\left(1 - \frac{2}{ku_e^+}\right) e^{ku_e^+} + \frac{2}{ku_e^+} + 1 - \frac{(u_e^+)^2}{6} - \frac{(u_e^+)^2}{12} - \frac{(u_e^+)^2}{40} - \frac{(u_e^+)^2}{180} \right]}{kE} \quad (B-90)$$

where $k=0.4$, $E=12$, and $u_e^+ = (2 / C_f)^{1/2}$.

B.3.2.2. Calculation of Thermal Effect by Holding Momentum Thickness Constant

The following method, described in Chapter 4, used the Spalding and Chi skin friction correlation based on momentum thickness to estimate the effect on the skin friction measurement due to the sensor being at a different temperature from the wall. The method assumes that temperature mismatch will not change the momentum thickness. A momentum thickness is calculated based on the measured wall skin friction and the estimated sensor surface temperature. Using this calculated momentum thickness, the true skin friction based on the metal wall temperature is calculated. The method is an iterative scheme that was implemented on a computer. The free stream conditions are assumed to

be known as well as the surface temperature of both the sensor and the surrounding metal wall.

- (a) Use the measured C_f
- (b) Evaluate h_{aw} from Eq (B-86)
- (c) Calculate sensor surface enthalpy, $h_{w(s)}$, from the Tannehill & Mugge (1974) correlation $h=h(p,\rho)$ using the calculated sensor temperature for T_w
- (d) Calculate $F_{r\theta}$ from Eq (B-85) using $h_{w(s)}$ for h_w
- (e) Guess a momentum thickness θ
- (f) Evaluate Re_θ using Eq (B-89)
- (g) Calculate Re_{θ_i} from Eq (B-88)
- (h) Guess C_{fi}
- (i) Calculate Re_{θ_i} from Eq (B-90) using the guessed C_{fi}
- (j) Compare the Re_{θ_i} calculated in step (i) to the Re_{θ_i} calculated in step (g). If the two values do not match, return to step (h) and guess a new C_{fi}
- (k) Calculate B and A^2 from Eq (B-68) using $h_{w(s)}$ for h_w
- (l) Calculate α and β from Eq (B-76)
- (m) Calculate F_c from Eq (B-84)
- (n) Calculate C_f from Eq (B-85)
- (o) Compare the C_f calculated in step (n) to the measured C_f from step (a). If the two values do not match, return to step (e) and guess a new θ
- (p) Using the calculated value for θ , repeat steps (b)-(n), omitting step (e), and this time using the actual (metal) wall temperature for T_w and subsequent calculations rather than the sensor temperature.

B.3.3. White and Christoff

The White and Christoff skin friction formula is a theoretically based correlation based on a law of the wall formulation (White, 1991:553). The same canonical form is used as for the Spalding and Chi correlation. F_c is the same as for Spalding and Chi. The

Reynolds number factor, written by White and Christoph in terms of T_e/T_w , is, in terms of h_e/h_w

$$F_{rx} = \frac{\left(\frac{\mu_e}{\mu_w}\right) \sqrt{\frac{h_e}{h_w}}}{\sqrt{F_c}} \quad (\text{B-91})$$

The incompressible correlation given by Eq (B-92) was used.

The White and Christoph method provides a C_f very close to the Van Driest II.

B.3.4. Sommer and Short

The Sommer and Short is an empirically derived reference temperature method. When converted to reference enthalpy form, the reference condition is given by (Hopkins and Inouye, 1971:995)

$$h_{ref} = h_e \left[1 + 0.035M_c^2 + 0.45 \left(\frac{h_w}{h_e} - 1 \right) \right] \quad (\text{B-92})$$

The canonical form is again used, with

$$F_c = \frac{h_{ref}}{h_e} \quad (\text{B-93})$$

$$F_{rx} = \frac{\mu_e h_e}{\mu_{ref} h_{ref}} \quad (\text{B-94})$$

To use this method in reference enthalpy form, a reference temperature must be calculated from the reference enthalpy and the pressure. The density at the reference condition is first calculated using the Tannehill and Mugge high temperature equilibrium thermochemistry curve fit $h=h(p,p)$. The curve fit $T=T(p,p)$ is then used to calculate the temperature, and the viscosity at the reference condition is then calculated using Sutherland's law.

B.4. Effective Strain Point for Strain Gauge at Base of Cantilever

This derivation on the effective strain point for the strain gauge is used in Section 3.3.1. The amount of strain which the strain gauge undergoes can be calculated by applying the engineering definition of normal strain (Beer and Johnston, 1981:33), so that

$$\varepsilon_{SG} = \frac{\Delta L_{SG}}{L_{SG}} \quad (B-95)$$

where ε_{SG} is the strain undergone by the strain gauge, L_{SG} is the unstrained length of the sensing portion of the strain gauge, and ΔL_{SG} represents the change in length. For a linear strain, the following definition can be used (Saada, 1974:7):

$$\varepsilon_{11} \equiv \frac{\partial u_1}{\partial x_1} \quad (B-96)$$

where u_1 represents displacement in the x_1 direction. If x_2 and x_3 are held constant, then,

$$du_1 = \varepsilon_{11} dx_1 \quad (B-97)$$

The elongation of the strain gauge can then be calculated as follows:

$$\Delta L_{SG} = \int_{x_{sg1}}^{x_{sg2}} du_1 = \int_{x_{sg1}}^{x_{sg2}} \varepsilon_{11} dx_1 \quad (B-98)$$

where x_{sg1} is the x_1 coordinate of the lower edge of the sensing surface of the strain gauge and x_{sg2} is the x_1 coordinate of the upper edge of the sensing surface. Using Eq (3-3) to give ε when $x_2 = -R$,

$$\Delta L_{SG(t)} = \int_{x_{sg1}}^{x_{sg2}} \frac{P(L-x_1)R}{EI} dx_1 = \frac{PR}{EI} (x_{sg2} - x_{sg1}) \left[L - \frac{1}{2}(x_{sg2} + x_{sg1}) \right] \quad (B-99)$$

The unstrained length of the sensing portion of the strain gauge is given by

$$L_{SG} = x_{sg2} - x_{sg1} \quad (B-100)$$

Substituting Eqs (B-99) and (B-100) into Eq (B-95) then gives

$$\varepsilon_{SG(t)} = \frac{\Delta L_{SG}}{L_{SG}} = \frac{PR}{EI} \left[L - \frac{1}{2}(x_{sg2} + x_{sg1}) \right] \quad (B-101)$$

The strain predicted by Eq (B-101) is identical to the strain given by Eq (B-99) if the value for x_1 is taken as

$$x_1 = \frac{1}{2}(x_{sg2} + x_{sg1}) \quad (B-102)$$

For the beam under end-loading, therefore, the strain measured by the strain gauge is the strain halfway between the two ends of the sensing portion of the strain gauge. For a symmetric strain gauge with an equal amount of non-sensory surface at either end of the

strain gauge, this halfway point between the ends of the sensing surface is identical to the halfway point between the ends of the strain gauge.

B.5. Moment of Inertia and Effect of Strain Gauge and Glue

The calculation on the effect of strain gauge and glue on the round beam moment of inertia was used in section 3.1.1. The definition of the moment of inertia is (Beer and Johnston, 1981:579):

$$I \equiv \int y^2 dA \quad (\text{B-103})$$

The strain gauge acts to increase the moment of inertia of the beam. The principle of superposition can be used to calculate the effect of the strain gauge on the moment of inertia. However, the strain gauge, made of silicon, has a higher modulus of elasticity than the beam material. This can be modeled by increasing the effective width of the strain gauge element in proportion to the increase in modulus (Figure B-2).

Equation (B-103) is used to calculate the increase in moment due to the strain gauge.

$$I = \int_{-R-t_f}^{-R} y^2 (b_{\text{eff}} dy) + \int_R^{R+t_f} y^2 (b_{\text{eff}} dy) = \frac{2}{3} b_{\text{eff}} [(R + t_{\text{SG}})^3 - R^3] \quad (\text{B-104})$$

The actual strain gauge modulus is 107 GPa (Clauser, 1963:616), compared to 3.3 GPa for the Ultem plastic, so the effective width of the strain gauge is 32.4 times the actual width. The increase in moment of inertia due to the strain gauge is then 0.245 mm⁴, compared to 2.04 mm⁴ for the beam alone.

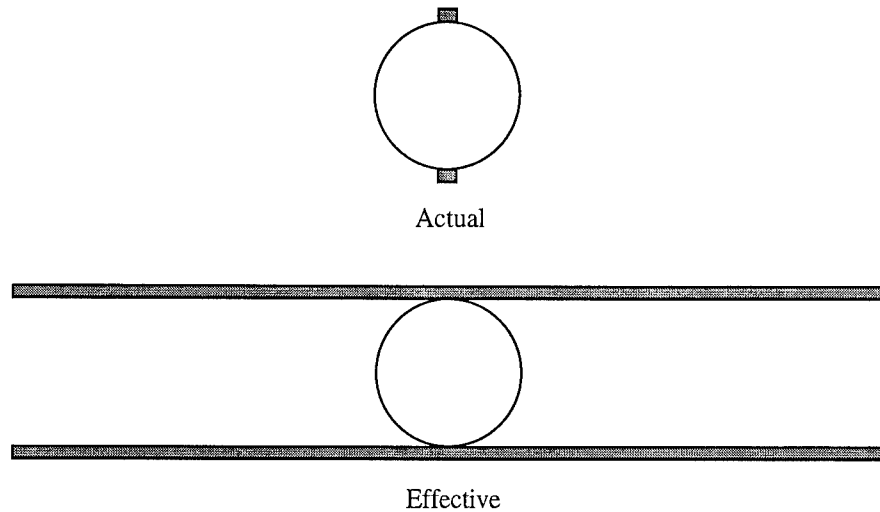


Figure B-2 Modeling of Strain Gauge Stiffness

The glue, a methyl cyanoacrylate, has an elastic modulus of 3.4 GPa (Skeist, 1985:469), which is approximately the same as the plastic. One of the skin friction gauges was measured with a micrometer, and it was found that the glue added approximately 10 percent to the longitudinal axis of the gauge, while the transverse axis was unchanged. The glue was therefore considered to form an elliptical shape about the beam (Figure B-3).

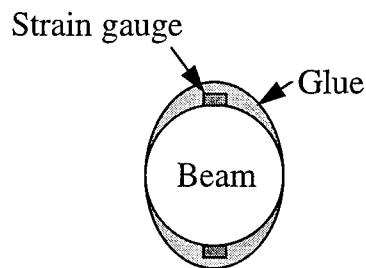


Figure B-3 Effect of Glue (dimensions exaggerated)

The moment of inertia for an ellipse is $I = \pi a^3 b / 4$, where a is the major axis and b the minor axis (Avallone and Baumeister, 1987:5-31). Using superposition, the increase in moment of inertia due to the glue is then

$$I = \frac{\pi(R + t_{\text{glue}})^3 R}{4} - \frac{\pi R^4}{4} \quad (\text{B-105})$$

For the baseline gauge, the increase in moment of inertia for a 10 percent increase in R due to the glue is 0.675 mm^4 , while for a 25 percent increase in R, the increase in moment of inertia is 1.94 mm^4 .

The combined increase in moment of inertia due to the strain gauge and glue then ranges from 0.920 mm^4 to 2.185 mm^4 . This represents an increase in the moment of inertia of 45-107 percent.

B.6. Trigonometric Identities

The following identities are used in the next derivation in Appendix B.7.

$$\begin{aligned}
 \sin \alpha &= \cos \alpha \tan \alpha \\
 &= \left(\sqrt{1 - \sin^2 \alpha} \right) \tan \alpha \\
 \sin^2 \alpha &= (1 - \sin^2 \alpha) \tan^2 \alpha \\
 \sin^2 \alpha + \sin^2 \alpha \tan^2 \alpha &= \tan^2 \alpha \\
 \sin^2 \alpha &= \frac{\tan^2 \alpha}{1 + \tan^2 \alpha} \\
 \sin \alpha &= \frac{\tan \alpha}{\sqrt{1 + \tan^2 \alpha}} \tag{B-106}
 \end{aligned}$$

A related identity was also used:

$$\begin{aligned}
 \tan \alpha &= \frac{\sin \alpha}{\cos \alpha} = \frac{\sqrt{1 - \cos^2 \alpha}}{\cos \alpha} \\
 \tan^2 \alpha &= \frac{1 - \cos^2 \alpha}{\cos^2 \alpha} \\
 \cos^2 \alpha \tan^2 \alpha &= 1 - \cos^2 \alpha \\
 \cos^2 \alpha \tan^2 \alpha + \cos^2 \alpha &= 1 \\
 \cos^2 \alpha &= \frac{1}{\tan^2 \alpha + 1} \tag{B-107}
 \end{aligned}$$

B.7. Solution to Equation of Motion for Vibrating Base

The solution was used in Section 3.2 to analyze the effect on the skin friction gauge if the model was vibrating. The solution makes use of the following equations from Chapter 3:

$$\omega_n^2 = \frac{k}{m} \quad (3-36)$$

$$c_{cr} = 4mk = \frac{2k}{\omega_n} \quad (3-52)$$

The single degree of freedom model for the base in motion is (Craig, 1981:21)

$$m\ddot{w} + c\dot{w} + kw = p(t) - m\ddot{z} \quad (B-108)$$

If the base motion is given by

$$z = Z \cos \Omega t \quad (B-109)$$

Equation (B-108) then becomes

$$m\ddot{w} + c\dot{w} + kw = p + mZ\Omega^2 \cos \Omega t \quad (B-110)$$

Since the differential equation is linear, solutions can be superimposed such that $w = w_h + w_p$. If underdamping is assumed, then the solution to the homogeneous problem is (Craig, 1981:1956)

$$w_h(t) = e^{-\zeta\omega_n t} (A \cos \omega_d t + B \sin \omega_d t) \quad (B-111)$$

The particular solution will be taken as

$$w_p = P + W \cos(\Omega t - \alpha) \quad (B-112)$$

where P , W , and α are yet to be determined. Differentiating, substituting into Eq (B-110), applying trigonometric identities, and rearranging, the following is obtained:

$$\begin{aligned} kP + (kW \cos \alpha - mW\Omega^2 \cos \alpha + cW\Omega \sin \alpha) \cos \Omega t \\ + (kW \sin \alpha - mW\Omega^2 \sin \alpha - cW\Omega \cos \alpha) \sin \Omega t \\ = p + mZ\Omega^2 \cos \Omega t \end{aligned} \quad (B-113)$$

Equating the coefficients, the following are derived:

$$P = \frac{k}{p} \quad (B-114)$$

$$\frac{W}{Z} = \frac{m\Omega/c}{\left(\frac{k - m\Omega^2}{c\Omega}\right) \cos \alpha + \sin \alpha} \quad (B-115)$$

$$\tan \alpha = \frac{c\Omega}{k - m\Omega^2} = \frac{\frac{c\Omega}{k}}{1 - \frac{m\Omega^2}{k}} \quad (\text{B-116})$$

Using Eq (B-116) in (B-115)

$$\frac{W}{Z} = \frac{m\Omega \sin \alpha}{c} \quad (\text{B-117})$$

Now, defining

$$r \equiv \frac{\Omega}{\omega_n} \quad (\text{B-118})$$

and the viscous damping factor (Craig, 1981:49)

$$\zeta \equiv \frac{c}{c_{cr}} = \frac{c}{2k/\omega_n} = \frac{c\omega_n}{2k} \quad (\text{B-119})$$

and using Eqs (3-36) and (3-52), Eq (B-116) becomes

$$\tan \alpha = \frac{2\zeta r}{1 - r^2} \quad (\text{B-120})$$

Then, substituting Eq (B-120) into the trigonometric identity $\sin \alpha = \tan \alpha / \sqrt{1 + \tan^2 \alpha}$ (derived in Appendix B.6) and defining (Craig, 1981:78)

$$D_s = \frac{1}{\sqrt{(1 - r^2)^2 + (2\zeta r)^2}} \quad (\text{B-121})$$

the following is derived:

$$\sin \alpha = 2\zeta r D_s \quad (\text{B-122})$$

Substituting into Eq (B-117) and applying Eqs (B-118), (B-119), (3-36), and (3-52), the following is obtained:

$$\frac{W}{Z} = 2 \left(\frac{1}{\omega_n^2} \right) \left(\frac{\omega_n}{2\zeta} \right) \Omega \zeta r D_s = r^2 D_s \quad (\text{B-123})$$

This result was derived for a slightly different case by Craig (1981:89) using complex variables.

Since Z and Ω are known, the particular solution is then obtained by substituting Eq (B-114) and (B-123) into Eq (B-112):

$$w_p = \frac{P}{k} + r^2 D_s Z \cos(\Omega t - \alpha) \quad (\text{B-124})$$

where α is defined by Eq (B-120). Adding this to the homogeneous solution of Eq (B-111) provides the general solution

$$w(t) = e^{-\zeta\omega_n t} (A \cos \omega_d t + B \sin \omega_d t) + \frac{P}{k} + r^2 D_s Z \cos(\Omega t - \alpha) \quad (\text{B-125})$$

Solving for the situation where the system is initially at rest, the initial conditions are

$$w(0) = 0 \quad \dot{w}(0) = 0 \quad (\text{B-126})$$

Applying the initial conditions results in

$$\begin{aligned} w(t) = & \frac{P}{k} \left[1 - e^{-\zeta\omega_n t} \left(\cos \omega_d t + \frac{\zeta\omega_n}{\omega_d} \sin \omega_d t \right) \right] \\ & + r^2 D_s Z \left\{ \cos \Omega t \cos \alpha + \sin \Omega t \sin \alpha \right. \\ & \left. - e^{-\zeta\omega_n t} \left[\cos \alpha \left(\cos \omega_d t + \frac{\zeta\omega_n}{\omega_d} \sin \omega_d t \right) + \frac{\Omega \sin \alpha}{\omega_d} \sin \omega_d t \right] \right\} \quad (\text{B-127}) \end{aligned}$$

As shown in Appendix B.6, $\cos \alpha = 1/\sqrt{\tan^2 \alpha + 1}$. Then, using the results of Eq (B-120),

$$\cos \alpha = (1 - r^2) D_s \quad (\text{B-128})$$

Substituting this result and Eq (B-120) into Eq (B-128), the general solution becomes

$$\begin{aligned} w = & \frac{P}{k} \left[1 - e^{-\zeta\omega_n t} \left(\cos \omega_d t + \frac{\zeta\omega_n}{\omega_d} \sin \omega_d t \right) \right] \\ & + r^2 D_s^2 Z \left\{ (1 - r^2) \cos \Omega t + 2\zeta r \sin \Omega t \right. \\ & \left. - e^{-\zeta\omega_n t} \left[(1 - r^2) \cos \omega_d t + (1 + r^2) \frac{\zeta\omega_n}{\omega_d} \sin \omega_d t \right] \right\} \quad (\text{B-129}) \end{aligned}$$

B.8. Electrical Response

The electrical response of the skin friction gauge in a Wheatstone Bridge was analyzed using basic circuit theory. The results are discussed in Chapter 4.

The Wheatstone bridge circuit diagram was previously shown as Figure 2-10. Since resistors are additive in series (Tipler, 1976:792), the total resistance over the strain gauge circuit is $R_c + R_t$. For the ideal case, the strain gauges have the same initial resistances and gauge factors, and the strain is the same for both strain gauges. Using Ohm's Law, $V = IR$, the voltage at point A is

$$V_A = \left(\frac{V_e}{R_c + R_t} \right) R_c \quad (\text{B-130})$$

Similarly for point B,

$$V_B = \left(\frac{V_e}{r_1 + r_2} \right) r_1 \quad (\text{B-131})$$

The voltage read by a voltmeter or data acquisition system is then

$$V = V_B - V_A = V_e \left[\frac{R_t r_1 - R_c r_2}{(r_1 + r_2)(R_c + R_t)} \right] \quad (\text{B-132})$$

Prior to operation, the strain gauges have resistances R_{t0} and R_{c0} . The bridge is in balance when $V = 0$. From Eq (B-132), this occurs when

$$R_{t0} r_1 = R_{c0} r_2 \quad (\text{B-133})$$

However, the bridge does not remain in perfect balance, so an initial voltage will be assumed to exist prior to the loading.

The change in resistance of a strain is related to the gauge factor:

$$\frac{\Delta R}{R} = k\varepsilon \quad (\text{B-134})$$

While the relation is defined in terms of the unstrained resistance, little accuracy is lost if the resistance is calculated by applying the gauge factor to the initially strained resistance. The initial resistance after application is

$$R_{t0} = R_{t0f} (1 + k\varepsilon_0)$$

where R_{tof} is the unstrained resistance when the strain gauge comes from the factory, and R_{t0} is the installed resistance. The resistance after deflection is then given by

$$R_{t(a)} = R_{tof} (1 + k\epsilon_0 + k\epsilon_t)$$

If the resistance is calculated from R_{t0} ,

$$\begin{aligned} R_t &= R_{t0} (1 + k\epsilon_t) = R_{tof} (1 + k\epsilon_0)(1 + k\epsilon_t) \\ &= R_{tof} [1 + k\epsilon_t + k\epsilon_0 + O(k^2\epsilon^2)] \\ &\approx R_{t(a)} \end{aligned} \quad (B-135)$$

The error even for a large initial strain of 10×10^{-6} would only be 0.1 percent. The resistance of the strain gauges under loading will therefore be represented by

$$R_t = R_{t0} (1 + k_t \epsilon_t) \quad R_c = R_{c0} (1 + k_c \epsilon_c) \quad (B-136)$$

Substituting these into Eq (B-132)

$$V = V_e \left\{ \frac{R_{t0} (1 + k_t \epsilon_t) r_1 - R_{c0} (1 + k_c \epsilon_c) r_2}{(r_1 + r_2) [R_{c0} (1 + k_c \epsilon_c) + R_{t0} (1 + k_t \epsilon_t)]} \right\} \quad (B-137)$$

This is the general case that applies to the skin friction gauge operation. For the design case,

$$\epsilon_t = -\epsilon_c \equiv \epsilon \quad (B-138)$$

$$R_{t0} = R_{c0} \equiv R_0 \quad (B-139)$$

$$k_t = k_c \equiv k \quad (B-140)$$

Substituting these into Eq (B-137), the voltage is then

$$V = \frac{V_e}{2} \left[\frac{r_1 - r_2 + (r_1 + r_2) k \epsilon}{r_1 + r_2} \right] \quad (B-141)$$

The initial voltage is

$$V_0 = \frac{V_e}{2} \left[\frac{r_1 - r_2 + (r_1 + r_2) k \epsilon_0}{r_1 + r_2} \right] \quad (B-141a)$$

so the change in voltage for a given change in strain is

$$V - V_0 = \frac{V_e k (\epsilon - \epsilon_0)}{2} \quad (3-101b)$$

If a balancing resistor is added in series to the compression side, the voltage equation becomes

$$V = V_e \left\{ \frac{R_{i0}(1 + k\varepsilon_t)r_1 - R_{c0}(1 + k\varepsilon_c)r_2 + R_B}{(r_1 + r_2)[R_{c0}(1 + k\varepsilon_c) + R_{i0}(1 + k\varepsilon_t)]} \right\} \quad (\text{B-137a})$$

For the general case encompassing the four factors of unequal strain, unequal gauge factors, unequal initial resistances, and a balancing resistor being present, the variations will be represented by small disturbance parameters δ , such that

$$\varepsilon_c = -(1 + \delta_e)\varepsilon_t = -(1 + \delta_e)\varepsilon \quad (3-142)$$

$$k_c = (1 + \delta_k)k_t = (1 + \delta_k)k \quad (3-112)$$

$$R_{c0} = (1 + \delta_R)R_{i0} \quad (4-19)$$

$$R_B = \delta_B R_{i0} \quad (4-20)$$

Then using basic circuit analysis along with series expansions, the voltage response is

$$V = \left(\frac{V_e r_1}{r_1 + r_2} \right) \left\{ \frac{1 - (1 + \delta_R + \delta_B) \frac{r_2}{r_1} + \left[1 + (1 + B) \frac{r_2}{r_1} \right] k\varepsilon}{2 + \delta_R + \delta_B - Bk\varepsilon} \right\} \quad (\text{B-142})$$

where

$$B \equiv (1 + \delta_R)(1 + \delta_k)(1 + \delta_e) - 1$$

Expanding the denominator of the term in brackets by Taylor's series about ε ,

$$\frac{1}{2 + \delta_R + \delta_B - Bk\varepsilon} \sim \frac{1}{2 + \delta_R + \delta_B} + \frac{Bk\varepsilon}{(2 + \delta_R + \delta_B)^2} + \frac{(Bk\varepsilon)^2}{(2 + \delta_R + \delta_B)^3} + O[(Bk\varepsilon)^3] \quad (\text{B-143})$$

where

$$B = \delta_R + \delta_k + \delta_e + \delta_R\delta_k + \delta_R\delta_e + \delta_k\delta_e + \delta_R\delta_k\delta_e = O(\delta)$$

and

$$\delta \equiv \text{Max}(|\delta_R|, |\delta_k|, |\delta_e|)$$

Substituting Eq (B-143) into Eq (B-142)

$$V = \left(\frac{V_e r_1}{r_1 + r_2} \right) \left[\frac{1 - (1 + \delta_R + \delta_B) \frac{r_2}{r_1}}{2 + \delta_R + \delta_B} + \frac{(2 + \delta_R + \delta_B + B) \left(1 + \frac{r_2}{r_1} \right) k \epsilon}{(2 + \delta_R + \delta_B)^2} \right. \\ \left. + \frac{(2 + \delta_R + \delta_B + B) \left(1 + \frac{r_2}{r_1} \right) B k^2 \epsilon^2}{(2 + \delta_R + \delta_B)^3} + O(\epsilon^3 \delta^2 k) \right] \quad (\text{B-144})$$

The initial voltage is given by using ϵ_0 in Eq (B-144), so the difference in voltage due to a change in strain $\epsilon - \epsilon_0$ is then

$$V - V_0 = \frac{V_e k (\epsilon - \epsilon_0) D}{2} \left[1 + \frac{Bk(\epsilon + \epsilon_0)}{2 + \delta_R + \delta_B} + O(\epsilon^2 \delta^2 k^2) \right] \quad (3-101c)$$

where

$$D = \frac{2(2 + \delta_R + B)}{(2 + \delta_R + \delta_B)^2} \quad (3-141a)$$

Because the balancing resistor is part of the D term, changing the resistor after calibration can introduce error. The maximum error was estimated by assuming that for calibration, the compression resistance ($R_{i0} + R_B$) was 30Ω less than the tension resistance, but that in the wind tunnel, the balancing resistor was changed so that $R_{i0} + R_B$ was 30Ω greater than the tension resistance.

Under hydrostatic pressure, the strains are equal

$$\epsilon_c = \epsilon_t = \epsilon$$

If the gauge factors are not the same, then a change in normal pressure can result in a voltage output. Assuming that the initial strains of the strain gauges are equal, then the strain after application of hydrostatic pressure is given by substituting Eq (3-112) into Eq (B-136):

$$R_t = R_0(1 + k\epsilon) \quad R_c = R_0(1 + k\epsilon + \delta_k \epsilon) \quad (\text{B-145})$$

Substituting these into Eq (B-132) and assuming that the bridge is initially in balance as described by Eq (3-133), the voltage output due to application of hydrostatic pressure is then

$$V = \frac{V k \epsilon \delta_k}{4} \left[\frac{1}{1 + \left(1 + \frac{1}{2} \delta_k\right) k \epsilon} \right] \approx \frac{V k \epsilon \delta_k}{4} \quad (3-111)$$

B.9. Helium/Air Mixture

This derivation of the equations to use for a mixture of gases was used to predict the shock tunnel performance in Chapter 6. From Dalton's Law of Partial Pressures (Liepmann and Roshko, 1957:26), the pressure can be considered as the sum of the pressure that each gas would exert if it filled the container alone:

$$p = \sum p_i \quad (B-146)$$

Since then air initially occupies the driver tube alone, the partial pressure of the air can be taken as the air pressure immediately before the helium is added. The

partial pressure of the helium is simply

$$p_{h4} = p_4 - p_{a4} \quad (B-147)$$

The mass fraction of each species is defined by the relation (Anderson, 1989:386)

$$x_i = \frac{\rho_i}{\rho} \quad (B-148)$$

The total density is $\rho = \rho_{a4} + \rho_{h4}$. Substituting into Eq (B-148) and using $\rho = p/RT$ results in

$$x_a = \frac{p_{a4} R_h}{p_{a4} R_h + p_{h4} R_a} \quad (B-149)$$

Substituting Eq (B-147) into Eq (B-149),

$$x_a = \frac{p_{a4} R_h}{p_{a4} R_h + (p_4 - p_{a4}) R_a} \quad (B-150)$$

The mass fraction of the helium is then given by

$$x_h = 1 - x_a \quad (\text{B-151})$$

Since the air-helium mixture is non-reacting, the mass fraction of each component remains constant throughout the run.

The internal energy of the mixture is given by (Liepmann and Roshko, 1957:26)

$$e = \sum x_i e_i(T) \quad (\text{B-152})$$

Since the internal energy of each component is given by $e=c_v T$, Eq (B-152) becomes

$$e = (x_a c_{v(a)} + x_a c_{v(h)}) T_4 \quad (\text{B-153})$$

For constant mass fractions and specific heats, then, Eq (B-153) can be written

$$e_4 = c_{v4} T_4 \quad (\text{B-154})$$

where

$$c_{v4} = x_a c_{v(a)} + x_a c_{v(h)} \quad (\text{B-155})$$

Similarly, the enthalpy of the mixture is given by (Liepmann and Roshko, 1957:26)

$$h = \sum x_i h_i(T) \quad (\text{B-156})$$

Using the equation of state $h=c_p T$, the enthalpy equation becomes

$$h_4 = c_{p(4)} T_4 \quad (\text{B-157})$$

where

$$c_{p4} = x_a c_{p(a)} + x_a c_{p(h)} \quad (\text{B-158})$$

The ratio of specific heats of the mixture is then

$$\gamma_4 = \frac{c_{p4}}{c_{v4}} = \frac{x_a c_{p(a)} + x_a c_{p(h)}}{x_a c_{v(a)} + x_a c_{v(h)}} \quad (\text{B-159})$$

The value of the gas constant R of the mixture is (Anderson, 1989:387)

$$R_4 = \sum x_i R_i \quad (\text{B-160})$$

The thermal conductivity of the mixture can be calculated from the relation (Schetz, 1993:73)

$$k = \frac{1}{2} \left[k_1 X_1 + k_2 X_2 + \frac{k_1 k_2}{(X_1 \sqrt{k_2} + X_2 \sqrt{k_1})^2} \right] \quad (\text{B-1611})$$

where X_1 and X_2 are the mole fractions of the species. The mole fractions can be related to partial pressures through the ideal gas relation (Tipler, 1976:425)

$$pV = n\mathfrak{R}T \quad (\text{B-162})$$

where n represents the number of moles and \mathfrak{R} is the universal gas constant. Using as p the partial pressures and V the volume of the driver section of the shock tube, Equation (B-162) can be written for the two components

$$n_a = \frac{p_a V}{\mathfrak{R}T} \quad n_{\text{He}} = \frac{p_{\text{He}} V}{\mathfrak{R}T} \quad (\text{B-162a})$$

The mole fraction for the air can then be written

$$X_a = \frac{n_a}{n_a + n_{\text{He}}}$$

which, using Eqs (22) becomes

$$X_a = \frac{p_a}{p_4} \quad (\text{B-163})$$

The mole fraction for the helium can be calculated similarly or from

$$X_{\text{He}} = 1 - X_a \quad (\text{B-164})$$

Appendix C - Numerical Procedures

C.1. Unsteady One-Dimensional Heat Conduction with Convective Heat Transfer at Surface

The numerical solution to the unsteady one-dimensional heat conduction equation was implemented in two forms. The first was used to compute the heat flux from measured wall temperatures for the Wright Laboratory Mach 6 test; the second to calculate wall temperatures from freestream conditions and convection heat transfer theory. Both methods used the Crank-Nicolson scheme, but the first method used an even grid, while the second used grid clustering. Both of these methods will be discussed, followed by convergence demonstration using the exact solution for constant wall heat flux which was developed in Appendix B.2.

C.1.1. Heat Flux from Measured Wall Temperature

For the unsteady one-dimensional heat conduction equation (Anderson, Tannehill, and Pletcher, 1984:108)

$$\frac{\partial T}{\partial t} = \alpha \frac{\partial^2 T}{\partial z^2} \quad (\text{C-1})$$

the Crank-Nicolson scheme can be stated (Anderson, Tannehill, and Pletcher, 1984:112)

$$\frac{T_j^{n+1} - T_j^n}{\Delta t} = \alpha \frac{T_{j+1}^{n+1} - 2T_j^{n+1} + T_{j-1}^{n+1} + T_{j+1}^n - 2T_j^n + T_{j-1}^n}{2(\Delta x)^2} \quad (\text{C-2})$$

where n denotes the time level and j the spatial coordinate. The temperature at time level n is known, while the temperatures at time level $n+1$ are unknown. The Crank-Nicolson scheme is an implicit algorithm which is second-order accurate in time and space and is unconditionally stable. Equation (C-2) can be re-written

$$-rT_{j+1}^{n+1} + (1 + 2r)T_j^{n+1} - rT_{j-1}^{n+1} = rT_{j+1}^n + (1 - 2r)T_j^n + rT_{j-1}^n \quad (\text{C-3})$$

where r is defined

$$r \equiv \frac{\alpha \Delta t}{2(\Delta x)^2} \quad (\text{C-4})$$

Equation (C-3) is used for all interior points. The unknown values of T are on the left-hand side, while the right-hand side contains known quantities. For the upper surface, where the temperature is specified (Figure C-1),

$$\begin{aligned} T_{j+1}^n &= T_e^n \\ T_{j+1}^{n+1} &= T_e^{n+1} \end{aligned} \quad (\text{C-5})$$

Eq (C-3) becomes

$$(1 + 2r)T_j^{n+1} - rT_{j-1}^{n+1} = r(T_e^n + T_e^{n+1}) + (1 - 2r)T_j^n + rT_{j-1}^n \quad (\text{C-6})$$

For the bottom surface a zero-heat flux condition will be assumed. From Fourier's law (Bejan, 1984:11), the heat flux is given by

$$\dot{q} = -k \frac{\partial T}{\partial z} \quad (\text{C-7})$$

so zero heat results in

$$\left. \frac{\partial T}{\partial z} \right|_{z=z_{\max}} = 0 \quad (\text{C-8})$$

The derivative can be represented in one-sided difference form by the second order accurate expression (Anderson, Tannehill, and Pletcher, 1984:44)

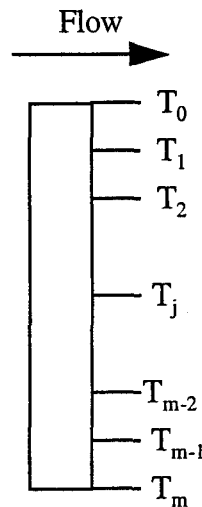


Figure C-1 Geometry for Numerical Solution to 1-D Heat Conduction

$$\frac{\partial T}{\partial z} \sim \frac{3T_{m+1} - 4T_m + T_{m-1}}{2\Delta z} \quad (C-9)$$

Substituting into Eq (C-8), then, results in

$$T_{m+1} = \frac{4}{3}T_m - \frac{1}{3}T_{m-1} \quad (C-10)$$

Substituting this expression into Eq (C-3) results in the following difference expression for the lower surface:

$$\left(1 + \frac{2}{3}r\right)T_m^{n+1} - \frac{2}{3}rT_{m-1}^{n+1} = \left(1 - \frac{2}{3}r\right)T_m^n + \frac{2}{3}rT_{m-1}^n \quad (C-11)$$

Using Eq (C-3) for the interior points, Eq (C-6) for the upper boundary, and Eq (C-11) for the lower boundary, the Crank-Nicolson scheme for this situation can be represented by the following matrix expression:

$$\begin{pmatrix} 1+2r & -r & 0 & \cdots & 0 & 0 \\ -r & 1+2r & -r & 0 & & \\ 0 & -r & 1+2r & -r & & \\ \vdots & & & \ddots & & \\ 0 & & -r & 1+2r & -r & \\ 0 & & 0 & -\frac{2}{3}r & 1+\frac{2}{3}r & \end{pmatrix} \begin{pmatrix} T_1^{n+1} \\ T_2^{n+1} \\ T_4^{n+1} \\ \vdots \\ T_{m-1}^{n+1} \\ T_m^{n+1} \end{pmatrix} = \begin{pmatrix} 1-2r & r & 0 & \cdots & 0 & 0 \\ r & 1-2r & r & 0 & & \\ 0 & r & 1-2r & r & 0 & \\ \vdots & & & \ddots & & \\ 0 & & 0 & r & 1-2r & r \\ 0 & & 0 & \frac{2}{3}r & 1-\frac{2}{3}r & \end{pmatrix} \begin{pmatrix} T_1^n \\ T_2^n \\ T_3^n \\ \vdots \\ T_{m-1}^n \\ T_m^n \end{pmatrix} + \begin{pmatrix} r(T_e^{n+1} + T_e^n) \\ 0 \\ 0 \\ \vdots \\ 0 \\ 0 \end{pmatrix} \quad (C-12)$$

Equation (C-12) is in the form $Ax=b$ where x is the matrix of unknowns. Since A is a tridiagonal matrix, the Thomas algorithm described in Appendix C.3 can be used for the solution.

The numerical solution was verified by using the exact solution for constant wall heat flux applied as a step function (Appendix B.2) to generate a wall temperature profile for a wall heat flux of 100,000 W, which was the approximate wall heat flux for the Mach 6 Run 57. The numerical solution was then used to calculate the wall heat flux from the generated wall temperatures. An accurate solution would calculate a heat flux of 100,000 W. The solution was run for two spatial grids, the first a coarse mesh of 21 grid points, and the second a medium grid of 51 gridpoints. The time increment was 0.0001 sec up to $t=0.1$ sec and then 0.01 sec thereafter. As can be seen in Figure C-2, the numerical solution was highly accurate, with the coarse grid solution being within 1 percent of the exact value after 0.28 sec, and the medium grid solution being within 1 percent of the exact value after 0.04 sec.

In reducing the actual data from the Mach 6 test, a time interval of 0.01 second was used. When the exact solution was used to generate the wall temperature, and the numerical solution was used to calculate the heat flux without temporal clustering (with a constant 0.01 sec interval), the results were less accurate, as can be seen in Figure C-3.

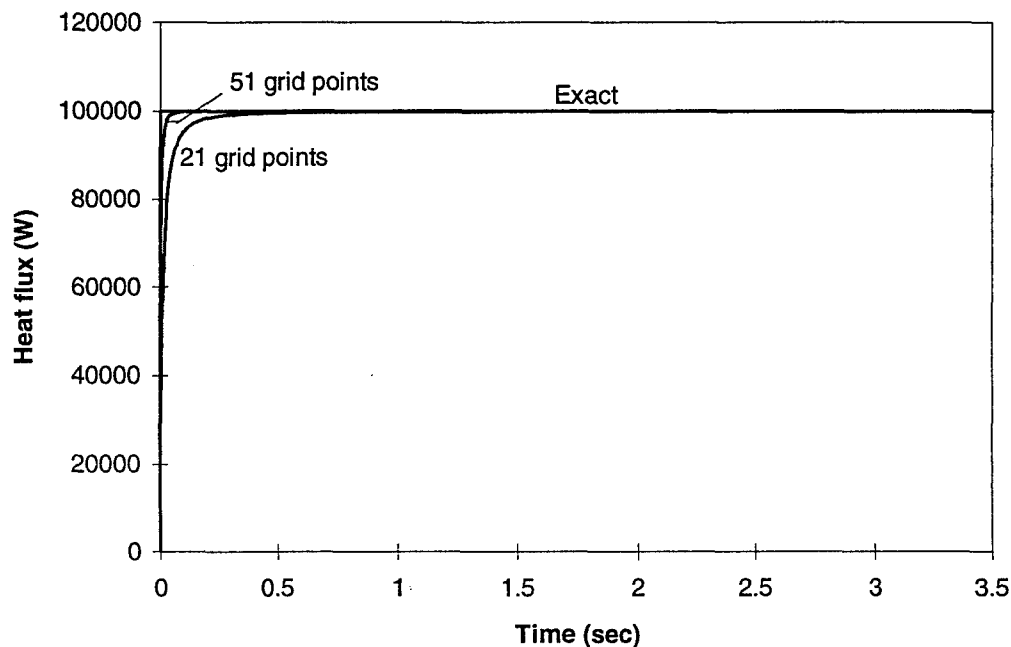


Figure C-2 Numerical vs. Exact solution, Heat Flux form Wall Temperature, with Temporal Clustering

Three spatial grids were used of 51, 101, and 151 increments, but the graphs overlay to such an extent as to be indistinguishable. In this case, the inaccuracy at the end of 3.5 seconds is 3.6 percent. However, the true data does not represent a step function so much as a steep ramp, so this is an artificially induced inaccuracy.

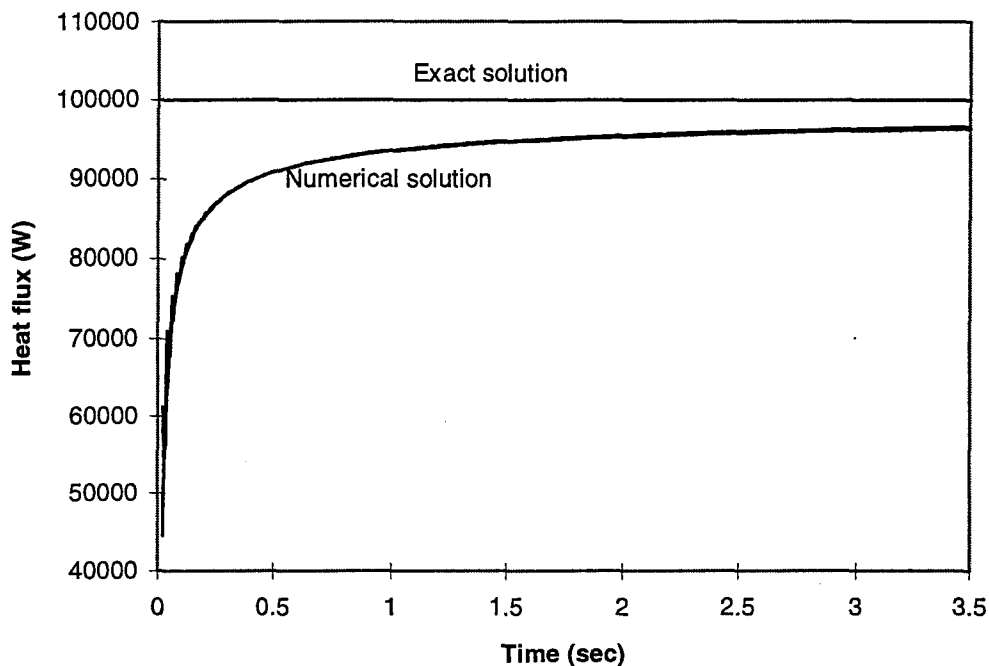


Figure C-3 Numerical vs. Exact solution, Heat Flux from Wall Temperature, without Temporal Clustering

To test whether a finer time mesh should be used with the temperatures interpolated, the Run 57 data was reduced in two forms, the first using the raw data with 0.01 second interval, and the second interpolating the temperatures to obtain a 0.001 sec interval. Both cases used 51 grid points for the spatial mesh. As can be seen in Figure C-4, the results are indistinguishable. The jagged nature of the graph is due to the fluctuations in the temperature data.

C.1.2. Wall Temperatures from Predicted Heat Flux

This solution is similar to the previous. However, for this case, the heat flux is first calculated from convection theory. The temperature for the next time level is then

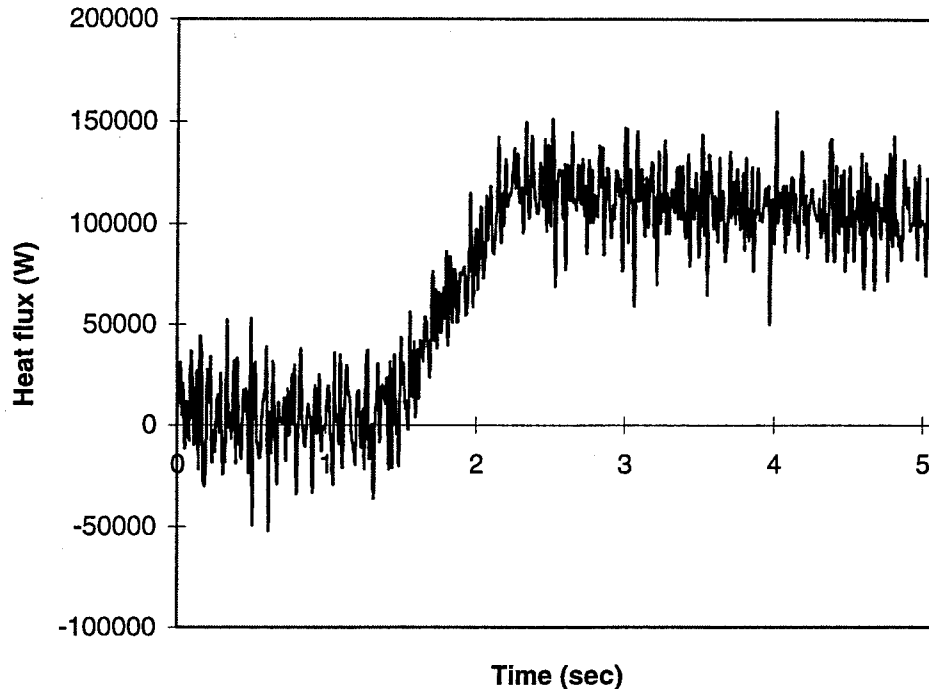


Figure C-4 Run 57 Heat Flux Calculation

computed using the calculated heat flux. Since the heat flux calculation is based on wall temperature, which is not known beforehand, iteration is required:

- (a) the wall temperature is guessed
- (b) the heat flux is calculated
- (c) the wall temperature (as well as interior points) is computed using the Crank-Nicolson scheme. If this wall temperature does not match the guessed wall temperature, then a new wall temperature is guessed and the process is repeated.

Since this iteration is performed at each time level, a more computationally efficient scheme was sought by clustering the grid points. A second reason for clustering is that, for the plastic sensor, the thermal effects are concentrated at the surface, while for the stainless steel wall in the Mach 6 tunnel, which the previous solution was used for, the thermal effects penetrated all the way to the backface.

For an uneven mesh, Taylor series expansion about the points $j+1$ and $j-1$ can be written

$$T_{j+1} = T_j + \Delta z_p T'_j + \frac{(\Delta z_p)^2}{2} T''_j + \frac{(\Delta z_p)^3}{6} T'''_j + O[(\Delta z_p)^4] \quad (C-13a)$$

$$T_{j-1} = T_j - \Delta z_p T'_j + \frac{(\Delta z_p)^2}{2} T''_j - \frac{(\Delta z_p)^3}{6} T'''_j + O[(\Delta z_p)^4] \quad (C-13b)$$

where Δz_p represents distance between the points $j+1$ and j and Δz_m represents distance between the points j and $j-1$. Dividing (C-13a) by Δz_p and (C-13b) by Δz_m results in

$$\frac{T_{j+1}}{\Delta z_p} = \frac{T_j}{\Delta z_p} + T'_j + \frac{\Delta z_p}{2} T''_j + \frac{(\Delta z_p)^2}{6} T'''_j + O[(\Delta z_p)^3] \quad (C-14a)$$

$$\frac{T_{j+1}}{\Delta z_m} = \frac{T_j}{\Delta z_m} - T'_j + \frac{\Delta z_m}{2} T''_j - \frac{(\Delta z_m)^2}{6} T'''_j + O[(\Delta z_m)^3] \quad (C-14b)$$

Now subtracting (C-14b) from (c-14a) and rearranging results in the following difference formula for the second derivative:

$$T''_j = \frac{\frac{T_{j+1}}{\Delta z_p} - \left(\frac{1}{\Delta z_p} + \frac{1}{\Delta z_m} \right) + \frac{T_{j-1}}{\Delta z_m}}{\frac{1}{2}(\Delta z_p + \Delta z_m)} + \frac{\frac{1}{3}(\Delta z_p^2 - \Delta z_m^2)}{\Delta z_p + \Delta z_m} T'''_j + O[(\Delta z_p)^2] \quad (C-15)$$

If Δz_p is close in size to the Δz_m , then the second term in Eq (C-15) is of order $(\Delta z_p)^2$, and Eq (C-15) is second order accurate.

In general terms, the Crank-Nicolson scheme can be stated as

$$T_j^{n+1} - T_j^n = \frac{1}{2} \alpha \Delta t (\delta^2 T_j^{n+1} + \delta^2 T_j^n) \quad (C-16)$$

where δ^2 represents the spatial second derivative difference term. From Eq (C-15), this difference term can be written

$$\delta^2 T_j \equiv r_m T_{j-1} - r T_j + r_p T_{j+1} \quad (C-17)$$

where

$$\begin{aligned}
r_m &= \frac{\alpha \Delta t}{\Delta z_m (\Delta z_p + \Delta z_m)} \\
r &= r \frac{\alpha \Delta t}{\Delta z_m \Delta z_p} \\
r_p &= \frac{\alpha \Delta t}{\Delta z_p (\Delta z_p + \Delta z_m)}
\end{aligned} \tag{C-18}$$

Substituting Eq (C-17) into Eq (C-16), the following expression is obtained for the interior points:

$$-r_m T_{j-1}^{n+1} + (1+r)T_j^{n+1} - r_p T_{j+1}^{n+1} = r_m T_{j-1}^n + (1-r)T_j^n + r_p T_{j+1}^n \tag{C-19}$$

For both the upper and lower boundaries, a uniform mesh spacing was used to improve accuracy. For the top boundary, for a specified heat flux, a one-sided difference expression of Fourier's Law can be written as

$$\frac{3T_0 - 4T_1 + T_2}{2\Delta z_1} = \frac{\dot{q}}{k} \equiv Q \tag{C-20}$$

This can be rearranged as

$$T_0 = \frac{4}{3}T_1 - \frac{1}{3}T_2 + \frac{2}{3}\Delta z_1 Q \tag{C-21}$$

Substituting into (C-19) and using the following since the boundary mesh is uniform,

$$\Delta z_m = \Delta z_p = \Delta z_1 \tag{C-22}$$

$$r_m = r_p = r_1 \tag{C-23}$$

the following equation is obtained for the upper boundary:

$$\left(1 + \frac{2}{3}r_1\right)T_j^{n+1} - \frac{2}{3}r_1 T_{j+1}^{n+1} = \left(1 - \frac{2}{3}r_1\right)T_j^n + \frac{2}{3}r_1 T_{j+1}^n + \frac{2}{3}r_1 \Delta z_1 (Q^{n+1} + Q^n) \tag{C-24}$$

For the lower boundary, Eq (C-11) applies. Then using Eq (C-19) for the interior points, Eq (C-24) for the upper boundary, and Eq (C-11) for the lower boundary, the Crank-Nicolson scheme for this situation can be represented by the following matrix expression:

$$\begin{pmatrix}
1 + \frac{2}{3}r_{m(1)} & -\frac{2}{3}r_{m(1)} & 0 & \dots & 0 & 0 \\
-r_{m(2)} & 1 + r_2 & -r_{p(2)} & 0 & 0 & 0 \\
0 & -r_{m(3)} & 1 + r_3 & -r_{p(3)} & 0 & 0 \\
\vdots & & & \ddots & & \vdots \\
0 & & & -r_{m(m-1)} & 1 + r_{m-1} & -r_{p(m-1)} \\
0 & 0 & \dots & 0 & -\frac{2}{3}r_{p(m)} & 1 + \frac{2}{3}r_{p(m)}
\end{pmatrix}
\begin{pmatrix}
T_1^{n+1} \\
T_2^{n+1} \\
T_3^{n+1} \\
\vdots \\
T_{m-1}^{n+1} \\
T_m^{n+1}
\end{pmatrix}
=
\begin{pmatrix}
1 - \frac{2}{3}r_{m(1)} & \frac{2}{3}r_{m(1)} & 0 & \dots & 0 & 0 \\
r_{m(2)} & 1 - r_2 & r_{p(2)} & 0 & 0 & 0 \\
0 & r_{m(3)} & 1 - r_3 & r_{p(3)} & 0 & 0 \\
\vdots & & & \ddots & & \vdots \\
0 & & & r_{m(m-1)} & 1 - r_{m-1} & r_{p(m-1)} \\
0 & 0 & \dots & 0 & \frac{2}{3}r_{p(m)} & 1 - \frac{2}{3}r_{p(m)}
\end{pmatrix}
\begin{pmatrix}
T_1^n \\
T_2^n \\
T_3^n \\
\vdots \\
T_{m-1}^n \\
T_m^n
\end{pmatrix}
+
\begin{pmatrix}
\frac{2}{3}r_1\Delta z_1(Q^{n+1} + Q^n) \\
0 \\
0 \\
\vdots \\
0 \\
0
\end{pmatrix}
\tag{C-25}$$

Again, Eq (C-25) is in the form $Ax=b$ where x is the matrix of unknowns. The Thomas algorithm was used for the solution.

The wall heat flux was calculated from convection theory. For the shock tunnel, the heat flux can be calculated using Eckert's reference enthalpy method (Kays & Crawford, 1980:304-305,308-309). The reference enthalpy method was developed to allow the use of an incompressible correlation for heat transfer and skin friction which is then corrected for compressibility. The Eckert reference temperature method is considered valid

up to Mach 20, and it was chosen for this application because it allows consideration of high temperature gas effects. The following treatment assumes that specific heats are not constant.

First a reference enthalpy is calculated.

$$h_R = h_e + 0.5(h_w - h_e) + 0.22(h_{aw} - h_e) \quad (C-26)$$

where

$$h_{aw} = h_e + \frac{1}{2} ru_e^2 \quad (C-27)$$

Here, h denotes specific enthalpy and the R-subscript denotes the reference condition. To account for high temperature effects, the Tannehill and Mugge (1974) correlations of statistical and tabulated thermodynamic data will be used. Boundary layer theory normally assumes that the wall pressure is the same as the pressure at the edge of the boundary layer, and this assumption will be used by letting $p_w = p_e$, although for hypersonic flows, this is not always true (Anderson, 1989:225-226). The pressure, along with the temperature, will provide the two state conditions necessary to calculate the enthalpy.

From the reference enthalpy, the reference temperature is computed, again using p_e as the second state variable. The recovery factor r is calculated from the Prandtl number at reference conditions, so iteration is required. Once the reference conditions are established, the reference Stanton number is calculated using an incompressible correlation, for example, the von Karman (1939) correlation:

$$St_R = \frac{\frac{1}{2} C_f}{1 + 5 \left(\frac{1}{2} C_f \right)^{1/2} \left\{ Pr - 1 + \ln \left[1 + \frac{5}{6} (Pr - 1) \right] \right\}} \quad (C-28)$$

with (White, 1991:432)

$$C_f = \frac{0.455}{\ln^2(0.06 Re_{x,R})} \quad (C-29)$$

The Reynolds number is calculated at reference conditions

$$Re_{x,R} = \frac{\rho_R u_e x \rho}{\mu_R} \quad (C-30)$$

From the reference Stanton number, the enthalpy conductance g_h can be computed:

$$St_R = \frac{g_h}{\rho_R u_e} \quad (C-31)$$

or,

$$g_h = St_R \rho_R u_e \quad (C-31a)$$

Finally, from the enthalpy conductance, the heat flux \dot{q} is obtained:

$$\dot{q}_w = g_h (h_w - h_{aw}) \quad (C-32)$$

For the Wright Laboratory mach 6 blow-down tunnel, the stagnation temperatures were lower, so the heat flux was computed using the Reynolds analogy (Cebeci and Bradshaw, 1988:349).

$$St = 1.16 \frac{C_f}{2} \quad (C-33)$$

The skin friction was calculated using the Van Driest II correlation as described in Appendix B-4. The Stanton number was then calculated using Eq (C-33), followed by the enthalpy conductance from

$$St = \frac{g_h}{\rho_e u_e} \quad (C-34)$$

The heat flux then follows from Eq (C-32).

This numerical scheme was also verified by comparison to the exact solution for constant wall heat flux. Both numerical and exact solutions were run for the case of a constant wall heat flux of 4,000,000 W/m² (the approximate wall heat flux for the inlet in the NASA Ames runs). The Ultem material properties were used. The spatial grid had a wall spacing of 0.0001 mm with backface spacing of 1.46 mm and thickness of 20.32 mm. The temporal grid used an initial time step of 1x10⁻⁸ msec with a final time step of 0.02 msec, with gradual change between 1x10⁻⁷ and 0.5 msec. The analysis was run for 6 msec. The time history of the wall temperature is shown in Figure C-5 and a comparison of the final temperature profiles in Figure C-6. In both charts, the numerical and exact solutions are close enough to be indistinguishable. The average absolute error for the wall temperature is 0.0568 percent and for the temperature profile, in the upper 0.2 mm (below which the thermal effects did not penetrate), the average absolute error is 0.0329 percent.

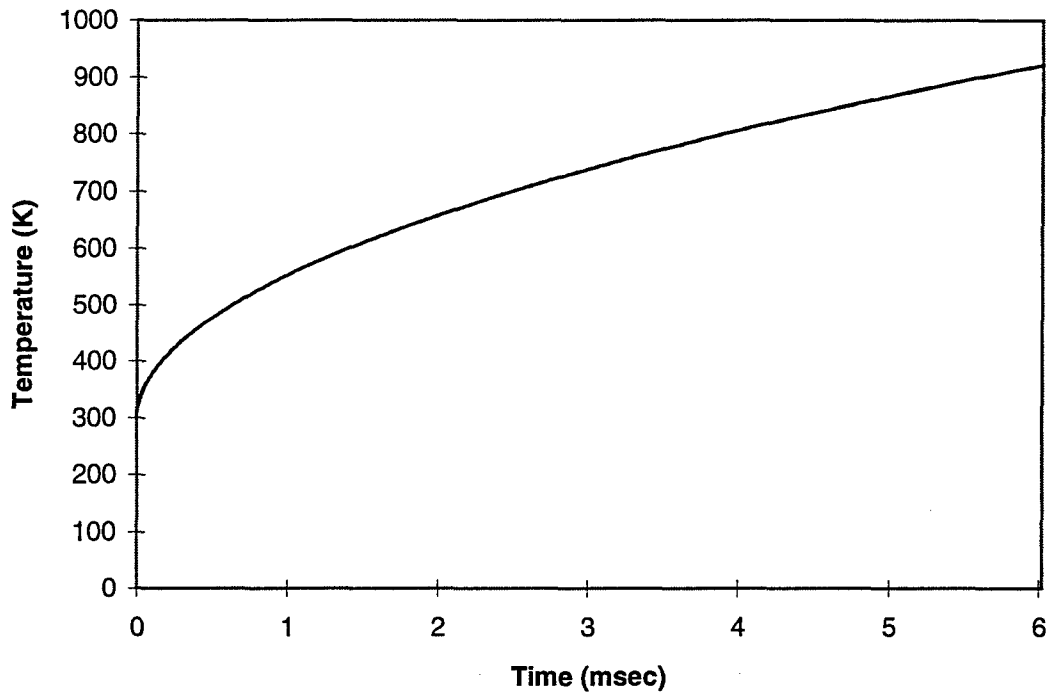


Figure C-5 Calculated Wall Temperature for Constant Heat Flux of $4,000,000 \text{ W/m}^2$ (Numerical vs. Exact)

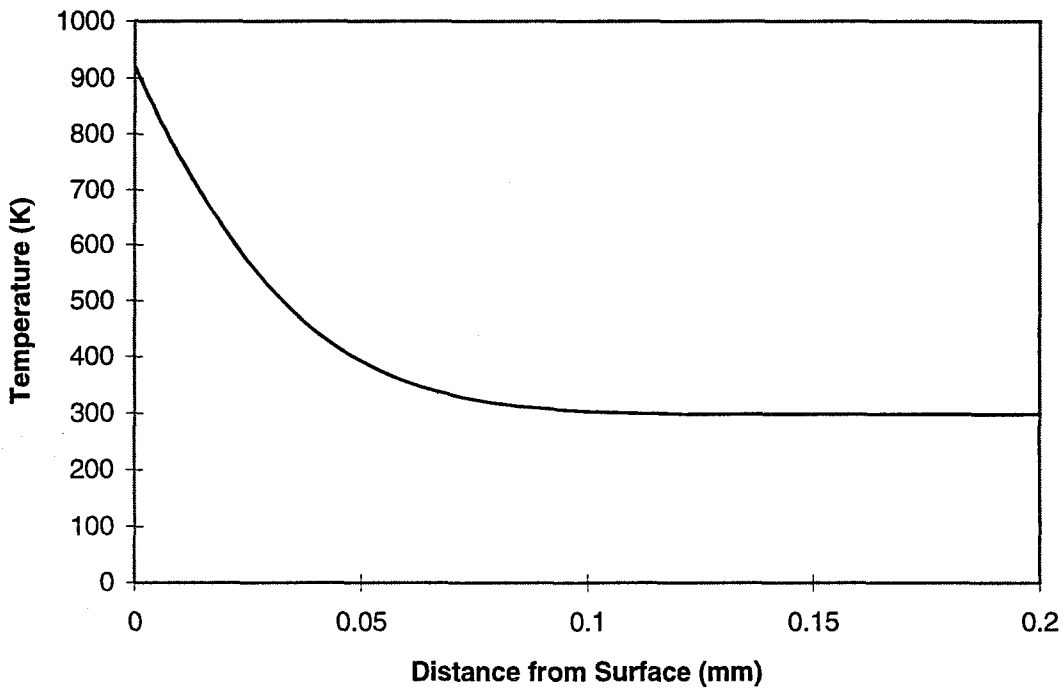


Figure C-6 Calculated Temperature Distribution for Constant Heat Flux of $4,000,000 \text{ W/m}^2$ after 6 msec (Numerical vs. Exact)

C.2. Unsteady Laminar Flow Through Concentric Annulus with Decreasing Pressure Gradient

This analysis was undertaken to determine the time required for the oil to flow into the gauge after application of back pressure. The results of this analysis were described in Chapter 4. Since the pressure inside the gauge increases as the oil flows into the gauge, a closed form solution was not possible, and a numerical procedure was applied. The numerical procedure consisted of solving the unsteady Navier-Stokes equations for incompressible flow through a concentric annulus.

C.2.1. Analytical computation

The time required to fill the gauge with oil will be estimated by assuming that the oil flow through the gap is fully developed laminar flow through a concentric annulus. For such flow, the volumetric flow rate has been calculated as (White, 1991:120)

$$Q = \frac{\pi}{8\mu} \left(-\frac{dp}{dz} \right) \left[a^4 - b^4 - \frac{(a^4 - b^4)^2}{\ln(a/b)} \right] \quad (C-35)$$

where Q is the volumetric flow rate, μ is the coefficient of viscosity, dp/dz is the pressure gradient, a is the inner radius of the annulus (for this case equal to the radius of the sensor head) and b is the outer radius of the annulus. If a and b are nearly equal, the term in brackets can be expanded in a series as (White, 1991:121)

$$\begin{aligned} a^4 - b^4 - \frac{(a^4 - b^4)^2}{\ln(a/b)} &= \frac{4}{3} b(a-b)^3 + \frac{2}{3} (a-b)^4 + O[(a-b)^5] \\ &= \frac{4}{3} R_H W^3 + \frac{2}{3} W^4 + O(W^5) \end{aligned} \quad (C-36)$$

where R_H represents the radius of the sensor head. Retaining the leading order term only, the volumetric flow rate through the gap is given by

$$Q = \frac{\pi R_H W^3}{6\mu} \left(-\frac{dp}{dz} \right) \quad (C-37)$$

The pressure gradient can be calculated as the difference in pressure between the top and bottom of the gap divided by the gap length. However, the air pressure in the gauge increases as the fluid enters the cavity, so the pressure gradient decreases with time. This variable pressure gradient requires numerical computation. However, for the ideal case where a perfect vacuum is obtained, the pressure gradient is constant. The time to fill the gauge will then be given by

$$t = \frac{V}{Q}$$

Substituting Eq (C-37)

$$t = \frac{6\mu V}{\pi R_H W^3 \left(-\frac{dp}{dz} \right)} \quad (C-38)$$

where V is the volume of the oil cavity in the gauge. The pressure gradient can be calculated as the difference in pressure between the bottom and top of the gap divided by the gap length:

$$\frac{dp}{dz} = \frac{p_0 - p_t}{T_L} \quad (C-39)$$

where p_0 , the fluid pressure at the bottom of the gap, is given by

$$p_0 = p_a + \frac{2\sigma}{W} \quad (C-40)$$

and p_t , the pressure at the top of the gap, is given by

$$p_t = p_b + \rho hg - \frac{4\sigma}{D} \quad (C-41)$$

The oil column height h decreases as oil enters the gauge. The variation of h can be represented by

$$h = h_0 - \frac{V_f}{\frac{1}{4}\pi D^2} \quad (C-42)$$

where V_f represents the instantaneous volume of the gauge which has been filled. If D is sufficiently large, however, the second term in Eq (C-42) is negligible, and h can be con-

sidered to be constant. Substituting Eqs (C-40) and (C-41) into Eq (C-39) then provides the pressure gradient:

$$\begin{aligned} \frac{dp}{dz} &= \frac{p_a + \frac{2\sigma}{W} - \left(p_b + \rho hg - \frac{4\sigma}{D} \right)}{T_L} \\ &= - \frac{p_b + \rho hg - p_a - 2\sigma \left(\frac{1}{W} - \frac{2}{D} \right)}{T_L} \end{aligned} \quad (C-43)$$

For this case, the air pressure in the oil cavity is zero, so the pressure gradient becomes

$$\frac{dp}{dz} = - \frac{p_b + \rho hg - 2\sigma \left(\frac{1}{W} - \frac{2}{D} \right)}{T_L} \quad (C-43a)$$

Substituting this result into Eq (C-38),

$$\begin{aligned} t &= \frac{6\mu V}{\pi R_H W^3 \left[\frac{p_b + \rho hg - 2\sigma \left(\frac{1}{W} - \frac{2}{D} \right)}{T_L} \right]} \\ &= \frac{6\mu V T_L}{\pi R_H W^3 \left[p_b + \rho hg - 2\sigma \left(\frac{1}{W} - \frac{2}{D} \right) \right]} \end{aligned} \quad (C-44)$$

In terms of the kinematic viscosity, with

$$v = \frac{\mu}{\rho} \quad (C-45)$$

Eq (C-44) becomes

$$t = \frac{6\rho v V T_L}{\pi R_H W^3 \left[p_b + \rho hg - 2\sigma \left(\frac{1}{W} - \frac{2}{D} \right) \right]} \quad (C-46)$$

Using the dimensions calculated in the previous section, with a viscosity of 200 cSt and the volume that of the baseline gauge. from Eq (C-46), the time to fill the gauge is then 0.042 second. Even for a high viscosity oil with kinematic viscosity of 10,000 cSt, the time to fill the gauge is only 2.1 seconds. However, this represents the lower limit of the

time required to fill the gauge; the actual pressure gradient decreases as the air bubble is compressed, slowing the flow; in addition, this solution ignores the starting dynamics. A more accurate time will be calculated numerically.

C.2.2. Numerical solution

The numerical solution will be developed from the unsteady Navier Stokes equations. First, it will be shown that the assumption of fully developed flow used in the exact solution is a valid approximation that will be retained for the numerical solution. Next, the equations will be developed to solve the flow-field.

C.2.2.1. Entrance region.

The flow at the entrance of a duct is characterized by boundary layers on the walls of the duct with inviscid flow at the center of the duct. The boundary layers grow in thickness until they meet at the center of the duct to form the fully developed viscous flow which is characteristic of duct flow. For flow of an incompressible flow in a two-dimensional duct (a duct made of two flat plates), the entrance length was calculated by Sparrow (1955) as

$$\frac{X}{D} = 0.0065 \text{Re}_D \quad (\text{C-47})$$

where X is the entrance length, D is the width of the duct, and Re_D is the Reynolds number based on duct length defined as

$$\text{Re}_D = \frac{UD}{\nu} \quad (\text{C-48})$$

where U is the velocity averaged across the duct area. Eq (C-47) applies to a two dimensional duct. While an annulus is not a two dimensional duct, for the annulus in question, the width of the gap is very small compared to the radius of the annulus, so the entrance length for the two-dimensional duct can be used to obtain the approximated length for the entrance region for the annulus.

The average velocity can be calculated using the flow rate given by Eq (C-37). First, the pressure gradient is calculated from Eq (C-43a). Then, the volumetric flow rate is calculated from Eq (C-37). The gap cross-sectional area is given by

$$A = \pi(R_o^2 - R_H^2)$$

The average flow velocity is then

$$U = \frac{Q}{A}$$

The Reynolds number is then calculated from Eq (C-48) and the entrance length from Eq (C-47). For oil with viscosity of 200 cSt, and the baseline gauge dimensions shown in Appendix A, the mean velocity is 2.86 m/s, the Reynolds number is 1.81, and $x/D=0.0118$. Thus, the entrance length is only 1 percent of the gap width. Since the length of the narrow section of the annulus is twice the gap width, the entrance length is 0.6 percent of the total length of the annulus, with the remaining 99.4 percent of the length being fully developed flow. Thus, it appears that the assumption of fully developed flow is a valid approximation.

While the above solution uses the assumption in the previous section, that the air pressure in the oil cavity is zero, the pressure is actually greater than zero, increasing to approximately atmospheric at the end of the oil filling process. The increasing pressure decreases the pressure gradient, which decreases the velocity and the Reynolds number. This, in turn, would shorten the entrance length in Eq (C-47), so the assumption of fully developed flow is valid for all pressure gradients that will be examined in the numerical solution.

C.2.2.2. Equations for the Numerical Solution

In cylindrical form for an incompressible, constant property fluid, the Navier Stokes equations can be rendered (Currie, 1974:422):

Continuity

$$\frac{1}{R} \frac{\partial}{\partial R} (R u_R) + \frac{1}{R} \frac{\partial u_\theta}{\partial \theta} + \frac{\partial u_z}{\partial z} = 0 \quad (C-49)$$

R-momentum

$$\rho \left(\frac{\partial u_R}{\partial t} + u_R \frac{\partial u_R}{\partial R} + \frac{u_\theta}{R} \frac{\partial u_R}{\partial \theta} - \frac{u_\theta^2}{R} + u_z \frac{\partial u_R}{\partial z} \right) = -\frac{\partial p}{\partial R} + \mu \left(\nabla^2 u_R - \frac{u_R}{R^2} - \frac{2}{R^2} \frac{\partial u_\theta}{\partial \theta} \right) + \rho f_R \quad (\text{C-50})$$

θ-momentum

$$\rho \left(\frac{\partial u_\theta}{\partial t} + u_R \frac{\partial u_\theta}{\partial R} + \frac{u_\theta}{R} \frac{\partial u_\theta}{\partial \theta} + \frac{u_R u_\theta}{R} + u_z \frac{\partial u_\theta}{\partial z} \right) = -\frac{1}{R} \frac{\partial p}{\partial \theta} + \mu \left(\nabla^2 u_\theta - \frac{u_\theta}{R^2} + \frac{2}{R^2} \frac{\partial u_R}{\partial \theta} \right) + \rho f_\theta \quad (\text{C-51})$$

z-momentum

$$\rho \left(\frac{\partial u_z}{\partial t} + u_R \frac{\partial u_z}{\partial R} + \frac{u_\theta}{R} \frac{\partial u_z}{\partial \theta} + u_z \frac{\partial u_z}{\partial z} \right) = -\frac{\partial p}{\partial z} + \mu \nabla^2 u_z + \rho f_z \quad (\text{C-52})$$

where

$$\begin{aligned} \nabla^2 &= \frac{1}{R} \frac{\partial}{\partial R} \left(R \frac{\partial}{\partial R} \right) + \frac{1}{R^2} \frac{\partial^2}{\partial \theta^2} + \frac{\partial^2}{\partial z^2} \\ &= \frac{\partial^2}{\partial R^2} + \frac{1}{R} \frac{\partial}{\partial R} + \frac{1}{R^2} \frac{\partial^2}{\partial \theta^2} + \frac{\partial^2}{\partial z^2} \end{aligned} \quad (\text{C-53})$$

The following assumptions will be made:

- (1) Properties are constant in the θ -direction
- (2) The only component of velocity is in the z -direction
- (3) The only body force is gravity, so the body force terms become

$$f_R = f_\theta = 0$$

$$f_z = g$$

With these simplifications, the Laplacian becomes

$$\nabla^2 = \frac{\partial^2}{\partial R^2} + \frac{1}{R} \frac{\partial}{\partial R} + \frac{\partial^2}{\partial z^2} \quad (\text{C-53a})$$

The continuity and momentum equations become

Continuity

$$\frac{\partial u_z}{\partial z} = 0 \quad (\text{C-49a})$$

R-momentum

$$\frac{\partial p}{\partial R} = 0 \quad (\text{C-50a})$$

θ -momentum

$$0 = 0 \quad (\text{C-51a})$$

z-momentum

$$\rho \left(\frac{\partial u_z}{\partial t} + u_z \frac{\partial u_z}{\partial z} \right) = -\frac{\partial p}{\partial z} + \mu \nabla^2 u_z + \rho g \quad (\text{C-52a})$$

Using the result from the continuity equation, Eq (C-49a), and also the definition of the Laplacian from Eq (C-53a), the z-momentum equation becomes

$$\rho \frac{\partial u_z}{\partial t} = -\frac{\partial p}{\partial z} + \mu \left(\frac{\partial^2 u_z}{\partial R^2} + \frac{1}{R} \frac{\partial u_z}{\partial R} + \frac{\partial^2 u_z}{\partial z^2} \right) + \rho g \quad (\text{C-52b})$$

Since from the continuity equation, $\partial u_z / \partial z = 0$, then

$$\frac{\partial^2 u_z}{\partial z^2} = 0 \quad (\text{C-54})$$

Substituting this result into Eq (C-52b) provides the final version of the momentum equation which is to be numerically solved:

$$\rho \frac{\partial u_z}{\partial t} = -\frac{\partial p}{\partial z} + \mu \left(\frac{\partial^2 u_z}{\partial R^2} + \frac{1}{R} \frac{\partial u_z}{\partial R} \right) + \rho g \quad (\text{C-52c})$$

or dividing through by ρ and rearranging,

$$\frac{\partial u_z}{\partial t} - \nu \left(\frac{\partial^2 u_z}{\partial R^2} + \frac{1}{R} \frac{\partial u_z}{\partial R} \right) = -\frac{1}{\rho} \frac{\partial p}{\partial z} + g \quad (\text{C-52d})$$

Equation (C-52d) is similar in form to the heat equation which was solved numerically in Section C.1. The boundary conditions are the no slip conditions at the walls:

$$u_z(R_H, t) = 0 \quad (\text{C-55})$$

$$u_z(R_o, t) = 0 \quad (\text{C-56})$$

The initial condition will assume that the fluid is at rest:

$$u_z(z, 0) = 0 \quad (\text{C-57})$$

Rearranging Eq (C-52c) and taking the derivative with respect to z reveals the following:

$$\frac{\partial p}{\partial z} = \mu \left(\frac{\partial^2 u_z}{\partial R^2} + \frac{1}{R} \frac{\partial u_z}{\partial R} \right) - \rho \frac{\partial u_z}{\partial t} + \rho g$$

$$\frac{\partial^2 p}{\partial z^2} = \frac{\partial}{\partial z} \left[\mu \left(\frac{\partial^2 u_z}{\partial R^2} + \frac{1}{R} \frac{\partial u_z}{\partial R} \right) - \rho \frac{\partial u_z}{\partial t} + \rho g \right] \quad (\text{C-58})$$

Since u is a function of only R and z , and μ , ρ , and g are constant. Thus, the right hand side of Eq (C-58) is zero, so Eq (C-58) becomes

$$\frac{\partial^2 p}{\partial z^2} = 0 \quad (\text{C-59})$$

Since Eq (C-50a) indicates that pressure is not a function of R , and θ -variation of all variables has been assumed to be zero, integrating Eq (C-59) results in

$$\frac{\partial p}{\partial z} = f(t) \quad (\text{C-60})$$

Thus, it can be concluded that the pressure gradient varies only with time but not with z . Thus, as in Section 3.4.1, the pressure has a linear distribution over z , with the pressure gradient being given by Eq (C-43)

$$\frac{dp}{dz} = - \frac{p_b + \rho hg - p_a - 2\sigma \left(\frac{1}{W} - \frac{2}{D} \right)}{T_L} \quad (\text{C-43})$$

The air pressure in the gauge increases as the fluid enters the cavity. Assuming no change in the air temperature, the air pressure is given by

$$p_a = p_v \left(\frac{V}{V_a} \right) \quad (\text{C-61})$$

where V is the volume of the oil cavity, and V_a is the volume of the air bubble, which is initially the same size as the cavity. The pressure gradient is then given by

$$\frac{\partial p}{\partial z} = - \frac{p_b + \rho hg - \frac{p_v V}{V_a} - 2\sigma \left(\frac{1}{W} - \frac{2}{D} \right)}{T_L} \quad (\text{C-62})$$

where the oil column height h is assumed to be constant

The instantaneous volume of the air bubble can be calculated from the amount of oil that has entered the cavity. The volumetric flow rate is given at any specific instant of time by

$$Q(t) = \int_{R_H}^{R_o} u(2\pi R) dR \quad (C-63)$$

The volume of the air bubble is then given by

$$V_a = V - \int_0^t Q d\tau \quad (C-64)$$

where t is a dummy variable of integration representing time.

C.2.2.3. Numerical Implementation

The equations which will be numerically implemented are summarized as follows:

$$\frac{\partial u_z}{\partial t} - v \left(\frac{\partial^2 u_z}{\partial R^2} + \frac{1}{R} \frac{\partial u_z}{\partial R} \right) = -\frac{1}{\rho} \frac{\partial p}{\partial z} + g \quad (C-52d)$$

subject to the following boundary and initial conditions:

$$u_z(R_H, t) = 0$$

$$u_z(R_o, t) = 0$$

$$u_z(z, 0) = 0$$

$$\frac{\partial p}{\partial z} = f(t)$$

where $f(t)$ is given by Eqs (C-62), (C-63), and (C-64). Since Eq (C-52d) is similar in form to the heat equation, the Crank-Nicolson implicit scheme will be adapted for the numerical solution. The Crank-Nicolson method is second order accurate in time and space, and is unconditionally stable.

In adapting the Crank-Nicolson method to Eq (C-52d), the following central difference formulas will be used (Anderson, Tannehill, and Pletcher, 1984:43-44):

$$\frac{\partial u}{\partial R} = \frac{u_{j+1} - u_{j-1}}{2\Delta R} + O[(\Delta R)^2] \quad (C-65)$$

$$\frac{\partial^2 u}{\partial R^2} = \frac{u_{j+1} - 2u_j + u_{j-1}}{(\Delta R)^2} + O(\Delta R^2) \quad (C-66)$$

Denoting u_z as u , the Crank-Nicolson representation of Eq (C-52d) is then

$$\frac{u_j^{n+1} - u_j^n}{\Delta t} = \frac{v}{2} [\delta_R^2 u_j^{n+1} + \delta_R^2 u_j^n] - \frac{1}{2\rho} \left(\frac{\partial p^{n+1}}{\partial z} + \frac{\partial p^n}{\partial z} \right) + g \quad (C-67)$$

where

$$\delta_R^2 u_j = \frac{u_{j+1} - 2u_j + u_{j-1}}{(\Delta R)^2} + \frac{u_{j+1} - u_{j-1}}{2R\Delta R} \quad (C-68)$$

Substituting Eq (C-68) into Eq (C-67) and rearranging,

$$b_j u_{j-1}^{n+1} + d u_j^{n+1} + a_j u_{j+1}^{n+1} = B_j u_{j-1}^n + D u_j^n + A_j u_{j+1}^n - \frac{\Delta t}{2\rho} \left(\frac{\partial p^{n+1}}{\partial z} + \frac{\partial p^n}{\partial z} \right) + \Delta t g \quad (C-69)$$

where

$$b_j = -\frac{v\Delta t}{2\Delta R} \left(\frac{1}{\Delta R} - \frac{1}{2R} \right) \quad (C-70)$$

$$d = 1 + \frac{v\Delta t}{(\Delta R)^2} \quad (C-71)$$

$$a_j = -\frac{v\Delta t}{2\Delta R} \left(\frac{1}{\Delta R} + \frac{1}{2R} \right) \quad (C-72)$$

$$B_j = \frac{v\Delta t}{2\Delta R} \left(\frac{1}{\Delta R} - \frac{1}{2R} \right) = -b_j \quad (C-73)$$

$$D = 1 - \frac{v\Delta t}{(\Delta R)^2} \quad (C-74)$$

$$A_j = \frac{v\Delta t}{2\Delta R} \left(\frac{1}{\Delta R} + \frac{1}{2R} \right) = -a_j \quad (C-75)$$

The factors d and D are not dependent upon the node, but b_j , a_j , B_j , and A_j are different for every node due to the presence of R . At the boundaries, $u_0 = 0$ and $u_{m+1} = 0$, where m is the number of grid spaces, so

$$d u_1^{n+1} + a_1 u_2^{n+1} = D u_1^n + A_1 u_2^n - \frac{\Delta t}{2\rho} \left(\frac{\partial p^{n+1}}{\partial z} + \frac{\partial p^n}{\partial z} \right) + \Delta t g \quad (C-76)$$

$$b_m u_{m-1}^{n+1} + du_m^{n+1} = B_m u_{m-1}^n + Du_m^n - \frac{\Delta t}{2\rho} \left(\frac{\partial p^{n+1}}{\partial z} + \frac{\partial p^n}{\partial z} \right) + \Delta t g \quad (C-77)$$

Equations (C-69), (C-76), and (C-77) can be stated in matrix terms in the following fashion:

$$\begin{pmatrix} d & a_1 & 0 & \cdots & 0 & 0 \\ b_2 & d & a_2 & 0 & & 0 \\ 0 & b_3 & d & a_3 & & 0 \\ \vdots & & & \ddots & & \vdots \\ 0 & & b_{m-1} & d & a_1 & 0 \\ 0 & 0 & \cdots & 0 & b_m & d \end{pmatrix} \begin{pmatrix} u_1^{n+1} \\ u_2^{n+1} \\ u_3^{n+1} \\ \vdots \\ u_{m-1}^{n+1} \\ u_m^{n+1} \end{pmatrix} = \begin{pmatrix} D & A_1 & 0 & \cdots & 0 & 0 \\ B_2 & D & A_2 & 0 & & 0 \\ 0 & B_3 & D & A_3 & & 0 \\ \vdots & & & \ddots & & \vdots \\ 0 & & B_{m-1} & D & A_1 & 0 \\ 0 & 0 & \cdots & 0 & B_m & D \end{pmatrix} \begin{pmatrix} u_1^n \\ u_2^n \\ u_3^n \\ \vdots \\ u_{m-1}^n \\ u_m^n \end{pmatrix} + \begin{pmatrix} \zeta \\ \zeta \\ \zeta \\ \vdots \\ \zeta \\ \zeta \end{pmatrix} \quad (C-78)$$

In terms of knowns and unknowns, the matrix relation is

$$Ax = By + \zeta \quad (C-79)$$

where x is the matrix of unknown velocity components. This relation can be stated more generally as

$$Ax = C \quad (C-80)$$

with $C=By+z$, or, at the n-time level,

$$C_1 = Du_1^n + A_1 u_2^n + \zeta \quad (C-81a)$$

$$C_j = B_j u_{j+1}^n + Du_j^n + A_j u_{j-1}^n + \zeta \quad (C-81b)$$

$$C_m = B_m u_{m-1}^n + Du_m^n + \zeta \quad (C-81c)$$

where

$$\zeta = -\frac{\Delta t}{2\rho} \left(\frac{\partial p^{n+1}}{\partial z} + \frac{\partial p^n}{\partial z} \right) + \Delta t g \quad (C-82)$$

The matrix A is a tri-diagonal matrix, so the system of equations can be solved with the Thomas algorithm which is described in Section C.3. For given Δx and Δt , the elements of the A matrix are fixed, so the factoring of the left hand side of Eq (C-78) only

needs to be carried out once. However, since the flow is initiated with an impulsive start, the time interval will initially be very small, and then increased as $\partial u/\partial t$ becomes smaller.

The pressure gradient is calculated from Eqs (C-62) - (C-64). Equation (C-63) is integrated using Simpson's 1/3 rule, which is fourth order accurate (Gerald, 1978:215):

$$\int_{R_H}^{R_o} u(2\pi R) dR = \frac{2\pi\Delta R}{3} (R_H u_0 + 4R_1 u_1 + 2R_2 u_2 + 4R_1 u_1 + 2R_2 u_2 + \dots + 2R_{m-1} u_{m-1} + 4R_m u_m + R_o u_{m-1})$$

$$= \frac{2\pi\Delta R}{3} (4R_1 u_1 + 2R_2 u_2 + 4R_1 u_1 + 2R_2 u_2 + \dots + 2R_{m-1} u_{m-1} + 4R_m u_m)$$

(C-83)

This method requires an even number of spaces, which means an odd number of grid lines.

The integral in equation (C-64) is integrated numerically using the trapezoidal rule, which is second order accurate (Gerard, 1978:210):

$$\int_0^t Q dt = \frac{\Delta t}{2} (Q^0 + 2Q^1 + 2Q^2 + 2Q^3 + \dots + 2Q^{n-1} + Q^n)$$

(C-84)

Equation (C-84) can be rearranged into the following form:

$$\int_0^t Q d\tau = \frac{\Delta t^1}{2} (Q^0 + Q^1) + \frac{\Delta t^2}{2} (Q^1 + Q^2) + \frac{\Delta t^3}{2} (Q^2 + Q^3) + \dots + \frac{\Delta t^{n-1}}{2} (Q^{n-2} + Q^{n-1}) + \frac{\Delta t^n}{2} (Q^{n-1} + Q^n)$$

(C-85)

Substituting this result into Eq (C-64)

$$V_a^n = V - \frac{\Delta t^1}{2} (Q^0 + Q^1) + \frac{\Delta t^2}{2} (Q^1 + Q^2) + \frac{\Delta t^3}{2} (Q^2 + Q^3) + \dots + \frac{\Delta t^{n-1}}{2} (Q^{n-2} + Q^{n-1}) + \frac{\Delta t^n}{2} (Q^{n-1} + Q^n)$$

(C-86)

Now, at the previous time level,

$$V_a^{n-1} = V - \frac{\Delta t^1}{2} (Q^0 + Q^1) + \frac{\Delta t^2}{2} (Q^1 + Q^2) + \frac{\Delta t^3}{2} (Q^2 + Q^3) + \dots + \frac{\Delta t^{n-1}}{2} (Q^{n-2} + Q^{n-1})$$

(C-87)

Substituting Eq (C-87) into Eq (C-86) results in the following:

$$V_a^n = V_a^{n-1} + \frac{\Delta t^n}{2}(Q^{n-1} + Q^n) \quad (C-88)$$

This result can be re-written so that

$$V_a^{n+1} = V_a^n + \frac{\Delta t^{n+1}}{2}(Q^n + Q^{n+1}) \quad (C-88a)$$

Note that the superscript denotes the time level, not a power.

Equation (C-88a) is used in Eq (C-63) to calculate the pressure gradient at the n+1 time level. As can be seen, in the original finite difference expression, Eq (C-69), the pressure gradient must be known at the new time level in order to calculate the velocity components at the new time level. This requires an iterative process in which the new pressure gradient is guessed, the new velocity components calculated, and the new pressure gradient calculated and compared to the guessed pressure gradient. The initial guess is the previous pressure gradient, and the calculated pressure gradient can then form the new guess. This process requires that the velocities and pressure gradient at the previous time level be retained until the iteration is complete.

C.2.2.4. Convergence

The numerical method was verified by grid refinement and by comparison with the exact solution for steady flow through an annulus, for which the velocity profile is (White 1991:120)

$$u_z = \frac{\pi}{8\mu} \left(-\frac{dp}{dz} \right) \left[R_o^4 - R_H^4 - \frac{(R_o^2 - R_H^2)^2}{\ln(R_o/R_H)} \right]$$

Results of the convergence studies for $\nu=200$ cSt are shown in Figures C-7 and C-8.

C.3. Thomas Algorithm

The Thomas algorithm is used to solve the matrix equation $Ax=C$, where A is a tridiagonal matrix. The Thomas algorithm was used for both the heat conduction and the flow through concentric annulus problem.

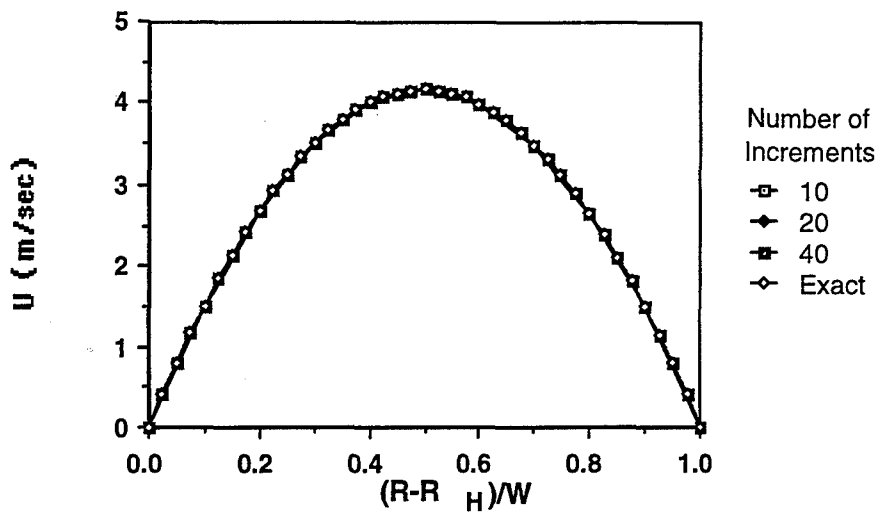


Figure C-7 Final Velocity Profiles for Different Spatial Increments

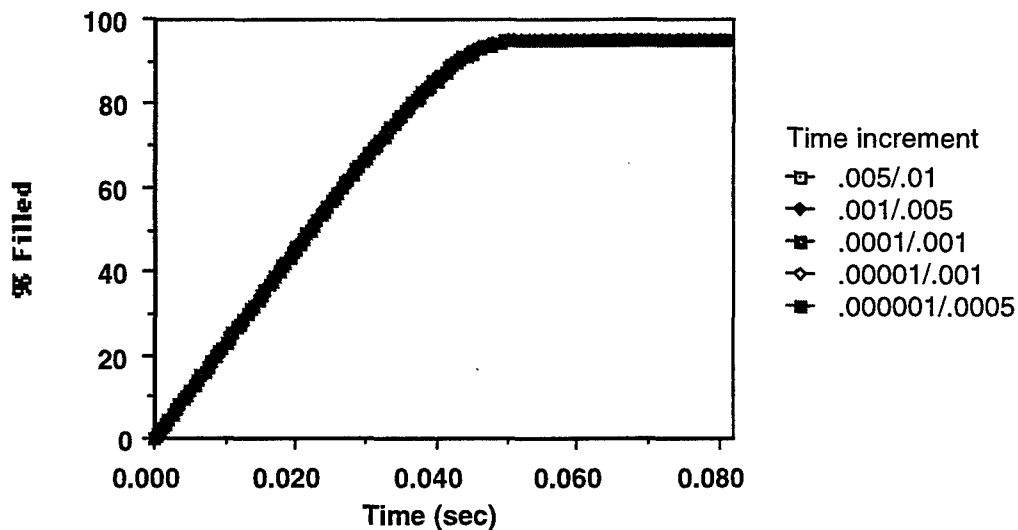


Figure C-8 Time to Fill for Different Temporal Increments

The Thomas algorithm works as follows (Anderson, Tannehill, and Pletcher, 1984:99): Wit the matrix notation as shown,

$$\begin{pmatrix} d_1 & a_1 & 0 & \cdots & 0 & 0 \\ b_2 & d_2 & a_2 & 0 & & 0 \\ 0 & b_3 & d_3 & a_3 & & 0 \\ \vdots & & & \ddots & & \vdots \\ 0 & & & b_{m-1} & d_{m-1} & a_1 \\ 0 & 0 & \cdots & 0 & b_m & d_m \end{pmatrix} \begin{pmatrix} x_1^{n+1} \\ x_2^{n+1} \\ x_3^{n+1} \\ \vdots \\ x_{m-1}^{n+1} \\ x_m^{n+1} \end{pmatrix} = \begin{pmatrix} C_1 \\ C_2 \\ C_3 \\ \vdots \\ C_{m-1} \\ C_m \end{pmatrix} \quad (\text{C-89})$$

the system is first put into upper triangular form by replacing the diagonal elements with

$$d_{j(\text{new})} = d_j - \frac{b_j}{d_{j-1}} a_{j-1} \quad j = 2, 3, \dots, m \quad (\text{C-90})$$

and the elements of the C matrix with

$$C_{j(\text{new})} = C_j - \frac{b_j}{d_{j-1}} a_{j-1} \quad j = 2, 3, \dots, m \quad (\text{C-91})$$

Back substitution is then used to compute the unknown x's:

$$x_m^{n+1} = \frac{C_m}{d_m} \quad (\text{C-92})$$

and

$$x_j^{n+1} = \frac{C_j - a_j x_{j+1}^{n+1}}{d_j} \quad j = m-1, m-2, \dots, 1 \quad (\text{C-93})$$

When the elements of the A matrix are fixed, the factoring in Eq (C-90) only needs to be carried out once. However, for both applications which used this algorithm, an impulsive start was involved, the time interval was initially be very small, and then increased as $\partial x / \partial t$ became smaller. This required that the elements of the A matrix be re-calculated for each change in Δt , which also required the factoring in Eq (C-90) to be reaccomplished. Equations (C-91) - (C-93) need to be recalculated at each time level.

C.4. Unsteady Reflected Expansion Wave

In a shock tunnel, the expansion of the driver gas reflects from the back of the driver tube and can then overtake the incident shock passing through the driven gas, de-

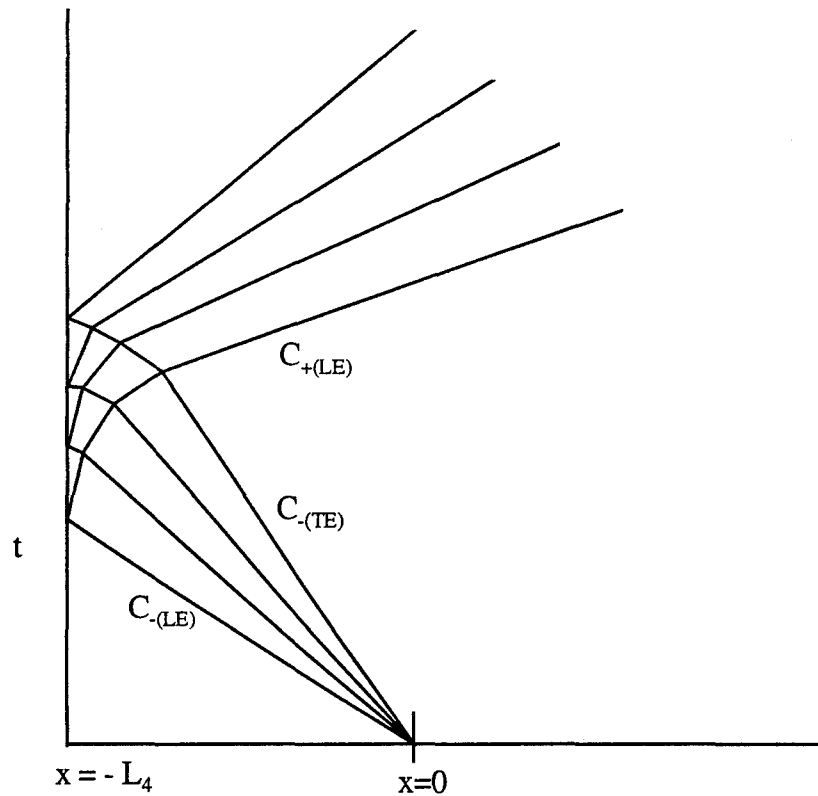


Figure C-9 Characteristics for Reflected Expansion Wave

pending on the length of the tube and the strength of the shock. To calculate the time for the reflected expansion to catch the contact surface requires calculation of the time that the reflection takes.

C.4.1. Method of Characteristics

The region where the reflected expansion passes through the initial expansion is a non-simple region in which two sets of characteristics govern the flow (Anderson, 1990:233). The time for the leading edge of the reflected wave to pass through this non-simple region can be determined through the method of characteristics (Figure C-9). The left running characteristics are denoted C_- , while the right-running characteristics are denoted C_+ .

The equations of the characteristics are given by (Anderson, 1990:229)

$$C_-: \frac{dx}{dt} = u - a \quad (C-94)$$

$$C_+: \frac{dx}{dt} = u + a \quad (C-95)$$

The Riemann invariants of the characteristics are (Anderson, 1990:229)

$$J_- = u - \int \frac{dp}{\rho a} \quad (C-96)$$

$$J_+ = u + \int \frac{dp}{\rho a} \quad (C-97)$$

Along each C. characteristic, the value of J_- is constant, while along each C_+ characteristic, the value of J_+ is constant. For a perfect gas, the Riemann invariants can be expressed in the following form:

$$J_- = u - \frac{2a}{\gamma - 1} \quad (C-98)$$

$$J_+ = u + \frac{2a}{\gamma - 1} \quad (C-99)$$

By adding Eqs (C-98) and (C-99), it can be seen that

$$u = \frac{1}{2}(J_+ + J_-) \quad (C-100)$$

while, by subtracting Eq (C-98) from Eq (C-99),

$$a = \frac{\gamma - 1}{4}(J_+ - J_-) \quad (C-101)$$

Then, substituting Eqs (C-100) and (C-101) into Eq (C-94), the following relations are obtained:

$$\frac{dx}{dt_-} = \left(\frac{1}{2} - \frac{\gamma - 1}{4}\right)J_+ + \left(\frac{1}{2} + \frac{\gamma - 1}{4}\right)J_- \quad (C-102)$$

Similarly, by substituting Eqs (C-100) and (C-101) into Eq (C-95),

$$\frac{dx}{dt_+} = \left(\frac{1}{2} + \frac{\gamma - 1}{4}\right)J_+ + \left(\frac{1}{2} - \frac{\gamma - 1}{4}\right)J_- \quad (C-103)$$

For the leading edge of the initial expansion, $u=0$, so, from Eq (C-98) and (C-99),

$$J_{-(LE)} = -\frac{2a_4}{\gamma_4 - 1} \quad (C-104)$$

$$J_{+(LE)} = \frac{2a_4}{\gamma_4 - 1} \quad (C-105)$$

For the trailing edge of the initial expansion, from Eq (C-98),

$$J_{-(TE)} = u_3 - \frac{2a_3}{\gamma_4 - 1} \quad (C-106)$$

Since u_3 and a_3 are already known from the shock tube pressure relations, this Riemann invariant can be calculated. Also, the leading edge of the reflected expansion is on the C_+ characteristic, so the J_+ invariant for the trailing edge is the same as for the leading edge:

$$J_{+(TE)} = \frac{2a_4}{\gamma_4 - 1} \quad (C-105)$$

C.4.2. Numerical Procedure

The numerical procedure divides the range of J characteristics into increments. Using the slopes for the characteristics, the position of each succeeding (x,t) point can be calculated. For this calculation, only the leading edge of the expansion of interest, because the purpose of the calculation is to determine the arrival time of the leading edge at the contact surface.

The time for the leading edge of the expansion to arrive at the back of the driver tube is given by

$$t_p = \frac{L_4}{a_4} \quad (C-107)$$

Also, for this point

$$x_p = L_4 \quad (C-108)$$

The slope of the J_+ characteristic is given by Eq (C-103), or denoting the reciprocal as m_+ ,

$$m_+ \equiv \frac{dt}{dx} = \frac{1}{\left(\frac{1}{2} + \frac{\gamma_4 - 1}{4}\right)J_+ + \left(\frac{1}{2} - \frac{\gamma_4 - 1}{4}\right)J_-} \quad (C-109)$$

The time position t_p and space position x_p of the previously calculated point are known. The m slope to the next point will be taken as the average of the slopes through the point (x_p, t_p) and the point (x_n, t_n) .

$$m_+ \approx \frac{1}{2}(m_{+p} + m_{+n}) \quad (\text{C-110})$$

The equation of the straight line with slope m_+ passing through the point (x_p, t_p) is given by

$$t = m_+x + b \quad (\text{C-111})$$

or, substituting in the values for the point (x_p, t_p) ,

$$b = t_p - m_+x_p \quad (\text{C-112})$$

so substituting this into Eq (C-111), the general equation of the line is then

$$t = m_+x + t_p - m_+x_p \quad (\text{C-113})$$

This line passes through the point (x_n, t_n) . The J. characteristic passing through this point has slope m_- which is calculated from Eq (C-102) as

$$m_- \equiv \frac{dt}{dx} = \frac{1}{\left(\frac{1}{2} - \frac{\gamma-1}{4}\right)J_+ + \left(\frac{1}{2} + \frac{\gamma-1}{4}\right)J_-} \quad (\text{C-114})$$

The equation of this line is

$$t_n = m_-x \quad (\text{C-115})$$

Substituting Eq (C-115) into Eq (C-113) to eliminate t results in

$$x_n = \frac{m_+x_p - t_p}{m_+ - m_-} \quad (\text{C-116})$$

The numerical procedure is as follows:

- (a) Calculate the J+ Riemann invariant from Eq (C-105)
- (b) Calculate the leading and trailing J- invariants from Eqs (C-104) and (C-106)

(c) Set

$$J_{-p} = J_{-(TE)} \quad (\text{C-117})$$

(d) Calculate m_{+p} from Eq (C-109)

(e) Divide the range of J- invariants into m increments

$$\Delta J_- = \frac{J_{-(LE)} - J_{-(TE)}}{m} \quad (\text{C-118})$$

(d) Calculate t_p and x_p from Eqs (C-107) and (C-108)

(e) Compute the next J invariant from

$$J_{-n} = J_{-p} + \Delta J_{-} \quad (C-119)$$

(f) Calculate the slopes m_{+n} and m_{-n} from Eqs (C-109) and (C-114)

(g) Calculate the average m_{+} slope from Eq (C-110)

(h) Compute x_n from Eq (C-116)

(i) Calculate t_n from Eq (C-115)

(j) Set $x_p = x_n$, $t_p = t_n$, and $J_{-p} = J_{-n}$

(h) Go to step (e) and repeat until $J_c = J_{-(LE)}$

C.4.3. Calculation of contact surface intercept point

The reflected expansion in the simple region travels with speed $u_3 + a_3$ and covers a distance of $x_c - x_n$ in the time period $t_c - t_n$. Mathematically, this can be expressed

$$(u_3 + a_3)(t_c - t_n) = x_c - x_n \quad (C-120)$$

In the time t_c , the contact surface has moved the distance x_c :

$$u_3 t_c = x_c \quad (C-121)$$

Substituting Eq (C-121) into Eq (C-120) to eliminate x_c and rearranging results in

$$t_c = \frac{(u_3 + a_3)t_n - x_n}{a_3} \quad (C-122)$$

The point of intercept is then given by Eq (C-121). These equations are valid provided that the speed of the contact surface has not changed, which would occur when the reflected shock strikes the contact surface. Since it is desired that the reflected shock strike the contact surface prior to the reflected expansion, the point of intercept x_c should be greater than the x location of the reflected shock/contact surface intercept.

C.4.4. Convergence

To verify convergence, the above method was used with several different increments for the following case:

$$a_3 = 923.281 \text{ m/s}$$

$$a_4 = 984.800 \text{ m/s}$$

$$a_3 = 677.807 \text{ m/s}$$

$$\gamma_4 = 1.66501$$

$$L_4 = 3.15 \text{ m}$$

The following results were obtained for the computation of the time t_n at which the leading edge of the reflected expansion finishes passing through the initial expansion:

Table C-1
Time vs. Number of
Increments

Number of increments	Time t_n (msec)
10	6.76583
20	6.76270
30	6.76212
40	6.76192
50	6.76184
60	6.76178
70	6.76176
80	6.76174
90	6.76174

Appendix D - High Temperature Gas Dynamics Iterative Procedures

D.1. Shock Tunnel Analysis

This section provides the iterative procedures which were used to analyze the shock tunnel performance. The development of the equations is described in Chapter 6.

D.1.1. Initial Shock

The five equations are

$$u_2 = a_4 \left(\frac{2}{\gamma_4 - 1} \right) \left[1 - \left(\frac{p_2}{p_4} \right)^{(\gamma_4 - 1)/2\gamma_4} \right] \quad (D-1)$$

$$u_s = \frac{p_2 - p_1}{\rho_1 u_2} \quad (D-2)$$

$$\rho_2 = \frac{\rho_1 u_s}{u_s - u_2} \quad (D-3)$$

$$h_2 = h_1 + \frac{1}{2} u_s^2 - \frac{1}{2} (u_s - u_2)^2 \quad (D-4)$$

$$h_2 = h(p_2, \rho_2) \quad (D-5)$$

The five unknowns are p_2 , u_2 , ρ_2 , u_s , h_2 . The iterative procedure is as follows:

- (a) Guess p_2
- (b) From Eq (D-1), calculate u_2
- (c) Compute u_s using Eq (D-2)
- (d) From Eq (D-3), calculate ρ_2
- (e) Use Eq (D-4) to compute h_2
- (f) Calculate h_2 from Eq (D-5)
- (g) Compare the h_2 from (f) to the h_2 from (e). If not within pre-determined error range, return to (a).

Reflected Shock and Converging Nozzle

The 12 equations are

$$u_s = \frac{p_2 - p_1}{\rho_1 u_2} \quad (D-2)$$

$$\rho_2 = \frac{\rho_1 u_s}{u_s - u_2} \quad (D-3)$$

$$h_2 = h_1 + \frac{1}{2} u_s^2 - \frac{1}{2} (u_s - u_2)^2 \quad (D-4)$$

$$h_2 = h(p_2, \rho_2) \quad (D-5)$$

$$\rho_5 = \frac{\rho_2 (u_2 + u_{sr})}{u_s + u_{sr}} \quad (D-6)$$

$$p_5 = p_2 + \rho_2 (u_2 + u_{sr})^2 - \rho_5 (u_s + u_{sr})^2 \quad (D-7)$$

$$h_5 = h_2 + \frac{1}{2} (u_2 + u_{sr})^2 - \frac{1}{2} (u_s + u_{sr})^2 \quad (D-8)$$

$$h_5 = h(p_5, \rho_5) \quad (D-9)$$

$$s = s(p_5, \rho_5) \quad (D-10)$$

$$h_t = h_5 + \frac{1}{2} u_5^2 \quad (D-11)$$

$$\rho_{th} = \rho(p_{th}, s) \quad (D-12)$$

$$h_{th} = h(p_{th}, \rho_{th}) \quad (D-13)$$

$$u_{th} = \sqrt{2(h_t - h_{th})} \quad (D-14)$$

$$a_{th} = a(p_{th}, s) \quad (D-15)$$

$$M_{th} = \frac{u_{th}}{a_{th}} \quad (D-16)$$

$$A_{th} = \left(\frac{\rho_5}{\rho_{th}} \right) \left(\frac{u_5}{u_{th}} \right) A_5 \quad (D-17)$$

The 12 unknowns are u_5 , u_{sr} , p_5 , ρ_5 , h_5 , h_t , s , u_{th} , p_{th} , ρ_{th} , h_{th} , and a_{th} . The iterative procedure is as follows:

- (a) Guess u_5
- (b) Guess u_{sr}
- (c) From Eq (D-6), calculate ρ_5
- (d) Compute p_5 using Eq (D-7)
- (e) From Eq (D-8), calculate h_5
- (f) Use Eq (D-9) to compute h_5
- (g) Compare the h_5 from (f) to the h_5 from (e). If not within pre-determined error range, return to (b)
- (h) From Eq (D-10), calculate s
- (i) Compute h_t using Eq (D-11)
- (j) Guess p_{th}
- (k) From Eq (D-12), calculate ρ_{th}
- (l) Compute h_{th} using Eq (D-13)
- (m) From Eq (D-14), calculate u_{th}
- (n) Use Eq (D-15) to compute a_{th}
- (n) Calculate M_{th} from Eq (D-16)
- (o) If the calculated M_{th} is not within pre-determined error range of 1, return to (j)
- (p) From (D-17), compute A_{th}
- (q) If the calculated A_{th} from (p) is not within pre-determined error range of actual A_{th} , return to (a)

D.1.3. Diverging Nozzle

The four equations are

$$\rho_6 = \rho(p_6, s) \quad (D-18)$$

$$h_6 = h(p_6, \rho_6) \quad (D-19)$$

$$u_6 = \sqrt{2(h_t - h_6)} \quad (D-20)$$

$$\rho_6 = \rho_{th} \left(\frac{u_{th}}{u_6} \right) \left(\frac{A_{th}}{A_6} \right) \quad (D-21)$$

The four unknowns are p_6 , ρ_6 , h_6 , and u_6 . The iterative procedure is as follows:

- (a) Guess p_6
- (b) From Eq (D-18), calculate ρ_6
- (c) Compute h_6 using Eq (D-19)
- (d) From Eq (D-20), calculate u_6
- (e) Use Eq (D-21) to compute ρ_6
- (f) Compare the ρ_6 from (e) to the ρ_6 from (b). If not within pre-determined error range, return to (a)

D.1.4. Test Section Stagnation Conditions

From the nozzle exit conditions, the stagnation properties can be calculated. Since the entropy s and total enthalpy h_t are known, the calculation makes use of the polynomial curve fits

$$h_t = h(p_t, \rho_t) \quad (D-22)$$

$$\rho_t = \rho(p_t, s) \quad (D-23)$$

The system consists of two equations with two unknowns p_t and ρ_t , which are solved using the following iterative procedure:

- (a) Guess p_t
- (b) From Eq (D-23), calculate ρ_t
- (c) Compute h_t using Eq (D-22)
- (d) Compare the h_t from (c) to the previously calculated h_t . If not within pre-determined error range, return to (a)

D.1.5. Tailored Condition

The three equations are

$$\rho_3(u_{sH} + u_3) = \rho_7(u_{sH} + u_5) \quad (D-24)$$

$$p_3 + \rho_3(u_{sH} + u_3)^2 = p_5 + \rho_7(u_{sH} + u_5)^2 \quad (D-24)$$

$$\frac{\gamma_4}{\gamma_4 - 1} \left(\frac{p_3}{\rho_3} \right) + \frac{1}{2} (u_{sH} + u_3)^2 = \frac{\gamma_4}{\gamma_4 - 1} \left(\frac{p_5}{\rho_7} \right) + \frac{1}{2} (u_{sH} + u_5)^2 \quad (D-25)$$

The three unknowns are p_5 , ρ_7 , u_{sH} . The p_5 here is not the actual p_5 , but is the p_5 required for the tailored condition. The iterative procedure is

- (a) Guess ρ_7
- (b) From Eq (D-23), calculate u_{sH}
- (c) Compute p_5 using Eq (D-22)
- (d) Use Eq (D-21) to compute p_5
- (e) Compare the p_5 from (d) to the p_5 from (c). If not within pre-determined error range, return to (a)

D.1.6. Speed of second shock reflection

The seven equations are

$$\rho_3(u_{sH} + u_3) = \rho_7(u_{sH} + u_7) \quad (D-26)$$

$$p_3 + \rho_3(u_{sH} + u_3)^2 = p_7 + \rho_7(u_{sH} + u_7)^2 \quad (D-27)$$

$$\frac{\gamma_4}{\gamma_4 - 1} \left(\frac{p_3}{\rho_3} \right) + \frac{1}{2} (u_{sH} + u_3)^2 = \frac{\gamma_4}{\gamma_4 - 1} \left(\frac{p_7}{\rho_7} \right) + \frac{1}{2} (u_{sH} + u_7)^2 \quad (D-28)$$

$$\rho_8(u_{sr2} - u_7) = \rho_5(u_{sr2} - u_5) \quad (D-29)$$

$$p_7 + \rho_8(u_{sr2} - u_7)^2 = p_5 + \rho_5(u_{sr2} - u_5)^2 \quad (D-30)$$

$$h_8 + \frac{1}{2} (u_{sr2} - u_7)^2 = h_5 + \frac{1}{2} (u_{sr2} - u_5)^2 \quad (D-31)$$

$$h_8 = h(p_7, \rho_8) \quad (D-32)$$

The seven unknowns are p_7 , ρ_7 , u_7 , ρ_8 , h_8 , u_{sH} , and u_{sr2} . The iterative procedure is as follows:

- (a) Guess u_{sH}
- (b) Guess u_7

- (c) From Eq (D-26), calculate ρ_7
- (d) Compute p_7 using Eq (D-27)
- (e) From Eq (D-28), calculate p_7
- (f) Compare the p_7 from (e) to the p_7 from (d). If not within pre-determined error range, return to (b)
- (g) Guess u_{st2}
- (h) From Eq (D-29), calculate ρ_8
- (i) Compute p_7 using Eq (D-30)
- (j) From Eq (D-31), calculate h_8
- (k) Use Eq (D-32) to compute h_8
- (l) Compare the h_8 from (k) to the h_8 from (j). If not within pre-determined error range, return to (g)
- (m) Compare the p_7 from (i) to the p_7 from (f). If not within pre-determined error range, return to (a)

D.1.7. Starting Dynamics

The eight equations are

$$\rho_{11}u_{SL} = \rho_{10}(u_{SL} - u_{10}) \quad (D-33)$$

$$u_{SL} = \frac{p_{10} - p_{11}}{\rho_{11}u_{10}} \quad (D-34)$$

$$h_{11} + \frac{u_{SL}^2}{2} = h_{10} + \frac{(u_{SL} - u_{10})^2}{2} \quad (D-35)$$

$$h_{10} = h(p_{10}, \rho_{10}) \quad (D-36)$$

$$\rho_9(u_{10} - u_{ST}) = \rho_6(u_6 - u_{ST}) \quad (D-37)$$

$$p_{10} + \rho_9(u_{10} - u_{ST})^2 = p_6 + \rho_6(u_6 - u_{ST})^2 \quad (D-38)$$

$$h_9 + \frac{(u_9 - u_{ST})^2}{2} = h_6 + \frac{(u_6 - u_{ST})^2}{2} \quad (D-39)$$

$$h_9 = h(p_{10}, \rho_9) \quad (D-40)$$

The eight unknowns are h_9 , ρ_9 , u_{ST} , h_{10} , u_{10} , p_{10} , ρ_{10} , and u_{SL} . The solution procedure is an iteration which first calculates conditions behind the trailing shock using a guessed u_{10} . The resulting p_9 is then set equal to p_{10} , and the leading shock calculation is carried out to determine u_{10} . A new guess for u_{10} is then generated, and the iteration is continued until u_9 and u_{10} are equal. The complete procedure is as follows:

- (a) Guess u_{10}
- (b) Guess u_{ST}
- (c) From Eq (D-37), calculate ρ_9
- (d) Compute p_{10} using Eq (D-38)
- (e) From Eq (D-39), calculate h_9
- (f) Use Eq (D-40) to compute h_9
- (g) Compare the h_9 from (f) to the h_9 from (e). If not within pre-determined error range, return to (b)
- (h) Guess u_{10}
- (i) From Eq (D-34), calculate u_{SL}
- (j) Compute ρ_{10} using Eq (D-33)
- (k) From Eq (D-35), calculate h_{10}
- (l) Use Eq (D-36) to compute h_{10}
- (m) Compare the h_{10} from (l) to the h_{10} from (k). If not within pre-determined error range, return to (h)
- (n) Compare the u_{10} from (h) to the u_{10} from (a). If not within pre-determined error range, return to (a)

D.2. Shock Tunnel Data Reduction Program

The equations are the same as used in the previous section. However, p_5 and p_6 are knowns, while p_2 is calculated from p_5 rather than from the helium conditions. The helium conditions are not used in the data reduction program.

D.2.1. Incident Shock, Reflected Shock, and Converging Nozzle

The 16 equations are

$$\text{Incident shock} \quad u_2 = \frac{p_2 - p_1}{\rho_1 u_s} \quad (\text{D-2a})$$

$$\rho_2 = \frac{\rho_1 u_s}{u_s - u_2} \quad (\text{D-3})$$

$$h_2 = h_1 + \frac{1}{2} u_s^2 - \frac{1}{2} (u_s - u_2)^2 \quad (\text{D-4})$$

$$h_2 = h(p_2, \rho_2) \quad (\text{D-5})$$

$$\text{Reflected shock} \quad \rho_5 = \frac{\rho_2 (u_2 + u_{sr})}{u_s + u_{sr}} \quad (\text{D-6})$$

$$p_5 = p_2 + \rho_2 (u_2 + u_{sr})^2 - \rho_5 (u_s + u_{sr})^2 \quad (\text{D-7})$$

$$h_5 = h_2 + \frac{1}{2} (u_2 + u_{sr})^2 - \frac{1}{2} (u_s + u_{sr})^2 \quad (\text{D-8})$$

$$h_5 = h(p_5, \rho_5) \quad (\text{D-9})$$

$$s = s(p_5, \rho_5) \quad (\text{D-10})$$

$$h_t = h_5 + \frac{1}{2} u_5^2 \quad (\text{D-11})$$

$$\text{Converging nozzle} \quad \rho_{th} = \rho(p_{th}, s) \quad (\text{D-12})$$

$$h_{th} = h(p_{th}, \rho_{th}) \quad (\text{D-13})$$

$$u_{th} = \sqrt{2(h_t - h_{th})} \quad (\text{D-14})$$

$$a_{th} = a(p_{th}, s) \quad (\text{D-15})$$

$$M_{th} = \frac{u_{th}}{a_{th}} \quad (\text{D-16})$$

$$A_{th} = \left(\frac{\rho_5}{\rho_{th}} \right) \left(\frac{u_5}{u_{th}} \right) A_5 \quad (\text{D-17})$$

The 16 unknowns are p_2 , u_2 , ρ_2 , u_s , h_2 , u_5 , u_{sr} , ρ_5 , h_5 , h_t , s , u_{th} , p_{th} , ρ_{th} , h_{th} , and a_{th} . The iterative procedure is as follows:

- (a) Guess p_2
- (b) Guess u_s
- (c) Compute u_2 using Eq (D-2a)
- (d) From Eq (D-3), calculate ρ_2
- (e) Use Eq (D-4) to compute h_2
- (f) Calculate h_2 from Eq (D-5)
- (g) Compare the h_2 from (f) to the h_2 from (e). If not within pre-determined error range, return to (b).
- (h) Guess u_5
- (i) Guess u_{sr}
- (j) From Eq (D-6), calculate ρ_5
- (k) Compute p_5 using Eq (D-7)
- (l) From Eq (D-8), calculate h_5
- (m) Use Eq (D-9) to compute h_5
- (n) Compare the h_5 from (m) to the h_5 from (l). If not within pre-determined error range, return to (i)
- (o) From Eq (D-10), calculate s
- (p) Compute h_t using Eq (D-11)
- (q) Guess p_{th}
- (r) From Eq (D-12), calculate ρ_{th}
- (s) Compute h_{th} using Eq (D-13)
- (t) From Eq (D-14), calculate u_{th}
- (u) Use Eq (D-15) to compute a_{th}
- (v) Calculate M_{th} from Eq (D-16)
- (w) If the calculated M_{th} is not within pre-determined error range of 1, return to (j)
- (x) From (D-17), compute A_{th}

(y) If the calculated A_{th} from (x) is not within pre-determined error range of actual A_{th} , return to (h)

(z) If the calculated p_5 from (k) is not within pre-determined error range of actual p_5 , return to (a)

D.2.2. Diverging Nozzle

The four equations are

$$\rho_6 = \rho(p_6, s) \quad (D-18)$$

$$h_6 = h(p_6, \rho_6) \quad (D-19)$$

$$u_6 = \sqrt{2(h_t - h_6)} \quad (D-20)$$

$$\rho_6 = \rho_{th} \left(\frac{u_{th}}{u_6} \right) \left(\frac{A_{th}}{A_6} \right) \quad (D-21)$$

The four unknowns are ρ_6 , h_6 , and u_6 , and A_6 (the actual A_6 is known, but the effective A_6 which results from the boundary layer displacement thickness, is not known). An iterative procedure is not required, since p_6 is known and the unknowns can be calculated in one cycle. The fourth equation is decoupled and can be omitted except as a check (the effective A_6 should be less than the actual A_6)

(b) From Eq (D-18), calculate ρ_6

(c) Compute h_6 using Eq (D-19)

(d) From Eq (D-20), calculate u_6

Stagnation properties are then calculated as described in Section D.1.4, the speed of sound in the test section from $a=a(p,s)$, the Mach number from $M=u/a$, and the dynamic pressure from $q=\rho u^2/2$.

D.3. Oblique Shock

The equations for the oblique shock were developed in Section 6.3. The oblique shock relations were used both to calculate the equivalent flight condition and to calculate the flow about the fin in Chapter 7.

For the oblique shock, the relevant equations from Chapter 6 are

Continuity $\rho_1 u_{1n} = \rho_2 u_{2n}$ (6-1d)

Momentum $p_1 + \rho_1 u_{1n}^2 = p_2 + \rho_2 u_{2n}^2$ (6-2d)

Energy $h_1 + \frac{u_{1n}^2}{2} = h_2 + \frac{u_{2n}^2}{2}$ (6-3d)

where the subscript 1 refers to conditions before the shock and 2 to conditions after the shock. The subscript n denotes the component of the velocity normal to the shock. The component of the velocity normal to the shock can be calculated from

$$u_{1n} = U_1 \sin \beta \quad (\text{D-23})$$

where U denotes the magnitude of the velocity vector, and β represents the shock angle. The high temperature analysis makes use of the Tannehill and Mugge (1974) polynomial curve fits which will be represented by the following equations:

$$h = h(p, \rho) \quad (\text{D-24})$$

The procedure for calculating the oblique shock properties uses an iterative procedure similar to the normal shock.

- (a) Select β
- (b) Calculate u_{1n} from Eq (D-23)
- (c) Guess ρ_2
- (d) Calculate u_{2n} from Eq (6-1d)
- (e) Calculate p_c from Eq (6-2d)
- (f) Calculate h_2 from Eq (6-3d)
- (g) Calculate h_c from Eq (D-24)
- (h) Compare the h_2 calculated in step (f) to the h_2 from step (g). If the two values for h_2 are not equal, guess a new value of ρ_2 and repeat steps (b) - (h). Iterate until the two values for h_2 are within a pre-determined error range.

D.4. Centered expansion fan

The centered expansion fan is a high temperature version of the Prandtl-Meyer expansion fan. The equation equations are described in Chapter 7. The process is isentropic and is governed by

$$\int_{\theta_1}^{\theta_2} d\theta = \int_{M_1}^{M_2} \sqrt{M^2 - 1} \frac{dU}{U} \quad (7-1)$$

where θ represents the angle of inclination, M the Mach number, and U the magnitude of the velocity. The subscript 1 designates conditions before the expansion and the subscript 2 designates conditions after the expansion.

For high temperatures, Eq (7-1) must be solved numerically. If equilibrium chemistry is used, the relevant polynomial curve fits are represented by

$$h = h(p, \rho) \quad (7-7)$$

$$T = T(p, \rho) \quad (7-8)$$

$$\rho = \rho(p, s) \quad (7-9)$$

$$a = a(p, s) \quad (7-10)$$

In addition, the following definition of total enthalpy is used:

$$h_t = h + \frac{U^2}{2} = \text{const} \quad (7-11)$$

where U is the magnitude of the velocity vector. Equation (7-1) is evaluated numerically by using Simpson's 1/3 rule in the following form, which is derived from Eq (7-1):

$$\begin{aligned} \theta_2 = \sum_{i=1}^{n-1} \frac{\Delta U_1}{6} \left(\frac{\sqrt{M_i^2 - 1}}{U_i} + \frac{\sqrt{M_{i+1/2}^2 - 1}}{U_{i+1/2}} + \frac{\sqrt{M_{i+1}^2 - 1}}{U_{i+1}} \right) \\ + \frac{\Delta U_2}{6} \left(\frac{\sqrt{M_n^2 - 1}}{U_n} + \frac{\sqrt{M_{n+1/2}^2 - 1}}{U_{n+1/2}} + \frac{\sqrt{M_{n+1}^2 - 1}}{U_{n+1}} \right) \end{aligned} \quad (7-12)$$

Equation (7-12) uses n increments of width ΔU_1 and one smaller increment of width ΔU_2 . For a given expansion angle θ_2 , the interval width ΔU_1 is specified. The number of increments, n , is initially unknown, but can be estimated using the perfect gas solution. The integration is carried out until the summation exceeds the specified angle θ_2 . The summation is then backed up to the previous spatial step, and an iterative process is carried out to determine the proper value of ΔU_2 that will match the specified value of θ_2 .

The numerical procedure is as follows:

(a) From the conditions at 1, calculate h_t from Eq (7-11) and entropy, s , from Eq (7-9). The calculation of entropy from Eq (7-9) requires iteration as with the unsteady 1-d expansion in the shock tube.

(b) Calculate the speed of sound, a_1 , from Eq (7-10) and the Mach number from $M_1=U_1/a_1$

(c) Specify a velocity increment ΔU_1 to use in Eq (7-12). The velocity increment can be set by subdividing the perfect gas solution U_2 by a specified number of increments.

(d) Evaluate Eq (7-12) with ΔU_2 initially set equal to zero. For a given local value of U , do the following:

(1) Calculate the corresponding value of h from Eq (7-11)

(2) Guess p . The maximum value for p is the value that corresponds to the previous value of U

(3) Calculate ρ from Eq (7-9)

(4) Calculate h from Eq (7-7) and compare to the h calculated in step (e1).

If the values do not match, return to step (d2) and guess a new value of p .

(5) Compute the local speed of sound, a , from Eq (7-10)

(6) Calculate local Mach number from $M=U/a$

(e) Continue to increase n until the value of the summation exceeds the expansion angle θ_2 . As each spatial increment is added, the value of the summation at the previous increment $n-1$ should be retained.

(f) Return to the value of the summation at point $n-1$.

(g) Guess a value for ΔU_2 less than ΔU_1 .

(h) Evaluate Eq (7-12) using the guessed value of ΔU_2 . Compare the resulting value of the summation to the specified value of θ_2 . If the values do not match, return to step g and guess a new value of ΔU_2 .

Appendix E - Summary of Shock Tunnel Runs

Runs in the NASA Ames shock tunnel are summarized in Table E-1. This table shows runs with both AFIT and VPI gauges. The gauge nomenclature is as follows

- A1-A13: AFIT ULTEM 10 kHz Baseline
- A14-A15: AFIT ULTEM 20 kHz I-Beam
- V1-V4: Virginia Tech ULTEM and Victrex 20 kHz
- V5: Virginia Tech Victrex 14 kHz
- V6-V7: Virginia Tech Victrex 14 kHz (rubber filled)

AFIT high pressure shock tunnel runs are summarized in Table E-2.

Table E-1 NASA Ames Run Summary

Run	Test Date	FSC01	FSC02	FSI01	FSI02
2060	3/24/94	V2 a=2524 G=2k	A5 a=1775 G=2k	V1 a=2611 G=2k	A1 a=2400 G=5k
2061	3/30/94	V2	A5	V1	A1
2062	4/1/94	V2	A5	V1	A1
2063	4/6/94	V2	A5	V1	A1
2066	4/21/94	A6 a=2708 G=1k	A9 a=2921 G=1k	A7 2950 G=1k	A8 3072 G=1k
2070	5/6/94	No Gauge	V1 a=5222 G=1k	No Gauge	V2 a=5048 G=1k
2071	5/10/94	No Gauge	A2 a=2133 G=2k	No Gauge	V3 a=5505 G=2k
2078	6/13/94	A? a=3694 G=1k	V? a=7163 G=1k	V? a=11010 G=1k	No Gauge
2079	6/16/94	A4 a=3362 G=1k	A3 a=4273 G=1k	V1 a=6639 G=1k	No Gauge
2080	6/21/94	A3	A4	V1	No Gauge
2082	8/5/94	V6 1563 G=4k	A5 2654 G=1k	No Gauge	No Gauge
2083		V6	A5	No Gauge	No Gauge
2085	8/26/94	A14 a=3069 G=1k	A15 a=4168 G=1k	No gauge	No Gauge
2086	8/29/94	A14	A15	No Gauge	No Gauge
2087	9/2/94	A13 a = 3818 G=1k	A11 a=4531 G=1k	No Gauge	No Gauge
2088	9/7/94	A13	A11	No Gauge	No Gauge
2089	9/9/94	A13	A11	No Gauge	No Gauge
2090	9/13/94	V7 a=5417 G=1k	A12 a=3323 G=1k	No Gauge	No Gauge
2091	9/16/94	V7	V8 a=5083 G=1k	No Gauge	No Gauge
2092	9/20/94	V7	V8	No Gauge	No Gauge
2093	9/23/94	V9 a=4474 G=1K	No gage	No Gauge	No Gauge
2094				No Gauge	No Gauge

Table E-2 Summary of AFIT High Pressure Shock Tunnel Runs

<i>Run</i>	<i>Purpose</i>	<i>Configuration</i>	<i>Test Section</i>
1	Shock tube characterization	Shock tube - short driver	None
2	Shock tube characterization	Shock tube - short driver	None
3	Shock tunnel characterization	Shock tunnel-short driver	None
4	Gauge and thermal test	Short Driver	Nozzle floor extension
5	Gauge and thermal test	Short Driver	Nozzle floor extension
6	Gauge and thermal test	Short Driver	Nozzle floor extension
7	Gauge and thermal test	Short Driver	Nozzle floor extension
8	Gauge and thermal test	Short Driver	Nozzle floor extension
9	Gauge and thermal test	Short Driver-pressurized driven section	Nozzle floor extension
10	Gauge and thermal test	Short Driver	Nozzle floor extension
11	Directional gauge test	Long Driver	Nozzle floor extension
12	Directional gauge test	Long Driver	Nozzle floor extension
13	Directional gauge test	Long Driver	Nozzle floor extension
14	Directional gauge test	Long Driver	Nozzle floor extension
15	Gauge Oil Test	Long Driver	Inverted nozzle floor extension
16	Fin measurements	Long Driver	Duct with short fin
17	Fin measurements	Long Driver	Duct with short fin
18	Fin measurements	Long Driver	Duct with short fin
19	Pressure transducer check	Long Driver	Duct
20	Pressure transducer check	Long Driver	Duct
21	Pressure transducer check	Long Driver	Duct
22	Pressure transducer check	Long Driver	Duct
23	Pressure transducer check	Long Driver	Duct
24	Fin measurements	Long Driver	Duct with short fin
25	Fin measurements	Long Driver	Duct with short fin
26	Fin measurements	Long Driver	Duct with short fin
27	Fin measurements	Long Driver	Duct
28	Fin measurements	Long Driver	Duct
29	Fin measurements	Long Driver	Duct with short fin
30	Fin measurements	Long Driver	Duct with short fin
31	Fin measurements	Long Driver	Duct with short fin
32	Fin measurements	Long Driver	Duct
33	Fin measurements	Long Driver	Duct
34	Fin measurements	Long Driver	Duct with long fin
35	Mach number calibration	Long Driver	Duct with Pitot tube

Appendix F - Predicted Performance of AFIT Shock Tunnel

Table F-1 shows the predicted performance of the AFIT shock tunnel using the method described in Chapter 6. The predicted performance does not account for shock attenuation. As noted in Section 7.2, the actual performance of the shock tunnel is somewhat less than predicted in terms of pressures and temperature.

Table F-1 Predicted Performance of AFIT Shock Tunnel

Shock tube		Nozzle exit								
P_4 (atm)	P_1 (atm)	M	q (MPa)	u	Re_x $\times 10^6$	P (atm)	ρ (kg/m^3)	T (K)	T_t (K)	Steady flow (msec)
47.6	1.0	2.96	.78	1288	7.43	1.31	0.945	488	1218	2.41
61.2	1.0	2.92	.93	1347	7.76	1.60	1.023	551	1340	2.12
74.8	1.0	2.88	1.05	1394	7.99	1.86	1.085	606	1444	1.92
88.4	1.0	2.85	1.17	1433	8.19	2.10	1.137	653	1533	1.78
102.0	1.0	2.83	1.27	1467	8.34	2.32	1.177	696	1612	1.68

Appendix G - Uncertainty Analysis

This uncertainties associated with the skin friction measurements fall into three categories: the uncertainty in the measurement itself, the uncertainty in the angular resolution, and the uncertainty in the dynamic pressure calculation which affects the C_f computation.

E.1. Wall Shear Stress Uncertainty

The factors which affect the magnitude measurement were examined in Chapters 3 and 4. In addition, the non-linearity of the calibration was examined by calibrating over 21 points, assigning odds of 20:1, and throwing out the highest non-linearity. The highest remaining non-linearity was then 0.7 percent. This will be considered the calibration error. The magnitude measurement uncertainty is then summarized in Table G-1.

Table G-1 Wall Shear Stress Error

Source of error	Percent error
Calibration	0.7
Protrusion (p 3-14)	0.03
Viscoelasticity	0.003
Normal pressure	2.0
Temperature mismatch	3.4
Total error	6.1

The variation between three gauges in the AFIT Run 32 was 6 percent. Thus, the above analysis appears reasonable. Pressure gradient sensitivity is an area for further research and was not quantified.

E.2. Direction Uncertainty

Of the factors shown in Table G-1, three would affect direction: calibration non-linearity, viscoelasticity, and normal pressure sensitivity. These have a total error of 2.703 percent. For a nominal flow angle of 45 degrees, for which $\tan\eta=1$, the maximum error would be

$$\begin{aligned}\eta_{\text{measured}} &= \text{Tan}^{-1}\left(\frac{1+.02703}{1-.02703}\right) \\ &= 46.5^{\circ}\end{aligned}\quad (\text{G-1})$$

The maximum angular error is thus 1.5 degrees.

E.3. Dynamic Pressure Uncertainty

The dynamic pressure uncertainty is a result of the error in the pressure measurements. The non-linearity of the pressure transducer calibration was assessed in the same manner as the skin friction gauges. The nozzle exit pressure transducer had a non-linearity of 0.836 percent, while the nozzle entrance transducer had non-linearity of 0.525 percent. The maximum error in the ratio p_s/p_e is then

$$\epsilon = \frac{1+.00836}{1-.00525} - 1 = 0.0137 \quad (\text{G-2})$$

or 1.37 percent error. This pressure ratio is equivalent to p_t/p_e . The Mach number is related to by p_t/p_e (Anderson, 1989:155)

$$\frac{p_t}{p} = \left(1 + \frac{\gamma-1}{2} M^2\right)^{1/(\gamma-1)} \quad (\text{G-3})$$

The inverse of this relation is

$$M^2 = \frac{2}{\gamma-1} \left[\left(\frac{p_t}{p}\right)^{(\gamma-1)/\gamma} - 1 \right] \quad (\text{G-4})$$

The Mach number is related to the dynamic pressure through the following:

$$q = \frac{1}{2} \rho u^2 = \frac{1}{2} \rho M^2 a^2 = \frac{1}{2} \rho M^2 \frac{\gamma p}{\rho} = \frac{1}{2} \gamma p M^2$$

With M^2 given by Eq (G-4) , a 1.37 percent error in p/p coupled with a 0.836 percent error in p results in an error in q of 1.5 percent. Using the error of 6.1 percent for the wall shear stress, the maximum error in the C_f calculation is then

$$\frac{(1+.061)\tau_w}{(1-.015)q} = 1.077C_f \quad (G-5)$$

Thus the C_f measurement has a potential error of 7.7 percent. This uncertainty in dynamic pressure would not show up in the comparison of C_f for Run 32 because for a single run, the dynamic pressure error would affect all the C_f calculations equally.

Bibliography

Allen, H. Julian, and Joseph M. Spiegel. "Wind Tunnel Measurements," in *High Speed Problems of Aircraft and Experimental Methods*, Ed. A.F. Donovan, H.R. Lawrence, F.E. Goddard, R.R. Gilruth. Princeton NJ: Princeton University Press, 1961, pp. 648-683.

Allen, J.M. "Improved Sensing Element for Skin-Friction Balance Measurements," *AIAA Journal*, Vol. 18, No. 11, 1980, pp. 1342-1345

Allen, J.M. "Systematic Study of Error Sources in Skin-Friction Balance Measurements," NASA TN D-8291. Washington: National Aeronautics and Space Administration, 1976.

Alpher, R.A., and D.R. White. "Flow in Shock Tubes with Area Change at the Diaphragm Section," *Journal of Fluid Mechanics*, Vol. 3, Pt 5, February 1958, pp. 457-470.

Alvi, F.S., and G.S. Settles. "Physical Model of the Swept Shock/Boundary-Layer Interaction Flowfield," *AIAA Journal*, Vol. 30, No. 9, 1992, pp. 2252-2258

Anderson, Dale A., John C. Tannehill, and Richard H. Pletcher. *Computational Fluid Mechanics and Heat Transfer*. Washington: Hemisphere Publishing Corporation, 1984.

Anderson, John D. Jr. *Hypersonic and High Temperature Gas Dynamics*. New York: MacGraw-Hill Book Company, 1989.

Anderson, John D. Jr. *Modern Compressible Flow*. New York: MacGraw-Hill Book Company, 1990.

Avallone, Eugene A., and Theodore Baumeister III, eds. *Marks Standard Handbook for Mechanical Engineers, Ninth Edition*. New York: MacGraw-Hill Book Company, 1987.

Baals, Donald D., and William R. Corliss. *Wind Tunnels of NASA*. Washington: National Aeronautics and Space Administration, 1981.

Baldwin, B.S., and H. Lomax. "Thin Layer Approximation and Algebraic Model for Separated Turbulent Flows," AIAA Paper no. 78-257. Washington: American Institute of Aeronautics and Astronautics, 1978.

Beer, Ferdinand P., and E. Russell Johnston, Jr. *Mechanics of Materials*. New York: MacGraw-Hill Book Company, 1981.

Bejan, Adrian. *Convection Heat Transfer*. New York: John Wiley and Sons, 1984.

Bertin, John J. *Hypersonic Aerothermodynamics*, AIAA Education Series, Washington: American Institute of Aeronautics and Astronautics, 1994.

Bleakney, Walker, and R.J. Emrich, "The Shock Tube," in *High Speed Problems of Aircraft and Experimental Methods*, Ed. A.F. Donovan, H.R. Lawrence, F.E. Goddard, R.R. Gilruth. Princeton NJ: Princeton University Press, 1961, pp. 596-647.

Bowcutt, K.G., John D. Anderson, Jr, and D. Capriotti. "Viscous Optimized Hypersonic Waveriders," AIAA Paper 87-0272, Washington: American Institute of Aeronautics and Astronautics, 1987.

Bowersox, Rodney D.W., Joseph A. Schetz, Ken Chadwick, and Steve Deiwert. "A Technique for Direct Measurement of Skin Friction in High Enthalpy Impulsive Scramjet Flow Fields", *AIAA Journal*, Vol. 30, No. 7, 1995, pp. 1286-1291.

Bowersox, R., and J. Schetz. "Skin Friction Gauges for High Enthalpy Flows," AIAA paper 93-5097. Washington: American Institute of Aeronautics and Astronautics, 1993.

Bradshaw, Peter. "An Improved Van Driest Skin Friction Formula for Compressible Turbulent Boundary Layers," *AIAA Journal*, Vol. 15, 1977, pp. 212.

Brinich, P.F. "Boundary Layer Transition at Mach 3.12 with and without Single Roughness Element," NACA Technical Note 3267, Washington: National Advisory Committee for Aeronautics, 1954.

Callen, Herbert B. *Thermodynamics and an Introduction to Thermostatistics, Second Edition*. New York: John Wiley and Sons, 1985.

Calleja, J., and J. Tamagno. "Calibration of HYPULSE of Hypervelocity Air Flows Corresponding to Flight Mach Numbers 13.5, 15, and 17," NASA Contractor Report 191578. Ronkonkoma NY: General Applied Science Laboratories, 1993.

Cebeci, Tuncer, and Peter Bradshaw. *Physical and Computational Aspects of Convective Heat Transfer*. New York: Springer-Verlag, 1988.

Chadwick, K.M. *An Actively Cooled Floating Element Skin Friction Balance for Direct Measurement in High Enthalpy Supersonic Flows*, Ph.D. Dissertation. Blacksburg VA: Virginia Polytechnic Institute and State University, 1993.

Clauser, H.R., ed. *The Encyclopedia of Engineering Materials and Processes*. New York: Rheinhold Publishing Corporation, 1963.

Cook, W.J., "Response of Hot-Element Wall Shear Stress Gages in Unsteady Turbulent Flows," *AIAA Journal*, Vol. 32, No. 7, 1994, pp. 1464-1471.

Craig, Roy R. *Structural Dynamics: An Introduction to Computer Methods*. New York: John Wiley and Sons, 1981.

Dally, James W., and William F. Riley. *Experimental Stress Analysis*. New York: MacGraw-Hill Book Company, 1978.

Daum, Fred L. and George Gyarmathy. "Condensation of Air and Nitrogen in Hypersonic Wind Tunnels", *AIAA Journal*, Vol. 6, No. 3, 1968, pp. 458-467.

DeTurreis, D.J., J.A. Schetz, and R.F. Hellbaum. "Direct Measurements of Skin Friction in a Scramjet Combustor," AIAA Paper 90-2342. Washington: American Institute of Aeronautics and Astronautics, 1990.

Dhawan, S. "Direct Measurements of Skin Friction," NACA Report 1121. Washington: National Advisory Committee for Aeronautics, 1953.

Deiwert, G.S., J.A. Cavolowsky, and M.P. Loomis. "Large Scale Scramjet Testing in the Ames 16-Inch Shock Tunnel," AIAA Paper No. 94-2519. Washington: American Institute of Aeronautics and Astronautics, 1994.

Dow Corning Corp. "Information About Dow Corning Silicone Fluids." Midland MI: Dow Corning Corp., 1992

Van Driest, E.R. "Turbulent Boundary Layer in Compressible Fluids," *Journal of the Aeronautical Sciences*, Volume 18, No. 3, March 1951, pp. 145-160.

Van Driest, E.R. "The Problem of Aerodynamic Heating", *Aeronautical Engineering Review*, Vol. 15, No. 10, 1956, pp. 26-41.

Van Driest, E.R. "Experiments on Boundary Layer Transition at Supersonic Speeds," *Journal of the Aeronautical Sciences*, Vol. 24, 1957, pp. 885-899.

DSP Development Corp., *The DADiSP Worksheet Data Analysis and Display Software User Manual*. Cambridge MA: DSP Development Corp., 1992.

Eringen, A. Cemal. *Mechanics of Continua, Second Edition*. Huntington NY: Robert E. Krieger Publishing Company, 1980.

Findley, William N., James S. Lai, and Kasif Onaran. *Creep and Relaxation of Nonlinear Viscoelastic Materials*. Mineola NY: Dover Publications, 1989.

Fox, Robert W. and Alan T. McDonald. *Introduction to Fluid Mechanics*, Third Edition. John Wiley and Sons, 1985.

Garrison, T.J., G.S. Settles, N. Narayanswami, and D.D. Knight, "Laser Interferometer Skin-Friction Measurements of Crossing Shock-wave/Turbulent Boundary Layer Interactions", *AIAA Journal*, Vol. 32, No. 6, 1994, pp. 1234-1241.

Gerald, Curtis F. *Applied Numerical Analysis*. Reading MA: Addison-Wesley Publishing Company, 1978.

Gibbings, J.C. "On Boundary Layer Transition Wires," Aeronautical Research Council, CP-462, 1959.

Hansen, C.F. "Approximation for the Thermodynamic and Transport Properties of High Temperature Air," NACA TN 3895, Washington: National Advisory Committee for Aeronautics, January 1959.

Hayes, J.R. "Prediction Techniques for the Characteristics of Fin Generated Three Dimensional Shock Wave Turbulent Boundary Layer Interactions", AFFDL-TR-77-10. Wright-Patterson AFB, OH: Air Force Flight Dynamics Laboratory, May 1977.

Hazelton, D.M., R.D.W. Bowersox, and J.A. Schetz, "Directional Skin Friction Gauge for High Impulse Facilities," AIAA Paper 96-2800. Washington: American Institute of Aeronautics and Astronautics, 1996.

Heiser, William H., and David T. Pratt. *Hypersonic Airbreathing Propulsion*. Washington: American Institute of Aeronautics and Astronautics, 1994.

Hirt, F., U. Zurfluh, and H. Thomann. "Skin Friction Balances for Large Pressure Gradients," *Experiments in Fluids*, 1986, pp. 296-300.

Holman, J.P. *Heat Transfer, Fifth Edition*. New York: MacGraw-Hill Book Company, 1981.

Hopkins, Edward J., and Mamoru Inouye. "An Evaluation of Theories for Predicting Turbulent Skin Friction and Heat Transfer on Flat Plates at Supersonic and Hypersonic Mach Numbers," *AIAA Journal*, Vol. 9, No. 6, 1991, pp. 993-1003. 1991.

Horstmann, C.C. "Computation of Sharp Fin-Induced Shock Wave/Turbulent Boundary-Layer Interactions," *AIAA Journal*, Vol. 24, No. 9, pp. 1433-1440. Washington: American Institute of Aeronautics and Astronautics, 1986.

Hosford, William F., and Robert M. Caddell. *Metal Forming: Mechanics and Metallurgy*. Englewood Cliffs, NJ: Prentice-Hall, Inc., 1983.

Huffman, R.E. "A Mach 2.9 Investigation into the Flow Structure in the vicinity of a Wrap-Around Fin," Masters Thesis. Wright-Patterson Air Force Base OH: Air Force Institute of Technology, 1995.

Jack, J.R., and W.S. Diaconis. "Variation of Boundary-Layer Transition with Heat Transfer at Mach Number 3.12," NACA TN 3562. Washington: National Advisory Committee for Aeronautics, 1955.

Jack, J.R., R.J. Wisniewski, and W.S. Diaconis. "Effects of Extreme Surface Cooling on Boundary Layer Transition," NACA TN 4094. Washington: National Advisory Committee for Aeronautics, 1957.

John, James E.A. *Gas Dynamics*. Boston: Allyn and Bacon, 1984.

Von Karman, T. "The Analogy between Fluid Friction and Heat Transfer," *Transactions of the American Society of Mechanical Engineers*, Vol. 61, pp. 705-710. New York: American Society of Mechanical Engineers, 1939.

Kays, W.M., and M.E. Crawford. *Convection Mass and Heat Transfer*, 2nd Ed. New York: MacGraw-Hill Book Company, 1980.

Kim, K.-S., and G.S. Settles. "Skin Friction Measurement by Laser Interferometry in Swept Shock/Boundary Layer Interactions," *AIAA Journal*, Vol. 28, No. 1, 1990, pp. 133-139.

Kim, K.-S., Y. Lee, F.S. Alvi, G.S. Settles, and C.C. Horstman. "Laser Skin Friction Measurement and CFD Comparison of Weak-to-Strong Swept Shock/Boundary Layer Interactions," *AIAA Journal*, Vol. 29, No. 10, 1991, pp. 1643-1650.

Klebanoff, P.S., and K.D. Tidstrom. "Mechanism by Which a Two-Dimensional Roughness Element Induces Boundary Layer Transition," *Physics of Fluids*, Vol. 15, No. 7, 1972, pp. 1173-1188.

Klein, E.J., and A.P. Margozi. "Exploratory Investigation of the Measurement of Skin Friction by Means of Liquid Crystals," NASA TM X-1774. Washington: National Aeronautics and Space Administration, 1969.

Knight, , D.D., C.C. Horstman, B. Shapey, and S.M. Bogdonoff. "The Flowfield Structure of the 3_D Shock Wave/Boundary-Layer Interaction Generated by a 20 Degree Sharp Fin at Mach 3," AIAA Paper 86-0343, Jan. 1986.

Kovach, Ladis D. *Boundary Value Problems*. Reading MA: Addison-Wesley Publishing Company, 1984.

Korkegi, R.H. "A Simple Correlation for Incipient Turbulent Boundary-Layer Separation due to a Skewed Shock Wave," *AIAA Journal*, Vol. 11, No. 11, 1973, pp. 1178-1579.

Kreyszig, Erwin. *Advanced Engineering Mathematics*, Fourth Edition. New York: John Wiley & Sons, 1979.

Krieger, R.J., and S.R. Vukelich. "Tactical Missile Drag," in *Tactical Missile Aerodynamics*, Ed. M.J. Hemsch and J.N. Nielson, AIAA series *Progress in Astronautics and Aeronautics*, Washington: American Institute of Aeronautics and Astronautics, 1984.

Liepmann, H.W., and A. Roshko. *Elements of Gasdynamics*. New York: John Wiley and Sons, 1957.

MacArthur, R.C. "Transducer for Direct Measurement of Skin Friction in the Hypersonic Shock Tunnel," Calspan Report No. 129. Buffalo NY: Calspan Corp., 1963.

Micro Gage, Inc., *Semiconductor Strain Sensors, General Bulletin and Specification Sheet*, Micro Gage, Inc., El Monte CA, 1979.

Mirels, Harold. "Shock Tube Test Time Limitation Due to Turbulent-Wall Boundary Layer," *AIAA Journal*, Vol. 2, No. 1, 1964, pp. 84-88.

Nagamatsu, Henry T., "Hypersonic Experimental Facilities," in *High Speed Problems of Aircraft and Experimental Methods*, Ed. A.F. Donovan, H.R. Lawrence, F.E. Goddard, R.R. Gilruth. Princeton NJ: Princeton University Press, 1961a.

Nagamatsu, Henry T., "Shock Tube Technology and Design," in *Fundamental Data Obtained from Shock-Tube Experiments*, Ed. Antonio Ferri. New York: Pergamon Press, 1961b.

• National Oceanic and Atmospheric Administration, National Aeronautics and Space Administration, and United States Air Force. *U.S. Standard Atmosphere, 1976*. Washington: U.S. Government Printing Office, 1976.

Neubert, Hermann K.P. *Strain Gages: Kinds and Uses*. London: Macmillan and Company, 1967.

Neumann, R.D., and J.R. Hayes. "Introduction to Aerodynamic Heating Analysis of Supersonic Missiles," in *Tactical Missile Aerodynamics*, Ed. M.J. Hemsch and J.N. Nielson, AIAA series *Progress in Astronautics and Aeronautics*, Washington: American Institute of Aeronautics and Astronautics, 1984.

Nitsche, W., C. Haberland, and R. Thunker. "Comparative Investigations on Friction Drag Measuring Techniques in Experimental Aerodynamics," *ICAS Proceedings 1984*, pp. 391-403. Washington: American Institute of Aeronautics and Astronautics, 1984.

Novean, Michael G.B. *Direct Measurement of Skin Friction in Complex Supersonic Flows*, Ph.D.Dissertation. Blacksburg VA: Virginia Polytechnic Institute and State University, 1996.

Novean, M., J. Schetz, D. Hazelton, and R. Bowersox. "Skin Friction Measurements in Short Duration, High Enthalpy Flows," AIAA Paper 95-6109. Washington: American Institute of Aeronautics and Astronautics, 1995.

O'Donnell, F.B., and J.C. Westkaemper. "Measurement of Errors Caused by Misalignment of Floating Element Skin Friction Balances," *AIAA Journal*, Vol. 3, No. 1, pp. 163-165. Washington: American Institute of Aeronautics and Astronautics, 1984.

Paik, S.W. *Simultaneous Direct Measurements of Skin Friction and Heat Flux in a Supersonic Flow*, Ph.D.Dissertation. Blacksburg VA: Virginia Polytechnic Institute and State University, 1993.

Pope, R.A. "Skin-Friction Measurements in Laminar and Turbulent Flows Using Heated Thin-Film Gauges. *AIAA Journal*, Vol. 10, No. 6, 1972, pp. 729-730.

Reda, D.C., and J.D. Murphy, "Shock Wave Turbulent Boundary Layer Interaction in Rectangular Channels, Part II: The Influence of Sidewall Boundary Layers on Incipient Separation and Scale of Interaction," AIAA Paper no. 73-234. Washington: American Institute of Aeronautics and Astronautics, 1973.

Roberson, John A., and Clayton T. Crowe. *Engineering Fluid Dynamics*. Boston: Houghton Mifflin Company, 1975.

Saada, Adel S. *Elasticity: Theory and Applications*. New York: Pergamon Press, 1974.

Schetz, Joseph A. *Foundations of Boundary Layer Theory for Momentum, Heat, and Mass Transfer*. Englewood Cliffs, NJ: Prentice-Hall, 1984.

Schetz, Joseph A. *Boundary Layer Analysis*. Englewood Cliffs, NJ: Prentice-Hall, 1993.

Schetz, J.A., and B. Nerny. "Turbulent Boundary Layer with Injection and Surface Roughness," *AIAA Journal*, Vol. 15, No. 9, 1977, pp. 1288-1294.

Schlichting, Hermann. *Boundary-Layer Theory*. New York: MacGraw-Hill Book Company, 1979.

Schultz-Grunow, F. "New Frictional Resistance Law for Smooth Plates," NACA TM 986. Washington: National Advisory Committee for Aeronautics, September 1941.

Settles, G.S., and D.S. Dolling. "Swept Shock Wave/Boundary-Layer Interactions," in *Tactical Missile Aerodynamics: General Topics*, Ed. M.J. Hemsch, AIAA series *Progress in Astronautics and Aeronautics*, Washington: American Institute of Aeronautics and Astronautics, 1992.

Settles, G.S., and R.L. Kimmel. "Similarity of Quasiconical Shock-Wave/Turbulent Boundary-Layer Interactions," *AIAA Journal*, Vol. 24, No. 1, Washington: American Institute of Aeronautics and Astronautics, January 1986.

Settles, G.S., and F.K. Lu. "Conical Similarity of Shock/Boundary-Layer Interactions Generated by Swept and Unswept Fins," *AIAA Journal*, Vol. 23, No. 7, Washington: American Institute of Aeronautics and Astronautics, July 1985.

Skiest, Irving, ed. *Handbook of Adhesives, Third Edition*. New York: Van Nostrand Reinhold, 1985.

Smith, C. Edward. "The Starting Process in a Hypersonic Nozzle," *Journal of Fluid Mechanics*, Vol. 24, Pt 4, 1965, pp. 625-640.

Smith, J.M., and H.C. Van Ness. *Introduction to Chemical Engineering Thermodynamics*, Third Edition. New York: MacGraw-Hill Book Company, 1975.

Spalding, D.B., and S.W. Chi. "The Drag of a Compressible Turbulent Boundary Layer on a Smooth Flat Plate with and without Heat Transfer," *Journal of Fluid Mechanics*, January 1964, pp. 117-143.

Stetson, Kenneth F. "On Predicting Hypersonic Boundary Layer Transition," AFWAL-TM-84-160-FIMG. Wright-Patterson AFB OH: Flight Dynamics Laboratory, Air Force Wright Aeronautical Laboratories, March 1987.

Stoney, W.E., Jr. "Collection of Zero-Lift Drag Data on Bodies of Revolution from Free-Flight Investigations," NASA TR-R-100. Washington: National Aeronautics and Space Administration, 1961.

Tannehill, J.C., and P.H. Muggé. "Improved Curve Fits for the Thermodynamic Properties of Equilibrium Air Suitable for Numerical Computation Using Time-Dependent or Shock-Capturing Methods", NASA CR-2470. Washington: National Aeronautics and Space Administration, 1974.

Thomas, George B. Jr. *Calculus and Analytic Geometry, Alternate Edition*. Reading MA: Addison-Wesley Publishing Company, 1972.

Tipler, Paul A. *Physics*. New York: Worth Publishers, 1976.

Tokarcik-Polsky, Susan, and Jean-Luc Cambier. "Numerical Study of Transient Flow Phenomena in Shock Tunnels," *AIAA Journal*, Vol. 32, No. 5, pp. 971-978, Washington: American Institute of Aeronautics and Astronautics, May 1994.

Voisenet, R.L.P. "Temperature Step Effects on Direct Measurement of Skin Friction Drag," AIAA Paper 78-0779. Washington: American Institute of Aeronautics and Astronautics, January, 1978.

Wang, S.-Y., and S.M. Bogdonoff. "A Re-Examination of the Upstream Influence Scaling and Similarity Laws for 3-D Shock Wave/Turbulent Boundary-Layer Interaction," AIAA Paper 86-0347, Washington: American Institute of Aeronautics and Astronautics, January, 1986.

Weast, R.C. *CRC Handbook of Chemistry and Physics, 53rd Edition*. Cleveland: CRC Press, 1973.

Westkaemper, J.C. "Step-Temperature Effects on Direct Measurements of Drag," *AIAA Journal*, Vol. 1, No. 7, July 1963, pp. 1708-1710.

White, Frank M. *Viscous Fluid Flow, Second Edition*. New York: MacGraw-Hill Book Company, 1991.

Winter, K.G. "An Outline of the Techniques Available for the Measurement of Skin Friction in Turbulent Boundary Layers," *Progress in Aerospace Sciences*, Vol. 18, 1977.

Witliff, Charles E., Merle R. Wilson, and Abraham Hertzberg, "The Tailored-Interface Hypersonic Shock Tunnel," *Journal of the Aero/Space Sciences*, April 1959, pp. 219-227.

Vita

Major David M. Hazelton [REDACTED]

[REDACTED] He moved with his family to Clute, Texas, in 1964, where he graduated from Brazoswood High School in 1977. He then attended Lamar University in Beaumont, Texas, and graduated with a Bachelor of Science degree in mathematics in 1981. He was commissioned as a Second Lieutenant in the U.S. Air Force in August 1981 through the Reserve Officers Training Corps. He was assigned to Nellis AFB, Las Vegas, Nevada, in November 1981, where he served as the Assistant Chief of the Resource Management Division for the 554th Range Group, which operated the Nellis bombing and gunnery range. In February 1985, he was reassigned to Headquarters Tactical Air Command, Langley AFB, Hampton, Virginia, where he served as Range Plans and Programs Manager and subsequently Chief of the Range Budget, Plans, and Programs Branch. While in this assignment, he attended part-time Old Dominion University in Norfolk, Virginia, graduating in 1990 with a Master of Engineering degree in mechanical engineering. He was assigned to the Ballistic Missile Organization, Norton AFB, San Bernardino, California, in October 1990, where he served first as Financial Manager for the Peacekeeper Rail Garrison System Program Office and then as Deputy Chief of the Program Operations Division for the National Launch System Joint Program Office. He entered the Graduate School of Engineering, Air Force Institute of Technology, in June 1993. Following his completion of the doctoral program, he will be reassigned to the Advanced Propulsion Division in the Wright Laboratory, Wright-Patterson Air Force Base. Major Hazelton is married to the former Kathleen Linda Torres, who was born in [REDACTED]. They have two children, Elisabeth [REDACTED] and David [REDACTED].

[REDACTED]

[REDACTED]

REPORT DOCUMENTATION PAGE

Form Approved
OMB No. 0704-0188

Public reporting burden for this collection of information is estimated to average 1 hour per response, including the time for reviewing instructions, searching existing data sources, gathering and maintaining the data needed, and completing and reviewing the collection of information. Send comments regarding this burden estimate or any other aspect of this collection of information, including suggestions for reducing this burden, to Washington Headquarters Services, Directorate for Information Operations and Reports, 1215 Jefferson Davis Highway, Suite 1204, Arlington, VA 22202-4302, and to the Office of Management and Budget, Paperwork Reduction Project (0704-0188), Washington, DC 20503.

1. AGENCY USE ONLY (Leave blank)	2. REPORT DATE June 1996	3. REPORT TYPE AND DATES COVERED Doctoral Dissertation	
4. TITLE AND SUBTITLE Direct Measurement of Skin Friction in High Temperature and Impulsively Started Supersonic Flowfields		5. FUNDING NUMBERS	
6. AUTHOR(S) David M. Hazelton, Major, USAF			
7. PERFORMING ORGANIZATION NAME(S) AND ADDRESS(ES) Air Force Institute of Technology Wright-Patterson AFB OH 45433-6583		8. PERFORMING ORGANIZATION REPORT NUMBER AFIT/DS/ENY/96-9	
9. SPONSORING / MONITORING AGENCY NAME(S) AND ADDRESS(ES) ASC/NA (no longer exists) Wright-Patterson AFB OH 45433		10. SPONSORING / MONITORING AGENCY REPORT NUMBER	
11. SUPPLEMENTARY NOTES			
12a. DISTRIBUTION / AVAILABILITY STATEMENT Approved for public release; distribution unlimited		12b. DISTRIBUTION CODE	
13. ABSTRACT (Maximum 200 words) <p>This study further developed and improved a miniature plastic cantilever floating element gauge for direct measurement of skin friction in shock tunnel tests. Gauge durability and usability were improved, and potential sources of error were quantified. A high frequency 30 kHz gauge (compared to the baseline 10 kHz gauge) was constructed by using an I-beam cantilever rather than a round beam. A directional gauge was developed and demonstrated by measuring the flowfield about a fin in the AFIT shock tunnel. The 10 kHz and 30 kHz gauges were used in two scramjet test sequences conducted at Mach 14 enthalpy (stagnation temperature of 6,000K); the first at the NASA Ames 16 inch shock tunnel with steady run time of 2 msec, the second at General Applied Science Laboratories' Hypulse facility with run time of 0.4 msec. A lower frequency gauge was used in Wright Laboratory Mach 6 wind tunnel tests.</p> <p>The cantilever gauge proved to be a rugged and accurate method of measuring skin friction. The I-beam gauge provides high frequency capability for facilities with very short run times. The directional gauge facilitates skin friction measurement where crossflow exists. The scramjet measurements provided engine designers with valuable efficiency data.</p>			
14. SUBJECT TERMS Skin friction, wall shear stress, shock tunnels, hypersonic wind tunnels, hypersonics, hypersonic ground testing, hypersonic propulsion, scramjets, high enthalpy flows, turbulent boundary layers			15. NUMBER OF PAGES 372
			16. PRICE CODE
17. SECURITY CLASSIFICATION OF REPORT UNCLASSIFIED	18. SECURITY CLASSIFICATION OF THIS PAGE UNCLASSIFIED	19. SECURITY CLASSIFICATION OF ABSTRACT UNCLASSIFIED	20. LIMITATION OF ABSTRACT UL